



PACIFIC EARTHQUAKE ENGINEERING RESEARCH CENTER

Experimental Assessment of Columns with Short Lap Splices Subjected to Cyclic Loads

Murat Melek

John W. Wallace

University of California, Los Angeles

and

Joel P. Conte

University of California, San Diego

Experimental Assessment of Columns with Short Lap Splices Subjected to Cyclic Loads

Murat Melek

Department of Civil and Environmental Engineering
University of California, Los Angeles

John W. Wallace

Department of Civil and Environmental Engineering
University of California, Los Angeles

Joel P. Conte

Department of Structural Engineering
University of California, San Diego

PEER Report 2003/04
Pacific Earthquake Engineering Research Center
College of Engineering
University of California, Berkeley

April 2003

ABSTRACT

Splices in reinforced concrete columns in older buildings, or within the nonparticipating frames in some newer buildings, were typically designed as compression lap splices. Compression lap lengths are typically short (20 to $24d_b$), and only light transverse reinforcement is provided over the lap length. Observations of column damage following earthquakes have revealed that these splices perform poorly; however, relatively sparse information exists to assess the expected performance for typical conditions. To address these needs, a PEER Center research program was undertaken at UCLA to conduct testing of full-scale columns under a variety of conditions. The test specimens consisted of cantilever columns with a point load applied at the top. The 450 mm square column sections were tested under reversed cyclic lateral load with constant axial load. The primary variables include the level of axial load, the ratio of moment to shear, and the load history. Information on the test program, experimental observations, results, and conclusions are presented in this report.

Specimens with $20d_b$ lap-splice length and poorly confined cross section behaved unsatisfactorily under cyclic lateral loading. The lateral strength of specimens started degrading at lateral drift levels of 1.0% – 1.5% . The lateral strength degradation was due to the deterioration of the bond between the reinforcement bars and the surrounding concrete. Although higher levels of the applied axial load slightly increased the lateral strength of the specimens, changes in shear demand did not appear to influence the lateral load at which bond deterioration initiated.

The degradation rate of the lateral strength was affected by the lateral displacement history and shear demand. The specimen subjected to a near-fault displacement history maintained more than half of its lateral strength up to a drift ratio of 5% , whereas the specimens with standard displacement history lost more than 75% of their lateral strength at that drift level. A comparison of specimens with moderate to high shear demand revealed that lateral strength degradation also increased with higher shear demand.

The rotational response of the specimen was predominantly influenced by the slippage of reinforcement bars. At 1.5% lateral drift ratio, 80% – 85% of the measured rotation was due to slip.

The measured average bond strength gave an average of $0.95\sqrt{f_c'}$ MPa ($11.5\sqrt{f_c'}$ psi), whereas bond strength implied by ACI 318-02 Equation 12-3 provided a lower bound.

ACKNOWLEDGMENTS

This work made use of Pacific Earthquake Engineering Research Center Shared Facilities supported by the Earthquake Engineering Research Centers Program of the National Science Foundation under award number EEC-9701568.

The authors would like to thank former undergraduate students Matt Brunnings, Nick Bucci, Timothy Chen, Jim Norum, Matt Pollard, Chris Petteys, and Bryan Waters for their contributions to the construction, instrumentation, and testing of the column specimens. The assistance of UCLA Senior Development Engineer Harold Kasper in the laboratory and for materials testing was greatly appreciated. Special appreciation is extended to UCLA graduate students Kutay Orakcal, Thomas Hyun-Koo Kang, Paul Ko, Leonardo Massone, Brian Sayre, and Eunjong Yu, who helped at various stages of the experimental program.

The authors would also like to acknowledge Dr. Thomas Sabol, of Englekirk and Sabol Consulting Engineers, for his assistance in the review of reinforcement and gravity load levels in older buildings; Ms. Brenda Guyader, a former UCLA graduate student, for her contributions during the early stages of the project; Assistant Professor Dawn E. Lehman, of the University of Washington, and Assistant Professor Halil Sezen, of Ohio State University, for their valuable advice.

CONTENTS

ABSTRACT.....	iii
ACKNOWLEDGMENTS	iv
TABLE OF CONTENTS.....	v
LIST OF FIGURES	vii
LIST OF TABLES	xiii
NOMENCLATURE	xv
1 INTRODUCTION	1
1.1 General.....	1
1.2 Observations from Earthquake Damage	3
1.3 Objectives and Scope.....	4
1.4 Related Research.....	5
2 DESCRIPTION OF EXPERIMENTAL PROGRAM	9
2.1 Specimens	9
2.2 Materials	10
2.3 Construction of Specimens	11
2.4 Testing Apparatus	12
2.5 Instrumentation and Data Acquisition	13
2.6 Testing Procedure	15
3 EXPERIMENTAL RESULTS.....	17
3.1 Experimentally Observed Damage and Behavior.....	17
3.2 Lateral Load versus Top Displacement Relations	23
3.3 Moment versus Rotation Relations.....	27
3.4 Steel Strain Profiles.....	28
3.5 Shear Distortion	31
4 SUMMARY AND CONCLUSIONS	33
4.1 Summary.....	33
4.2 Conclusions.....	33
REFERENCES	37
APPENDIX: Strain Histories.....	129

LIST OF FIGURES

Figure 1.1	Splice Damage: Northridge Earthquake.....	39
Figure 1.2	Anchorage and Splice Damage	39
Figure 1.3	Comparison of Test Results (Aboutaha et al., 1996)	40
Figure 1.4	Lateral Load-Top Displacement Relations (Chai et al., 1991).....	40
Figure 1.5	Reinforcement Details.....	41
Figure 1.6	Comparison of Test Results (Valluvan et al., 1993)	41
Figure 1.7	Comparison of Test Results (Coffman et al., 1996).....	42
Figure 1.8	Test Setup (Lynn et al., 1996).....	43
Figure 1.9	Lateral Load-Top Displacement Relations (Lynn et al., 1996).....	44
Figure 2.1	Reinforcing Details	45
Figure 2.2	Standard Concrete Compressive Test	47
Figure 2.3	Stress-Strain Diagram for Specimens: S10MI, S20MI, and S30MI	48
Figure 2.4	Stress-Strain Diagram for Specimens: S20HI, S20HIN, and S30XI	48
Figure 2.5	Pedestal Reinforcement Details	49
Figure 2.6	Reinforcement Cage	50
Figure 2.7	Reinforcement Cages before Placing Concrete.....	50
Figure 2.8	Column Cross Section.....	51
Figure 2.9	Splice Region	51
Figure 2.10	Specimen	52
Figure 2.11	Joint Close-up.....	52
Figure 2.12	Test Setup	53
Figure 2.13	Test Setup with Reaction Frame	54
Figure 2.14	Test Setup during Experiment	54
Figure 2.15	Actuator Control Schematic	55
Figure 2.16	Strain Gauge Layout.....	56
Figure 2.17	Strain Gauge Labeling Scheme.....	57
Figure 2.18	External Instrumentation Grid (S10MI, S20MI, S30MI).....	58
Figure 2.19	Transducers Used to Measure Total and Slip Rotation at Column Base (S10MI, S20MI, S30MI).....	58

Figure 2.20	External Instrumentation (S20HI, S20HIN, S30XI)	59
Figure 2.21	Shear Instrumentation (S20HI, S20HIN, S30XI).....	59
Figure 2.22	External Instrumentation Layout (S10MI, S20MI, S30MI).....	60
Figure 2.23	External Instrumentation Layout (S20HI, S20HIN, S30XI).....	60
Figure 2.24	Test Specimen with Cable-Extension Position Transducers.....	62
Figure 2.25	Data Acquisition Device and MTS 407 Controller	62
Figure 2.26	Data Acquisition Schematic	63
Figure 2.27	Strain Gauge Amplifier	64
Figure 2.28	Data Logger Program Window	64
Figure 2.29	Standard Displacement History.....	65
Figure 2.30	Near-Fault Displacement History.....	65
Figure 3.1	Longitudinal Cracks Indicating Bond Deterioration (S20HI at 1.5% Drift) (Left)	68
Figure 3.2	Longitudinal and Shear Cracking (S20HIN at 5.8% Drift) (Right)	68
Figure 3.3	Concrete Spalling (S30XI at 3% Drift)	68
Figure 3.4	Specimen S20MI at 0.50% Lateral Drift.....	69
Figure 3.5	Specimen S20MI at 1.0% Drift (Left).....	69
Figure 3.6	Specimen S20MI at 1.5% Drift (Right)	69
Figure 3.7	Specimen S20MI at 2.0% Lateral Drift.....	70
Figure 3.8	Specimen S20MI at 3.0% Lateral Drift.....	70
Figure 3.9	Specimen S20MI at 5.0% Lateral Drift.....	71
Figure 3.10	Specimen S20MI at 7.0% Lateral Drift.....	71
Figure 3.11	Column Free-Body Diagram.....	72
Figure 3.12	Lateral Drift-Top Rotation	73
Figure 3.13	Lateral Drift-Axial Load	74
Figure 3.14	Specimen S10MI at 10% Lateral Drift—Axial Load Capacity Maintained	75
Figure 3.15	Specimen S20MI at 7% Lateral Drift after Axial Load Capacity Lost.....	75
Figure 3.16	Specimen S30MI at 5% Lateral Drift after Axial Load Capacity Lost.....	76
Figure 3.17	Specimen S20HI at 7% Lateral Drift after Axial Load Capacity Lost	76
Figure 3.18	Specimen S20HIN at 12% Lateral Drift—Axial Load Capacity Maintained.....	77
Figure 3.19	Specimen S30XI at 5% Lateral Drift after Axial Load Capacity Lost	77

Figure 3.20	Top Displacement due to Pedestal Rotation	78
Figure 3.21	Top Displacement due to Pedestal Rotation	79
Figure 3.22	Top Displacement due to Pedestal Movement	80
Figure 3.23	Top Displacement due to Pedestal Movement.....	81
Figure 3.24	Modified Lateral Displacement Histories	82
Figure 3.25	Modified Lateral Displacement Histories	83
Figure 3.26	Specimen S10MI Lateral Load-Top Displacement.....	84
Figure 3.27	Specimen S20MI Lateral Load-Top Displacement	84
Figure 3.28	Specimen S30MI Lateral Load-Top Displacement.....	85
Figure 3.29	Specimen S20HI Lateral Load-Top Displacement	85
Figure 3.30	Specimen S20HIN Lateral Load-Top Displacement	86
Figure 3.31	Specimen S30XI Lateral Load-Top Displacement	86
Figure 3.32	Base Moment/Yield Moment Comparison of S10MI, S20MI, and S30MI	87
Figure 3.33	Base Moment/Yield Moment Comparison of S20MI, S20HI, and S20HIN	88
Figure 3.34	Base Moment/Yield Moment Comparison of S30MI and S30XI.....	88
Figure 3.35	Measured Secant Stiffness— S10MI.....	89
Figure 3.36	Measured Secant Stiffness—S20MI	89
Figure 3.37	Measured Secant Stiffness— S30MI	90
Figure 3.38	Measured Secant Stiffness— S20HI	90
Figure 3.39	Measured Secant Stiffness— S20HIN	91
Figure 3.40	Measured Secant Stiffness— S30XI.....	91
Figure 3.41	Actual and Elastic-Perfectly-Plastic Load-Displacement Responses	92
Figure 3.42	Total Energy Dissipated by Actual and EPP Columns	93
Figure 3.43	Normalized Energy Dissipation	94
Figure 3.44	S10MI Base Moment-Total Rotation along Lap-Splice Length	95
Figure 3.45	S20MI Base Moment-Total Rotation along Lap-Splice Length	95
Figure 3.46	S30MI Base Moment-Total Rotation along Lap-Splice Length	96
Figure 3.47	S20HI Base Moment-Total Rotation along Lap-Splice Length	96
Figure 3.48	S20HIN Base Moment-Total Rotation along Lap-Splice Length.....	97
Figure 3.49	S30XI Base Moment-Total Rotation along Lap-Splice Length	97
Figure 3.50	S10MI Base Moment-Slip Rotation along Lap-Splice Length	98

Figure 3.51	S20MI Base Moment-Slip Rotation along Lap-Splice Length	98
Figure 3.52	S30MI Base Moment-Slip Rotation along Lap-Splice Length	99
Figure 3.53	S20HI Base Moment-Slip Rotation along Lap-Splice Length.....	99
Figure 3.54	S20HIN Base Moment-Slip Rotation along Lap-Splice Length	100
Figure 3.55	S30XI Base Moment-Slip Rotation along Lap-Splice Length.....	100
Figure 3.56	S10MI Moment-Rotation Envelopes	101
Figure 3.57	S20MI Moment-Rotation Envelopes	101
Figure 3.58	S30MI Moment-Rotation Envelopes	102
Figure 3.59	S20HI Moment-Rotation Envelopes	102
Figure 3.60	S20HIN Moment-Rotation Envelopes	103
Figure 3.61	S30XI Moment-Rotation Envelopes	103
Figure 3.62	Expected Strain Distribution along Splice Length.....	104
Figure 3.63	S10MI Strain Distribution along Splice Length—Exterior (NW) Bar	105
Figure 3.64	S10MI Strain Distribution along Splice Length—Interior (W) Bar	105
Figure 3.65	S20MI Strain Distribution along Splice Length—Exterior (NW) Bar	106
Figure 3.66	S20MI Strain Distribution along Splice Length—Interior (W) Bar	106
Figure 3.67	S30MI Strain Distribution along Splice Length—Exterior (NW) Bar	107
Figure 3.68	S30MI Strain Distribution along Splice Length—Interior (W) Bar	107
Figure 3.69	S20HI Strain Bar Distribution along Splice Length—Exterior (NE) Bar.....	108
Figure 3.70	S20HI Strain Distribution along Splice Length—Interior (W) Bar	108
Figure 3.71	S20HIN Strain Distribution along Splice Length—Exterior (NW) Bar	109
Figure 3.72	S20HIN Strain Distribution along Splice Length—Interior (W) Bar	109
Figure 3.73	S30XI Strain Distribution along Splice Length—Exterior (NW) Bar	110
Figure 3.74	S30XI Strain Distribution along Splice Length—Interior (W) Bar	110
Figure 3.75	Bilinear Steel Stress-Strain Model	111
Figure 3.76	S10MI Bond Stress-Lateral Drift (Bar NW).....	112
Figure 3.77	S10MI Bond Stress-Lateral Drift (Bar W).....	112
Figure 3.78	S20MI Bond Stress-Lateral Drift (Bar NW).....	113
Figure 3.79	S20MI Bond Stress-Lateral Drift (Bar W).....	113
Figure 3.80	S30MI Bond Stress-Lateral Drift (Bar NW).....	114
Figure 3.81	S30MI Bond Stress-Lateral Drift (Bar W)	114

Figure 3.82	S20HI Bond Stress-Lateral Drift (Bar NE)	115
Figure 3.83	S20HI Bond Stress-Lateral Drift (Bar W).....	115
Figure 3.84	S20HIN Bond Stress-Lateral Drift (Bar NW).....	116
Figure 3.85	S20HIN Bond Stress-Lateral Drift (Bar W).....	116
Figure 3.86	S30XI Bond Stress-Lateral Drift (Bar NW).....	117
Figure 3.87	S30XI Bond Stress-Lateral Drift (Bar W).....	117
Figure 3.88	S10MI Normalized Average Bond Stress-Lateral Drift.....	118
Figure 3.89	S20MI Normalized Average Bond Stress-Lateral Drift.....	118
Figure 3.90	S30MI Normalized Average Bond Stress-Lateral Drift.....	119
Figure 3.91	S20HI Normalized Average Bond Stress-Lateral Drift	119
Figure 3.92	S20HIN Normalized Average Bond Stress-Lateral Drift.....	120
Figure 3.93	S30XI Normalized Average Bond Stress-Lateral Drift	120
Figure 3.94	$u/\sqrt{f'_c}$ Comparison of Cyclic Column and Monotonic Beam Tests.....	122
Figure 3.95	Normalized Bond Stress vs. c_{\min}/d_b	122
Figure 3.96	Shear Deformation Measurement (S10MI, S20MI, and S30MI).....	123
Figure 3.97	S10MI Shear Deformation along Splice Length ($20d_b$)	123
Figure 3.98	S20MI Shear Deformation along Splice Length ($20d_b$)	124
Figure 3.99	S30MI Shear Deformation along Splice Length ($20d_b$)	124
Figure 3.100	Shear Deformation Measurement (S20HI, S20HIN, and S30XI)	125
Figure 3.101	S20HI Shear Deformation along Splice Length ($20d_b$)	126
Figure 3.102	S20HIN Shear Deformation along Splice Length ($20d_b$)	127
Figure 3.103	S30XI Shear Deformation along Splice Length ($20d_b$)	128

LIST OF TABLES

Table 1.1	Test Matrix (Lynn et al., 1996).....	43
Table 2.1	Test Matrix.....	46
Table 2.2	Calculated Shear Strengths	46
Table 2.3	Concrete Mix Design.....	46
Table 2.4	Aggregate Gradation (with Vulcan Materials, San Gabriel Valley (Reliance) Aggregates).....	47
Table 2.5	Concrete Properties.....	47
Table 2.6	Reinforcement Bar Properties.....	47
Table 2.7	Potentiometer Coordinates.....	61
Table 2.8	Data Point Numbers (S10MI, S20MI, S30MI, S20HI, S30XI).....	66
Table 2.9	Data Point Numbers (S20HIN).....	66
Table 3.1	Test Results Summary	67
Table 3.2	Observed Damage.....	67
Table 3.3	Axial Load Capacity Loss	67
Table 3.4	Moment Capacities	87
Table 3.5	Beam Tests Results.....	121

NOMENCLATURE

(Partial list: Additional variables used locally in text)

α	=	Reinforcement Location Factor
γ	=	Reinforcement Size Factor
β	=	Coating Factor
λ	=	Lightweight Aggregate Concrete Factor
Δ_y	=	Yield displacement
A_g	=	Gross Cross-Sectional Area
A_s	=	Area of Nonprestressed Tension Reinforcement
b_w	=	Column Width
c	=	Spacing or Cover Dimension
d	=	Effective Depth of The Column
d_b	=	Nominal Diameter of Reinforcing Bar
f_c	=	Concrete Compressive Strength
f_{ct}	=	Concrete Split-Tension Strength
f_r	=	Concrete Rupture Strength
f_y	=	Steel Yield Stress
h	=	Column Height
K_{tr}	=	Transverse Reinforcement Index
l_s	=	Splice Length
M_y	=	Yield Moment
M_n	=	Nominal Moment Strength
V_c	=	Concrete Shear-Strength
V_n	=	Nominal Shear-Strength
V_s	=	Steel Shear-Strength
V_u	=	Ultimate Shear

1 Introduction

1.1 GENERAL

Splices of column longitudinal reinforcement in older buildings (e.g., pre-1973) were commonly designed for compression only with relatively light transverse reinforcement enclosing the lap. For example, compression lap lengths of 20 longitudinal bar diameters are commonly found in older buildings, such as those designed with the 1956 and 1963 ACI codes. Under earthquake actions, a column may develop significant moments subjecting the longitudinal reinforcement to tensile stresses, particularly if the splice is located just above the floor slab, which is common in older construction. Given that required lap lengths for tension substantially exceed those required for compression, slip may occur along the splice length at load levels less than required to reach the nominal moment capacity of the column. The load-deformation responses of columns with splices that are representative of those found in older buildings are not well understood, and in particular, the degradation of strength and stiffness and the ability of the column to resist axial load after loss of lateral load capacity are of interest.

Splices of column longitudinal reinforcement for moment frames in new buildings (e.g., designed according to ACI 318-02 provisions) are required to be located within the middle third of the column, encased within closely spaced transverse reinforcement, and to develop the yield stress of the bar in tension. Deformation compatibility requirements often govern the design of splices for columns not designed to be part of the lateral-force-resisting system (UBC-94, Section 1631.2.4, and UBC-97, Section 1633.2.4). More stringent requirements for transverse reinforcement for these nonparticipating columns were incorporated within ACI 318-95, and subsequently into UBC-97, following damage observed in the 1994 Northridge earthquake. The need for these new provisions indicates that substandard lap-splice (and shear reinforcement) details exist even in relatively recent building construction (e.g., pre-1995).

Relatively little research has been conducted on the behavior of columns with deficient lap splices. Early work focused primarily on developing rehabilitation options for splices. Testing was conducted on columns subjected to pure tension (Valluvan et al., 1993) and columns subjected to uniaxial bending with no superimposed axial load (Aboutaha et al., 1996). Rehabilitation measures studied included the addition of external and internal ties, as well as the use of jackets (e.g., steel angles with straps or steel-plate jackets with and without through-bolts). For most rehabilitation options, brittle splice failures were suppressed and substantial inelastic (flexural) deformations were observed prior to the loss of lateral load capacity. Improving splice behavior is sometimes referred to as a “local” rehabilitation strategy, as the local capacities (strength, stiffness, ductility) of the element are improved.

For many older buildings, deficient column splices are likely to exist in a majority of building columns at many locations over the height of a building. Although rehabilitation of these columns is possible, as noted above, the rehabilitation methods typically result in substantial disruption to building functions and possibly even displacement of the occupants; therefore, it may not be economical or practical to rehabilitate column splices in buildings. To address these issues, rehabilitation options that minimize the impact on the occupants and building operations are desirable. A common strategy employed is to limit the drift imposed on the deficient columns by adding braces, shear walls, or a protective system (e.g., isolators, dampers) to the building such that the lateral deformations of the building are reduced to an acceptable level. By limiting the lateral building deformations, the forces imposed on the column splices are limited such that the spliced reinforcement is not subjected to significant tension. Rehabilitation guidelines (“Guidelines,” 1997) have been developed in recent years that are used by the engineering profession to accomplish this task (albeit, with unknown reliability). This rehabilitation strategy is sometimes referred to as a “global” rehabilitation strategy, as the goal is commonly to limit roof drift (a global response parameter) such that local responses (e.g., column moments, shears, and plastic rotations) meet specified acceptance criteria.

Although the “global” rehabilitation strategy is well accepted and the guidelines exist to assist in implementing the selected strategy, very sparse data exist on the performance of columns with “deficient” lap splices. This lack of knowledge on how the lateral-load behavior of column splices is influenced by important parameters such as axial load, shear, and load history leads to considerable uncertainty, and conservative and costly rehabilitation measures.

1.2 OBSERVATIONS FROM EARTHQUAKE DAMAGE

Brief summaries of splice damage observed in the 1994 Northridge, 1999 Izmit, and 1999 Chi-Chi, earthquakes are provided to identify common damage patterns associated with splices as well as to establish important performance issues.

Following the Northridge earthquake, shear and splice failures in reinforced concrete columns were commonly observed in older buildings and in building columns designed as nonparticipating elements. Splice damage at the base of an exterior column in a one-story parking structure is shown in Figure 1.1(a) (Sherman Oaks, near the 101/405 interchange). The column is approximately 450 mm square with $20d_b$ lap splices. Cross sections of the interior columns of this structure had been significantly increased to provide longer seat lengths for the precast floor girders; however, no apparent changes had been made to the exterior columns. Damage to the column indicated that slip had occurred along the splice, with spalling of concrete, which is fairly common for splice failures. Diagonal cracks in some of the exterior columns indicated that the shear capacities of these columns might have been compromised. The shear distress in some columns (and the lack of significant observed damage in the splice region) indicates a range of behavior for columns with presumably similar details.

Damage to columns of an eight-story parking structure located across the street (Ventura Boulevard) from the structure shown in Figure 1.1(a) is shown in Figure 1.1(b). The structure was designed using the 1982 UBC, and built in the mid-1980s. Although the columns in this structure had been designed with the lap splice near the mid-height of the column, “nonstructural” reinforced concrete exterior panels were cast directly against the columns, creating a captive column. The maximum moment for the captive column was shifted to the splice region, possibly leading to the observed damage. Splice damage was limited in this structure due to the extensive use of shear walls, which limited the lateral drift imposed on the columns.

Poor behavior of splices in exterior columns may have been a significant contributing factor in the collapse of buildings in the 1999 Izmit, Turkey, and Chi-Chi, Taiwan, earthquakes. Figure 1.2(a) shows a close-up of a typical beam-column connection region for a five- or six-story apartment building just east of Gölcük, Turkey. Straight anchorage lengths were used on the interior column bars, and the exterior column bars were extended through the joint and

anchored with short hooks into the top of the column in the story below. The failure surface between the column and the floor slab indicates that the interior column longitudinal bars were inadequately anchored, and pulled out, most likely at relatively low load levels, allowing the column to rotate freely. Lateral loads imposed on the columns under this condition lead to higher axial compression in the column (because the axial load for lateral and gravity loads are additive). The axial compression, when coupled with the column rotation caused by reinforcement slip, could lead to premature buckling of the exterior column longitudinal reinforcement passing through the joint.

Damage in the splice region was observed in a 12-story building in Nantou (Fig. 1.2(b)), Taiwan; however, the use of shear walls was a significant factor in limiting the damage to the columns. Damage also was observed at some of the exterior beam-column connections in a three-story building near Nantou, Taiwan. Failure at the exterior connection regions for this building may have been initiated by slip along the interior column splice bars, leading to significant rotation of the column. Under the column rotation, large compression would be exerted at the column edge, potentially leading to the peeling away of the concrete in the joint region.

In summary, column damage associated with the poor performance of splices has been consistently observed in recent earthquakes. In cases where the building system contains well-distributed shear walls, column damage has not led to collapse. Damage to exterior columns and building collapses observed in the 1999 earthquakes in Turkey and Taiwan may have been significantly impacted by splice behavior or poor anchorage.

1.3 OBJECTIVES AND SCOPE

The primary focus of this research is to produce essential and well-documented data on the behavior of full-scale interior columns with lap splices subjected to constant axial load and cyclic lateral load. The experimental program consists of design, construction, and testing of six reinforced concrete column specimens with pre-1963 construction details. The effects of axial loading, shear demand, and displacement history on specimen response were investigated. A detailed description of the experimental program is presented in Chapter 2, followed by a presentation of the experimental results (Chapter 3), and conclusions (Chapter 4).

1.4 RELATED RESEARCH

Studies of the behavior of lap splices subjected to cyclic loads date from the 1970s, with initial efforts focused on determining development length requirements for code provisions.

Studies by Orangun et al. (1977) and Sozen and Moehle (1990) summarized experimental results from beams with lap splices and formulated equations to improve existing code provisions for development and recommended splice lengths for deformed bars in tension. These studies revealed that development length and splice length could be evaluated in terms of steel stress, concrete strength, bar diameter, concrete cover, and transverse reinforcement (confinement). Based on these studies, new code provisions were introduced into the 1989 and 1995 ACI Building Codes (“Building,” 1989; 1995).

Additional work has been conducted to evaluate the response of lap splices in members subjected to earthquake induced cyclic loads, as well as techniques to improve the performance of inadequate lap splices. Several of these studies are summarized in the paragraphs that follow.

Research by Paulay et al. (1981) revealed the importance of confinement on the performance of members with lap splices. Twelve specimens with either 406.4 mm x 304.8 mm (16 in. x 12 in.) or 406.4 mm (16 in.) square cross sections with inadequate lap splice length ($l_{s \text{ provided}}/l_{s \text{ required}} = 0.82 \text{ to } 0.95$) were tested. Although inadequate splice lengths were provided, well-confined splices were able to develop the tensile yield stress of the reinforcement and maintain their lateral load capacity up to a displacement ductility of four. It was concluded that increasing the splice length did not have a significant effect on the lateral strength; however, closely spaced transverse reinforcement substantially improved the cyclic response of the lap splice by preventing splitting of concrete and maintaining the shear transfer along the splice. The beneficial effect of confinement on the behavior of members with lap splices directed researchers to investigate increasing confinement as a rehabilitation measure to improve splice performance. Several different methods of providing improved confinement to deficient splices were evaluated.

Two studies were conducted that focused on confining the splice region by using steel jackets. Chai et al. (1991) investigated the performance of circular bridge columns with pre-1971 construction details under constant axial and cyclic lateral loading, whereas Aboutaha et al. (1996) investigated the use of steel jackets on building columns with square and rectangular

cross sections. No axial load was applied to the columns in both of these test programs. Both sets of experiments revealed that reference specimens, with 20 bar diameter lap-splice lengths, experienced bond deterioration prior to reaching the nominal moment capacity at the critical section. An evaluation of the test results produced by Aboutaha (Fig. 1.3) and Chai (Fig. 1.4) indicates that using a steel jacket is an effective method for improving the cyclic response of the columns with compression lap splices. Even damaged specimens, once repaired with steel jackets, showed ductile behavior (Chai, 1991). Aboutaha concluded that rehabilitation of splices in members with rectangular cross sections required the steel jacket to be longer than the splice length and adhesive anchor bolts on each face of the column.

Valluvan et al. (1993) constructed and tested twelve, approximately two-thirds scale column specimens to investigate various rehabilitation measures. The test columns were 482.6 mm (19 in.) square and reinforced with 28.7 mm (#9) longitudinal bars and 9.5 mm (#3) hoops spaced 457.2 mm (18 in.) on center (Fig. 1.5). The specimens were subjected to reversed, cyclic axial loads (no bending). A reference specimen (no rehabilitation) was tested, and several approaches for providing confinement along the splice length were investigated, including the use of (1) steel angles and straps, (2) internal or external ties, or (3) welds along the spliced bars. The reference (no rehabilitation) specimen exhibited poor behavior under cyclic loading, with a sudden loss in the lateral load capacity at approximately two thirds the nominal moment capacity of the critical section (Fig. 1.6). The use of external steel angles and straps or ties were effective in improving splice performance, provided grout was used to achieve good contact between the existing concrete and the added confinement steel. Welding splices worked well provided additional ties were used to resist outward thrust produced by the eccentricity between the spliced bars. The use of internal ties was less effective, apparently because the removal of concrete cover to place the ties resulted in concrete micro-cracking that reduced the bond strength.

Coffman et al. (1993) also investigated the effectiveness of using external ties as a rehabilitation measure on bridge columns with $35d_b$ lap-splice lengths. Four, one-half scale, circular reinforced concrete columns with construction details representative of those used in the 1950s through the mid-1970s were tested. The splice regions of the specimens were confined with prestressed external hoops along the lower 1219.2 mm (4 ft) of the column. The size and spacing of the external hoops were varied to establish the effectiveness of adding prestressed

hoops. Columns were subjected to cyclic lateral and constant axial load ($0.10A_g f'_c$). The control specimen, with a $35d_b$ lap-splice length, was able to maintain the lateral load capacity up to a displacement ductility of four (Fig. 1.7) and reinforcing strains of five times the yield strain. The response of specimens rehabilitated with prestressed hoops indicated that the external hoops did not increase the lateral strength of specimens appreciably; however, the energy-dissipation capacity at each cycle was improved and the displacement ductility capacity increased (i.e., the lateral load capacity was maintained for an increased number of cycles to higher drift ratios).

Lynn (1996) investigated columns with pre-1970s construction details (Fig. 1.8). Eight, 457.2 mm (18 in.) square columns with eight longitudinal reinforcing bars and 9.525 mm (#3) hoops/ties at either 304.8 mm (12 in.) or 457.2 mm (18 in.) spacing on center were constructed. Longitudinal reinforcement consisted of either 25.4 mm (#8) or 32.3 mm (#10) diameter bars. Five specimens had continuous longitudinal reinforcement, whereas three specimens were provided with splices ($20d_b$ and $25d_b$) at the bases of the columns. Table 1.1 presents a summary of the test variables.

The specimens were subjected to reversed cyclic lateral displacements while the axial stress was held constant for the duration of the test at either $0.12f'_c$ or $0.35f'_c$. The applied lateral displacement history was a function of calculated yield displacement (Δ_y), with three cycles with peak displacement of $0.25\Delta_y$ and $0.5\Delta_y$, followed by cycles with peak displacement levels of Δ_y , $2\Delta_y$, and $3\Delta_y$, until the lateral load capacity of the specimens degraded substantially.

Lateral load, top displacement response of specimens tested by Lynn are shown in Figure 1.9. All specimens exhibited lateral strength degradation due to shear failure. Specimens with low axial load and steel ratio (2CLH18 and 2SLH18) showed fairly ductile response (displacement ductility of 4.2 and 3.5, respectively) compared with other specimens. Although the yield stress was reached in the spliced bars, cracks along the lap splice led to strength degradation and eventually shear failure (just above the splice) in the specimens with low axial stress (2SLH18 and 3SLH18). For the specimens with high axial stress, abrupt shear failures were observed for columns with and without the lap splices, shortly after reaching the bar yield stress in tension; therefore, the splice did not substantially influence the observed behavior.

Specimens with abrupt shear failure lost axial load-carrying capacity just after the degradation of lateral strength. Specimens that displayed moderately ductile behavior after flexural yielding were able to maintain axial loads for larger displacement levels.

The experimental studies briefly summarized herein mainly focus on rehabilitation measures used for columns with inadequate lap-splice lengths. These tests were beneficial for the evaluation of local retrofitting methods. Among the rehabilitation options explored, adding external ties/hoops or using steel jackets were the most effective in improving the behavior of columns with deficient lap splices.

However, for “global” rehabilitation strategies, it is important to understand the force versus deformation behavior of columns with short splice lengths to allow for design of reliable and economical rehabilitation measures. Available information is limited, with the tests conducted by Lynn et al. (1996) providing the bulk of the information. In general, columns with inadequate splice lengths display little energy-dissipation capacity, and in some cases, do not reach the nominal flexural strength at the critical section.

The research presented in the following chapters focused on addressing this gap in information by conducting experimental studies on columns with short tension splice lengths subjected to reverse cyclic lateral loads. This report focuses on describing the experimental program (Chapter 2) and the experimental results (Chapter 3). Findings from the experimental study are presented in Chapter 4.

2 Description of Experimental Program

2.1 SPECIMENS

Six reinforced concrete column specimens with pre-1960s construction details are tested. The test specimens consist of a cantilever column with a foundation block attached to a strong floor (Fig. 2.1). The specimens represent a building column from column mid-height between floors to the column-joint interface for an interior column. The column cross section is 18 in. (457 mm) square with 8 - #8 ($d_b = 1.0$ in.; 25.4 mm) longitudinal reinforcing bars and #3 ($d_b = 0.375$ in.; 9.53 mm) ties @ 12 in. (304.8 mm) spacing with 90° hooks. The column cross-section and reinforcement details are the same as in the UC Berkeley test program (Lynn et al., 1996). The column height is selected to ensure that the shear strength of the columns (using ACI 318-99 Eq. 11-4 and 11-15) are sufficient to develop the lateral load required to reach the nominal moment capacity at the base of each column, where a lap splice is located. A lap splice length of $20d_b$ is used based on the requirements for compression splices in older buildings.

Table 2.1 provides an overview of the primary variables of the test program, which include (1) axial load (0.1, 0.2 and $0.3A_g f'_c$), shear (low, moderate, and high levels), and lateral load history. The required development lengths according to ACI 318-99 (12-1) for the actual material properties are calculated as 793.5 mm (31.2 in.), or $31d_b$ for the splice length used ($20d_b$); the splice was expected to deteriorate when the column moment reached approximately 60% to 70% of the nominal moment capacity.

$$\frac{l_d}{d_b} = \frac{3}{40} \frac{f_y}{\sqrt{f'_c}} \frac{\alpha\beta\gamma\lambda}{\left(\frac{c + K_{tr}}{d_b}\right)} \quad \text{ACI 318-99 (12-1)} \quad (2-1)$$

The first three specimens (S10MI, S20MI, and S30MI) were tested using a standard cyclic lateral load history with the axial load held constant for the duration of the tests at 0.1, 0.2,

and $0.3A_gf'_c$, respectively. The objective of this test series is to assess the influence of axial load on lap splices with low shear stress and light transverse reinforcement.

The second series of three specimens are companions to the first three, and are tested to assess the importance of shear and load history on splice behavior. Two specimens (S20HI and S20HIN) are tested with a moderate shear stress level and axial load ($0.20A_gf'_c$). A near-fault displacement history is applied to specimen S20HIN to evaluate the effect of loading history on splice performance. The last specimen (S30XI) is subjected to a standard displacement history with high shear stress level and axial load. The shear stress level at the initiation of splice deterioration was increased by decreasing the column height from 1828.9 mm (6 ft.) to 1676.6 mm (5 ft. 6 in.) for specimens S20HI and S20HIN, and 1524 mm (5 ft.) for S30XI.

The specimen identification (ID) labels define the level of the applied axial load, the shear demand level at the lateral load expected to result in splice deterioration, and the applied lateral displacement history. For example, label S20HIN corresponds to S = Spliced; 20 = 0.20 $A_gf'_c$; H = High Shear Demand; I = Interior Column; N = Near-Fault Lateral Displacement History.

As mentioned, column heights are selected to ensure that specific levels of shear demand would be present when bond deterioration was expected to initiate. The fifth column of Table 2.1 shows the ratio of shear demand when lateral strength degradation was expected to initiate, divided by the calculated nominal shear strength. Nominal shear strength of specimens is calculated using equations 2.2 and 2.3 for actual material properties.

$$V_c = 2 \cdot \left(1 + \frac{N_u}{2000 \cdot A_g} \right) \cdot \sqrt{f'_c} \cdot b_w \cdot d \quad \text{ACI 318-99 (11-4)} \quad (2-2)$$

$$V_s = \frac{A_v \cdot f_y \cdot d}{s} \quad \text{ACI 318-99 (11-15)} \quad (2-3)$$

2.2 MATERIALS

Normal weight, 24.1 MPa (3500 psi) concrete, with maximum aggregate size of 25.4 mm (1.0 in.) was used to construct the columns. The mix design and aggregate gradation are given in Tables 2.3 and 2.4, respectively. A retardant was added to the mix to allow more time for placement and finishing. After placement, the concrete was covered with burlap and kept moist

for 10 days. Test cylinders (152.4 mm x 304.8 mm; 6 in. x 12 in.) were made following ASTM Specification C31/C31M-00e1.

Standard compressive strength tests (ASTM C31-39) on 152.4 mm x 304.8 mm (6 in. x 12 in.) cylinders were done 7 and 28 days after concrete placement. In addition, stress-strain relations were also obtained at the test dates (Fig. 2.2). Concrete stress-strain diagrams are given in Figures 2.3 and 2.4. Split cylinder tests (ASTM C496) were also conducted. The concrete mechanical properties are presented in Table 2.5 where concrete rupture strength is calculated using equation 2.4.

$$f_r = 7.5 \cdot \sqrt{f_c'} \quad \text{ACI 318-99 (9-9)} \quad (2-4)$$

Longitudinal and transverse reinforcement are deformed ASTM A 615 Grade 60. Three different batches of longitudinal reinforcement bars are used. ASTM A307 tensile strength tests were performed on reinforcement bar samples to obtain the mechanical properties (yield and fracture strength, Table 2.6).

2.3 CONSTRUCTION OF SPECIMENS

Two sets of three column specimens were fabricated in the UCLA Structural Engineering Laboratory. Three forms were constructed for the first set of specimens using 2x4's and ½ in. thick plywood. These forms were dismantled after concrete placement and used for the second set of specimens. For convenience, all specimens were constructed in a horizontal position.

Reinforcement cages for the foundation blocks (or pedestals) were fabricated first. Column pedestals are reinforced with 6 - #8 ($d_b = 1.0$ in.; 25.4 mm) top and bottom longitudinal reinforcing bars. Shear reinforcement consists of a #3 hoop and two #3 ties ($d_b = 0.375$ in.; 9.53 mm) spaced at 203.2 mm (8 in.) on center. Pedestal reinforcement details are shown in Figure 2.5. Reinforcement used was provided by C&M Steel, located in Fontana, California. Finished pedestal cages were placed in the forms using a crane.

Reinforcement for the column was cut and bent, and then strain gauges were affixed to the column longitudinal bars and column hoops. A diagram of a completed reinforcing cage is shown in Figure 2.6. The complete cages were lifted using a crane and placed in the formwork, which was oiled to ease stripping of the formwork. Before placing concrete, PVC pipes were

arranged within the forms (Fig. 2.7) to allow for affixing the specimen to the strong floor, as well as to provide a duct for running strain gauge wires. Details of the splice and the strain gauge wires are shown in Figures 2.8 and 2.9. Figures 2.10 and 2.11 show the starter bars extending out of the pedestal that are spliced with the column longitudinal bars.

Concrete was provided by a local supplier, Catalina Pacific. Concrete for all three specimens was placed from one truck within approximately 30 minutes. After final finishing, the concrete was covered with burlap and plastic sheets and kept moist. The forms were removed after 2 weeks. The 152.4 x 304.8 mm (6 in. x 12 in.) test cylinders were cured adjacent to the specimens under the same conditions.

The specimens were lifted and moved into position for testing using a crane. Tie-down rods were placed through the PVC pipes and threaded into the strong floor to anchor the base of the specimen. A thin layer of grout was placed between the pedestal and strong floor to ensure that the specimens were level for testing. The axial load assembly at the top of the column (described below) and the 12.7 mm (½ in.) plates under the tie-down nuts were also grouted.

2.4 TESTING APPARATUS

The test setup is shown in Figures 2.12 through 2.14. The lateral load is applied with a 556 kN (125 kip) ATLAS hydraulic actuator with 609.6 mm (24 in.) stroke. The actuator is bolted to the column specimen at one end and to a steel reaction frame at the other end using rod eye-clevis bracket connections that allow free rotation in the vertical plane of the actuator (Fig. 2.11). An MTS 407 controller connected to a hydraulic power supply is used to control the actuator load and displacement. A schematic of the control system is given in Figure 2.15.

The axial load on each specimen is held constant for the duration of the applied lateral displacement history. The axial load assembly consists of two, 889.6 kN (200 kip) Enerpac RCH-1003 hollow plunge cylinders, two 46 mm (1 ¾ in.) diameter Dywidag Threadbar® Prestressing steel rods (Grade 150), two MC 18x51.9 A 572 (Grade 50) steel channels, and two 76.2 mm (3 in.) thick steel plate assemblies. The connection at the top of the column to the axial load assembly was established using 15.9 mm (5/8 in.) diameter J-bolts that were anchored in the concrete at the top of the column. The specimens are subjected to axial load by placing the 46 mm (1.75 in.) diameter Dywidag rods in tension. The Dywidag rod is anchored to a 76.2 mm (3

in.) plate which is anchored to the strong floor with four 31.8 mm (1.25 in.) diameter, threaded, high-strength steel tie-down rods. A hand pump with a reservoir was used to pressure the Enerpac cylinders. The applied axial load was monitored from pressure dial gauges connected to the Enerpac hydraulic cylinders. Pressure-force calibration of the dial gauges was done prior to testing. During testing, the hydraulic pressure was continuously monitored and adjusted to maintain the desired level of constant axial load.

2.5 INSTRUMENTATION AND DATA ACQUISITION

Different types of instrumentation were used to monitor the applied lateral load and displacement, strain of longitudinal and transverse reinforcement, flexural and shear deformations of the column, and pedestal translation and rotation.

For each specimen, reinforcing bar strains were measured using 27 longitudinal and 6 transverse reinforcement strain gauges, as shown in Figure 2.16. Two types of Vishay Measurements Group, Inc., strain gauges (EP-08-250BG-120 and EA-06-125BT-120) were used, both with a 5% strain limit. These strain gauges are commonly used for post-yield static testing. In order to place strain gauges, reinforcement bars were filed and then the steel surface was prepared with chemicals. Strain gauges were attached to the prepared steel surface with M-Bond 200 adhesive which allows up to 3% elongation. Finally, M-Coat W1 and M-Coat J were applied on the strain gauges for water and abrasion protection, respectively. Belden 8451c U1000 black cable was used to connect strain gauges to the data acquisition system.

The strain gauge-labeling scheme is given in Figure 2.17. Strain gauges are named according to the type of the reinforcement bar: L= Longitudinal, S= Strarter, T= Transverse; height with respect to the column-pedestal interface in inches; and cross-sectional position. For example: L12-NW stands for the strain gauge placed on a longitudinal (L) bar 12 inches above pedestal level (12) at the north-west corner of the cross section (NW).

Column deformations (flexure, shear and lateral displacement) were measured with linear voltage transducers (+/- 1.5 in.; 38.1 mm). The instrumentation layout was modified slightly between the first set of three specimens and the second set of three specimens. External instrumentation for the first set of three specimens (S10MI, S20MI, and S30MI) consisted of 31 linear transducers, 25 on one side of the specimen to form a grid as shown in Figure 2.18. Four

transducers were placed on the opposite face of the column to obtain rotational response at the column base due to flexure and slip (Fig. 2.19). The instrumentation layout was changed for the second set of specimens, where the number of linear potentiometers used was reduced from 31 to 18. Of the 18 linear potentiometers, six pairs were utilized to measure the flexural response (average curvature) of the specimen over the column height (Fig. 2.20). The measurement of shear distortions was made possible by using four wire potentiometers (Fig. 2.21) that were placed diagonally on the opposite face of the column. Two additional transducers were placed on two ends of the pedestal base to monitor any rotation of the foundation system. The external instrumentation layout and the labeling scheme are given in Figures 2.22 and 2.23, respectively. Potentiometers are connected to the reinforced concrete column with 6.35 mm (1/4") diameter fine threaded rods which were placed prior to concrete placement. Locations of the threaded rods are given in Table 2.7. All transducers were calibrated prior to testing.

The lateral load was measured using a 667 kN (150 kip) Lebow load cell. The column top lateral displacement was monitored using a MTS Temposonic transducer (+/- 12 in.; +/- 304.8 mm) mounted on the cylinder. In addition, a Celesco wire potentiometer (+/- 20 in.; +/- 508 mm) was mounted between the specimen and a rigid external reference frame to measure the lateral displacement at the point of lateral load application (top displacement). Besides top displacement, mid-height and pedestal lateral displacements were measured relative to the rigid reference frame using wire potentiometers (Fig. 2.24).

A National Instruments PCI 6052E card connected to a NI SCXI 1001 chassis was used for data acquisition (Fig. 2.25). The SCXI 1001 chassis has ten slots for analog or digital input modules. Eight of these slots were filled with SCXI 1121 four-channel isolated universal transducer modules, and the remaining two were occupied by SCXI 1100 32-channel differential multiplexer/amplifiers. A schematic of the data acquisition system is given in Figure 2.26.

Strain gauges were excited with an input voltage and the obtained output was amplified using strain gauge amplifiers manufactured at UCLA (Fig. 2.27). Each amplifier card can excite and amplify one strain gauge channel. For each channel, proper gain was selected depending on the strain limit expected, and the bridge voltage was set to 4 Volts. Each strain gauge channel was adjusted to zero before the application of the axial load.

The output voltage was transmitted from the amplifiers to the SCXI 1100 analog input module, and then to the PCI 6052E data acquisition card where the voltage was recorded.

Amplified voltage outputs from the strain gauges are in the range of 0 to 10 volts. Data acquisition software scales the voltage to strain before it is recorded. The relation between voltage and strain is given as:

$$\varepsilon = \frac{4 \cdot V_{out}}{V_{bridge} \cdot k \cdot A} \quad (2-5)$$

where V_{bridge} is set to 4 Volts, k is the strain gauge factor provided by the gauge manufacturer, and A is the gain provided by the amplifier.

Linear voltage transducers (potentiometers) do not require amplifiers; however, they need to be excited with an input voltage. For a given input voltage of V_{in} , the transducer produces an output of zero Volts for the closed position and V_{in} volts for full stroke (3 in.; 76.2 mm for the transducers used in this experiment). Four potentiometers were connected to each SCXI 1121 modules. The voltage is scaled to inches and recorded. The relationship between displacement and voltage is given as:

$$\delta = V_{out} \cdot c \quad (2-6)$$

where c is the calibration factor (in./V).

In order to process the test data more effectively, readings were taken only at specified load steps. Each cycle consisted of 32 load steps, with eight readings obtained between zero and the peak displacement (the actuator was stopped and held in position to obtain readings). This was accomplished by developing a data-logging program in LABVIEW shown in Figure 2.28. Besides recording the logged data as a spreadsheet, the program also allowed real-time data visualization for several transducers/gauges and provided a load displacement plot during the test. Each recording point is labeled as a data point number (DPN). Data point numbers corresponding to target peak lateral drift levels are given in Tables 2.8 and 2.9.

2.6 TESTING PROCEDURE

The specimens are subjected to constant axial load and cyclic uniaxial bending by the application of a cyclic displacement at the top of the column. Two different lateral displacement histories are applied to specimens, a standard history and a near-fault history. The standard displacement history is fairly typical (Fig. 2.29), and consists of three cycles at each displacement level with monotonically increasing drift levels (0.1, 0.25, 0.5, 0.75, 1.0, 1.5, 2.0, 3, 5, 7, and 10%).

The specimen subjected to the near-fault displacement history is cycled three times at 0.1, 0.25, 0.5 and 1.0% drift levels, followed by one half cycle to 1.5% lateral drift level in one direction, followed by monotonically increasing drift in the opposite direction until failure is reached (Fig. 2.30).

One objective of the tests is to apply large displacement amplitudes to assess both the loss of lateral load capacity and the loss of axial load-carrying capacity. The latter is important in evaluating life-safety and collapse prevention performance levels. Due to this consideration, lateral drift cycles were continued after the loss of lateral strength until axial load-carrying capacity was lost.

3 Experimental Results

Six specimens (Table 2.1) with the same construction details were tested with different levels of axial load, shear demand, and displacement history. Lateral load versus top displacement, moment versus base rotation, reinforcement steel strains, and shear distortion responses of the specimens, either measured directly or derived from the measured data, are presented in this chapter.

3.1 EXPERIMENTALLY OBSERVED DAMAGE AND BEHAVIOR

Column specimens were subjected to cyclic lateral displacements and constant axial load at three levels (0.10, 0.20, 0.30 $A_g f'_c$). Specimen performance was generally poor, with little to no ductility, for all levels of axial load and shear demand (moderate to high), for both standard and near-field displacement histories. Lateral strength degradation was observed in all specimens due to bond deterioration along the splice prior to reaching the calculated yield displacement. Table 3.1 summarizes the test results.

Application of the standard displacement history involved subjected each specimen to three lateral displacement cycles at each prescribed drift level. As mentioned in Chapter 2, instead of continuous readings, readings were taken at prescribed points such that 32 readings were taken during each cycle. The progression of damage for each specimen is documented with photos and figures, with legends provided to indicate the displacement level and data point. For ease of reference, Table 2.8 presents the applied peak lateral drift levels and the corresponding data point numbers.

Although tested under different conditions, the response of the specimens to cyclic

loading was similar. Observations of the response of specimens during experiments are presented in this report.

During testing of specimen S10MI, initial flexural cracks were observed at the column-pedestal interface right after lateral loading has started. Flexural cracking on the column face started at a drift ratio of 0.25% (Data point numbers (DPN) 157 and 172 on the west and east column faces, respectively.) The number of observed flexural cracks increased with the increasing lateral drift ratios. Flexural cracks observed along the splice length were 114, 229 and 406 mm above the pedestal level. Longitudinal cracking along the splice length began at the third cycle of 0.75% lateral drift ratio (DPN 361). This first crack was observed at a corner bar as a vertical hairline crack between the column-pedestal interface and the flexural crack 114 mm above the pedestal. This initial vertical crack did not appear to propagate during subsequent cycles at 1.0% and 1.5% drift ratios until a sudden crack extension occurred that coincided with the peak lateral strength at 1.5% drift. For 1.5% and higher drift ratios, the lateral load strength diminished, indicating that bond along the spliced bars was deteriorating. The length and width of the hairline longitudinal cracks along the spliced bars increased for higher drift levels. Cracking at the column-pedestal interface became more significant as the experiment progressed.

Concrete crushing at 2.0% drift ratio was later followed by the spalling of concrete cover along the splice length on the east and west sides of the column. Concrete spalling started at the corners of the column as a sign of bond deterioration between the concrete and the reinforcement bars. The amount of spalled concrete increased as the lateral drift ratios were increased. At 7% lateral drift ratio, the spliced longitudinal reinforcement bars were clearly visible, and the end of the longitudinal columns bars was observed to extend as much as 19 mm upwards from the pedestal level (DPN 873).

S20MI was the second specimen tested. Flexural cracking on the column face started as early as the first cycle of 0.25% lateral drift ratio (DPN 105). When the lateral drift ratio reached to 0.75%, cracks were observed from the pedestal-column interface to a height of 864 mm above the pedestal (47% of the column height). Similar to specimen S10MI, longitudinal cracks observed during the first cycles to a peak drift level of 0.75% (DPN 297 pushing east, DPN 313 pulling west) occurred between the column-pedestal interface at the NW and NE corners of the column and the first flexural crack above the pedestal (approximately 100 mm). During the first cycle of 1.0% drift level, sudden and substantial crack propagation along the splice length (to a

total length of 508 mm) was observed at NE corner of the column (DPN 409). Lateral strength degradation initiated during the first cycle to 1.0% drift ratio (DPN 409) for the negative (east) direction and during the first cycle of 1.5% drift ratio (DPN 489) on the positive (west) direction. At 1.0% lateral drift, when lateral strength degradation initiated, longitudinal cracks were observed only at the south-west and north-east corners of the specimen. Cracks were narrow and had lengths of 114 mm on the east face and 514 mm on the west face. After completion of three cycles of 1.5% lateral drift, longitudinal cracks were present on west and east column faces along the lap-splice length. Bond deterioration was evident for all the longitudinal bars located on these two faces of the column. Initial hairline shear (diagonal) cracks were observed during the first cycle of 0.75% drift level (DPN 313). Additional shear cracks formed during the first cycle to 1.5% lateral drift ratio (DPN 487); however, after lateral strength degradation initiated, no new diagonal cracks were observed. Concrete crushing and spalling also were observed adjacent to the column-pedestal interface during the cycle to 1.5% lateral drift ratio (DPN 489). After the first cycle of 3.0% lateral drift was completed, all concrete cover on the east and west faces had spalled off over the bottom 127 mm of the column, and the longitudinal bars located at the south-west corner of the column were clearly visible. Pictures of Specimen S20MI from 0.5% to 7% drift ratio are presented in Figures 3.4 through 3.10. These pictures efficiently summarize the damage progress during testing.

Specimen S30MI was subjected to $0.30A_g f'_c$ constant axial and cyclic lateral loading. Flexural cracking initiated during the first cycle to 0.50% drift level (DPN 217). The response of the specimen to cyclic loading was similar to specimens S10MI and S20MI with low and moderate axial loading, respectively, except that longitudinal cracks were observed to form suddenly at 1.5% lateral drift ratio (DPN 489) where lateral strength degradation has observed to begin (concrete crushing also was observed just above the pedestal). Prior to this, no longitudinal cracks were observed. Concrete spalling became more significant during the cycle to 2.0% lateral drift as fairly large sections of concrete cover spalled. During the cycle to 3.0% lateral drift (DPN 697), concrete cover on the east and west faces was severely damaged along the splice length. At 5.0% lateral drift, just before the end of the test, all concrete cover was completely lost along the splice length. Shear cracking was observed at 0.75% lateral drift (DPN 297) but these cracks were not significant throughout the duration of the test.

S20HI was the first specimen tested in the second set of three column specimens.

Specimen S20HI is a companion to specimen S20MI, but with higher shear demand (with decreased column height from 1823 mm to 1676 mm). At the sixth step of the first cycle to 0.25% lateral drift ratio (DPN 103), the first flexural cracks were observed. This coincided with a change in initial stiffness of the lateral force-displacement plot, which was monitored on a computer screen during the experiment. At 0.50% lateral drift ratio, flexural cracks became abundant on the tension column face up to a height of 685 mm above the pedestal (41% of the column height). Crack widths were very small (<1.5 mm). Longitudinal cracking along the splice length was first observed during the cycle to 0.75% lateral drift (DPN 313). After three cycles of 1.5% lateral drift were completed, longitudinal cracks propagated along the column to as much as 660 mm above the pedestal level. Crack widths were limited, generally less than 1.5 mm. Concrete crushing also was observed at this drift level (DPN 537), and concrete cover spalling occurred as drift levels were increased. At 3.0% lateral drift, the corner reinforcement bars were visible. At 7.0% lateral drift, all concrete cover over the bottom 400 mm of the column had spalled off. Shear cracks were observed on the north and south faces of the column starting at a drift level of 0.5% (DPN 201). Some minor cracking also was observed on the north side of the pedestal at this drift level. At 0.75% lateral drift, additional shear cracks were observed (DPN 297), generally located between one-quarter and one-half column depths away from the column base (114 mm to 229 mm). Although observed shear cracking was more significant than that observed for the first three specimens (S10MI, S20MI, and S30MI), longitudinal cracking was dominant indicating that bond deterioration caused lateral strength degradation.

S20HIN was the only specimen tested with the near-fault displacement history (Fig. 2.30). Initial lateral displacement cycles were identical with the standard displacement history (Fig. 2.29), except for the absence of the cycles to 0.75% lateral drift. Response of the specimen was similar to that for the other specimens. Initial flexural cracks were observed during the first cycle of 0.50% lateral drift (DPN 105 and 121 on the east and west faces of the specimen, respectively). Longitudinal cracking started during the first cycle to 1.0% lateral drift (DPN 297 and 312). At 1.0% lateral drift, 53% of the column height (890 mm) displayed flexural cracks. Longitudinal cracks along the splice length first appeared over a length of 100 mm at the bottom of the column. After completion of the second cycle to 1.0% lateral drift, longitudinal cracks had propagated along the entire splice length ($20d_b$). When 4.0% lateral drift was reached, longitudinal crack propagation had ceased and crack widths were as wide as 4 mm. For higher

drift ratios, the crack at the column-pedestal interface increased substantially due to the slip of longitudinal bars relative to the starter bars anchored within the pedestal. Concrete spalling started around 4.0% lateral drift, but it was not significant compared to the other specimens, mainly due to the lack of a cyclic displacement history.

The test program concluded with testing of specimen S30XI. Initial flexural cracks were observed on the west and east face of the column during the second cycle to 0.25% lateral drift (DPN 137) and during the first cycle to 0.50% lateral drift (DPN 216), respectively. Flexural cracking propagated along the column height as the applied lateral drift level was increased. After the application of three cycles of 0.50% lateral drift (DPN 289), flexural cracks were observed over the bottom 0.7 meters of the column (45% of the column height). Longitudinal cracking initiated during the first cycle of 0.75% lateral drift at data point numbers 297 and 313 on the west and east faces of the column, respectively. Observed longitudinal cracks were less prominent than for other specimens, and occurred only over the bottom 100 mm of the column on the north-west and north-east corners of the specimen. These cracks propagated up the column to a height of 686 mm (45% of the column height) when the lateral drift reached 2.0% (DPN 585). Concrete crushing was first observed at 1.5% lateral drift, and followed by spalling of concrete during the first cycle to 2.0% drift. Specimen S30XI was subjected to the highest shear demand of the columns tested; consequently wider shear cracks were observed. However, the extent of longitudinal cracking along the splice suggests that lateral strength loss was due to bond deterioration.

Cracks were observed on the foundation pedestals during the experiments. As mentioned in Chapter 2, pedestals were designed to be strong enough to prevent cracking. Since columns were constructed and cast horizontally, one side of the pedestal was not covered with formwork. Although this large surface was kept moist with burlap covered with plastic during curing, some minor cracks formed due to shrinkage. In addition to these minor cracks, some longitudinal hairline cracks were also observed during testing; however, these cracks were not significant. Pedestal cracks were observed during the second cycle to 1.0% lateral drift (DPN 445) at the south-west starter bar of S10MI, during the first cycle to 1.5% lateral drift (DPN 489) at the south-west starter bar of S20MI, and during the first cycle to 0.75% lateral drift (DPN 313) at the south-east starter bar, and during the first cycle to 1.0% lateral drift (DPN 393) at the south starter bar of S30XI. These cracks indicate some bond distress along starter bars; however, since

strain readings along starter bars within the pedestal are not available, it is not possible to quantify this distress.

The ability of the specimens to maintain the axial load-carrying capacity during the experiment was an important consideration during testing. The applied axial load was continuously monitored and held constant throughout the duration of each experiment. Although pressure on the hydraulic cylinders was constant during the test, the design of experimental setup led to variations. Since the axial load was applied at the top of the column and the mechanism used to apply the axial load displaced with the column, the displacements imposed on the column caused an inclination of the applied axial load (Fig. 3.11). As a result, the corrected applied axial load at the column base is equal to:

$$N = P \cdot \cos(\alpha) \quad (3-1)$$

where α is the measured top rotation and P is the applied axial load. Top rotation versus lateral drift is given on Fig. 3.12.

The change in the axial load due to top rotation is less than 1% for all specimens (Fig. 3.13). Since the axial load variation was negligibly small, effectively, the axial was constant throughout each experiment.

Two of the five specimens: S10MI (low axial load, standard displacement history) and S20HIN (intermediate axial load, near-fault displacement history) were able to carry the applied axial load to the maximum lateral drift that could be applied by the actuator (10% for S10MI, Fig. 3.14; and 12% for S20HIN, Fig. 3.18). After completion of the lateral displacement history, the lateral drift applied to specimen S10MI was returned to zero, and the axial load was monotonically increased until failure, which occurred when an axial load of $0.20A_g f'_c$ was reached. Unlike specimens S10MI and S20HIN, specimens S20MI, S30MI, S20HI, and S30XI lost axial load-carrying capacity during the test. Specimens with moderate and high axial load reached 7% and 5% lateral drift, respectively. Table 3.3 shows the data point and corresponding lateral displacement at the loss of the axial load-carrying capacity. The axial load-carrying capacity generally began to degrade when hoops at the 101.6 mm and 406.4 mm levels above the pedestal opened allowing the vertical bars to buckle. The hoops were fabricated with only 90° hooks, as is common with older construction, and these hooks provided little lateral support to suppress buckling once the concrete cover was lost. Figures 3.15 to 3.17 and 3.19 show column specimens after loss of the axial load-carrying capacity. Buckled longitudinal bars can be clearly

seen on these figures, as well as the opening of the 90° hoops.

Although specimen S20HIN was subjected to moderate axial load and pushed beyond 12% drift, the axial load-carrying capacity did not degrade. After reaching 12% lateral drift, specimen S20HIN was brought back to zero applied drift (original position prior to testing) and then two cycles of 2% and 4% lateral drift were applied, followed by pushing the specimen back to 12% lateral drift. No degradation in the axial load capacity was observed. The additional cycles did produce additional damage, such as concrete spalling and slight buckling of compression reinforcement; however, significant cover concrete was intact to keep the hoops with 90° hooks from opening. Consequently the longitudinal bars did not buckle, so the axial stability of S20HIN was maintained. Specimen S20HIN at 12% lateral drift is shown in Figure 3.18.

3.2 LATERAL LOAD VERSUS TOP DISPLACEMENT RELATIONS

Lateral load versus top displacement plots were prepared to evaluate the overall response of the specimens. By investigating the plots, it is possible to comment on lateral strength, rate of strength degradation, energy-dissipation capacity, and ductility of the specimens.

Lateral load versus top displacement graphs of the specimens are given in Figures 3.26 through 3.31. In the graphs, positive (+) load and displacement correspond to pulling of the specimen toward the reaction frame, and negative (-) values correspond to pushing the specimen away from the reaction frame. The plots are modified to eliminate the external factors, such as the displacement of the reaction frame and the pedestal, such that the relation plotted reflects the applied lateral load and displacement of the top of the column relative to the base of the column.

The applied lateral load is measured with a 667 kip load cell. However, due to the inclination of the top of the column during testing, base moments and applied shears are influenced by the horizontal component of applied axial load. Although the effect of the axial load is not reflected in the plotted lateral load, top displacement relations, it should be considered when calculating base moment and applied shear.

At the undeformed position, the base moment is equal to the applied lateral load (F) multiplied by the column height (h). However, due to the applied displacement history at the top of the column, the axial load acts through an eccentricity (e) such that the moment at the base of

the column is (Fig. 3.11):

$$M = F \cdot h - P \cdot e \quad (3-2)$$

Similarly, the applied shear at the top of the column is calculated considering the inclination (α) of the applied axial load (P) as:

$$V = F - P \cdot \sin(\alpha) \quad (3-3)$$

The rotation at the top of the column is calculated using the linear wire potentiometers WP2 and WP3, because external displacement potentiometers placed longitudinally along the column surface were removed from the column at larger drift levels in order to prevent damage to the equipment. For this reason measuring column rotation by these transducers is not suitable for lateral load modification purposes. Wire potentiometers were kept on the column throughout the experiments, allowing the displaced shape to be estimated. A comparison of displaced shapes obtained from longitudinal potentiometers mounted along the column height and wire potentiometers indicate that the linear deformed shape at the top half of the column is a reasonable assumption to calculate top rotation; therefore, column top rotation is calculated using wire potentiometer data as:

$$\alpha = \tan^{-1} \left(\frac{\Delta_{WP3} - \Delta_{WP2}}{h_{WP3} - h_{WP2}} \right) \quad (3-4)$$

Values obtained using Equation (3-4) is plotted versus lateral drift levels plotted in Figure 3.12. These plots indicate that the top rotation is linearly proportional with the applied lateral drift and that the top rotation is slightly greater than the corresponding lateral drift.

The wire potentiometer at the top of the column (WP3) and the Temposonic transducer within the cylinder were used to measure the lateral displacement of the specimen. The wire potentiometer (WP3) measures the lateral displacement between the column and a rigid reference frame, whereas the transducer in the cylinder measures the lateral displacement of the column and the lateral displacement of the reaction frame. Therefore lateral load, top displacement graphs are determined using data from the wire potentiometer (WP3) modified to account for the influence of pedestal movement (translation and rotation) on the column top displacement. Measured pedestal rotation and sliding displacement are given in Figures 3.20 through 3.23. Assuming that the pedestal rotates as a rigid body, the top displacement due to pedestal rotation is:

$$\Delta_{pedestal_rotation} = (\Delta_{PR2} - \Delta_{PR1}) \cdot (h_{column} + h_{pedestal}) / (L_{pedestal} + 25.4mm) \quad (3-5)$$

where Δ_{PR1} and Δ_{PR2} are the measurements from the two linear potentiometers placed on the east and west sides of the pedestal, respectively. The distance between the two transducers is the sum of the length of the pedestal and the thickness of the plastic brackets used to mount the potentiometers on the pedestal (25.4 mm). Top displacement due to pedestal translation is directly obtained from the wire potentiometer WP1 which measures the relative lateral displacement between the reference frame and pedestal (Eq. 3-6).

$$\Delta_{pedestal_translation} = \Delta_{WP1} \quad (3-6)$$

As shown in Figures 3.20 through 3.23, the top displacement due to pedestal rotation and translation are very small relative to the values recorded at the top of the column. Despite this small contribution, the applied lateral displacement histories were corrected to remove the influence of pedestal rotation and translation by subtracting the sum of lateral displacements due to pedestal translation and rotation from the measured top displacement. Modified lateral displacement histories are presented in Figures 3.24 and 3.25.

The corrected lateral load, top displacement plots are given in Figures 3.26 through 3.31. All specimens exhibit similar responses, with sudden lateral strength degradation at drift levels between 1% and 1.5%. Lateral strength degradation started just prior to, or just after reaching, yielding of the starter reinforcement bars. The responses were nonductile, that is, no displacement ductility was observed and the specimens displayed limited ability to dissipate energy. The peak lateral strength reached for each specimen was influenced by the level of the applied axial load, with increased lateral load capacity with increased axial load.

An elastic-perfectly-plastic (EPP) model was used to normalize and compare the energy-dissipation capacities of the specimens, as shown in Figure 3.41. Using lateral load versus top displacement responses, the amount of energy dissipated by the specimen and the EPP model are calculated by finding the area bounded by the load-displacement relations. Figure 3.42 plots the energy dissipated by both the EPP model and the test specimens. At the end of the applied displacement history, the total energy dissipated by each specimen was similar ($\sim 2 \times 10^5$ kN-mm), except for specimen S20HIN. At the end of the 2% and 5% lateral drift cycles, energy dissipated by the specimens with standard displacement history were 47% to 61% and 31% to 43% of the energy dissipated by an EPP model respectively (Fig. 3.43). Among the specimens with the same displacement history, S30MI and S10MI gave the largest and smallest normalized energy-

dissipation capacity, respectively. Specimen S20HIN dissipated 74% of the energy dissipated by the EPP model at the end of lateral drift cycles of 2% and 5%.

Lateral drift cycles exceeding 1.5% drift led to significant reduction of lateral strength for all specimens, with the rate of degradation influenced greatly by the applied lateral displacement history (standard versus near fault), and somewhat by the level of the applied axial load. Specimen S20HIN, with near-fault displacement history, was able to maintain more than 50% of its peak lateral strength at drift levels up to 10%. However, specimens subjected to the standard cyclic lateral displacement history exhibited more significant lateral strength degradation, with residual lateral strength of not more than 30% of the peak value. These trends are evident in Figure 3.33, where the normalized moment, lateral drift response histories of specimens subjected to standard (S20HI, S20MI) and near-fault (S20HIN) displacement histories are compared. The rate of strength degradation of the specimens with the same lateral displacement history (i.e., standard) is similar. A normalized moment, lateral drift comparison of specimens S10MI, S20MI, and S30MI (Fig. 3.32), as well as the measured secant stiffness (Figs. 3.35, 3.36, and 3.37), indicate similar lateral strength degradation for all specimens. Measured secant stiffness values given in Figures 3.35 through 3.40 are calculated at peak lateral drift levels.

The effect of shear demand on specimen response was investigated for specimens with moderate and high levels of axial load. Since lateral strength degradation was dominated by bond deterioration along the splice length, the influence of increased shear demand on the behavior of the specimens was insignificant. A comparison of responses of the specimens with moderate axial load (S20MI, S20HI and S20HIN) is shown in Figure 3.33. In this plot, the ratio of measured base moment to yield moment determined by section analysis of specimens S20MI, S20H, and S20HIN are plotted. Although shear demand at onset of splice deterioration was increased substantially by reducing the column height, specimens with low $[(V_u @ M_n)/V_n=0.70]$ and moderate $[(V_u @ M_n)/V_n=0.81]$ shear demand displayed similar behavior. The increased shear demand did not significantly impact the lateral strength nor the rate of strength degradation of specimens with moderate axial load. Comparisons of specimens with high axial load (S30MI and S30XI) reveal similar results. Normalized base moment versus lateral drift relations (Fig. 3.34) of these specimens indicated that although shear demand on the section is increased substantially (0.67 to 0.93), the normalized moment strengths reached in the two columns are very close ($M_u/M_y \approx 1.03$ for both columns); however, S30XI displayed more lateral strength degradation

than S30MI after the peak lateral strength was achieved. Specimens S30MI and S30XI had normalized moment ratios of 0.33 and 0.23, respectively, at 5% lateral drift just prior to axial strength degradation occurred.

3.3 MOMENT VERSUS ROTATION RELATIONS

The moment-rotation response of the specimens is used to assess the contribution of slip to the overall rotation and displacement response of the specimens. The moment versus total rotation response of the specimens is plotted in Figures 3.44 through 3.49. These responses represent the rotation at the top of the column caused by flexural deformations over the column height and rotations caused by slippage of reinforcement bars over the splice length ($20d_b$). Total moment at the base of the column is calculated by summing the moments caused by lateral load and vertical load, as given by Equation 3.2, rewritten as:

$$M = F \cdot h + P \cdot \cos(\alpha) \cdot \Delta_{lateral} - P \cdot \sin(\alpha) \cdot h \quad (3-7)$$

It is desirable to separate slip rotation from total rotation to assess the impact of slip rotation, as well as to provide a means to calibrate moment versus slip-rotation springs that are used to model splice behavior (e.g., Reyes and Pincheira, 1999). Rotation due to slip of the reinforcement bars along the splice is calculated by using the measured potentiometer and strain gauge data. Linear displacement transducers measured the total rotation over the splice length at the base of the column, whereas several strain gauges attached to the longitudinal bars monitored the strain at several locations along the splice length. Average reinforcement strains were calculated using the strain gauge data. Slip rotation was taken as the difference between the total rotation and the rotation calculated using the average reinforcement strain along the splice length. Figures 3.50 through 3.55 show the moment-slip rotation plots over the splice length. Since measurement of slip rotation is based on strain gauge data, presented data are limited up to the point where strain gauge data are collected.

Moment-rotation envelopes are also presented in Figures 3.56 through 3.61. Slip rotation constitutes a significant portion of the total rotation such that at the first peak of 0.5% lateral drift, the ratio of slip rotation to total rotation is in between 50% to 60% for all specimens. When 1.5% lateral drift ratio is reached, slip rotations for specimens S10MI, S20MI, S20HI, S20HIN, and S30XI are measured as 85%, 82%, 83%, 81%, and 88% of the total rotation, respectively. As

lateral drift levels are increased, the contribution of slip to base rotation becomes dominant.

3.4 STEEL STRAIN PROFILES

Each specimen was instrumented with 33 reinforcing steel strain gauges. Of these, 27 gauges were used to monitor the strain histories of the longitudinal (flexural) column reinforcement (including the starter bars anchored into the pedestal) and 6 gauges were placed on the transverse reinforcement. The strain profiles obtained from the strain gauges were valuable for monitoring the stress transfer between column longitudinal and starter bars, as well as evaluating the impact of test variables such as axial load and displacement history on bond strength between reinforcement bars and the surrounding concrete.

The initial strain gauge readings (as well as other instruments) were taken before and after the application of the axial load and prior to the application of the lateral displacement. Strain measurements were continued through the experiment and recorded values were logged at every data point.

Strain histories for longitudinal column reinforcement were used to plot the strain distribution along the splice length at peak values for each cycle of lateral drift from 0.1% to 3%. Steel strain distribution along the splice length is useful to evaluate the stress transfer between column longitudinal bars and the starter bars embedded into the pedestal. Strain distribution profiles can be used to determine the bond stress-slip relations needed for calibration of analytical models. Damage to the specimens ultimately led to damage of the strain gauges placed on longitudinal reinforcement; generally at about 3% lateral drift; therefore, readings for higher drift ratios are generally not available.

Axial stress on the longitudinal (vertical) column reinforcing bars due to the combined bending and axial load is transferred to the starter bars embedded into the pedestal through bond between the reinforcing bar and the surrounding concrete. Prior to bond deterioration, a triangular strain distribution is commonly assumed, as shown in Figure 3.62. Figures 3.63 through 3.74 show the longitudinal strain distribution for corner (NW) and middle (W) bars along the splice length. As shown in Figure 2.16, there are three strain gauges on the column longitudinal bar (blue) and two gauges on the starter bar (yellow). Also, it is known that the

longitudinal strain is equal to zero at the ends of the longitudinal reinforcement bars. Strain distribution profiles are plotted using these values.

Although measured longitudinal strain distributions are not perfectly linear, strain distribution profiles for the initial lateral drift levels (e.g., 0.10% to 1.5%) are similar to the expected strain distribution. Lateral strength degradation coincided with the initiation of bond deterioration along the splice length. Bond deterioration was most significant at the lower half of the splice length, where the maximum moment occurred.

Strain profiles indicate that corner and middle longitudinal bars behave differently. For all specimens subjected to standard cyclic displacement histories, bond deterioration was first observed at the corner bar (NW) after 1% lateral drift, whereas bond deterioration for the middle (W) longitudinal bar was not observed until a drift ratio of 1.5%. This trend is especially evident for the strain distributions of the interior and exterior bars of specimen S30MI, as shown in Figures 3.73 and 3.74. In this plot, the negative sign on the recorded strain at 3% indicates the residual strain due to the buckling of longitudinal bars. Consequently, S30MI lost its axial load-carrying capacity during the next half cycle to a lateral drift level of 5%.

The peak average bond stress developed along the splice was calculated and compared with values typically used in design. The average bond stress (u) between reinforcement bars and the surrounding concrete was calculated using the variation of longitudinal steel strains over the splice length. A bilinear hysteretic steel stress-strain model (Fig. 3.75) was utilized to transform measured steel strains (ϵ) to longitudinal steel stresses (f_s). Strain hardening was neglected since bond deterioration typically occurred prior to reaching yield. The calculated longitudinal stresses were later transformed into average bond stresses as:

$$u = \frac{f_s \cdot d_b}{4 \cdot l} \quad (3-7)$$

where f_s is the axial stress on the bar, d_b is the nominal bar diameter, and l is the length of the bar.

Calculated average bond stress (u) and lateral drift plots are given in Figures 3.76 through 3.87. Maximum average bond strengths attained by longitudinal bars of all specimens are normalized by dividing with $\sqrt{f'_c}$ in Figure 3.88. As seen in the plot, $0.5\sqrt{f'_c}$ MPa ($6\sqrt{f'_c}$ psi) and the bond stress implied by ACI 318-02 provide a lower bound for the measured bond strengths under cyclic loading. The average bond strength values given by ACI 318-02 are

obtained by calculating the required development length (l_d) using ACI 318-02 equation 12-1 and substituting the calculated values for l_d and f_y into equation 3-7 for l and f_s , respectively.

$$\frac{l_d}{d_b} = \frac{3}{40} \frac{f_y}{\sqrt{f_c'}} \frac{\alpha\beta\gamma\lambda}{\left(\frac{c + K_{tr}}{d_b}\right)} \quad \text{ACI 318-99 (12-1)}$$

The maximum average bond strengths obtained from the column tests were later compared with results for beam tests with splices conducted by Heflin (1992) and beam tests results organized by Sozen and Moehle (1990) in Fig. 3.89. All test specimens represented in this plot had a clear cover to bar diameter ratio smaller than or equal to 2.5 ($c/d_b \leq 2.5$) with single or multiple #8 (25.4 mm) longitudinal bars and with or without stirrups (Table 3.4). Results for the beam and column tests also are compared by normalizing the experimental derived maximum bond stress with $\sqrt{f_c'}$. The major differences between the column and beam tests include the cover and spacing, as well as the axial load and the applied displacement history. Prior beam tests were subjected to monotonic loading, whereas column specimens were subjected to cyclic loading. The arithmetic mean of average bond strengths obtained from 15 longitudinal bars in the 6 column specimens is calculated as $0.95 \sqrt{f_c'}$ (MPa) ($11.5 \sqrt{f_c'}$ (psi)), whereas a mean of $0.83 \sqrt{f_c'}$ (MPa) ($9.95 \sqrt{f_c'}$ (psi)) is calculated for the monotonic beam tests. Figures 3.94 and 3.95 compare results for the cyclic column and monotonic beam tests. Figure 3.94 plots the implied bond stress determined for each test specimen, whereas Figure 3.95 plots normalized bond stresses versus the minimum clear cover divided by the bar diameter (c_{\min}/d_b). Although subjected to cyclic loading, column specimens reached similar normalized peak bond stresses as did the monotonic beam specimens; therefore, the results indicate cyclic loading may not influence the peak bond stress significantly. However, cyclic loading may still impact the rate of post-peak strength deterioration. Comparison of average bond strengths measured from three column specimens with the same shear level but different axial loading (S10MI, S20MI and S30MI) indicates a slight increase of maximum average bond strength with increased axial loading: $0.99 \sqrt{f_c'}$ (MPa) ($11.98 \sqrt{f_c'}$ (psi)), $1.01 \sqrt{f_c'}$ (MPa) ($12.17 \sqrt{f_c'}$ (psi)), and $1.07 \sqrt{f_c'}$ (MPa) ($12.92 \sqrt{f_c'}$ (psi)) for specimens with $0.10A_g f_c'$, $0.20A_g f_c'$, $0.30A_g f_c'$, respectively. The

rate of strength degradation after reaching peak load decreases moderately as the axial load increases from $0.10A_g f'_c$ to $0.30A_g f'_c$ (see Figures 3.88 – 3.90).

3.5 SHEAR DISTORTION

Shear distortion over the column height was measured using linear voltage transducers. As mentioned in Chapter 2, two different layouts of instrumentation were used to measure shear deformations on the column face. The shear demand on the section was calculated by using equation 3.3.

The transducer layout for the first set of specimens S10MI, S20MI, and S30MI (Fig. 2.22) consists of diagonal, longitudinal, and horizontal linear transducers. Shear distortion is calculated using measured horizontal (Δ_H), longitudinal (Δ_L), and diagonal (Δ_D) deformations as:

$$\gamma = \sqrt{(d + \Delta_D)^2 - (h + \Delta_L)^2} - \frac{b + \Delta_H}{h + \Delta_L} \quad (3-8)$$

where b , h and d stand for horizontal, longitudinal, and diagonal dimensions of the potentiometer grid, respectively (Fig. 3.96). There are two levels of diagonal transducers placed along splice length. Total shear distortion over the lap splice length was calculated by summing the shear distortions measured by these two sets of transducers.

Two diagonal wire potentiometers were utilized for a second set of specimens. This layout for measuring shear deformations reduced the number of potentiometers and increased the magnitudes of the measured displacements due to the larger gauge lengths. For this case, the shear distortion was calculated as:

$$\gamma = \frac{\Delta_{D1} \cdot d_1 - \Delta_{D2} \cdot d_2}{2 \cdot h \cdot l} \quad (3-9)$$

where Δ_{D1} and Δ_{D2} are the diagonal deformations measured by the diagonal wire potentiometers (Fig. 3.100).

The measured shear distortions are presented in Figures 3.97 through 3.103. The nominal shear strength (V_n) and the nominal shear strength provided by concrete (V_c) are calculated for each specimen and are also presented with shear distortion plots. Measured shear force versus shear strain relationship is linear until the lateral strength starts to degrade. The increase in shear

distortions after the initiation of lateral strength decay is attributed to the longitudinal cracking along the splice length due to bond deterioration (Fig. 3.96, Fig. 3.100), as diagonal shear cracks observed during the experiments were generally small compared with longitudinal cracks.

Additional comparisons are made for specimens with the same axial load and displacement history to assess shear strength degradation. The variation in strength degradation between specimens S20MI-S20HI and S30MI-S30XI can be attributed to increased shear deformations, as all other parameters are held constant. Shear strength degradation rates of S20MI and S20HI were similar, i.e., at 2% lateral drift, 68% and 62% of the peak lateral load were maintained, respectively, and at 3% drift, 44% of the peak lateral loads were maintained for both specimens. Slightly different shear strength degradations were noted between specimens S30MI and S30XI, where 73% and 64% of the peak lateral load was maintained at 2% drift, respectively, and only 45% and 38% of the peak lateral load was maintained at 3% drift.

Transverse reinforcement strain gauges were placed on stirrups 102, 406, and 711 mm above column base. Strain gauge histories of these gauges are presented in the Appendix. Transverse reinforcement histories indicate that strain on some of the stirrups increased significantly during testing. Strain on stirrups continued to increase even after lateral strength degradation started, and reached yield for some gauges at latter stages of the experiment. Sudden increases generally correspond to bucking of vertical bars, whereas sudden drops correspond to opening of hoops due to the loss of cover and the use of 90° hoop bends.

4 Summary and Conclusions

4.1 SUMMARY

Older reinforced concrete columns have design deficiencies such as short compression lap splices and widely spaced ties. Knowledge of the behavior of these “nonductile” columns under earthquake loads is necessary to develop efficient and reliable rehabilitation measures; however, existing data for full-scale columns tested are very limited. A research program that included conducting tests on six full-scale column specimens under a variety of conditions was designed to address this shortcoming. The influence of variables such as the level of axial load, the ratio of moment to shear, and the load history on column behavior are investigated.

The column test specimens were subjected to constant axial loading levels during testing of either 0.10, 0.20, and $0.30A_g f'_c$. A single lateral load was applied at the top of each specimen to generate shear and bending moment within the cantilever column specimens. The height of the applied lateral load was varied to produce various ratios of shear demand (shear at expected failure divided by the shear capacity of 0.67 to 0.93) to moment strength. The influence of loading history on specimen response was studied by using two applied displacement histories, referred to as “standard” and “near-field.”

Results of the tests were compared to assess the influence of the test variables on column behavior.

4.2 CONCLUSIONS

Specimens with $20d_b$ lap splice length and a poorly confined cross section behaved unsatisfactorily under cyclic lateral loading. Degradation in lateral strength initiated prior to reinforcement yield in all specimens, typically at lateral drift ratios of 1.0% to 1.5%. Lateral strength degradation resulted from bond deterioration between reinforcement bars and the

surrounding concrete, and the rate of degradation was dependent on the level of axial loading, the level of the applied shear, as well as the loading history.

Changes in shear strength ratios V_{\max}/V_n between 0.67 and 0.93 did not appear to influence the lateral load at which bond deterioration initiated; however the lateral strength degradation rate was increased slightly with increasing shear level.

Plots of normalized moment (M/M_y) for specimens tested with 0.10, 0.20, and $0.30A_g f'_c$ and low shear level indicated that variation in the axial load had only a marginal impact on the lateral load at which bond deterioration initiated. As well, degradation of the lateral strength was similar. The axial load level did impact the normalized column energy-dissipation capacity, which decreased as the axial load level increased.

Significantly less strength degradation was noted for the specimen subjected to the near-fault displacement history. At 2% and 5% lateral drift, the specimen subjected to the near-fault displacement history maintained 89% and 63% of peak lateral force applied, compared with average values of 73% ($73/89 = 82\%$) and 36% ($36/63 = 57\%$) for specimens subjected to the standard displacement history displayed.

Specimens with low axial load were able to maintain the axial load-carrying capacity to very high drift ratios, typically about 10% of the column height. Columns with medium and high axial load levels lost the axial load-carrying capacity during the cycles to 7% and 5% lateral drift, respectively. Specimens with low axial load maintained a residual axial load capacity of approximately 20% the peak axial load capacity. The lack of axial load failures until very high interstory drift ratios indicates that splice failures at interior connections may not create a collapse hazard.

Investigation of moment-rotation responses of the specimens indicated that rotation caused by slippage of longitudinal bars accounted for a significant portion of the total rotation. After bond deterioration initiated, rotational response was mainly controlled by slip.

Average bond strengths along the spliced bars were computed using data from strain gauges. The implied bond strengths for Equation (12-3) in ACI 318-02 provided a lower-bound estimate to the peak bond strengths derived from the test data; however, deterioration of bond strength (slip) resulted in fairly rapid loss of column lateral load capacity.

Measured shear deformations were quite small for the specimens tested. Although shear demand was increased up to 93% of the shear capacity for specimen S30XI, specimen responses were dominated by the lateral strength loss due to bond deterioration.

REFERENCES

- Aboutaha, R., M. D. Engelhardt., J. O. Jirsa, M. E. Kreger., (1996). "Retrofit of Concrete Columns with Inadequate Lap Splices by the Use of Rectangular Steel Jackets," *Earthquake Spectra*, Vol. 12, No. 4, November 1996, pp. 693-714.
- American Concrete Institute, "*Building Code Requirements for Reinforced Concrete: ACI 318*," Farmington Hills, MI, 1956, 1963, 1989, 1995, 1999 and 2002.
- Chai, Yuk; Priestley, M.; and Seible, Frieder; "Seismic Retrofit of Circular Bridge Columns for Enhanced Flexural Performance," *ACI Structural Journal*, V88., No.5, September-October 1991, pp. 572-584.
- Coffman, Harvey L.; Marsh, M. Lee; Brown, Colin B., "Seismic Durability of Retrofitted Reinforced-Concrete Columns", *Journal of Structural Engineering*, Vol. 119, No. 5, pp.1643-1661.
- DeVries, R., J. P. Moehle, W. Hester. (1990). "Lap Splice Strength of Plain and Epoxy-Coated Reinforcement," Report to the Department of Civil Engineering, University of California at Berkeley, Feb. 1990.
- Federal Emergency Management Agency, "Guidelines for the Seismic Rehabilitation of Buildings," *Report No. FEMA-273*, October 1997.
- Heflin, W. E. (1992). "A Study of the Effects of Cover and Spacing on Development Length Requirements for Reinforced Concrete Beams," Master of Science Thesis, Clarkson University, Potsdam, NY, April 1992.
- International Conference of Building Officials, "*Uniform Building Code*," Whittier, CA, 1994, 1997.
- Lynn, A. C., J. P. Moehle, S. A. Mahin, W. T. Holmes. (1996). "Seismic Evaluation of Existing Reinforced Concrete Building Columns," *Earthquake Spectra*, Vol. 12, No. 4, November 1996, pp. 715-739.
- Orangun, C. O., J. O. Jirsa, J. E. Breen (1977). "A Reevaluation of Test Data on Development Length and Splices", *ACI Journal*, March 1977
- Paulay, T, T. M. Zanza, A. Scarpas. (1981). "Lapped Splices in Bridge Piers and in Columns of Earthquake Resisting Reinforced Concrete Frames", Research Report 81-6, Dept. of Civil Engineering, Univ. of Canterbury, Christchurch, New Zealand, Aug. 1981
- Reinforced Concrete Column Test Database, <http://ce.washington.edu/~peera1/>

Reyes, O.; Pincheira, J. (1999), "RC Columns with Lap Splices Subjected to Earthquakes," *Structural Engineering in the 21st Century: Proceedings, 1999 Structures Congress*, April 18-21, 1999, New Orleans, Louisiana, ASCE, Reston, Virginia, 1999, pp. 369-372.

Sozen, M. A., J. P. Moehle. (1990) "Development and Lap-Splice Lengths for Deformed Reinforcing Bars in Concrete," *Report to Portland Cement Association and Concrete Reinforcing Steel Institute*, 1990.

Uniform Building Code (1997)," *International Conference of Building Officials*, Whittier, California

Valluvan, R., M. E. Kreger, J. O. Jirsa. (1993). "Strengthening of Column Splices for Seismic Retrofit of Nonductile Reinforced Concrete Frames," *ACI Structural Journal*, V. 90, No. 4, July-Aug. 1993, pp 432-440.

Wallace, J. W., and Melek, M., "Column Splices: Observed earthquake damage, modeling approaches, and experimental studies," *Proceedings, Second US-Japan Workshop of Performance-Based Engineering of RC Buildings*, Sapporo, Japan, Sept. 2000.

Xiao, Y., Ma, Rui (1997), "Seismic Retrofit of RC Circular Columns Using Prefabricated Composite Jacketing," *Journal of Structural Engineering*, ASCE, 123(10), pp. 1357-1374.



(a) One-Story Parking Structure



(b) 8-Story Parking Structure

Fig. 1.1 - Splice Damage: Northridge Earthquake



(a) Connection region— Gölcük, Turkey



(b) 12-Story Building— Nantou

Figure 1.2 - Anchorage and Splice Damage

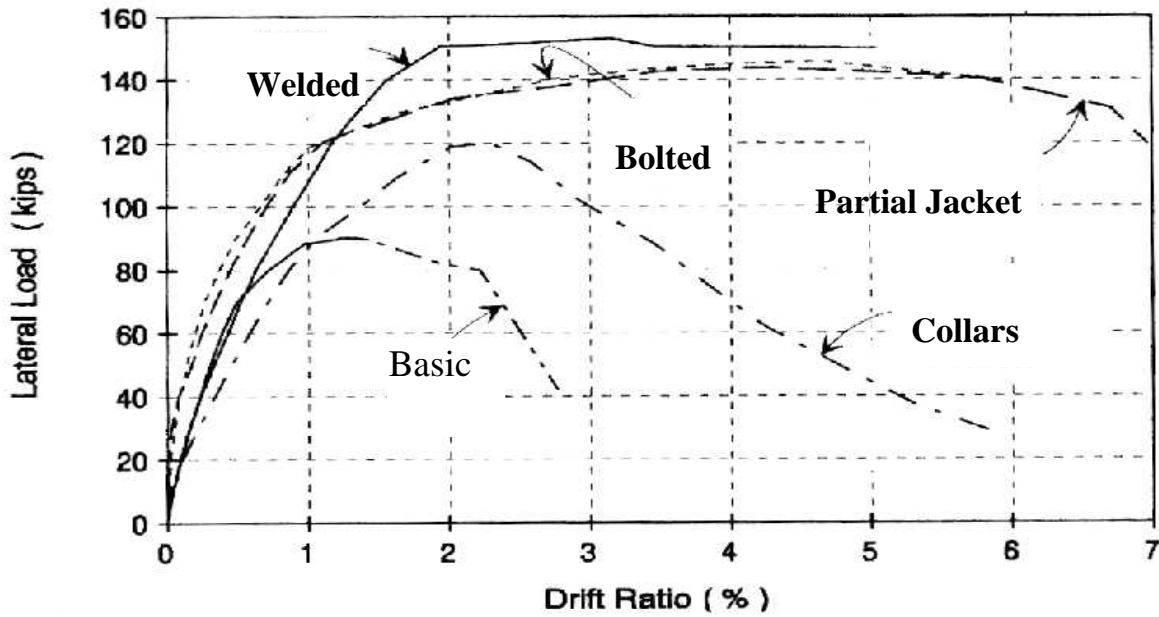


Figure 1.3 - Comparison of Test Results (Aboutaha et al., 1996)

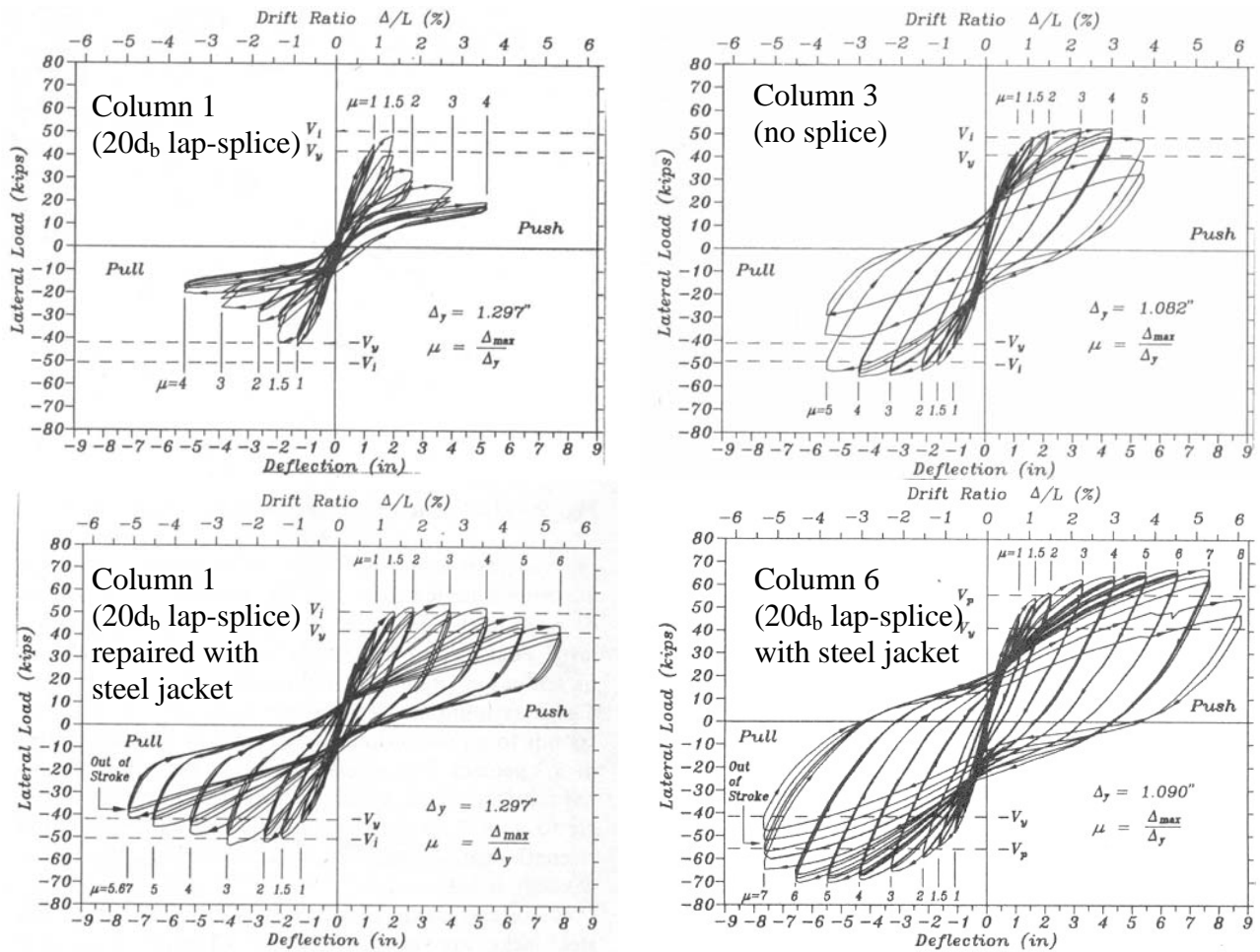
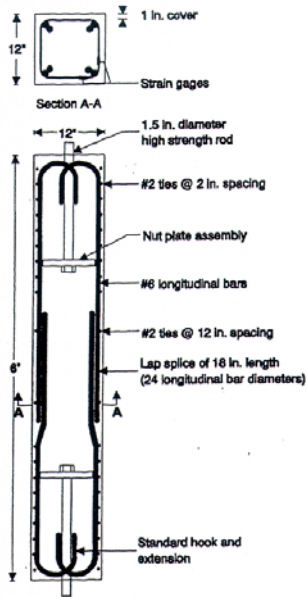


Figure 1.4 – Lateral Load – Top Displacement Relations (Chai et al., 1991)



Valluvan et al. (1993)

Figure 1.5 - Reinforcement Details

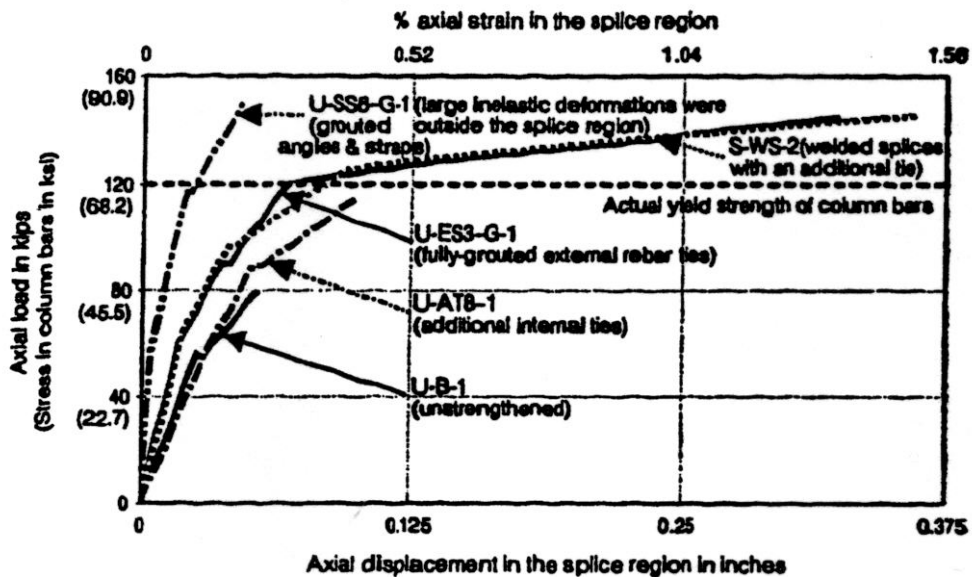


Figure 1.6 - Comparison of Test Results (Valluvan et al., 1993)

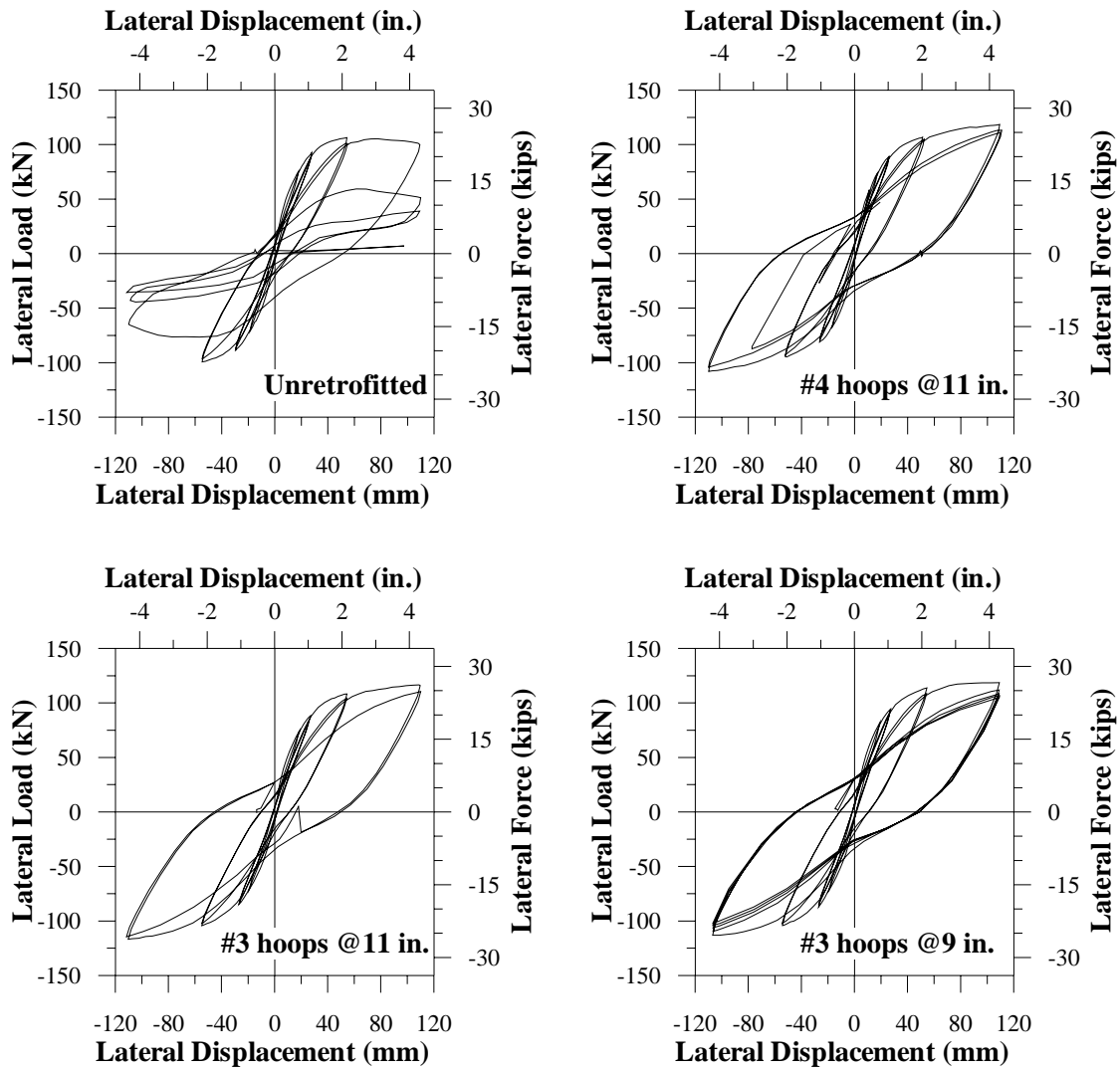


Figure 1.7 - Comparison of Test Results (Coffman et al., 1996)

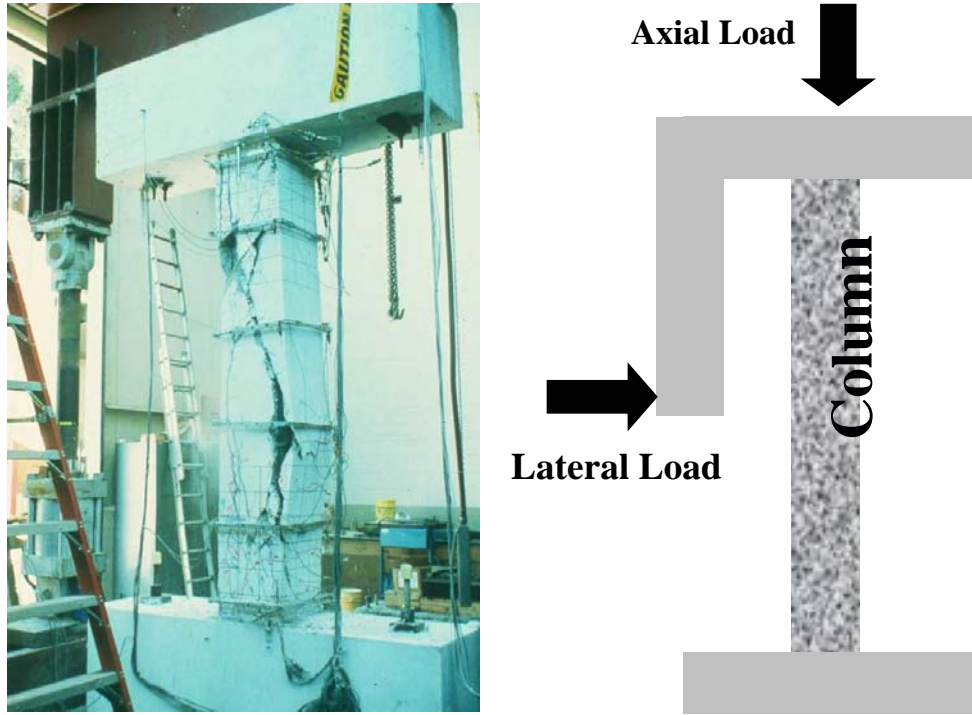


Figure 1.8 - Test Setup (Lynn et al., 1996)

Table 1.1 Test Matrix (Lynn et al., 1996)

Specimen	Longitudinal Reinforcement	Axial Load Applied	Ties	Hoop Spacing (mm; in)	Splice Length (d_b)
3CLH18	8 - #10	$0.12A_g f'_c$	Hoop	457.2 (18)	no splice
2CLH18	8 - #8	$0.12A_g f'_c$	Hoop	457.2 (18)	no splice
3SLH18	8 - #10	$0.12A_g f'_c$	Hoop	457.2 (18)	25
2SLH18	8 - #8	$0.12A_g f'_c$	Hoop	457.2 (18)	20
2CMH18	8 - #8	$0.35A_g f'_c$	Hoop	457.2 (18)	no splice
3CMH18	8 - #10	$0.35A_g f'_c$	Hoop	457.2 (18)	no splice
3CMD12	8 - #10	$0.35A_g f'_c$	Diamond	304.8 (12)	no splice
3SMD12	8 - #10	$0.35A_g f'_c$	Diamond	304.8 (12)	25

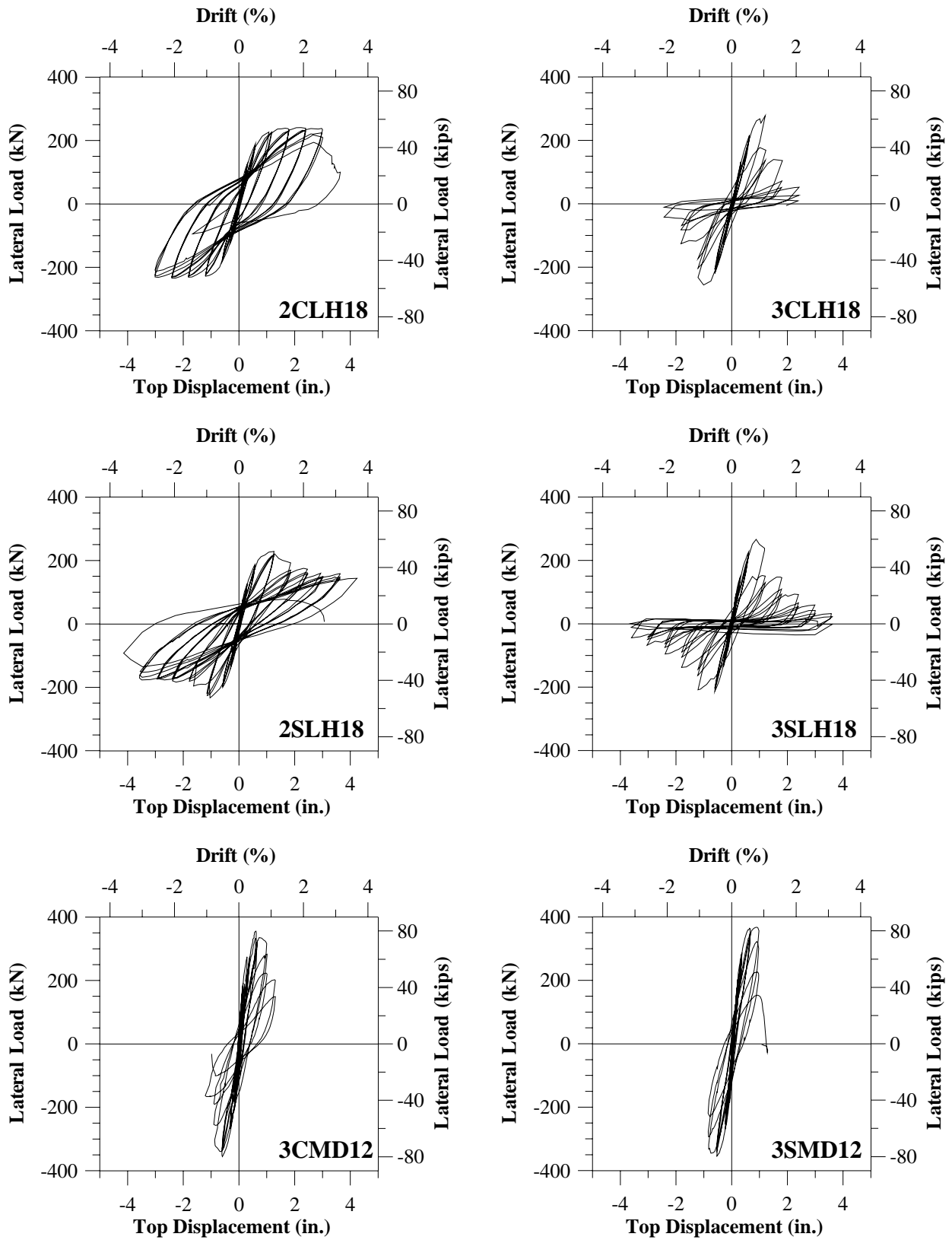


Figure 1.9 - Lateral Load-Top Displacement Relations (Lynn et al., 1996)

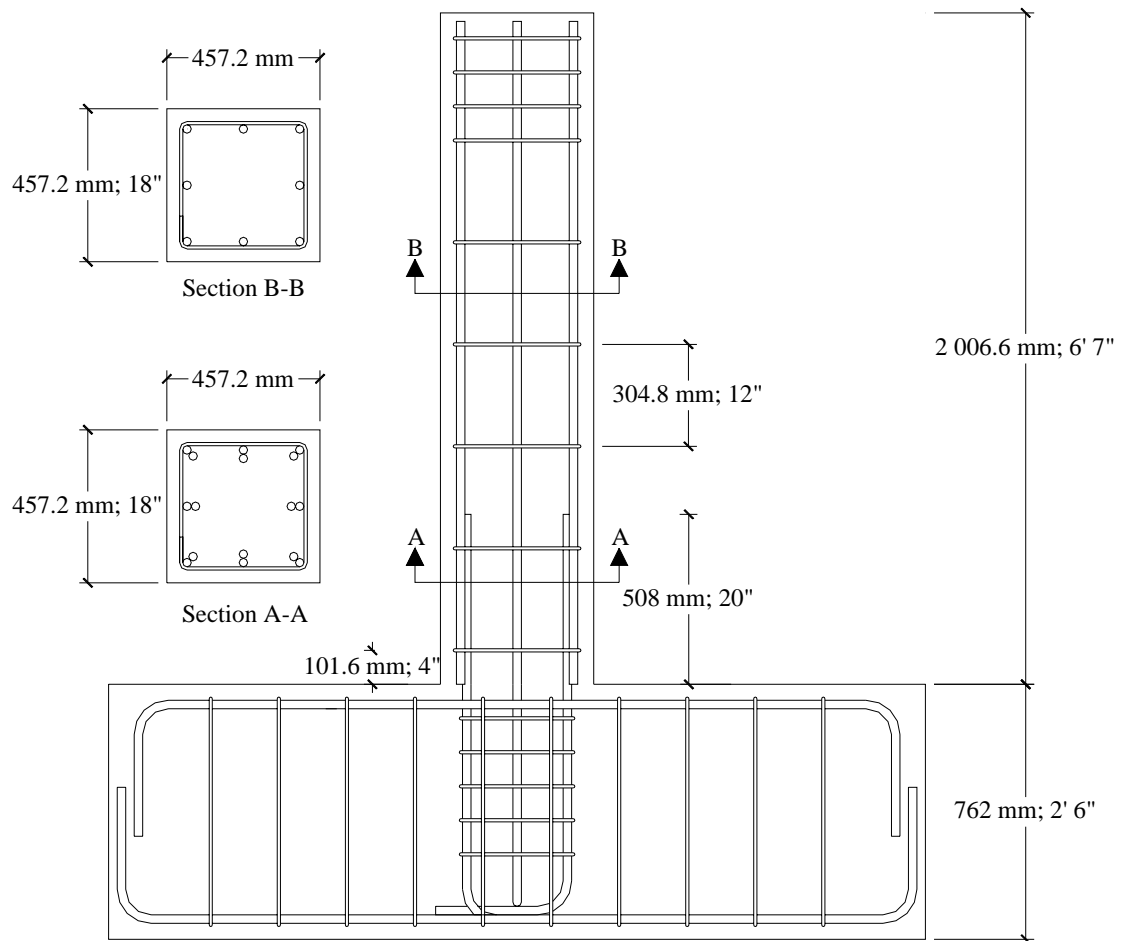


Figure 2.1 - Reinforcing Details

Table 2.1 Test Matrix

Specimen	Axial Load (%A _g f' _c)	Splice Length	$\frac{l_{s_provided}}{l_{s_required}}$	Shear (V _u @ M _n)/V _n	Column Height	Load History
S10MI	10	20d _b	0.65	0.67	1828.8 mm; 6' 0"	Standard
S20MI	20	20d _b	0.65	0.70	1828.8 mm; 6' 0"	Standard
S30MI	30	20d _b	0.65	0.78	1828.8 mm; 6' 0"	Standard
S20HI	20	20d _b	0.64	0.81	1676.4 mm; 5' 6"	Standard
S20HIN	20	20d _b	0.64	0.81	1676.4 mm; 5' 6"	Near Fault
S30XI	30	20d _b	0.64	0.93	1524.0 mm; 5' 0"	Standard

Table 2.2 Calculated Shear Strengths

Specimen	V _c (kN; kips)	V _s (kN; kips)	V _n (kN; kips)
S10MI	211.8; 47.6	88.8; 20.0	300.6; 67.6
S20MI	244.9; 55.1	88.8; 20.0	333.7; 75.0
S30MI	278.0; 62.5	88.8; 20.0	366.8; 82.5
S20HI	241.9; 54.4	88.8; 20.0	330.7; 74.3
S20HIN	241.9; 54.4	88.8; 20.0	330.7; 74.3
S30XI	274.5; 61.7	88.8; 20.0	363.3; 81.7

Table 2.3 Concrete Mix Design

Material	Batch Weights (kg; lbs)		Specific Gravity (gr/cm ³ ; lbs/ft ³)	Absolute Volume
Cement – Type II	255.8; 564	6.00 sacks	3.15; 196.56	2.87
W. C. Sand	643.2; 1418	45.0%	2.66; 165.98	8.54
Gravel 3/8"	213.2; 470	15.0%	2.65; 165.36	2.84
Gravel 1"	576.1; 1270	40.1%	2.67; 166.61	7.62
Water (Maximum)	137.5; 303.2	36.4 gals	1.00; 62.4	4.86
Daratard 17	0.48; 1.1			
1% Entrapped Air				0.27
Total	1825.8; 4025.2			27.0

Method: Los Angeles City Building Code Section 1905.3.3.2/RGA 2-90

Water/Cement Ratio: 6.1 gals/sack (0.54)

Table 2.4 Aggregate Gradation (with Vulcan materials, San Gabriel Valley (Reliance) Aggregates)

Aggregates	2"	1½"	1"	¾"	½"	3/8"	#4	#8	#16	#30	#50	#100	#200
W.C. Sand						100	96	81	62	41	18	6	2
3/8" Aggr.					100	92	10	4	2	0	0	0	0
1" Aggr.		100	96	69	30	10	3	0	0	0	0	0	0
Combined	100	100	98	88	72	63	46	37	28	18	8	3	1

Table 2.5 Concrete Properties

Specimen	f'c (psi; MPa)	fct (psi; MPa)	f_r (psi; MPa)
S10MI-S20MI-S30MI	5255 (36)	491 (3.4)	544 (3.8)
S20HI-S20HIN-S30HI	5125 (35)	-	537 (3.7)

Table 2.6 Reinforcement Bar Properties

Description	Bar Size	Yield Stress (ksi; MPa)	Tensile Strength (ksi; MPa)
Column Longitudinal Bars	# 8 (25.4 mm)	74.0 (510)	118.6 (818)
Starter Bars & Pedestal (1 st set)	# 8 (25.4 mm)	75.6 (521)	108.1 (746)
Starter Bars & Pedestal (2 nd set)	# 8 (25.4 mm)	73.5 (507)	117.1 (807)
Transverse Reinforcement	# 3 (9.53 mm)	69.7 (481)	108.7 (750)



Figure 2.2 - Standard Concrete Compressive Test

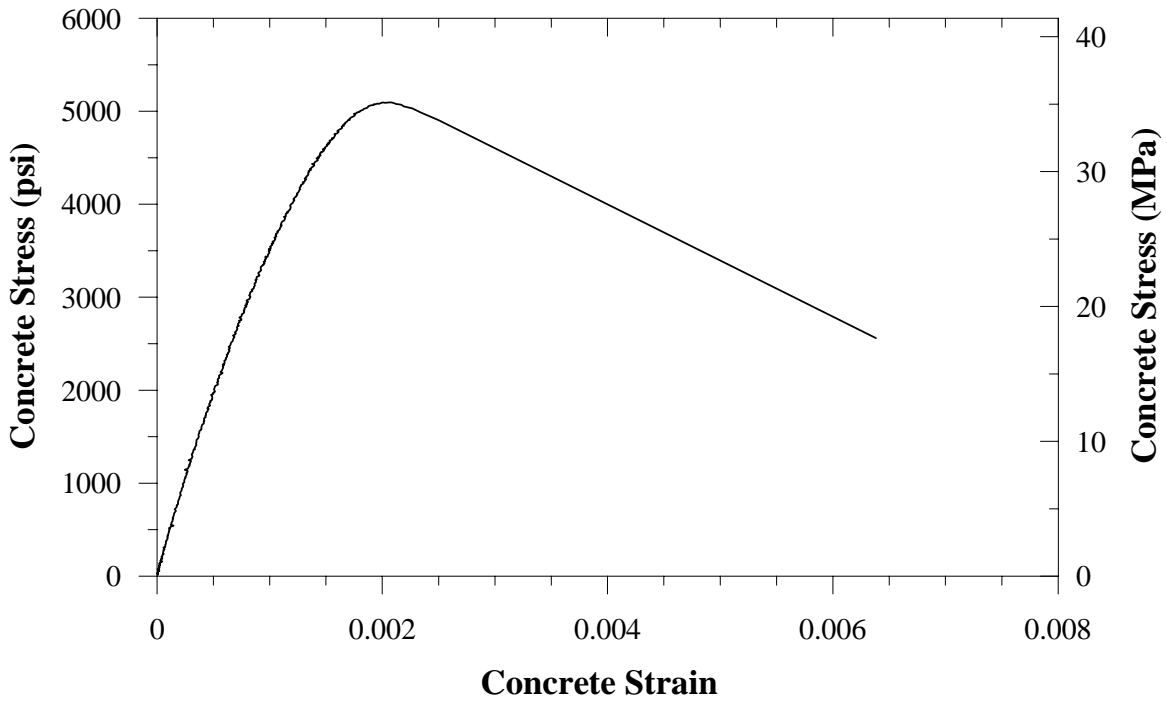


Figure 2.3 - Stress-Strain Diagram for Specimens: S10MI, S20MI, and S30MI

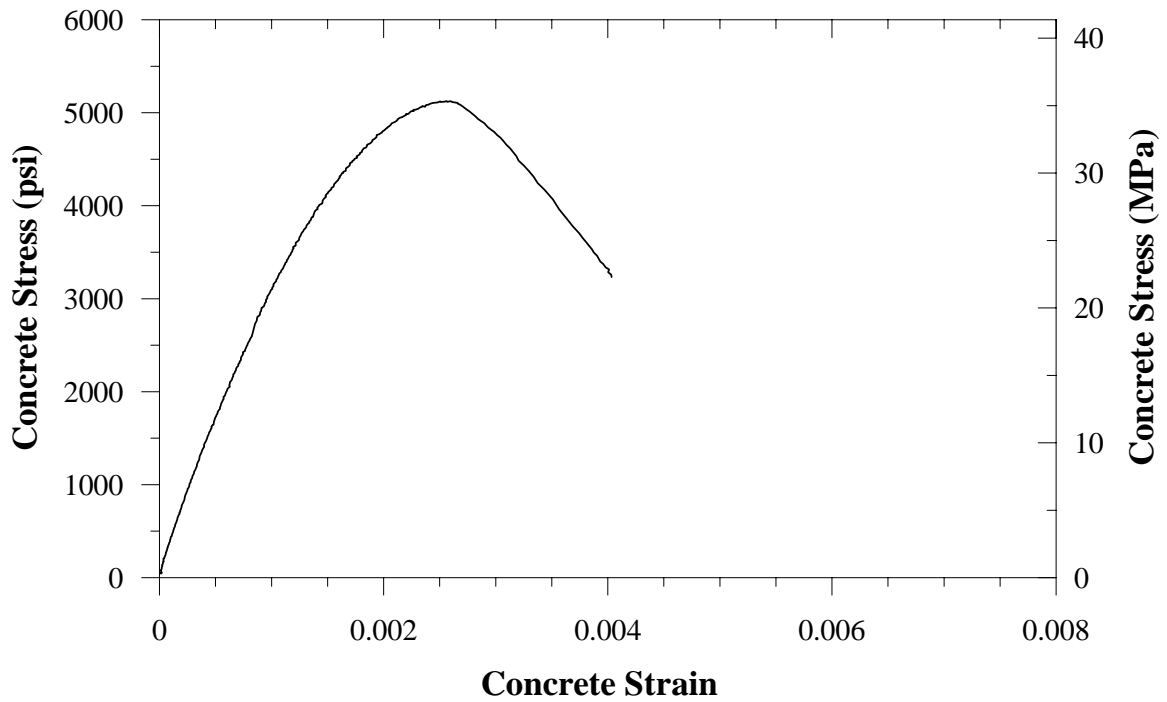


Figure 2.4 - Stress-Strain Diagram for Specimens: S20HI, S20HIN, and S30XI

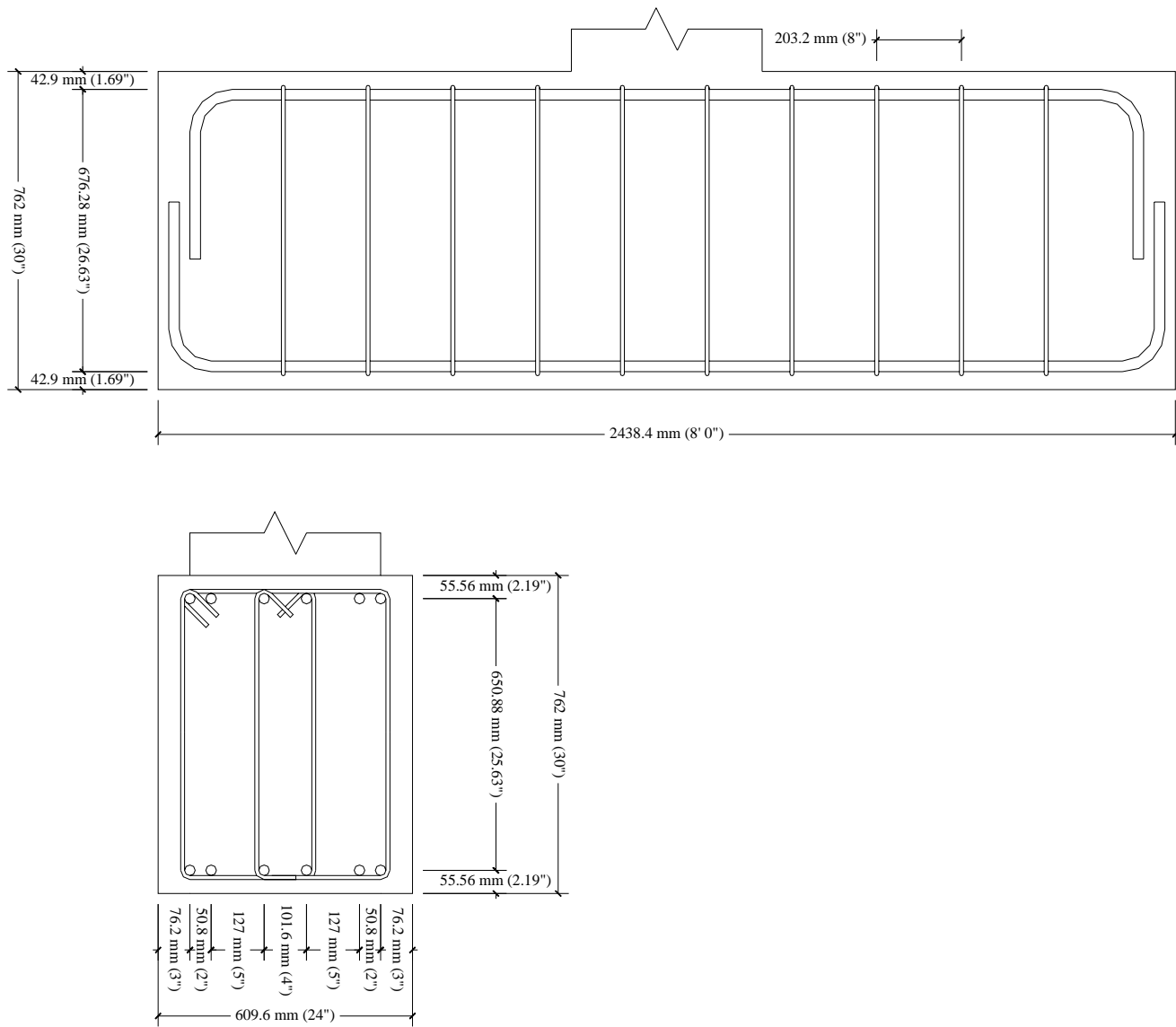


Figure 2.5 - Pedestal Reinforcement Details

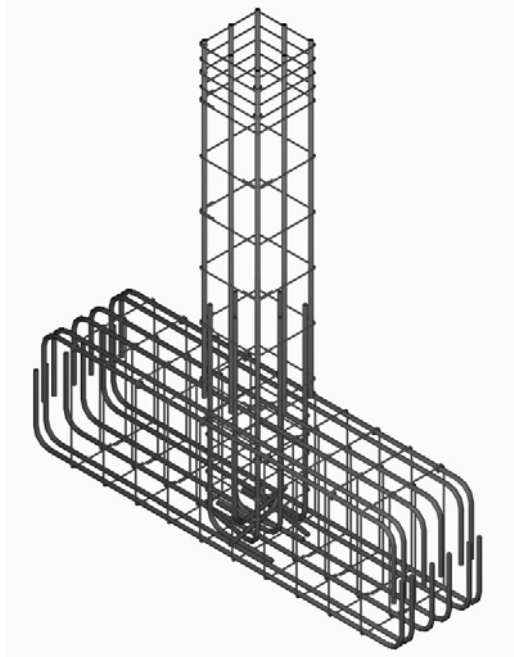


Figure 2.6 - Reinforcement Cage



Figure 2.7 - Reinforcement Cages before Placing Concrete



Figure 2.8- Column Cross Section

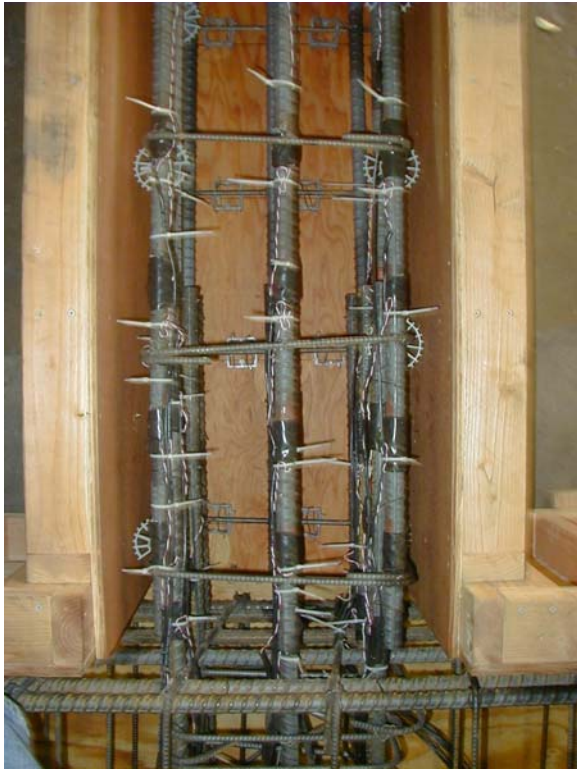


Figure 2.9- Splice Region



Figure 2.10 - Specimen



Figure 2.11 - Joint Close-up

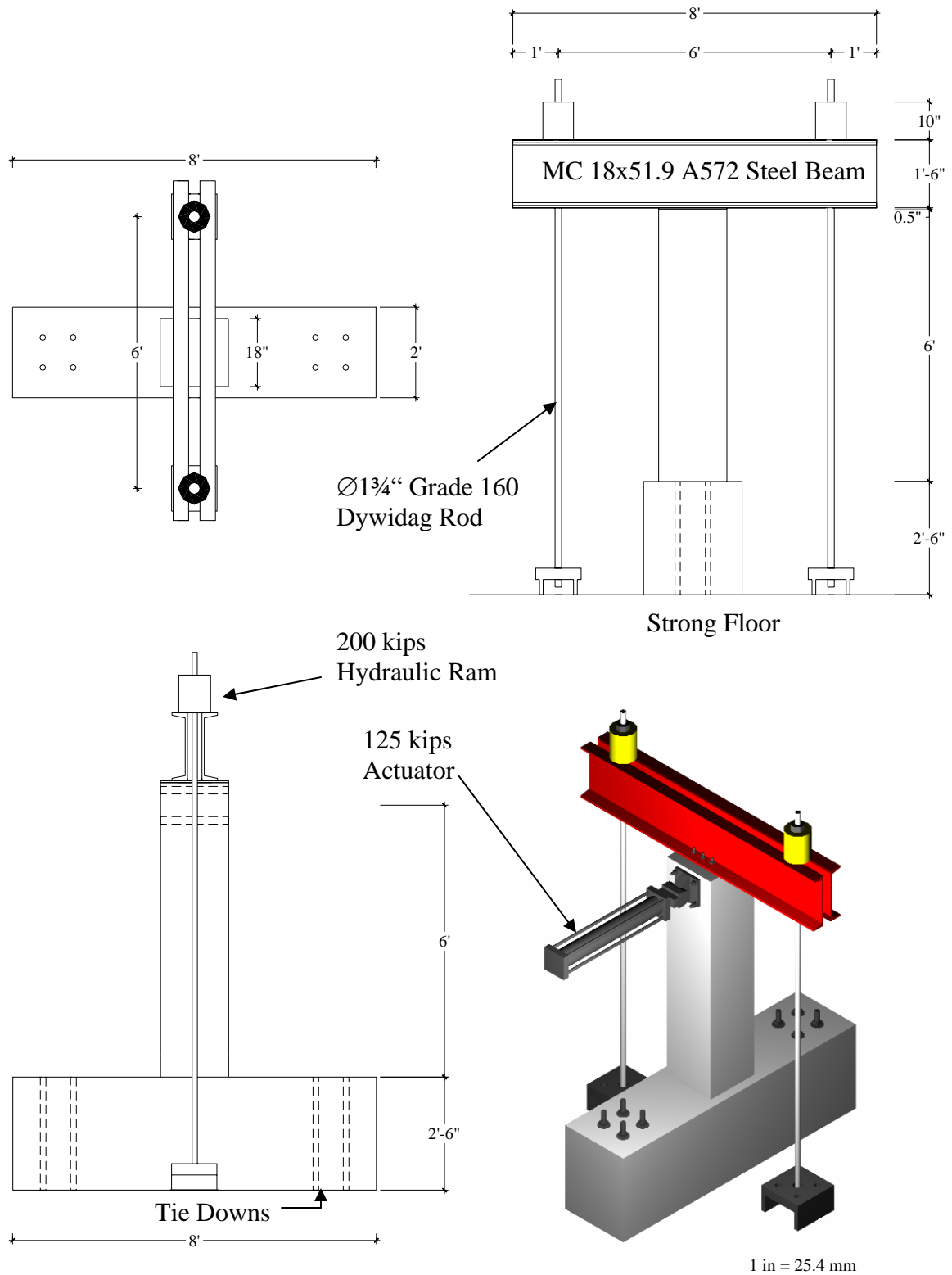


Figure 2.12 - Test Setup

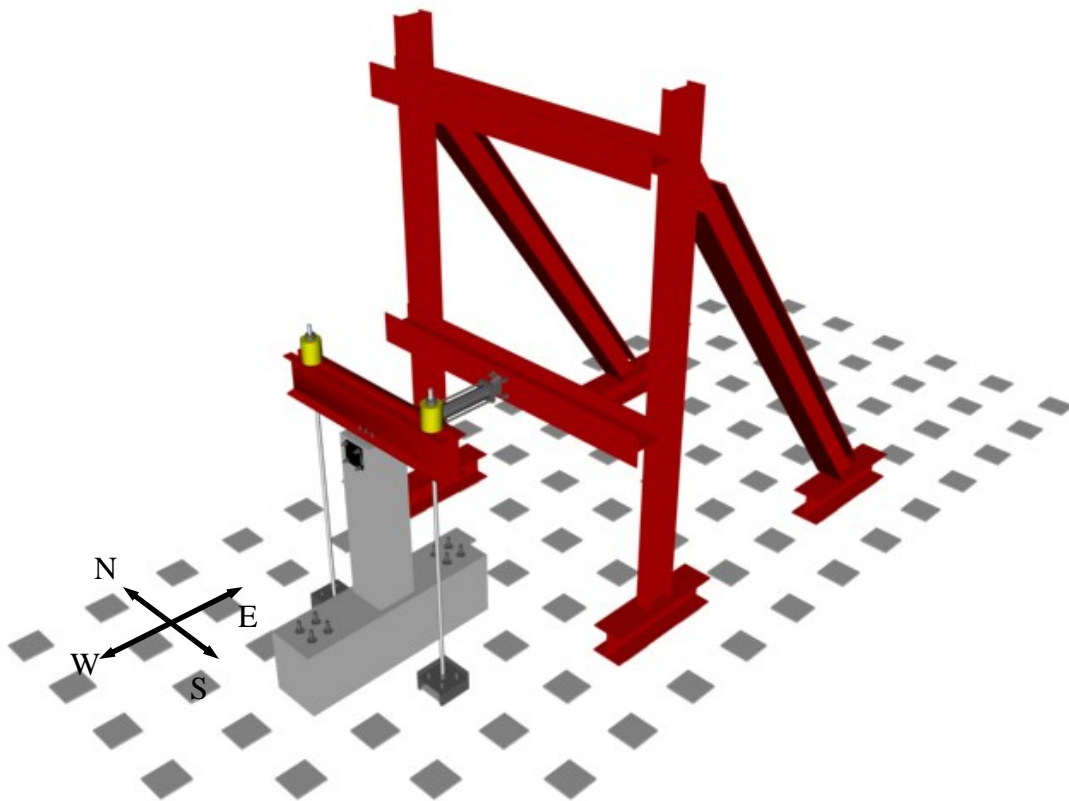


Figure 2.13 - Test Setup with Reaction Frame



Figure 2.14 - Test Setup during Experiment

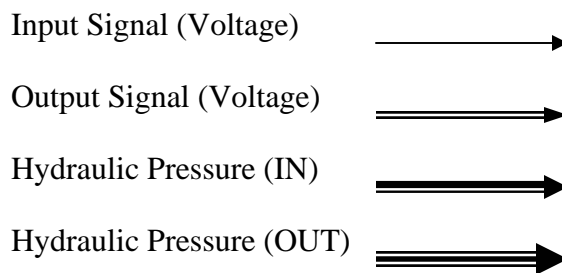
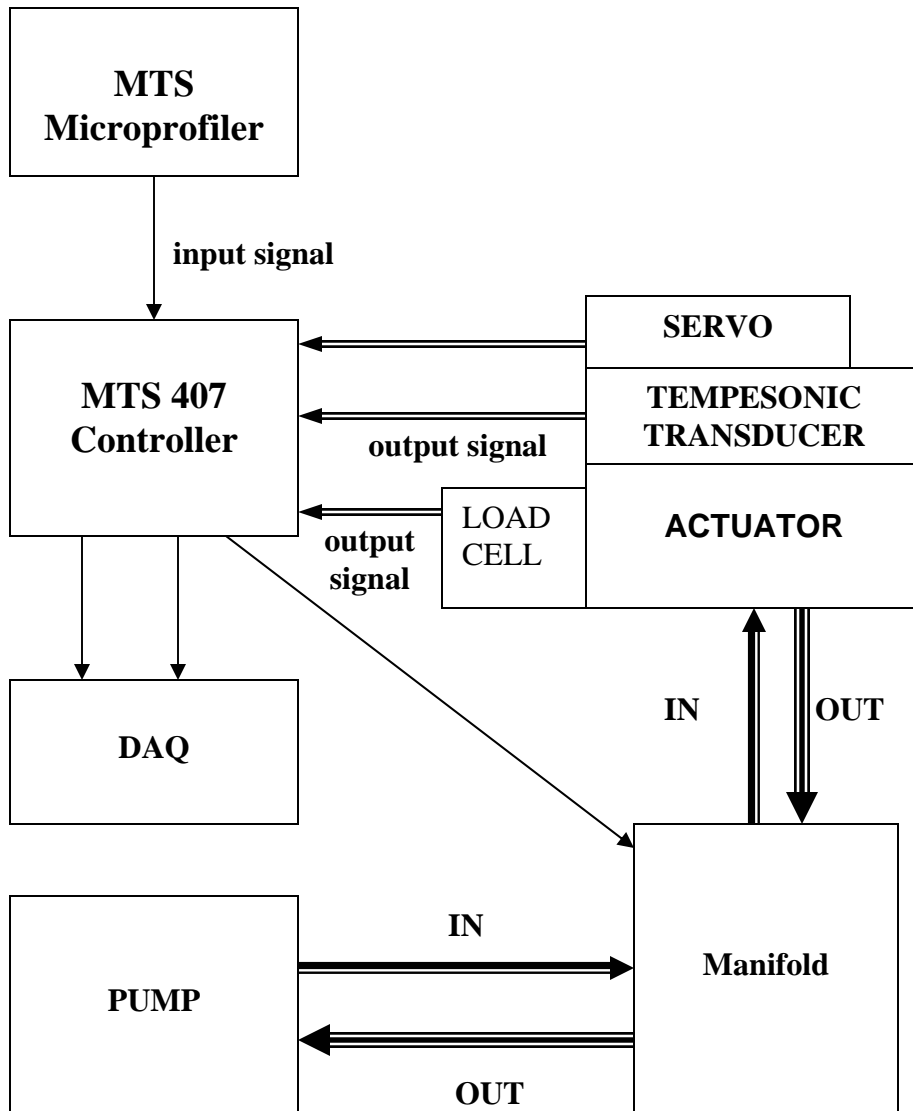


Figure 2.15 - Actuator Control Schematic

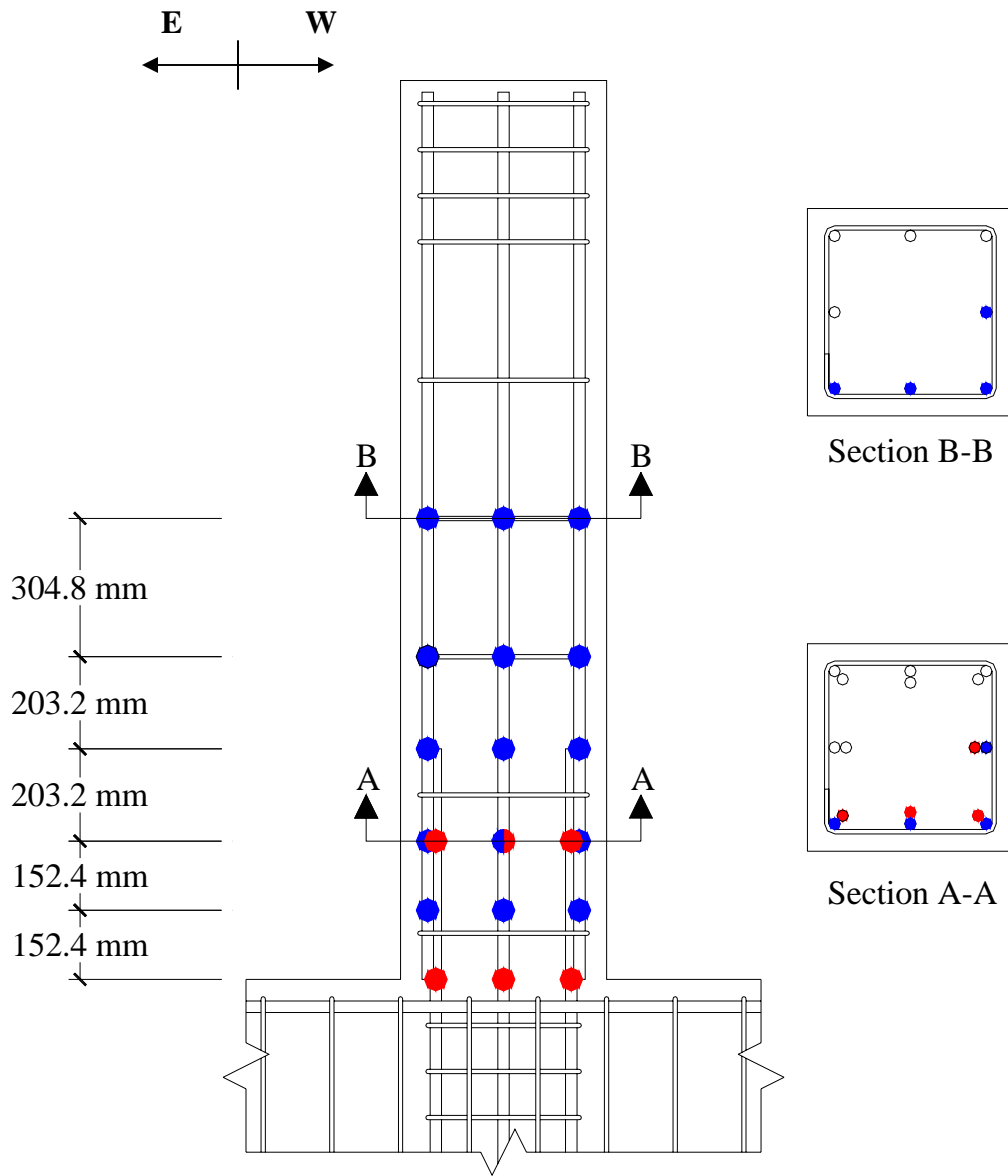


Figure 2.16 - Strain Gauge Layout

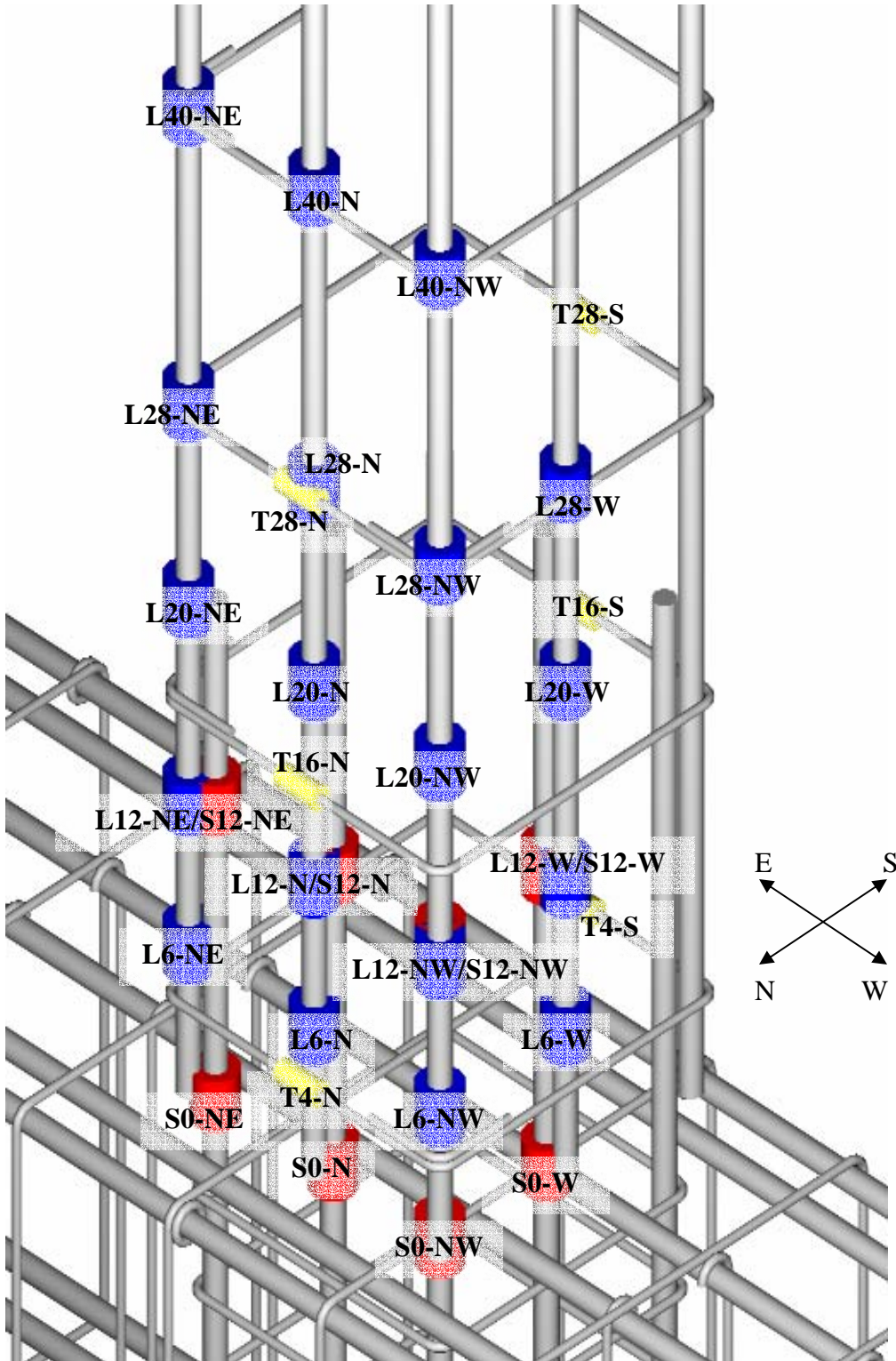


Figure 2.17 - Strain Gauge Labeling Scheme

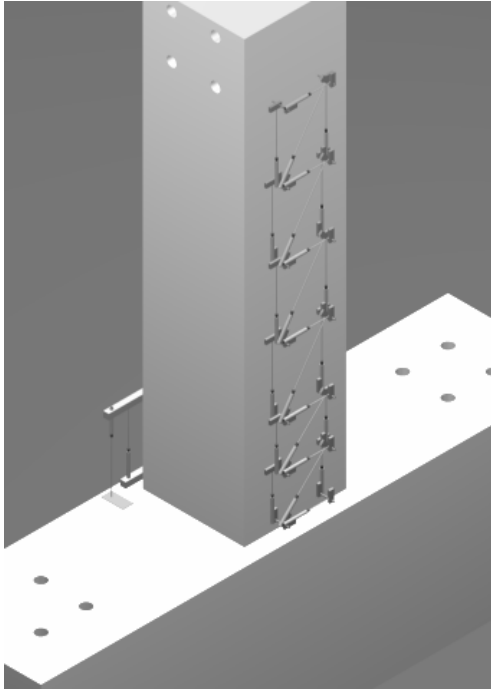


Figure 2.18 - External Instrumentation Grid (S10MI, S20MI, S30MI)

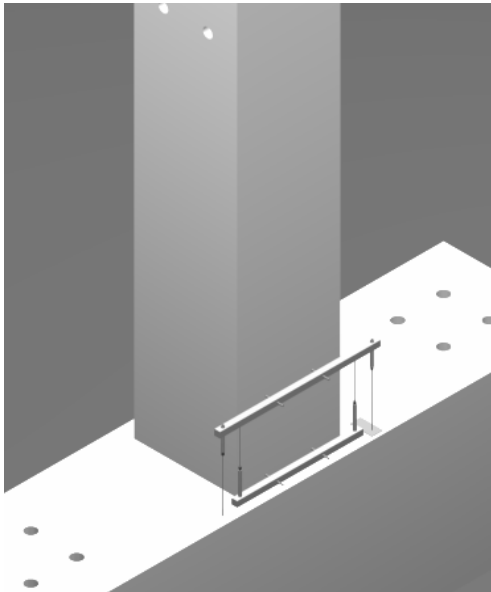


Figure 2.19 - Transducers Used to Measure Total and Slip Rotation at Column Base (S10MI, S20MI, S30MI)

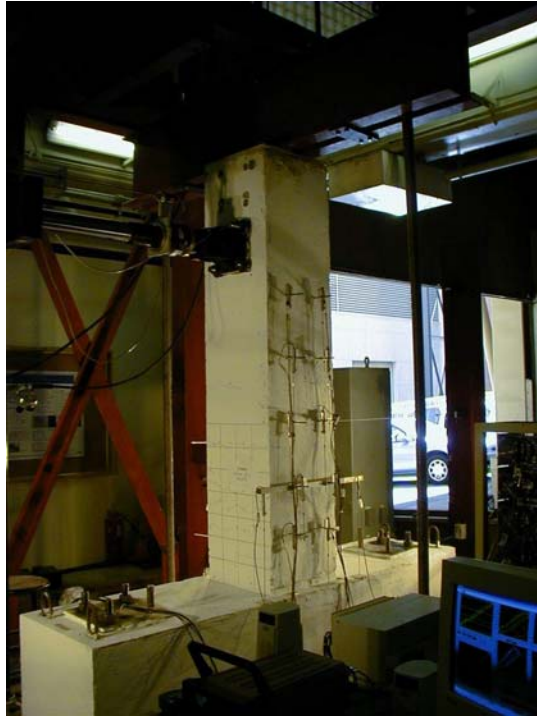


Figure 2.20 - External Instrumentation (S20HI, S20HIN, S30XI)



Figure 2.21 - Shear Instrumentation (S20HI, S20HIN, S30XI)

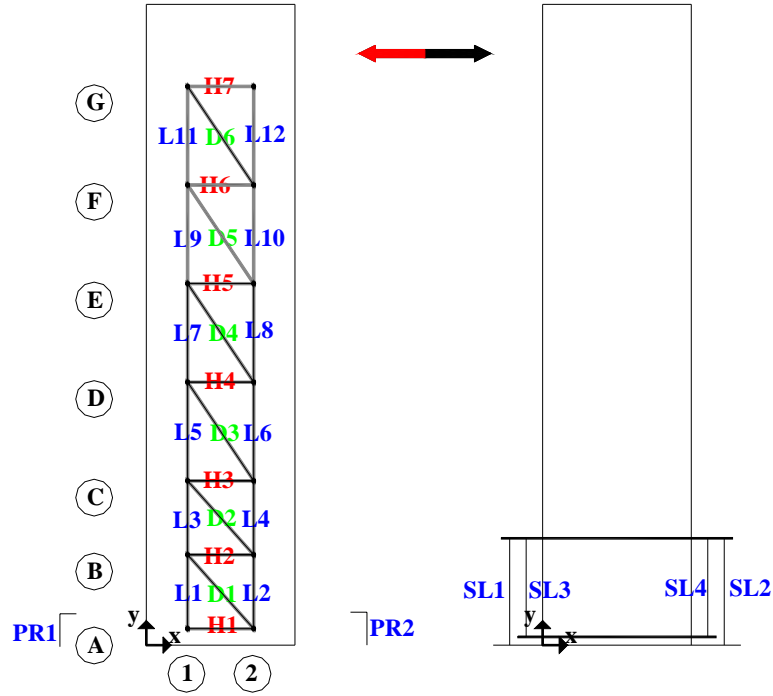


Figure 2.22 - External Instrumentation Layout (S10MI, S20MI, S30MI)

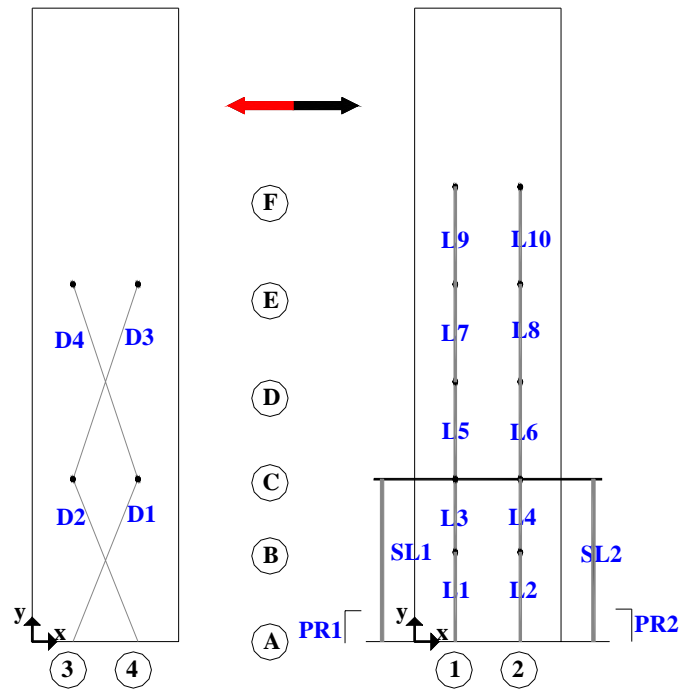


Figure 2.23 - External Instrumentation Layout (S20HI, S20HIN, S30XI)

Table 2.7 Potentiometer Coordinates

	S10MI		S20MI		S30MI		S20HI		S20HIN		S30XI		
	x (in.)	y (in.)	x (in.)	y (in.)	x (in.)	y (in.)	x (in.)	y (in.)	x (in.)	y (in.)	x (in.)	y (in.)	
A	1	5.00	2.00	5.00	1.88	4.00	2.00	5.00	0.00	4.50	-0.38	5.00	-0.56
	2	13.00	2.00	12.81	1.88	12.63	2.00	13.00	0.00	13.50	-0.38	13.00	-0.56
	3	5.00	1.00	5.19	1.13	5.00	1.25	5.00	0.00	5.63	0.00	5.00	0.00
	4	13.00	1.00	13.00	1.13	13.00	1.25	13.00	0.00	12.75	0.00	13.00	0.00
B	1	5.00	10.50	5.06	11.38	4.13	11.25	5.00	10.88	4.94	11.00	5.00	11.13
	2	12.75	10.50	12.69	11.25	12.38	11.25	13.00	11.00	12.88	10.94	13.06	11.00
	3	5.00	13.00	5.25	12.94	5.00	12.75	5.13	10.94	-	-	5.00	10.88
	4	13.00	13.00	13.06	12.81	13.00	12.75	13.00	11.06	-	-	13.13	11.00
C	1	4.75	19.25	5.13	20.50	4.50	20.00	5.25	19.88	4.94	20.06	5.00	20.19
	2	13.25	19.50	12.50	20.50	12.13	19.75	13.00	19.88	12.88	19.88	13.00	20.06
	3	-	-	-	-	-	-	5.06	19.94	5.00	19.97	5.06	19.94
	4	-	-	-	-	-	-	13.06	20.00	13.25	19.94	13.06	20.00
D	1	4.94	31.50	5.44	31.89	5.00	32.00	5.00	31.75	4.81	32.00	5.13	32.19
	2	13.19	31.50	12.25	32.50	12.50	31.88	13.00	31.88	12.81	31.81	13.19	32.06
	3	-	-	-	-	-	-	4.88	31.75	-	-	5.00	32.13
	4	-	-	-	-	-	-	13.00	31.69	-	-	12.94	31.94
E	1	4.50	43.00	5.50	43.75	4.63	44.13	5.00	43.75	4.75	43.94	5.13	44.19
	2	13.00	43.00	12.44	43.63	12.63	43.88	13.00	43.88	12.75	43.81	13.19	44.06
	3	-	-	-	-	-	-	4.88	44.25	4.94	43.97	4.94	43.94
	4	-	-	-	-	-	-	13.00	43.88	12.81	43.94	13.03	44.00
F	1	4.75	55.25	5.44	54.94	4.88	55.88	5.00	55.81	4.88	56.06	5.00	56.19
	2	13.25	55.00	12.50	55.38	12.50	56.13	13.00	55.94	12.81	55.94	13.00	56.06
	3	-	-	-	-	-	-	5.06	55.88	-	-	-	-
	4	-	-	-	-	-	-	12.94	55.88	-	-	-	-
G	1	5.00	66.25	5.69	66.44	4.63	67.38	-	-	-	-	-	-
	2	13.00	66.50	12.50	66.88	12.50	67.38	-	-	-	-	-	-

1 in. = 25.4 mm

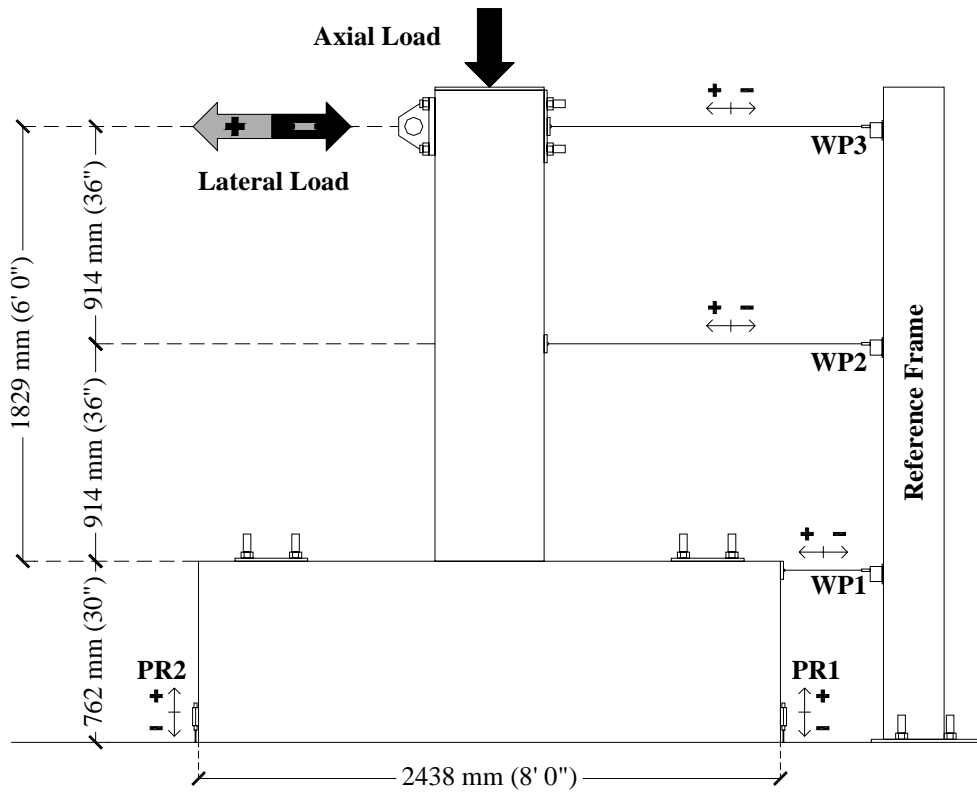


Figure 2.24 - Test Specimen with Cable-Extension Position Transducers



Figure 2.25 - Data Acquisition Device and MTS 407 Controller

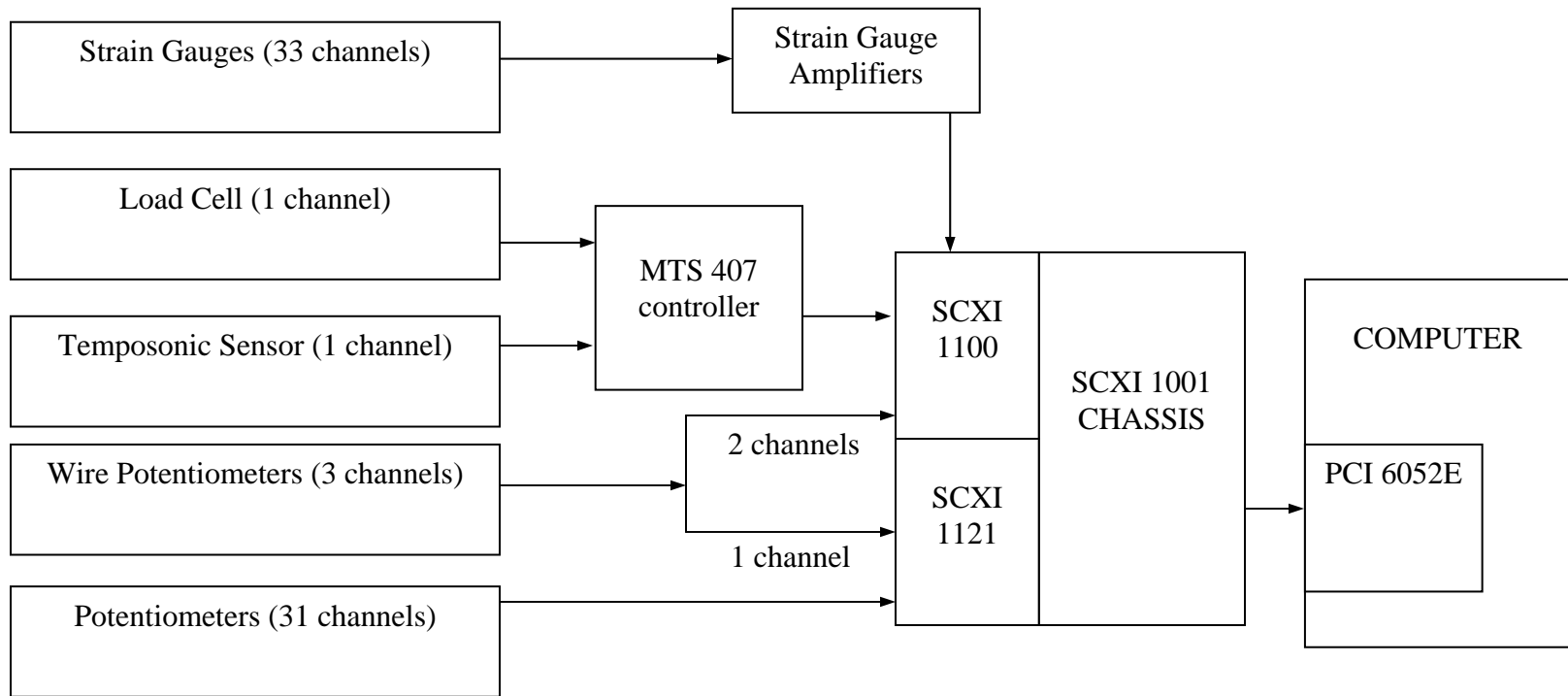


Figure 2.26 - Data Acquisition Schematic



Figure 2.27 - Strain Gauge Amplifier

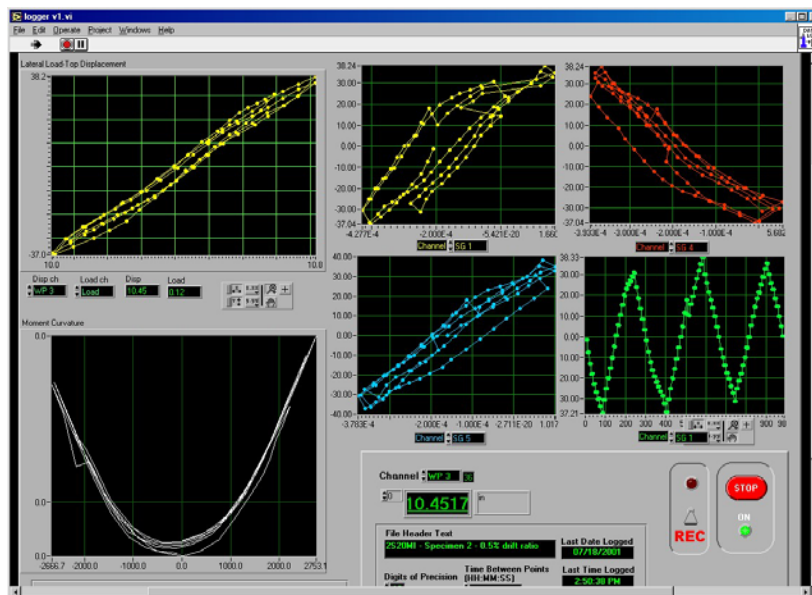


Figure 2.28 - Data Logger Program Window

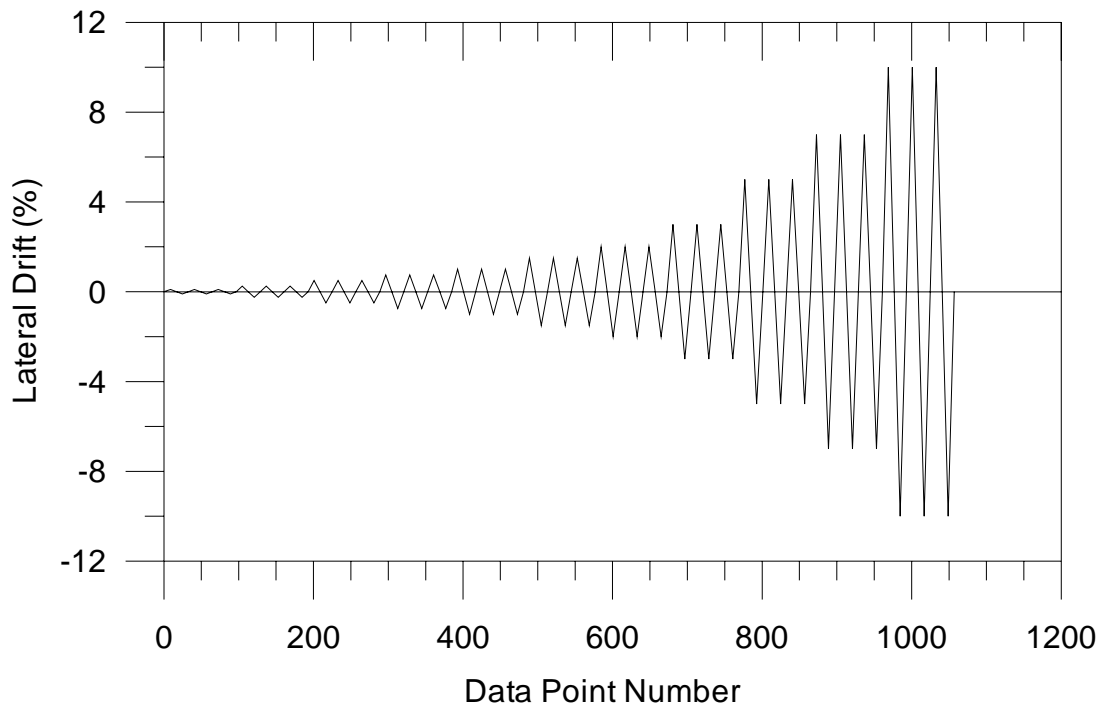


Figure 2.29 - Standard Displacement History

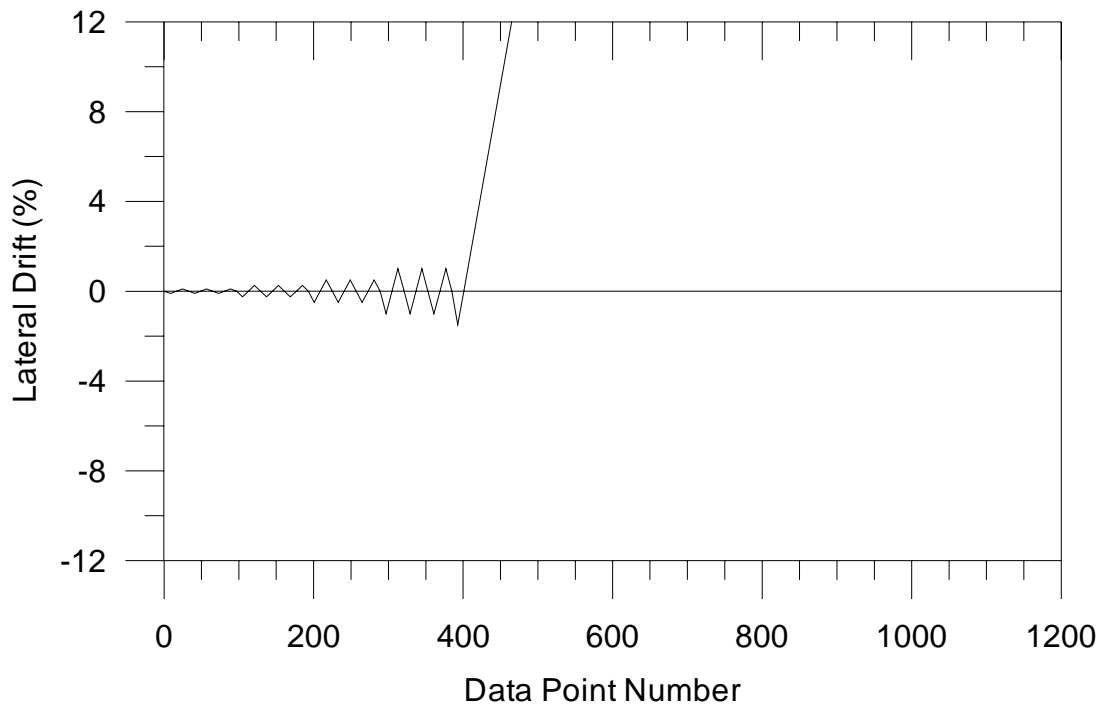


Figure 2.30 - Near-Fault Displacement History

Table 2.8 Data Point Numbers (S10MI, S20MI, S30MI, S20HI, S30XI)

Lateral Drift (%)	1st Cycle	2nd Cycle	3rd Cycle
-0.10	9	41	73
0.10	25	57	89
-0.25	105	137	169
0.25	121	153	185
-0.50	201	233	265
0.50	217	249	281
-0.75	297	329	361
0.75	313	345	377
-1.00	393	425	457
1.00	409	441	473
-1.50	489	521	553
1.50	505	537	569
-2.00	585	617	649
2.00	601	633	665
-3.00	681	713	745
3.00	697	729	761
-5.00	777	809	841
5.00	793	825	857
-7.00	873	905	937
7.00	889	921	953
-10.00	969	1001	1033
10.00	985	1017	1049

Table 2.9 Data Point Numbers (S20HIN)

Lateral Drift (%)	1st Cycle	2nd Cycle	3rd Cycle
-0.10	9	41	73
0.10	25	57	89
-0.25	105	137	169
0.25	121	153	185
-0.50	201	233	265
0.50	217	249	281
-1.00	297	329	361
1.00	313	345	377
-1.50	393	-	-
1.50	409	-	-
2.00	412	-	-
3.00	417	-	-
4.50	425	-	-
6.00	432	-	-
7.50	440	-	-
9.00	447	-	-
12.00	460	-	-

Table 3.1 Test Results Summary

Specimen	Maximum Lateral Load (kN)	Maximum Lateral Load Reached at	Type of Failure	Applied Axial Load (kN)
S10MI	202.7	1.50% Drift	Bond Det.	534
S20MI	233.5	1.28% Drift	Bond Det.	1068
S30MI	285.3	1.45% Drift	Bond Det.	1601
S20HI	269.5	1.33% Drift	Bond Det.	1068
S20HIN	267.4	1.00% Drift	Bond Det.	1068
S30XI	340.7	1.50% Drift	Bond Det.	1601

Table 3.2 Observed Damage

Specimen	Flexural Cracking		Longitudinal Cracking		Shear Cracking		Concrete Crushing	
	Data Point	Lateral Load (kN)	Data Point	Lateral Load (kN)	Data Point	Lateral Load (kN)	Data Point	Lateral Load (kN)
S10MI	152	83	361	155	306	38	562	44
S20MI	105	103	297	182	313	210	489	204
S30MI	217	157	489	264	297	235	489	264
S20HI	103	107	313	227	297	231	537	210
S20HIN	105	118	297	262	297	262	404	260
S30XI	137	115	297	263	313	301	489	310

Table 3.3 Axial Load Capacity Loss

Specimen	Applied Axial Load		Axial Capacity Lost at	
		(kN)	Drift (%)	DPN
S10MI	$0.10A_g f'_c$	534	-	-
S20MI	$0.20A_g f'_c$	1068	7 (third cycle)	929
S30MI	$0.30A_g f'_c$	1601	5 (second cycle)	814
S20HI	$0.20A_g f'_c$	1068	7 (second cycle)	947
S20HIN	$0.20A_g f'_c$	1068	-	-
S30XI	$0.30A_g f'_c$	1601	5 (first cycle)	800

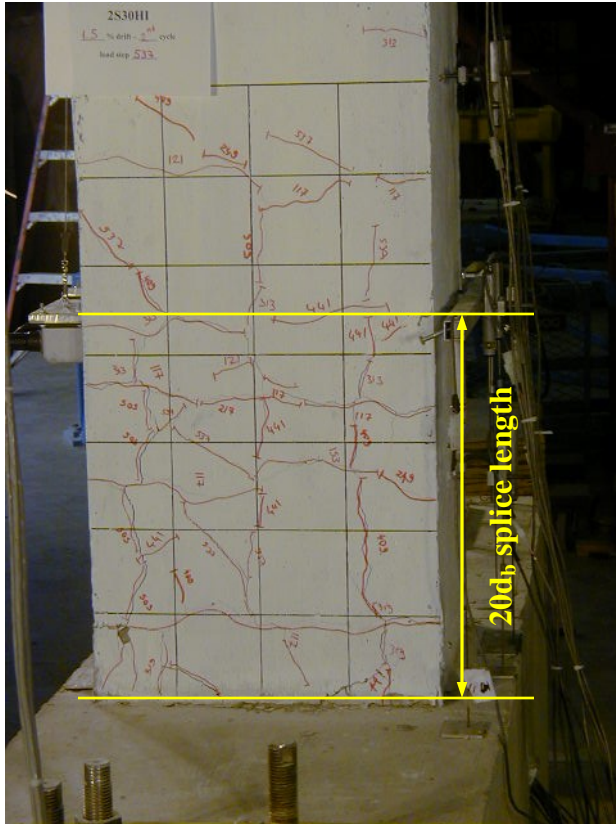


Figure 3.1 - Longitudinal Cracks Indicating Bond Deterioration (S20HI at 1.5% Drift) (Left)

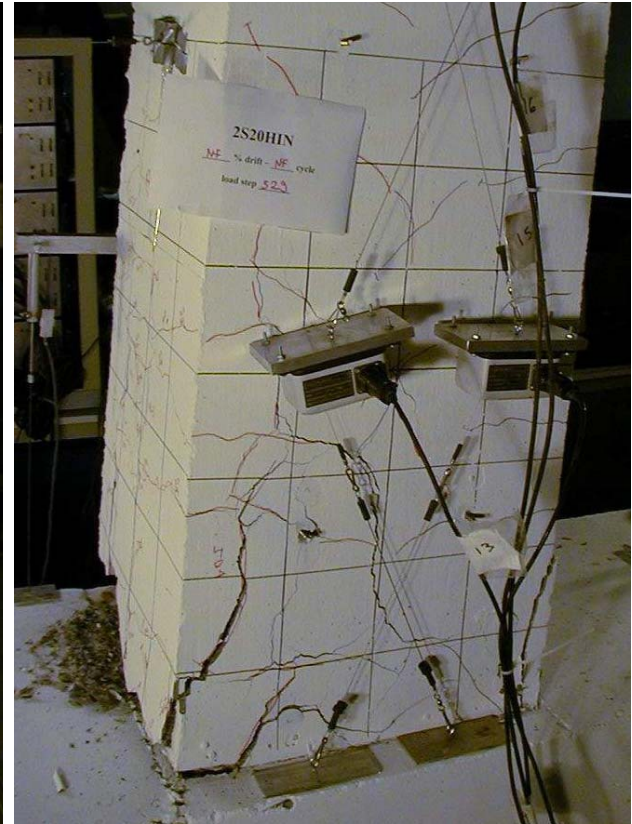


Figure 3.2 - Longitudinal and Shear Cracking (S20HIN at 5.8% Drift) (Right)

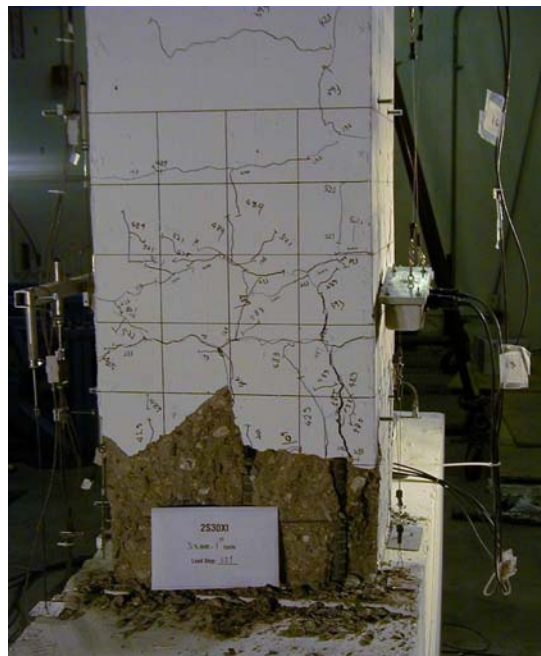


Figure 3.3 - Concrete Spalling (S30XI at 3% Drift)

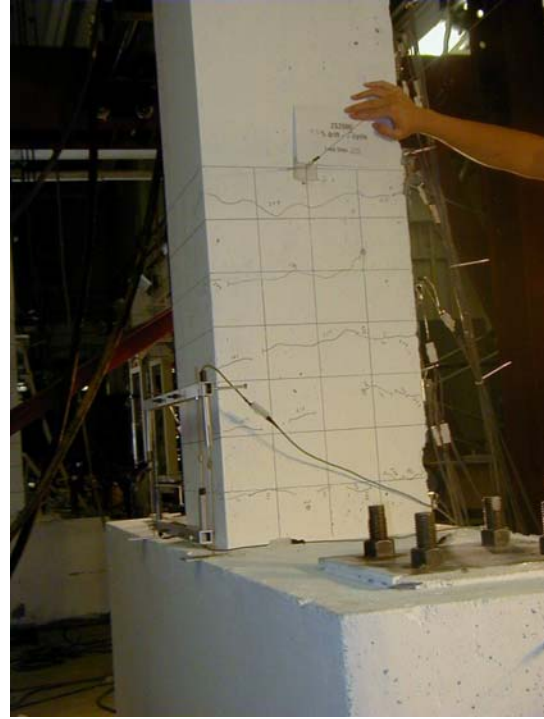
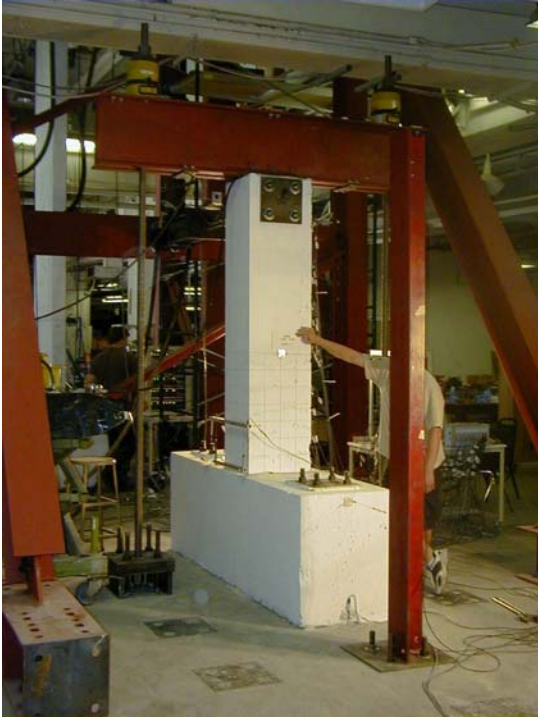


Figure 3.4 -Specimen S20MI at 0.50% Lateral Drift

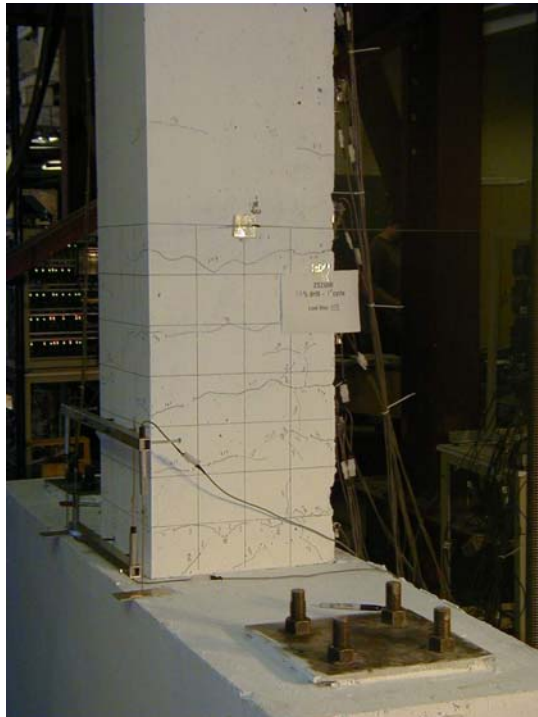


Figure 3.5 - Specimen S20MI at 1.0% Drift (Left)

Figure 3.6 - Specimen S20MI at 1.5% Drift (Right)



Figure 3.7 - Specimen S20MI at 2.0% Lateral Drift

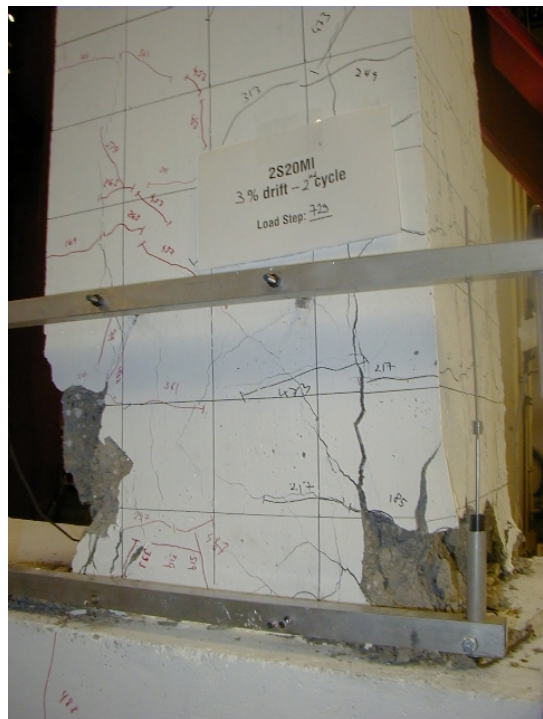


Figure 3.8 - Specimen S20MI at 3.0% Lateral Drift



Figure 3.9 - Specimen S20MI at 5.0% Lateral Drift



Figure 3.10 - Specimen S20MI at 7.0% Lateral Drift

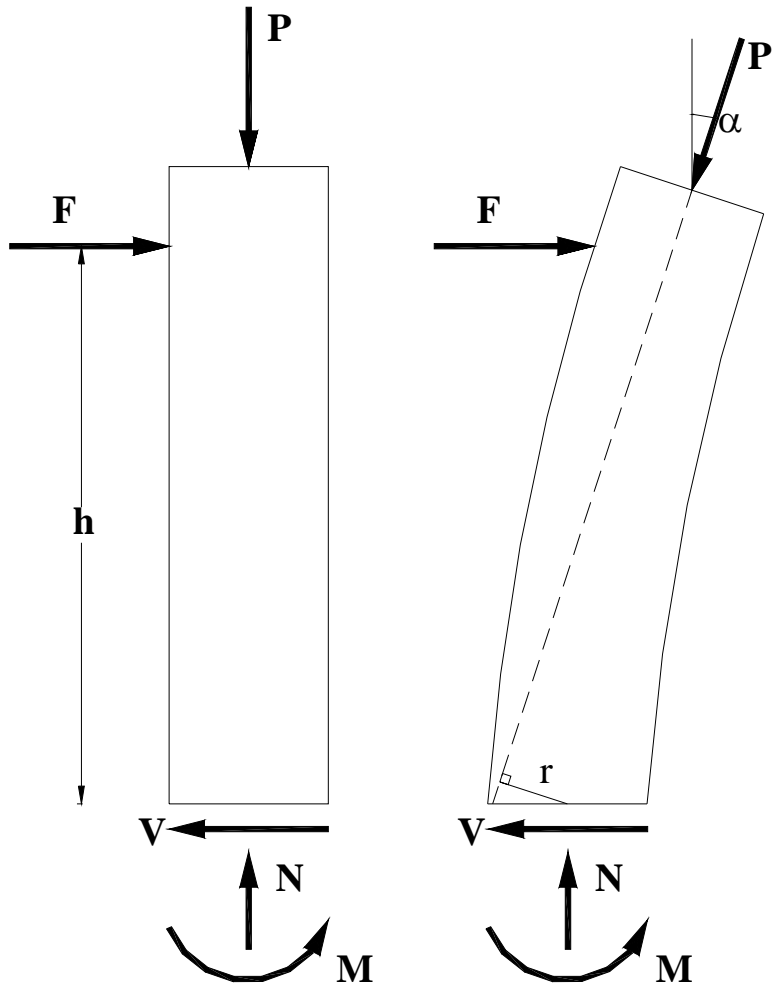


Figure 3.11 - Column Free-Body Diagram

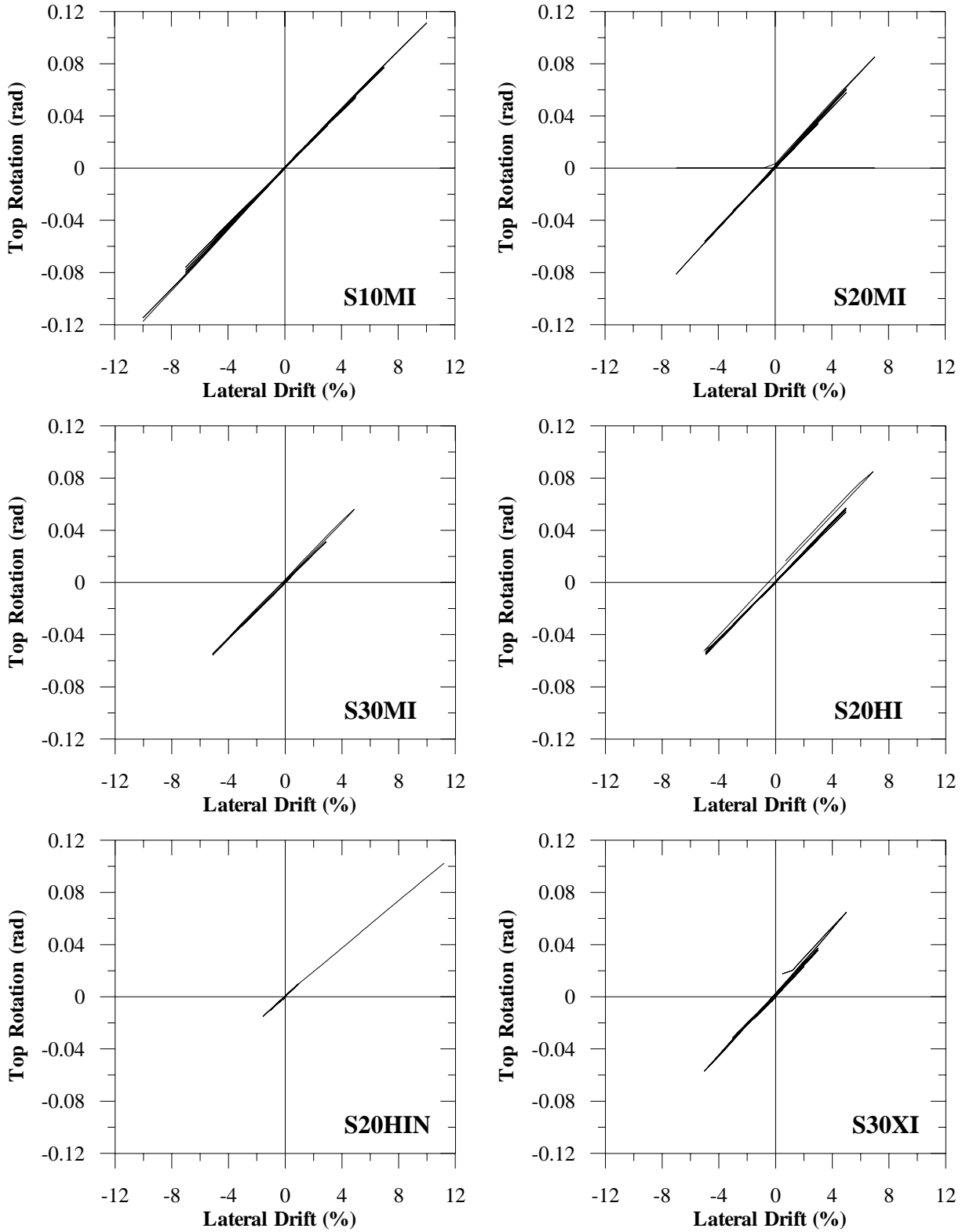


Figure 3.12 - Lateral Drift-Top Rotation

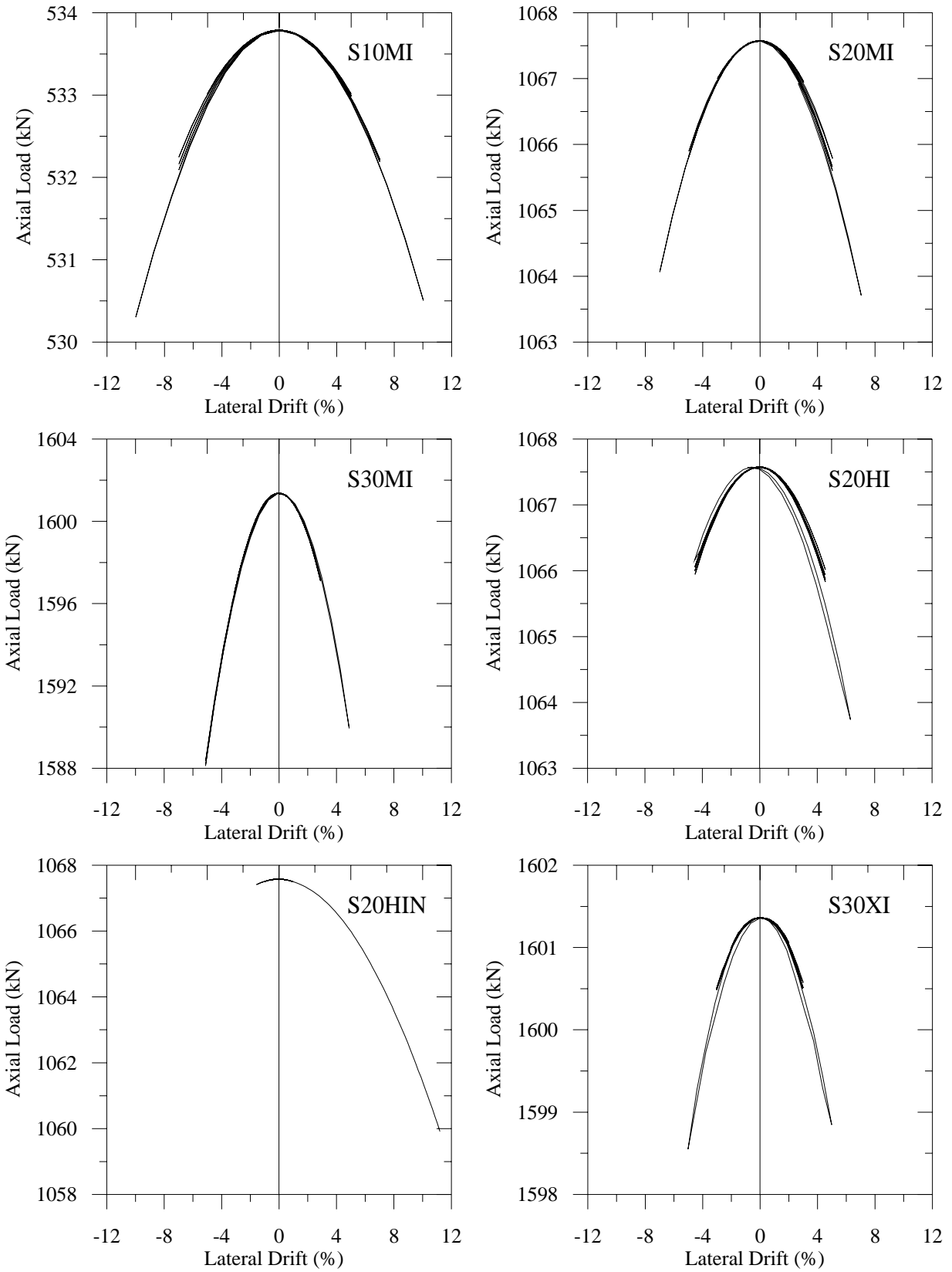


Figure 3.13 - Lateral Drift-Axial Load

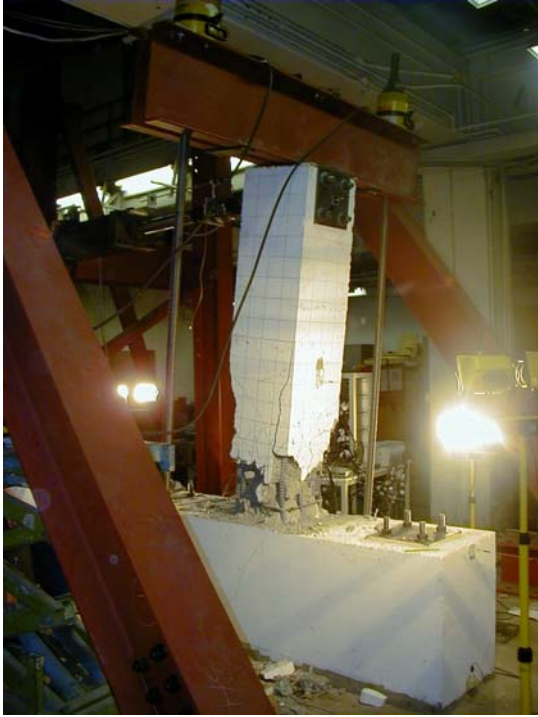


Figure 3.14 - Specimen S10MI at 10% Lateral Drift—Axial Load Capacity Maintained



Figure 3.15 - Specimen S20MI at 7% Lateral Drift after Axial Load Capacity Lost



Figure 3.16 - Specimen S30MI at 5% Lateral Drift after Axial Load Capacity Lost



Figure 3.17 - Specimen S20HI at 7% Lateral Drift after Axial Load Capacity Lost

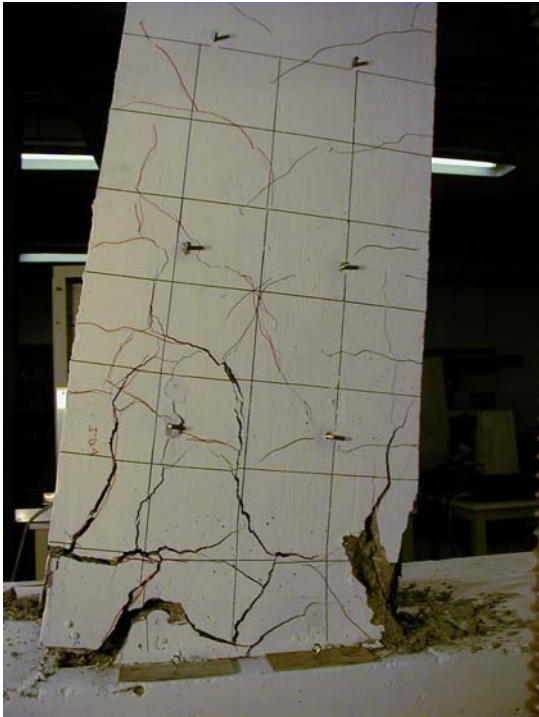


Figure 3.18 - Specimen S20HIN at 12% Lateral Drift—Axial Load Capacity Maintained



Figure 3.19 - Specimen S30XI at 5% Lateral Drift after Axial Load Capacity Lost

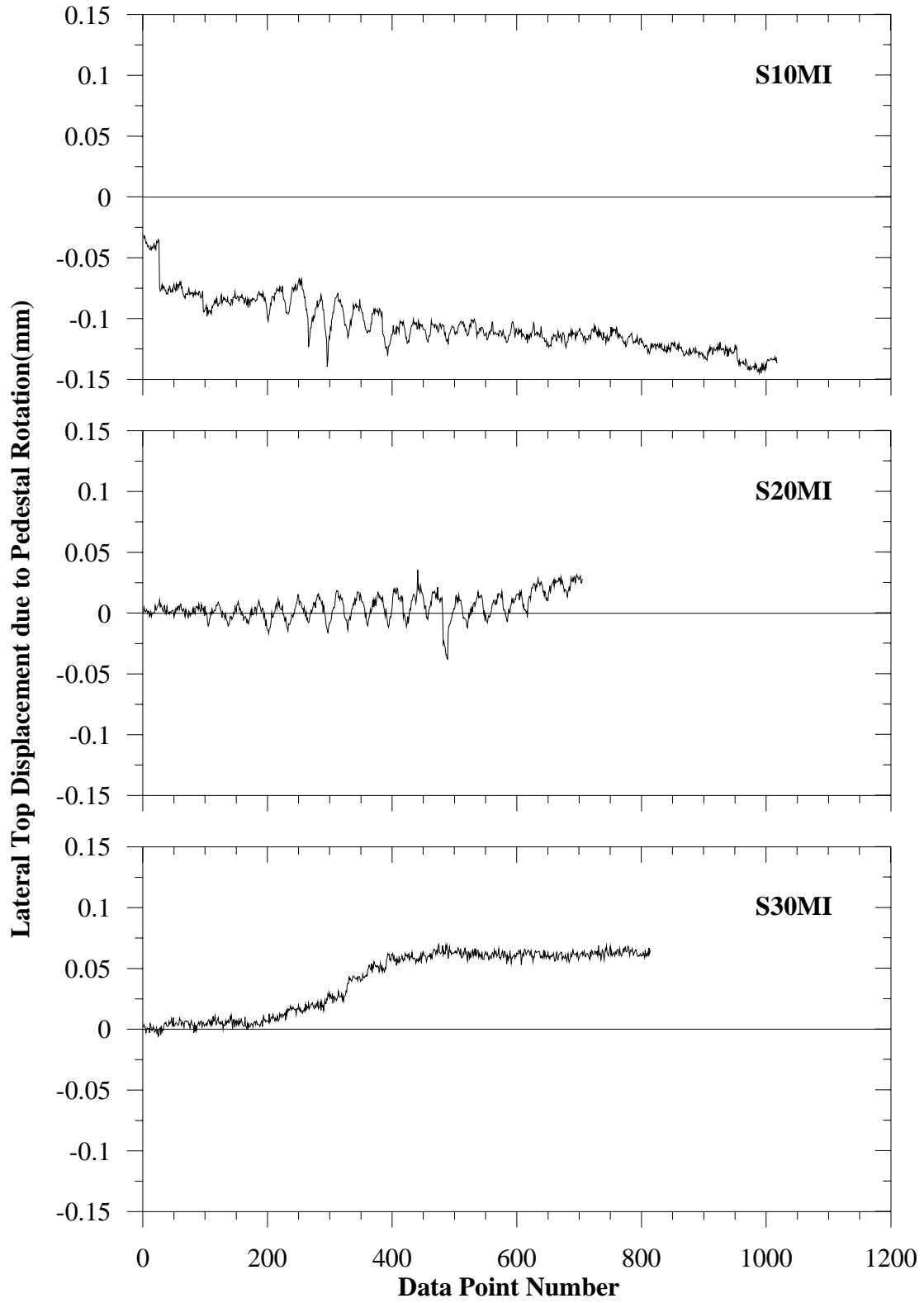


Figure 3.20- Top Displacement due to Pedestal Rotation

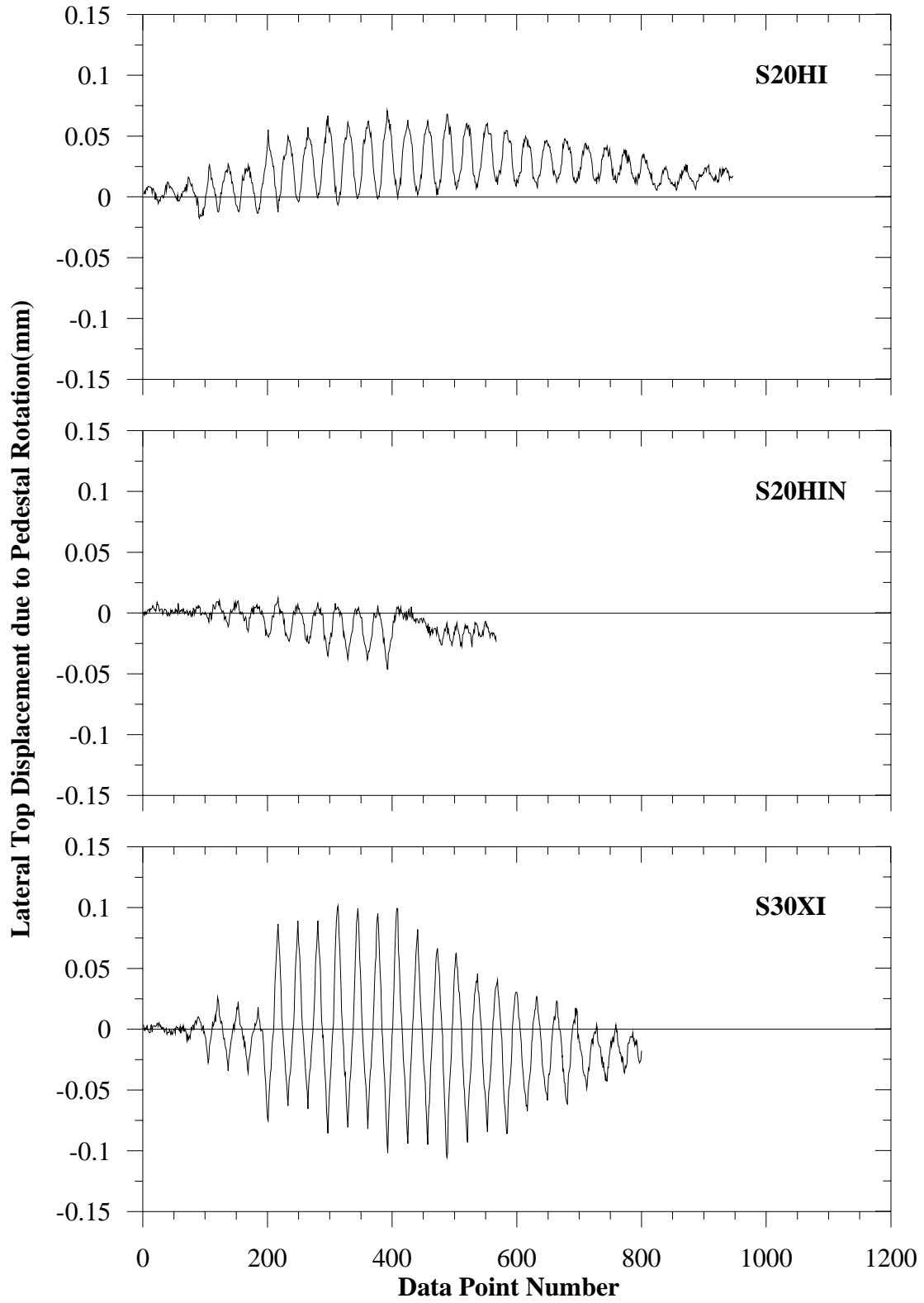


Figure 3.21 - Top Displacement due to Pedestal Rotation

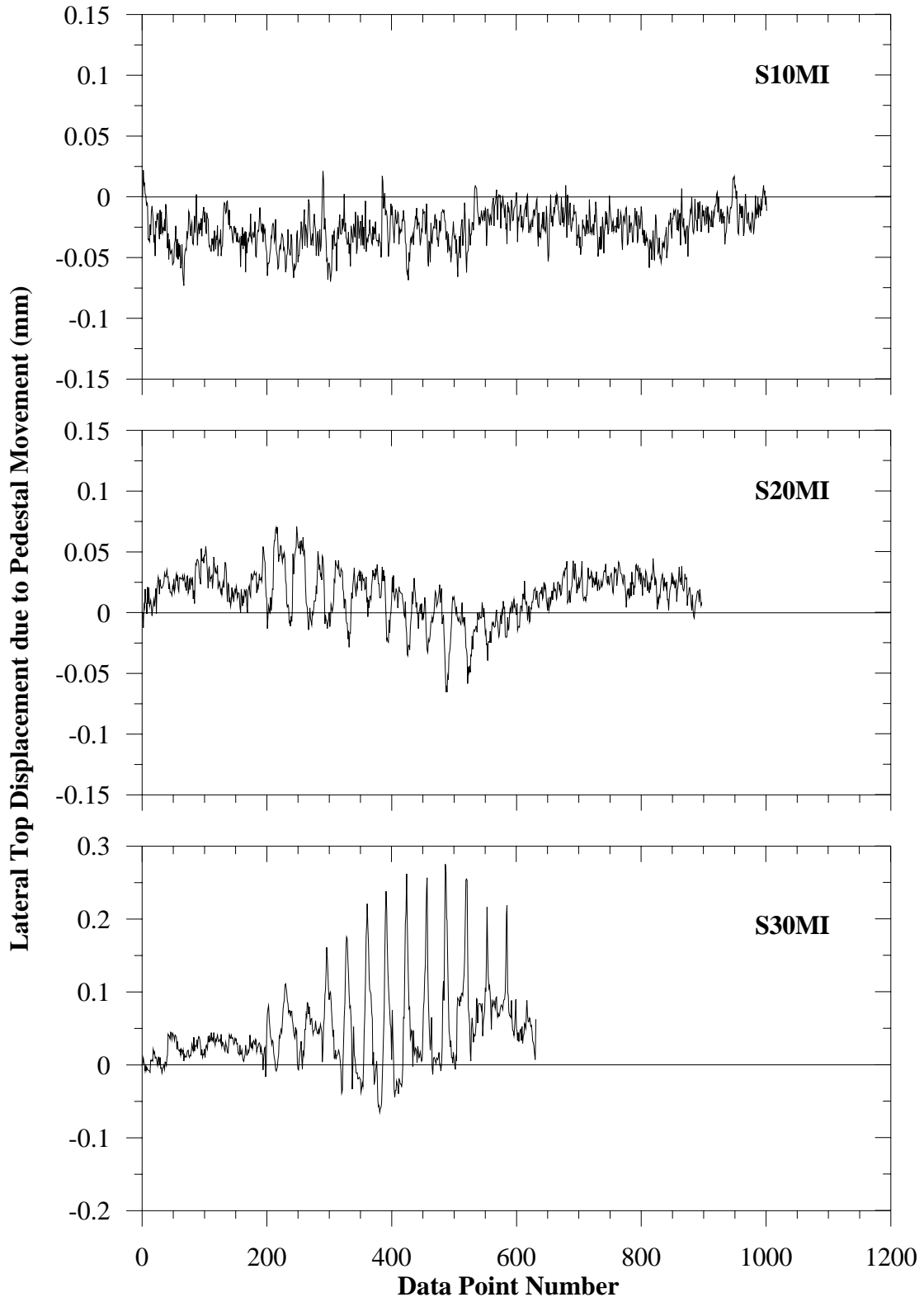


Figure 3.22 - Top Displacement due to Pedestal Movement

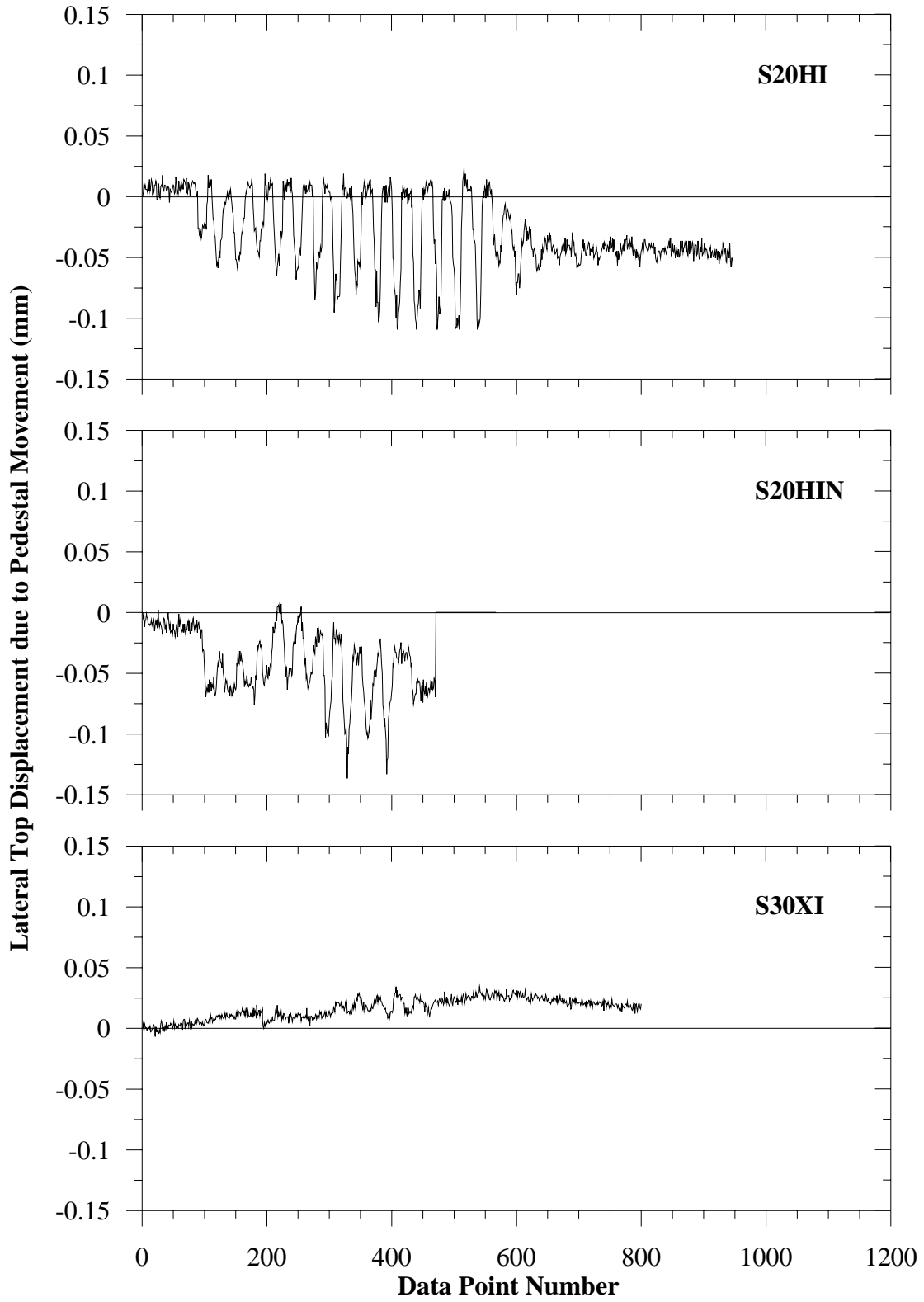


Figure 3.23 - Top Displacement due to Pedestal Movement

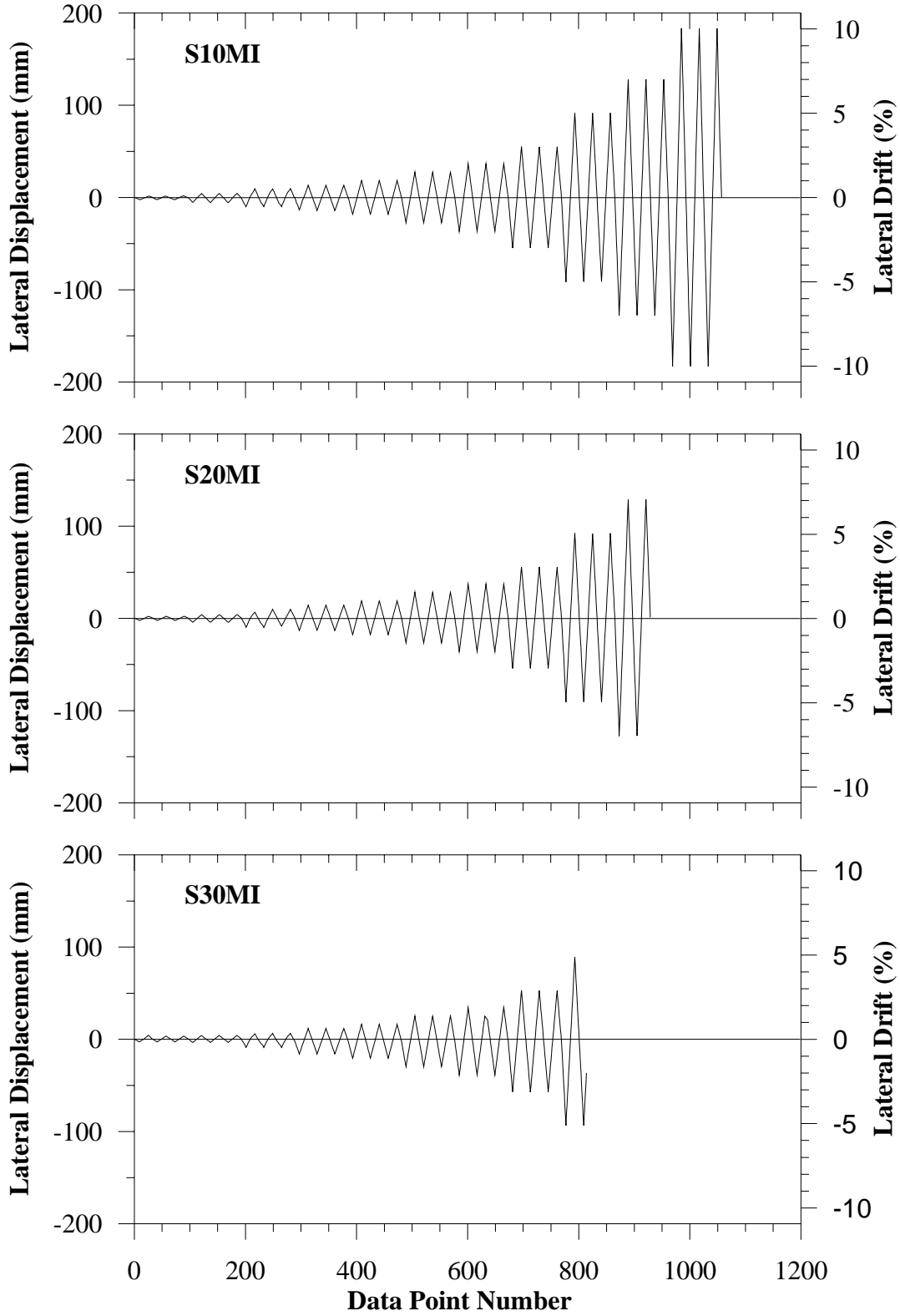


Figure 3.24 - Modified Lateral Displacement Histories

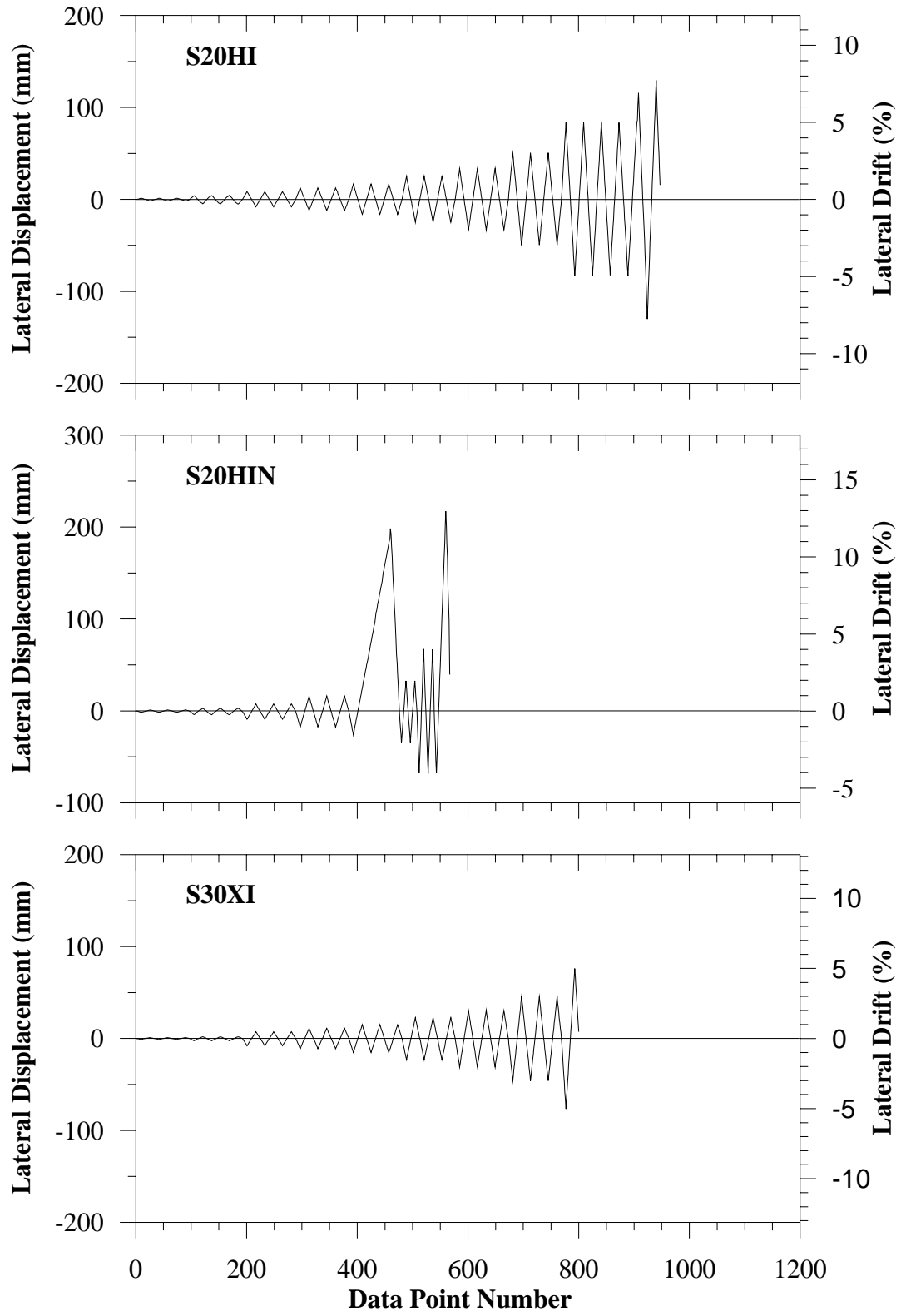


Figure 3.25 - Modified Lateral Displacement Histories

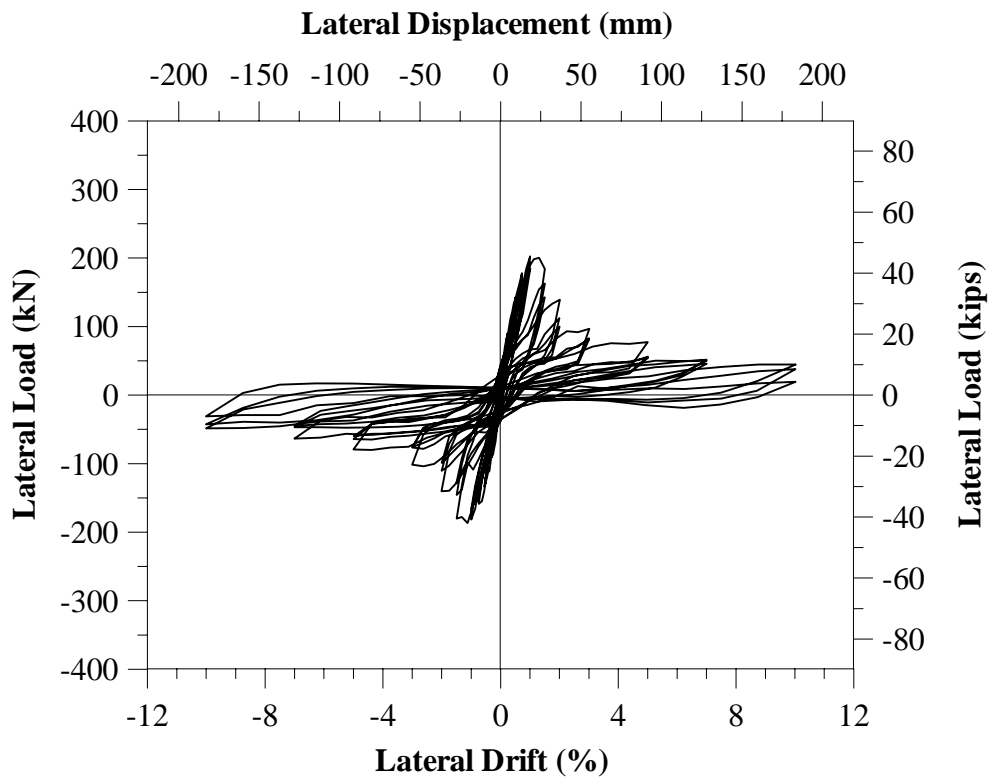


Figure 3.26 - Specimen S10MI Lateral Load-Top Displacement

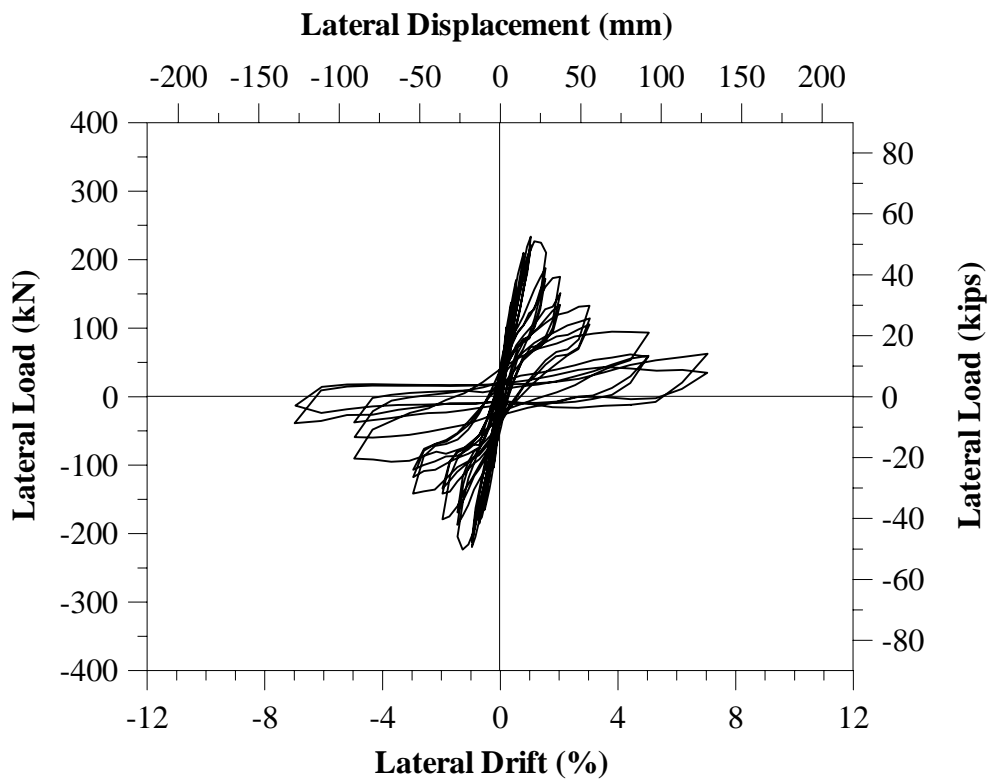


Figure 3.27 - Specimen S20MI Lateral Load-Top Displacement

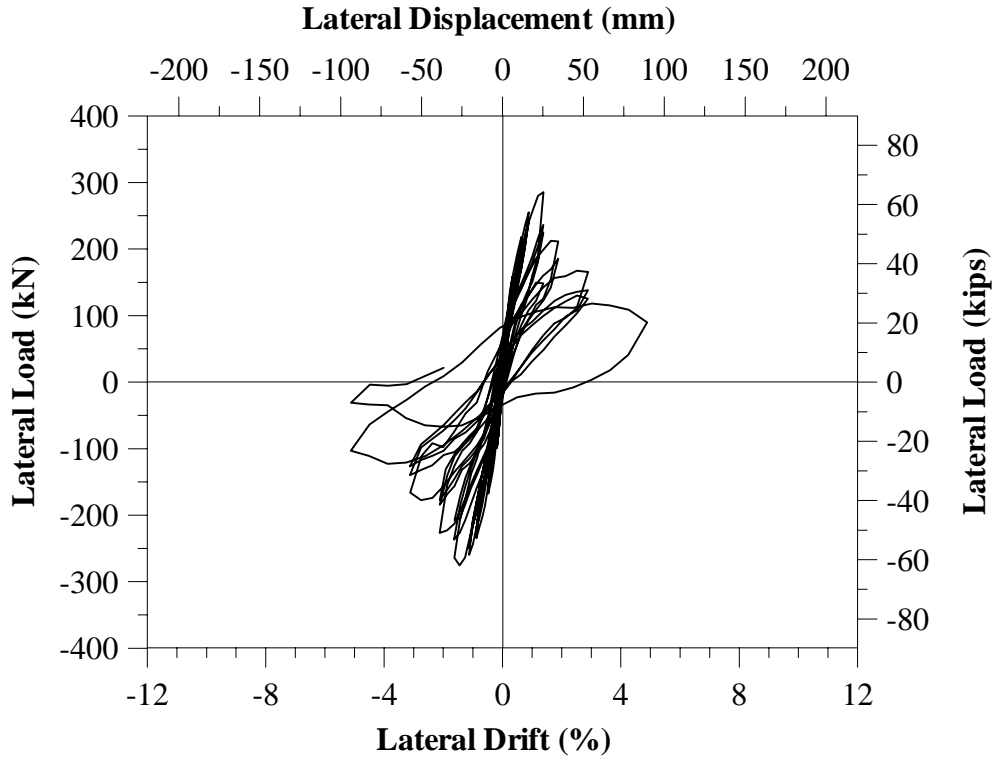


Figure 3.28 - Specimen S30MI Lateral Load-Top Displacement

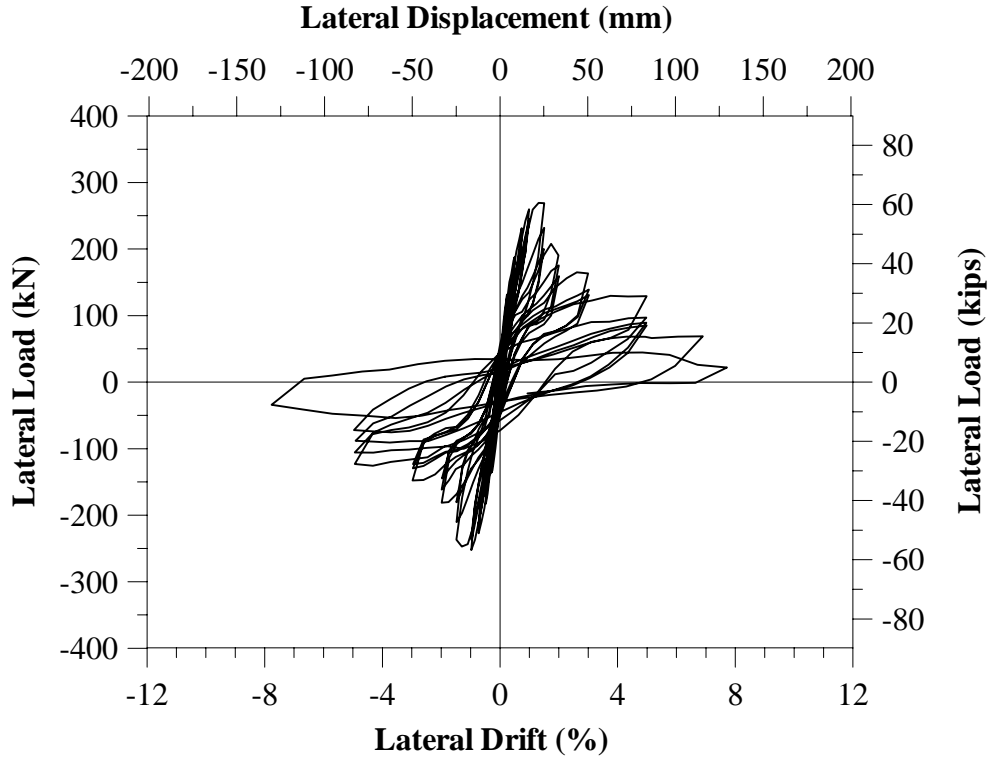


Figure 3.29 - Specimen S20HI Lateral Load-Top Displacement

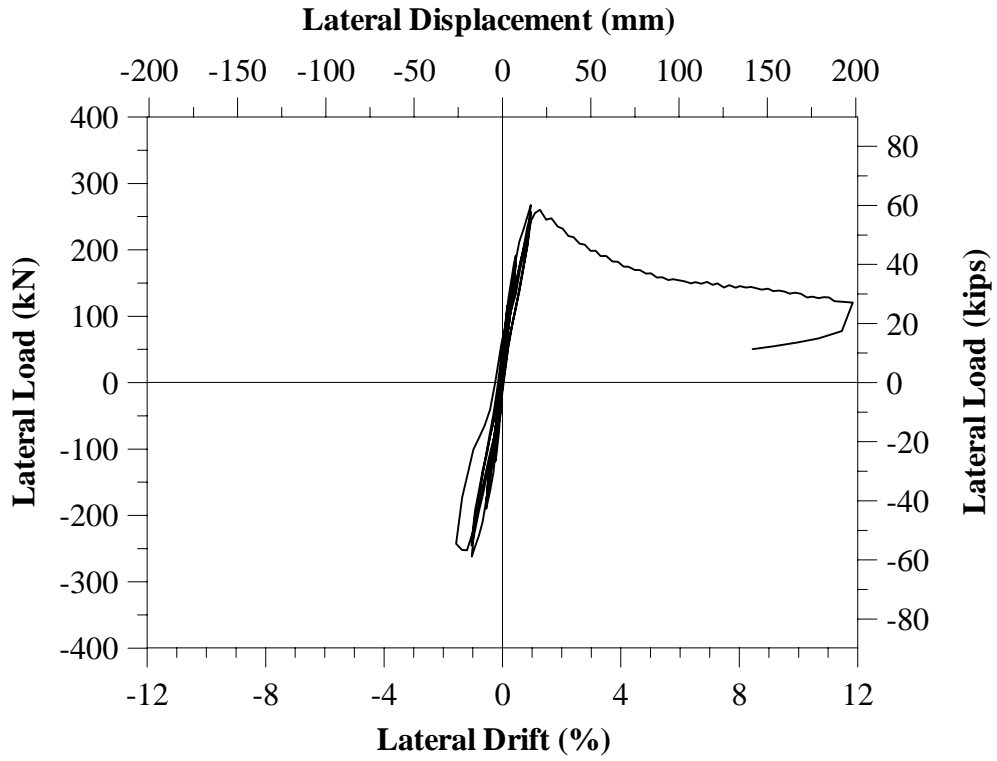


Figure 3.30 - Specimen S20HIN Lateral Load-Top Displacement

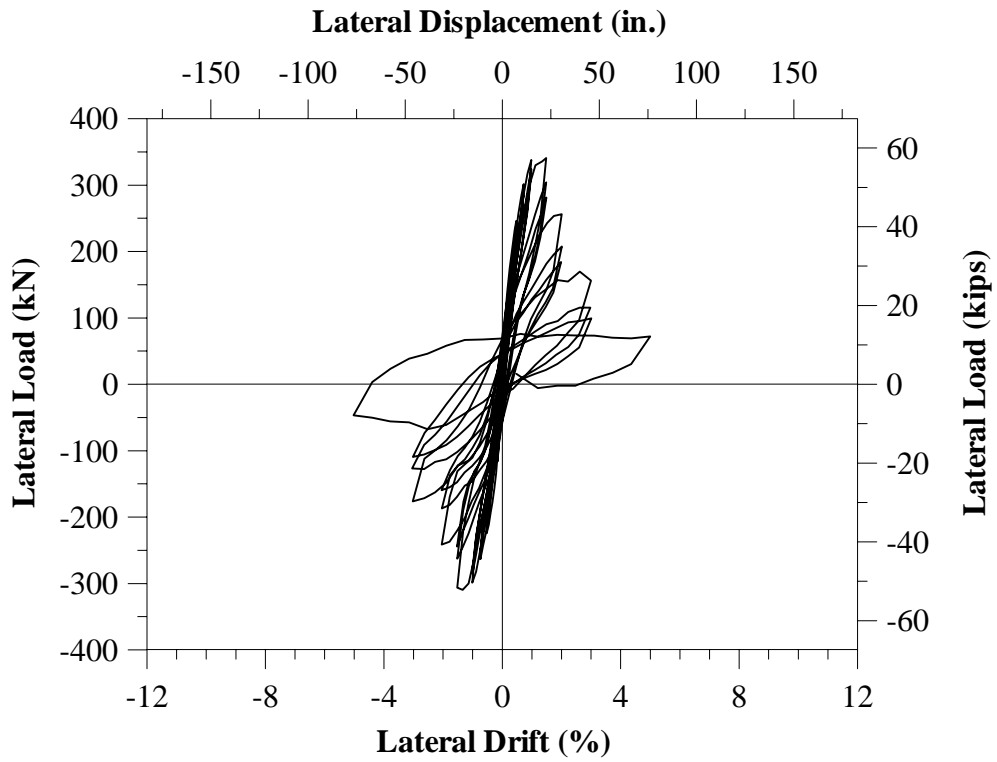


Figure 3.31 - Specimen S30XI Lateral Load-Top Displacement

Table 3.4 Moment Capacities

Specimen	Maximum Lateral Load (kN)	Normalized* Lateral Load (kN)	Analytical Yield Moment M_y (kN-m)	Max Base Moment M_u (kN-m)	M_u/M_y
S10MI	202.7	202.7	381.3	370.7	0.97
S20MI	233.5	233.5	450.4	427.0	0.95
S30MI	285.3	285.3	509.0	521.8	1.03
S20HI	269.5	247.0	441.5	451.8	1.02
S20HIN	267.4	245.1	441.5	448.3	1.02
S30XI	340.7	283.9	499.5	519.2	1.04

* Normalized ($F_{normalized} = F_{measured} \cdot h_{column} / h_{S10MI}$)

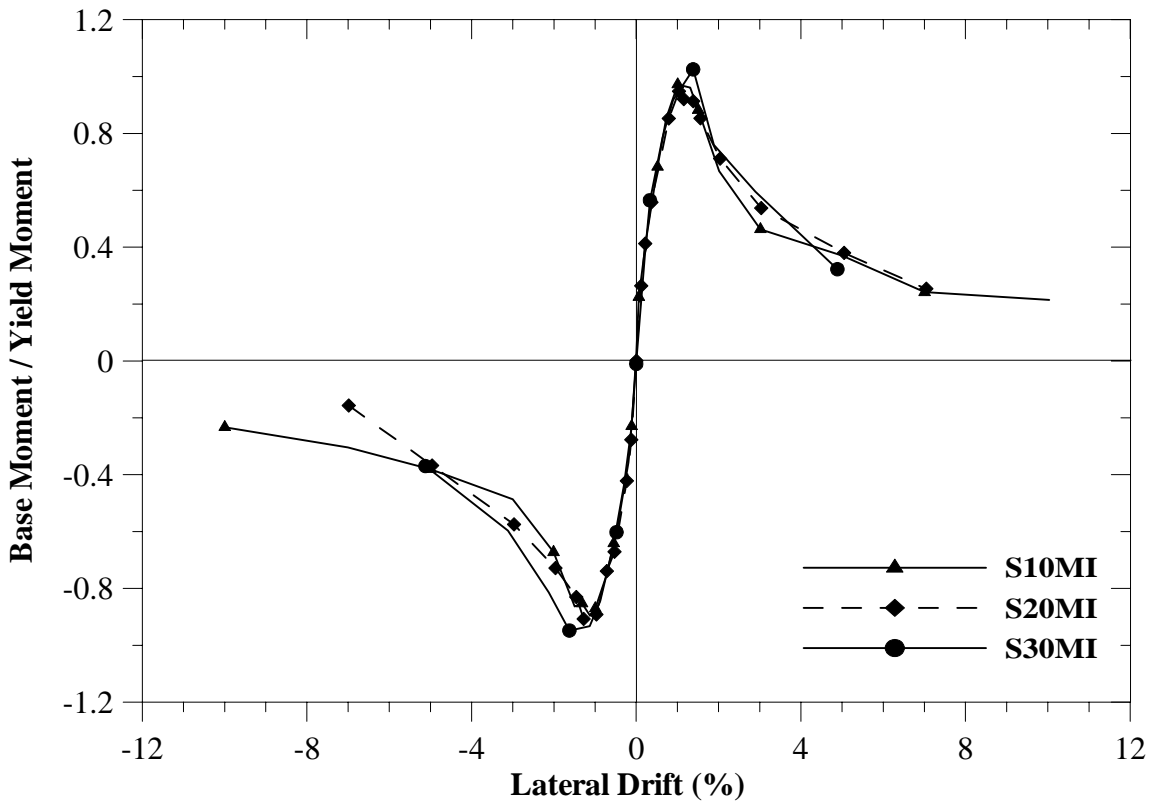


Figure 3.32 - Base Moment/Yield Moment Comparison of S10MI, S20MI, and S30MI

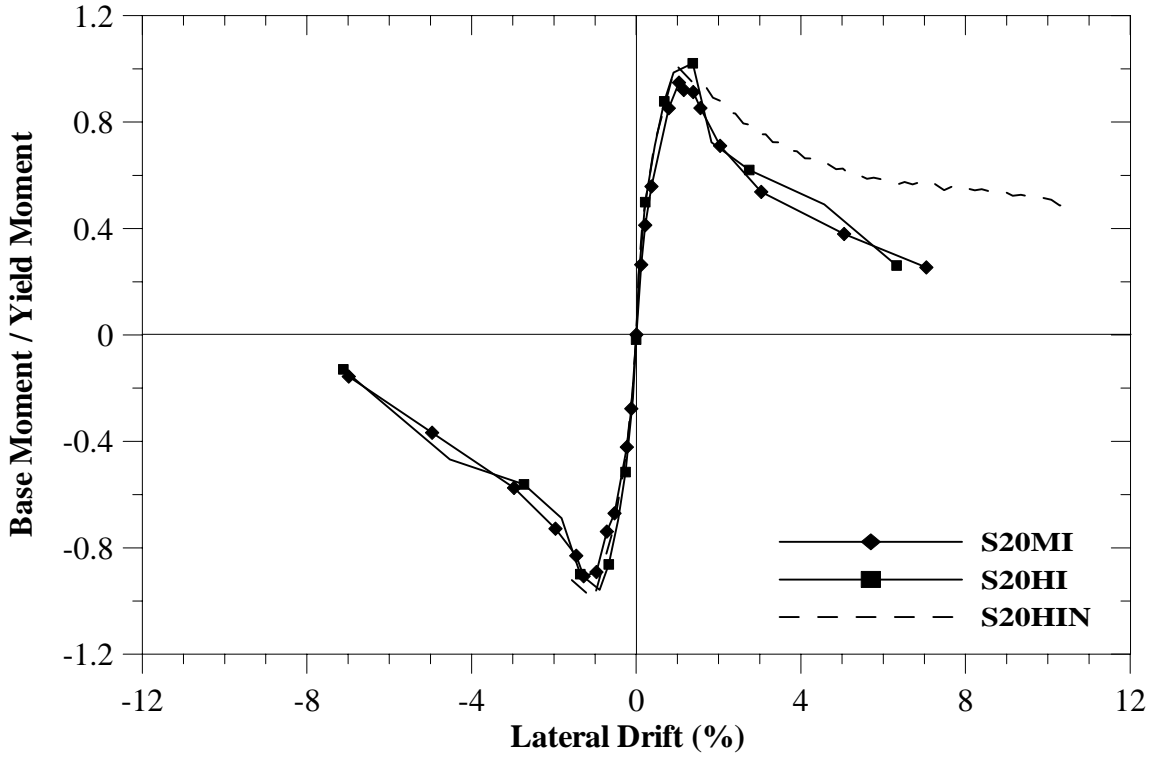


Figure 3.33 - Base Moment/Yield Moment Comparison of S20MI, S20HI, and S20HIN

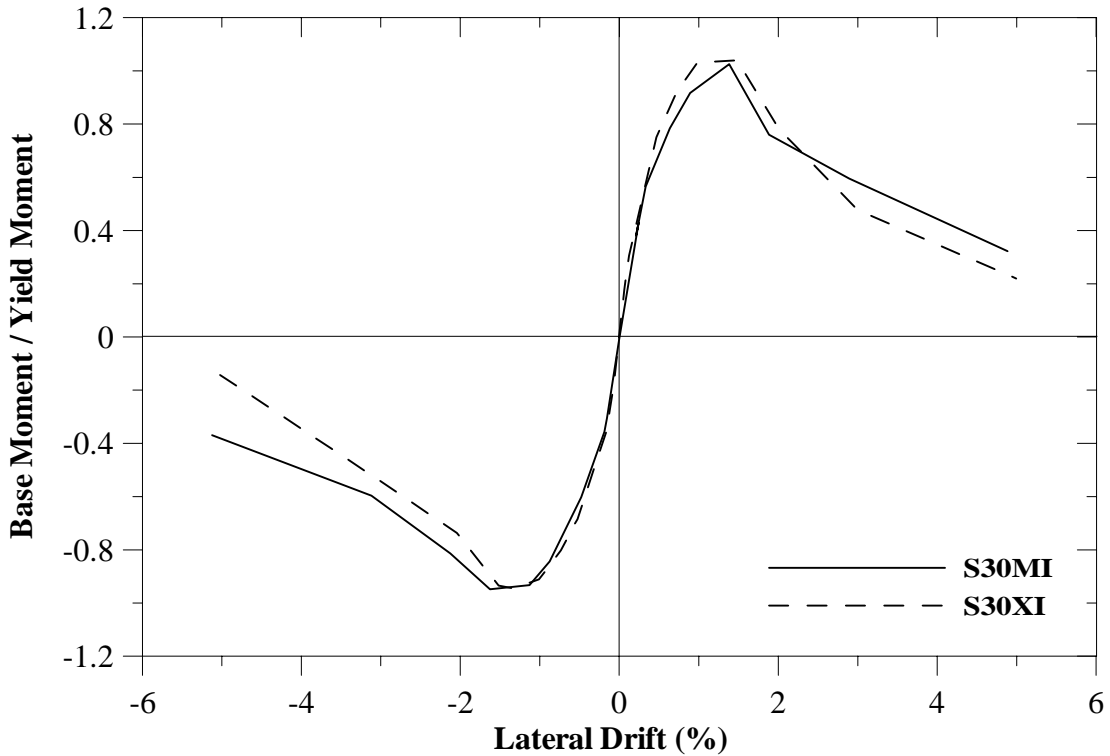


Figure 3.34 - Base Moment/Yield Moment Comparison of S30MI and S30XI

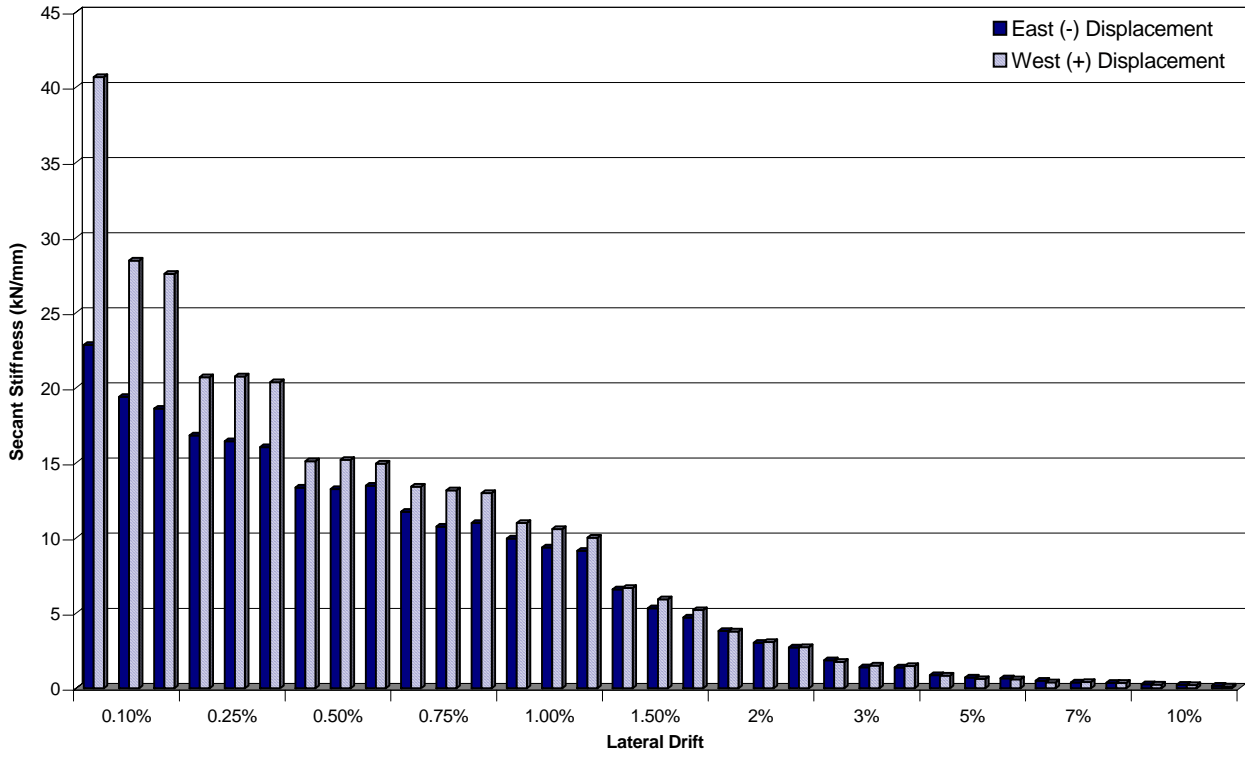


Figure 3.35 Measured Secant Stiffness— S10MI

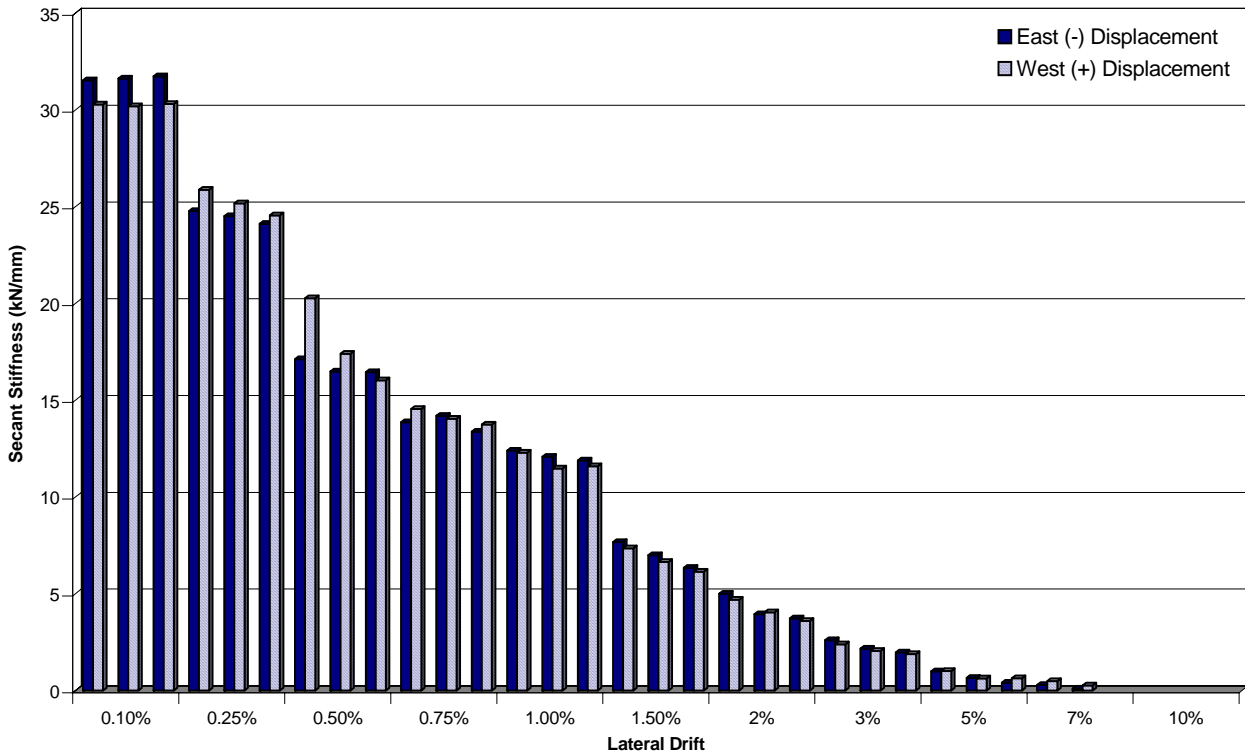


Figure 3.36 - Measured Secant Stiffness—S20MI

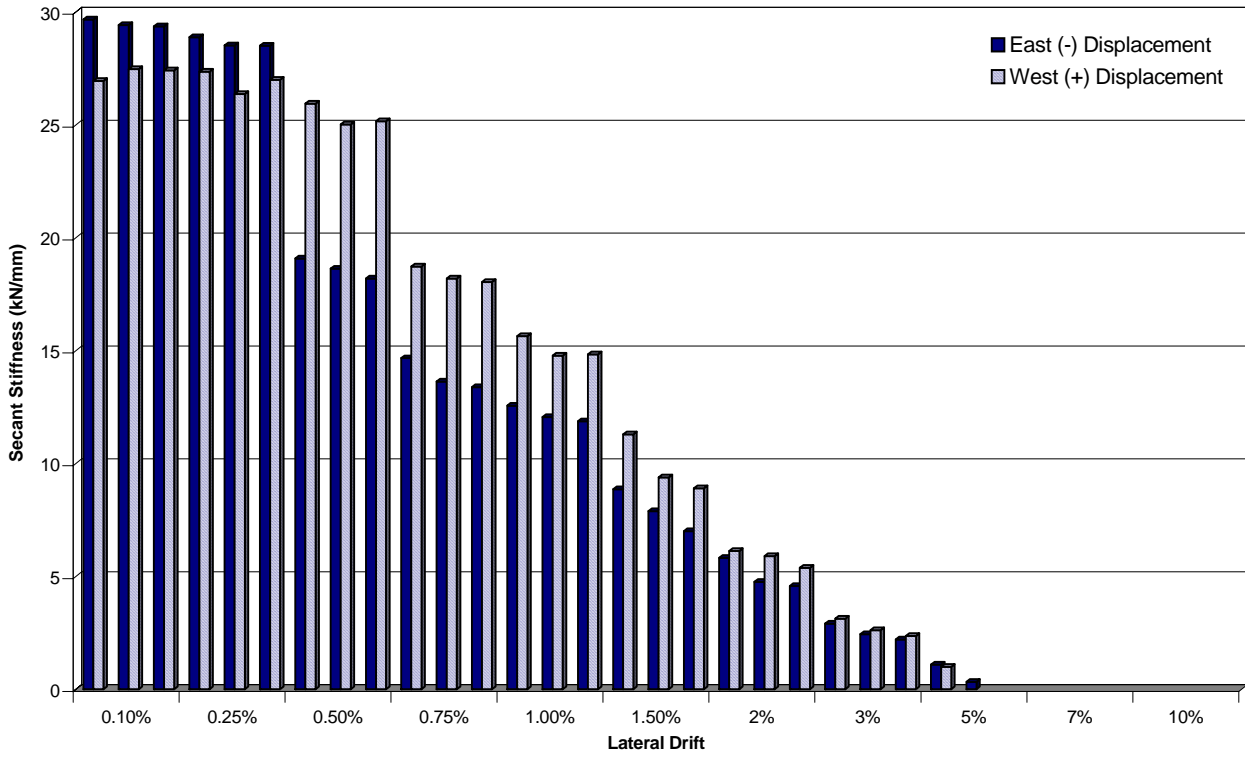


Figure 3.37 - Measured Secant Stiffness— S30MI

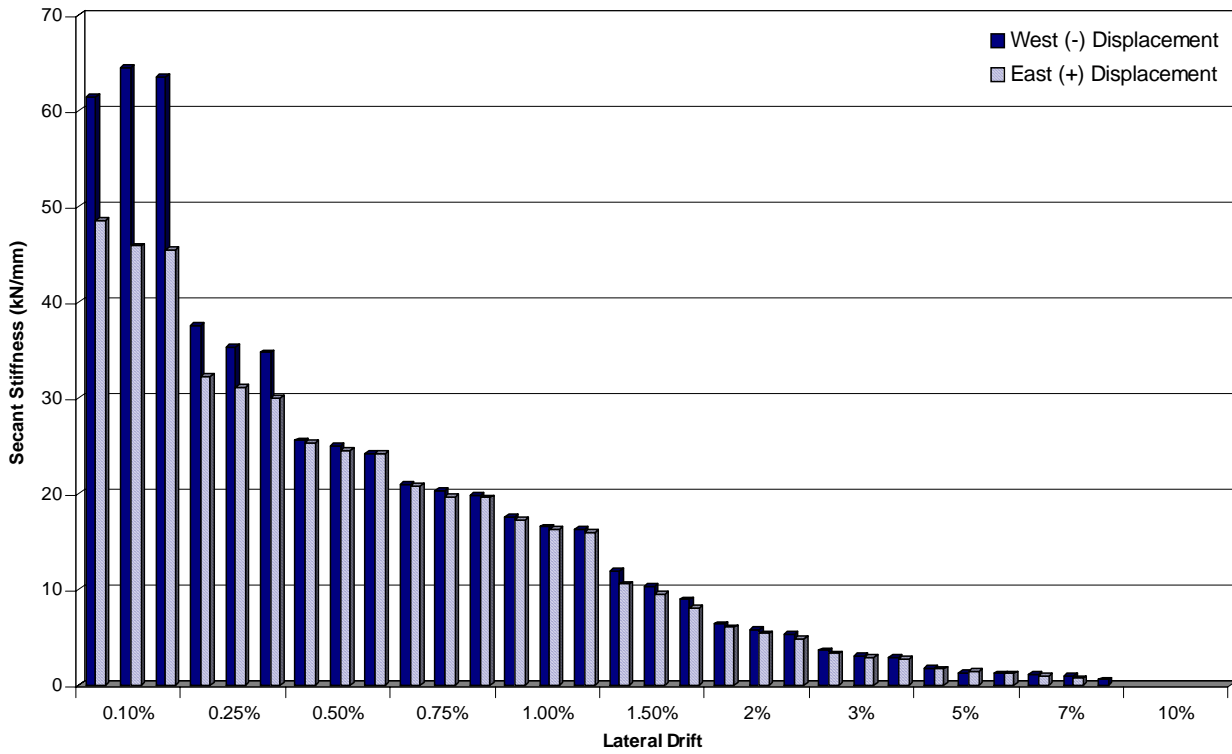


Figure 3.38- Measured Secant Stiffness— S20HI

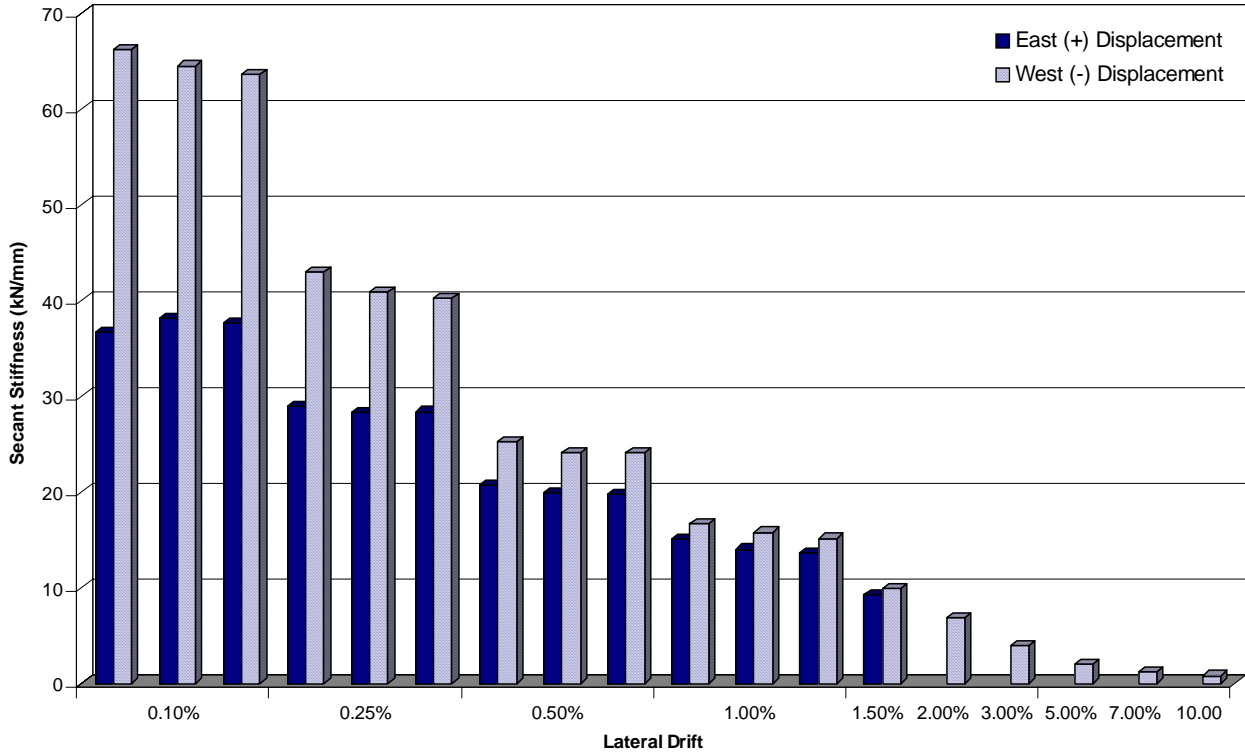


Figure 3.39- Measured Secant Stiffness— S20HIN

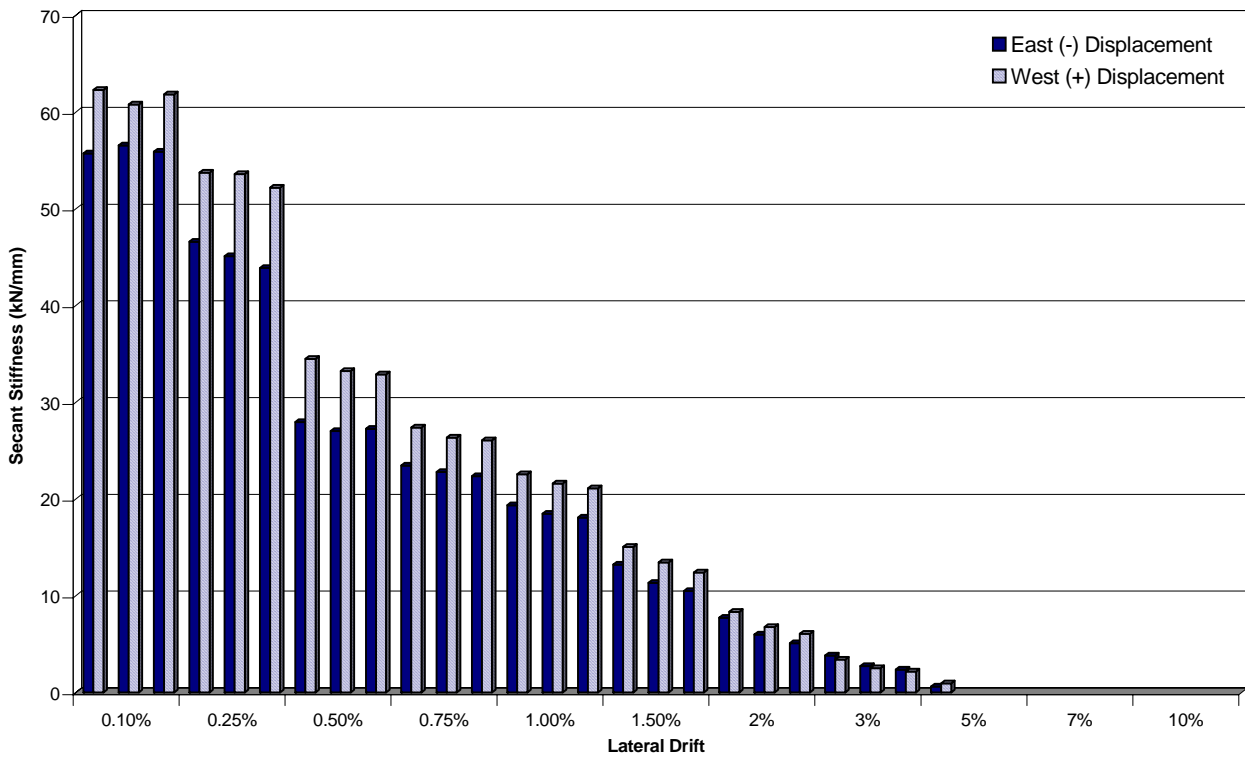


Figure 3.40 - Measured Secant Stiffness— S30XI

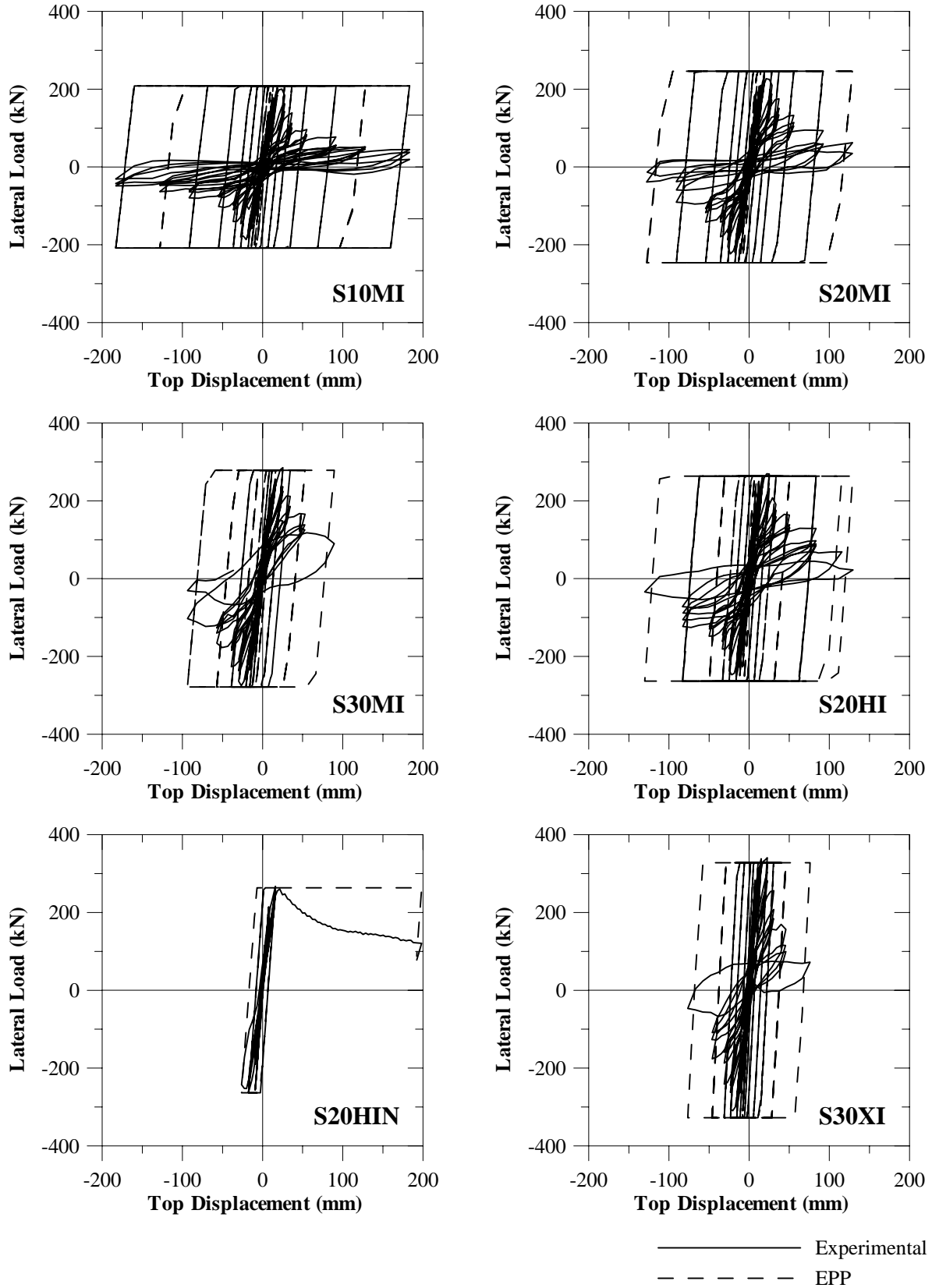


Figure 3.41 - Actual and Elastic-Perfectly-Plastic Load-Displacement Responses

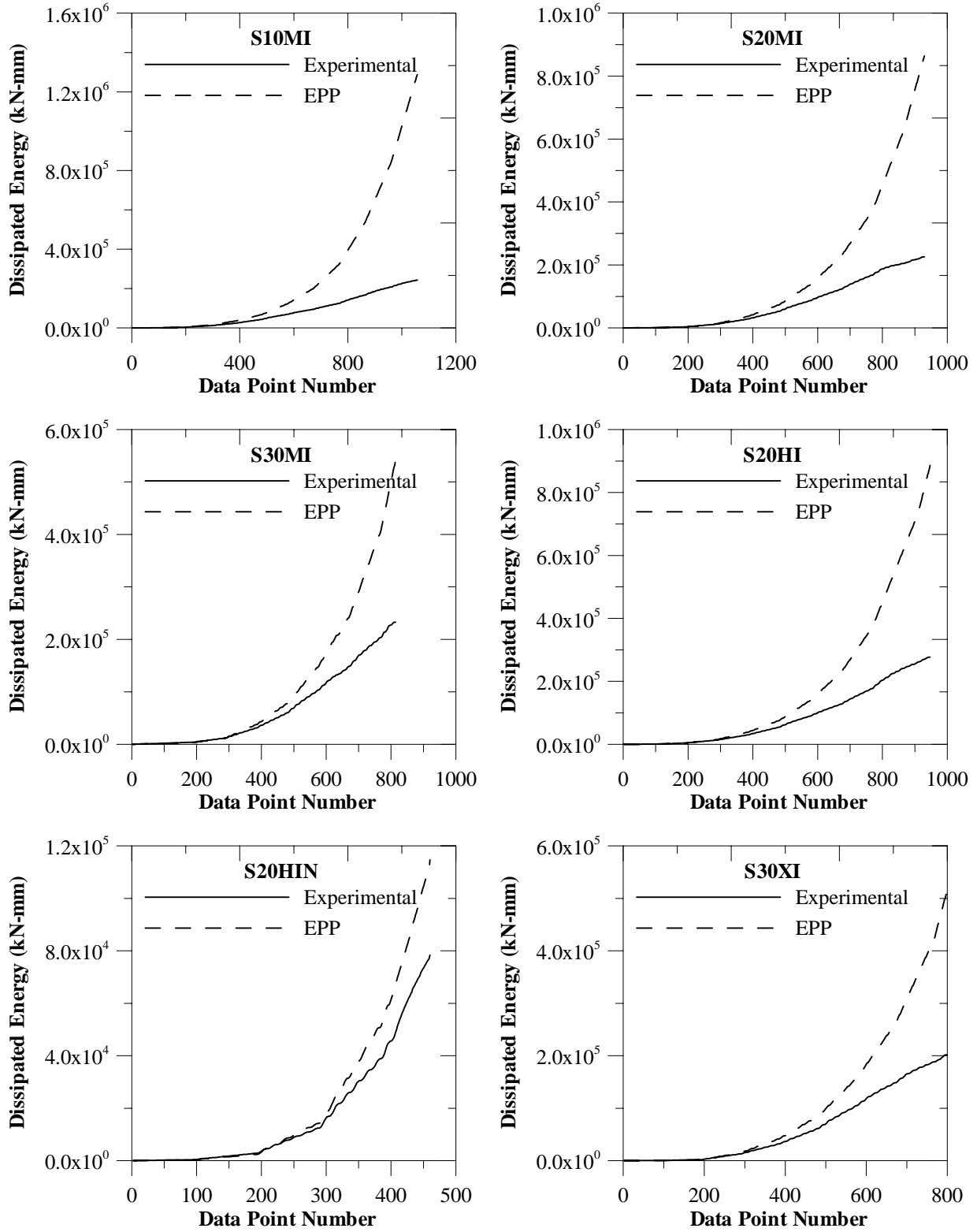


Figure 3.42- Total Energy Dissipated by Actual and EPP Columns

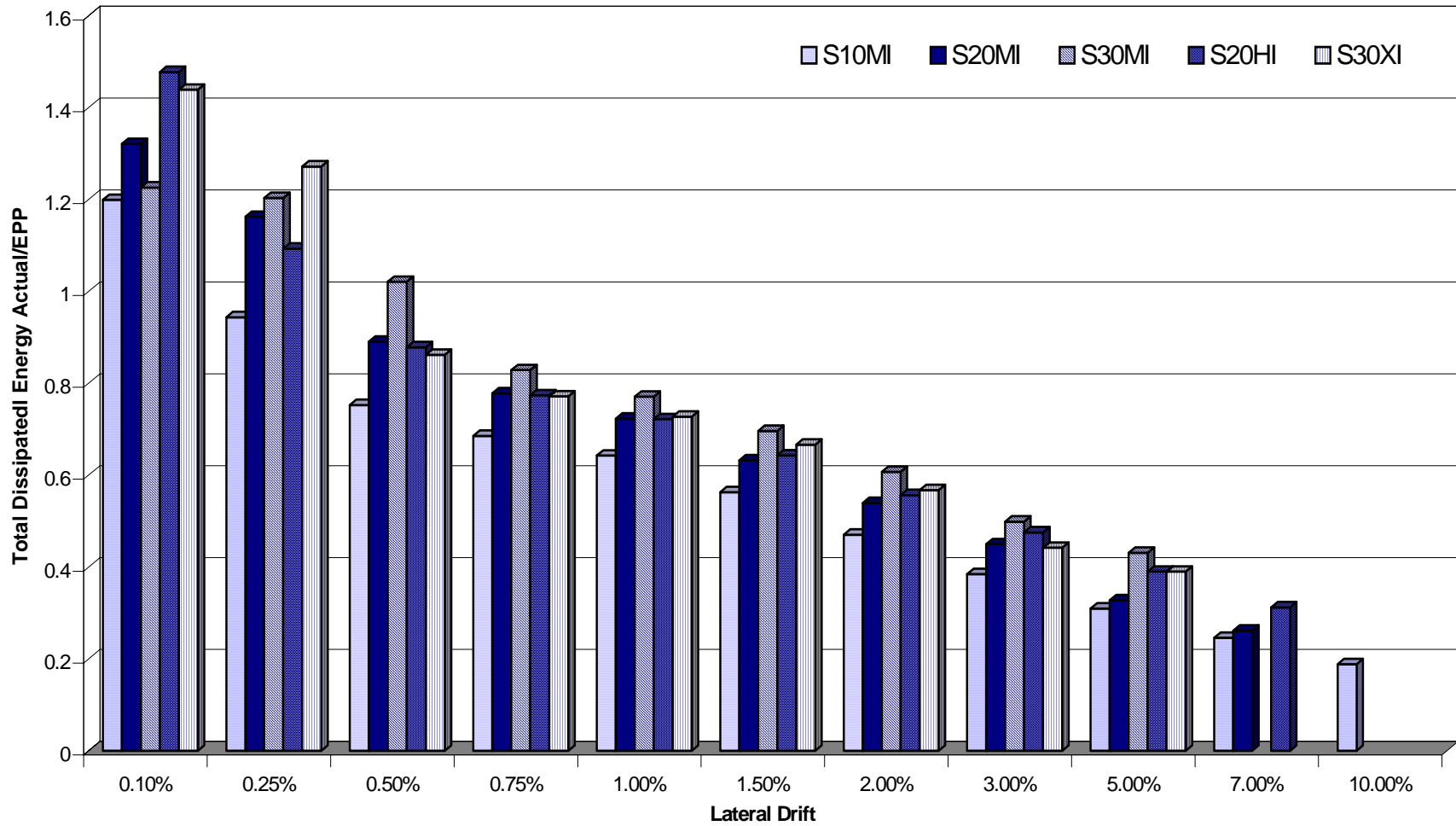


Figure 3.43 - Normalized Energy Dissipation

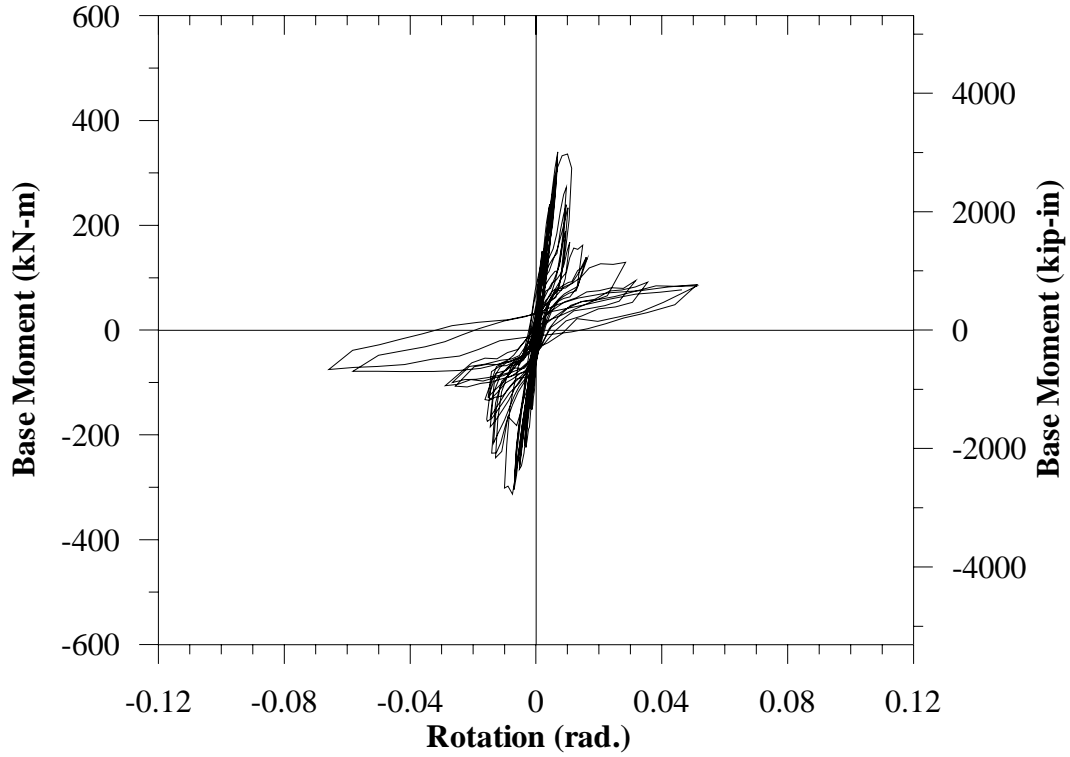


Figure 3.44 - S10MI Base Moment – Total Rotation along Lap-splice Length

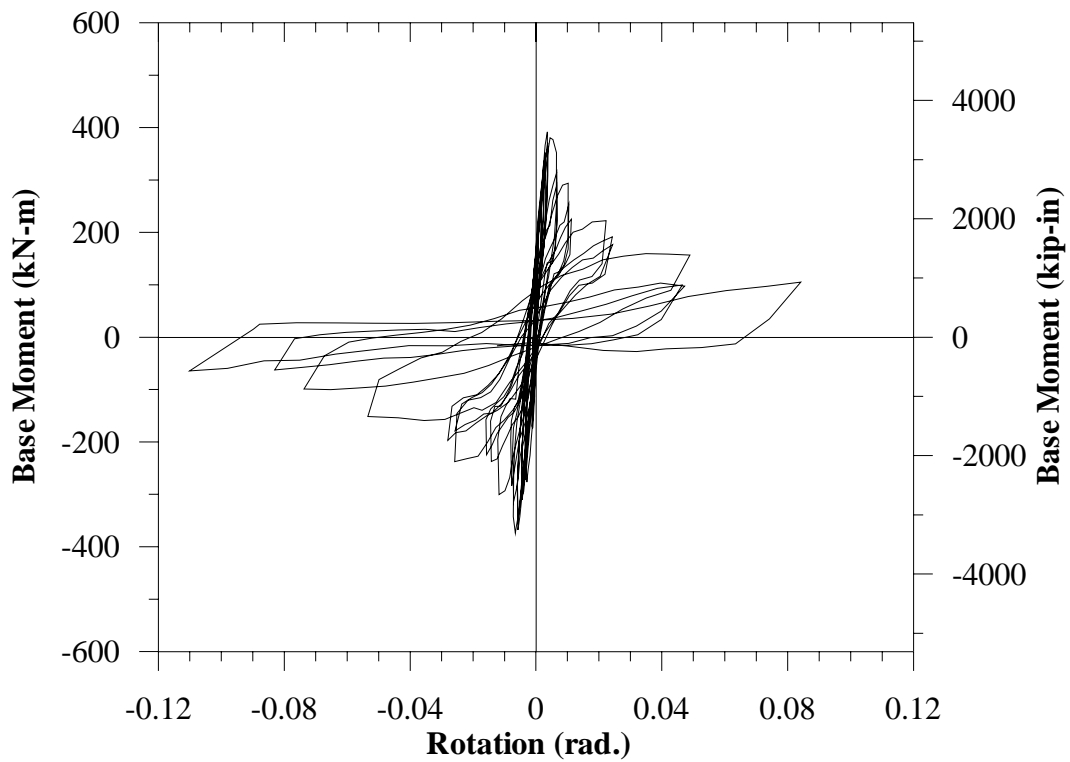


Figure 3.45 – S20MI Base Moment – Total Rotation along Lap-splice Length

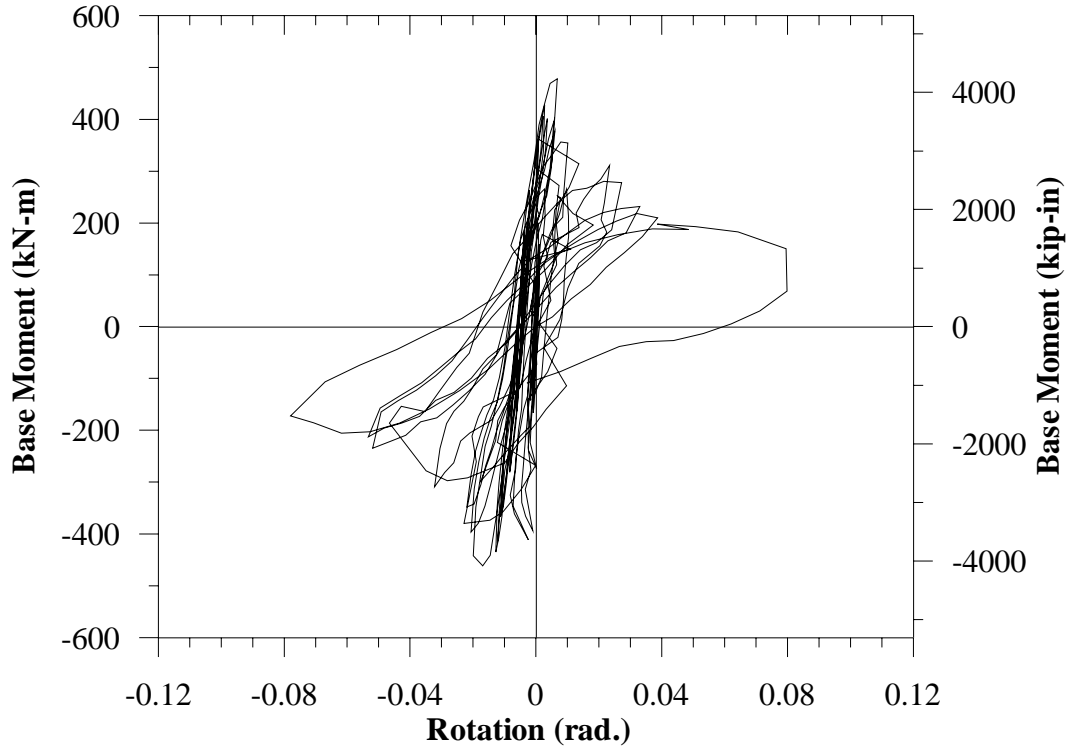


Figure 3.46 – S30MI Base Moment – Total Rotation along Lap-splice Length

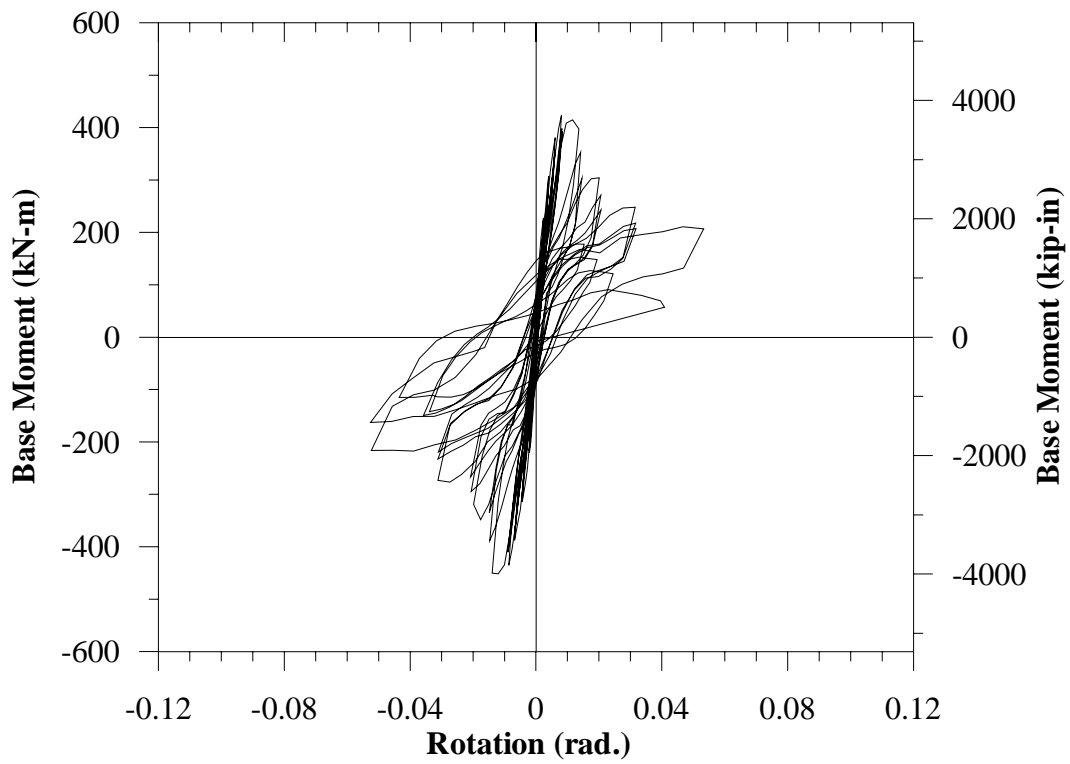


Figure 3.47 S20HI Base Moment—Total Rotation along Lap-splice Length

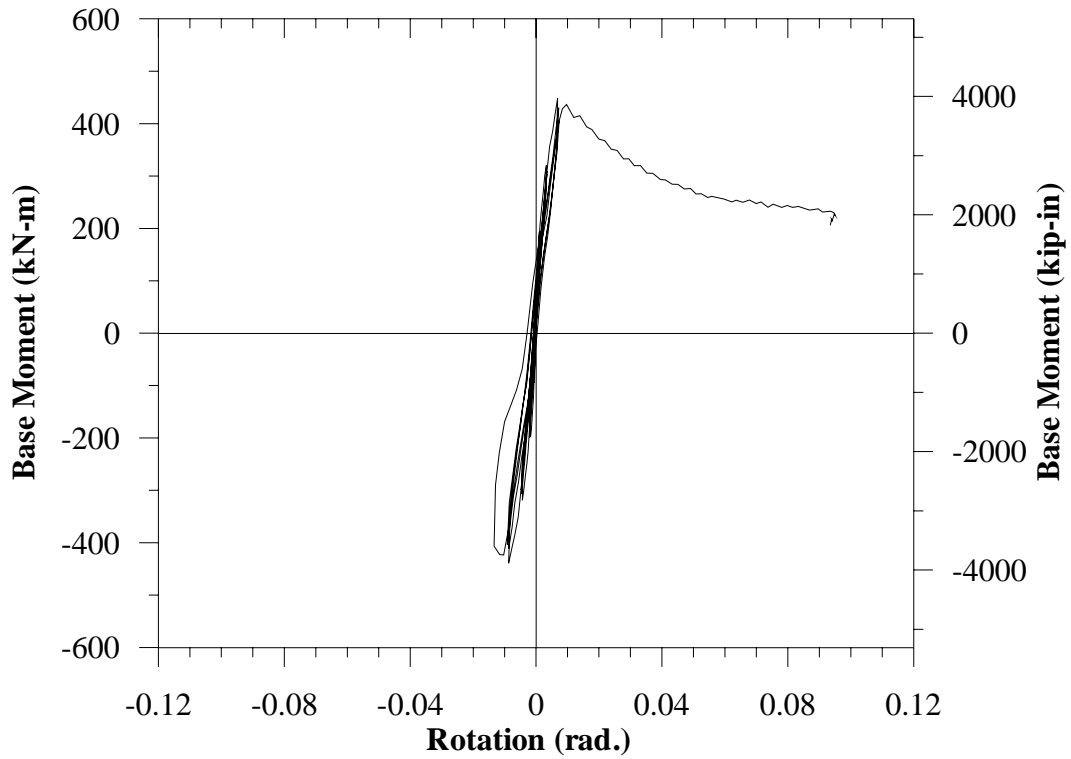


Figure 3.48 - S20HIN Base Moment – Total Rotation along Lap-splice Length

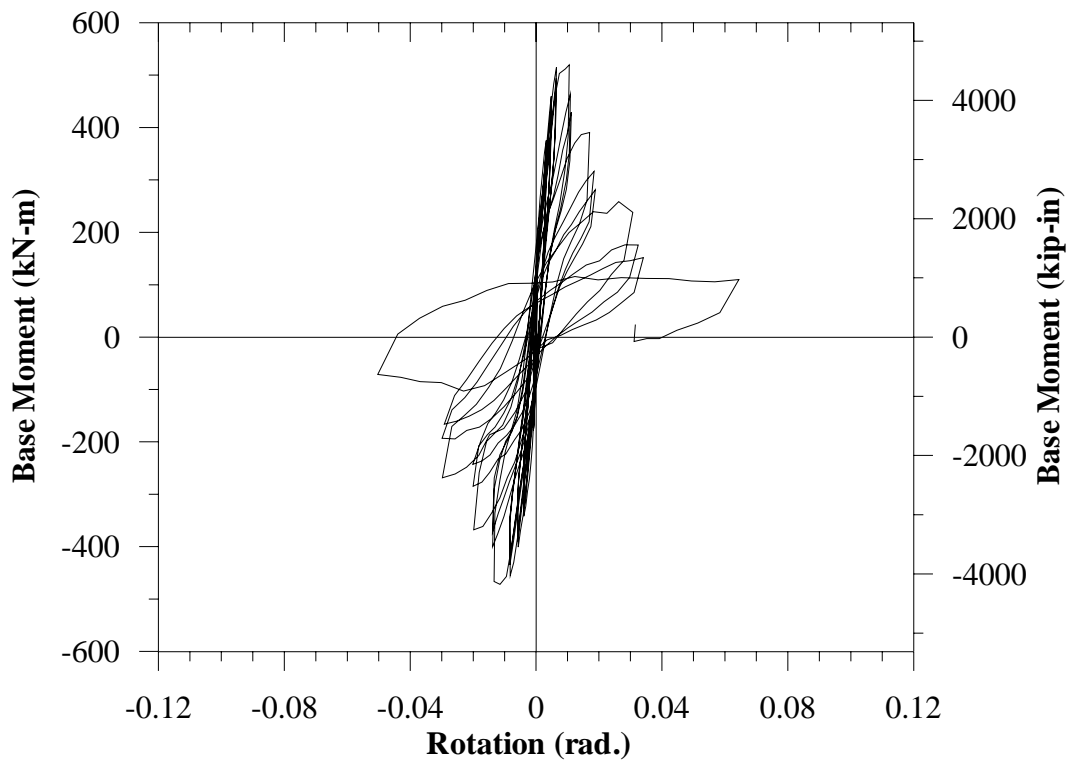


Figure 3.49 S30XI Base Moment—Total Rotation along Lap-splice Length

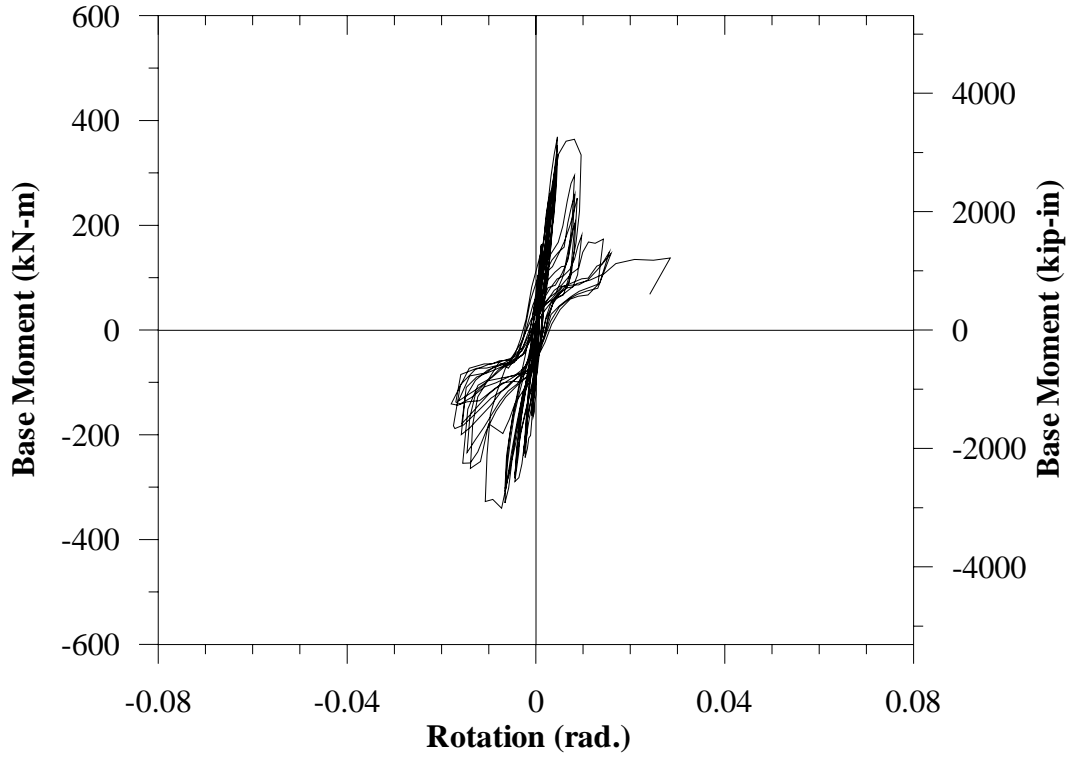


Figure 3.50 – S10MI Base Moment – Slip Rotation along Lap-splice Length

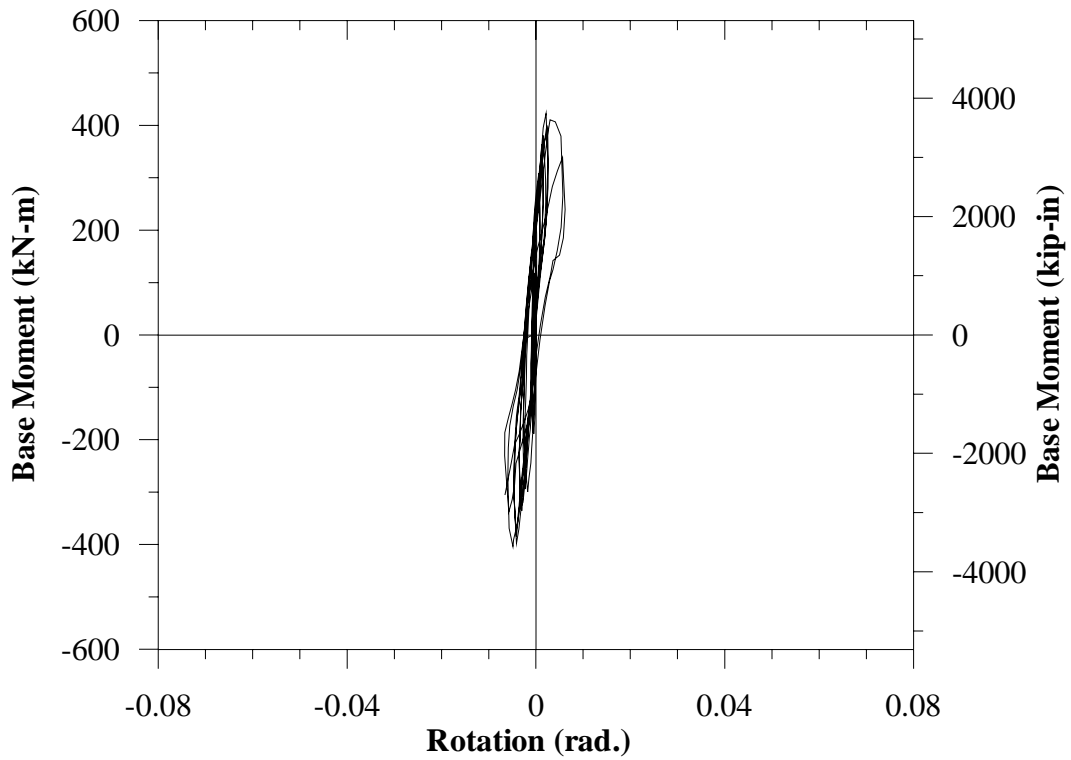


Figure 3.51 S20MI Base Moment—Slip Rotation along Lap-splice Length

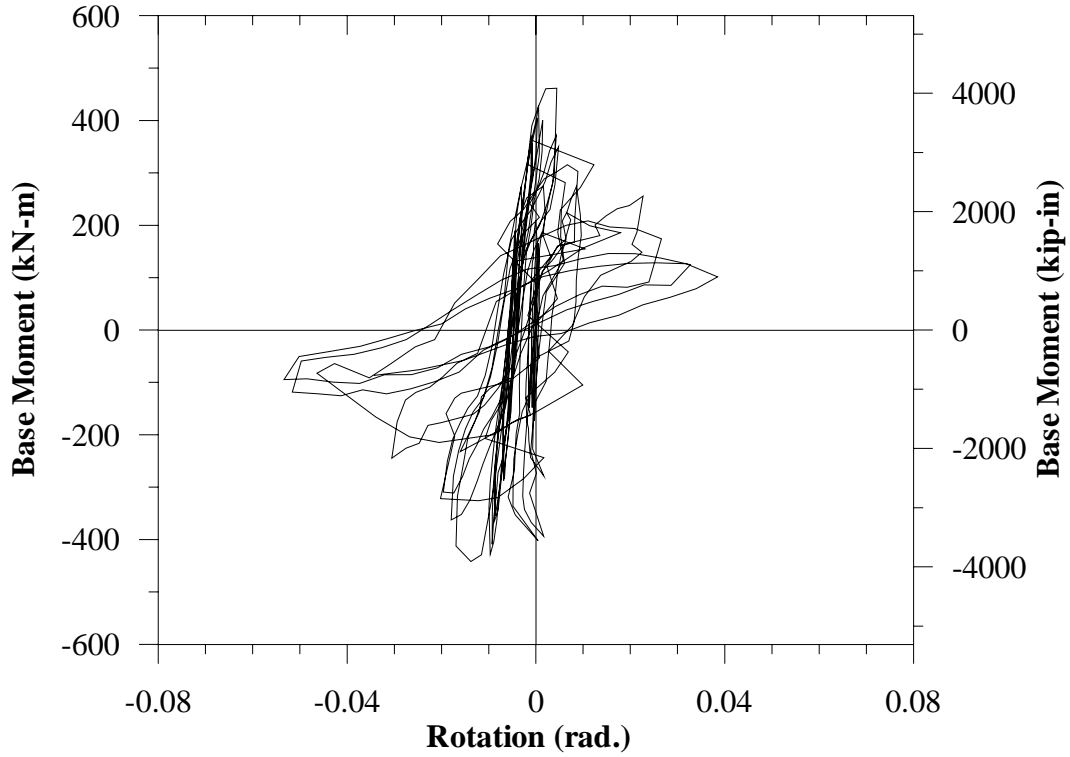


Figure 3.52 – S30MI Base Moment – Slip Rotation along Lap-splice Length

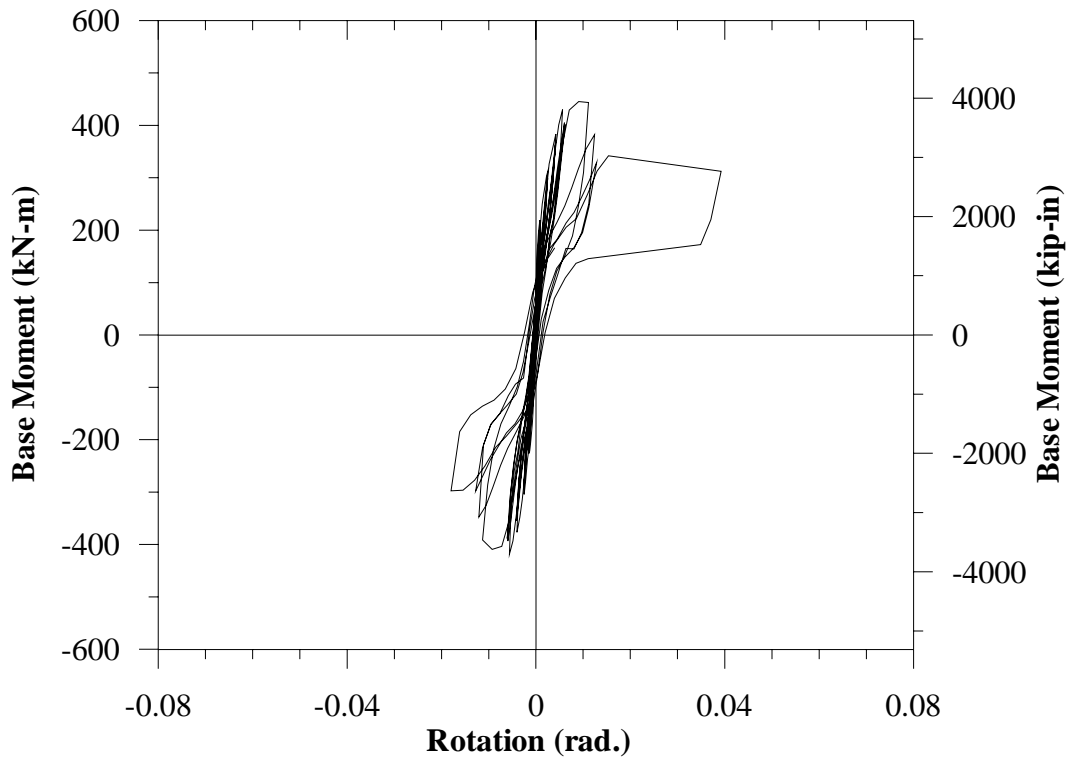


Figure 3.53 S20HI Base Moment—Slip Rotation along Lap-splice Length

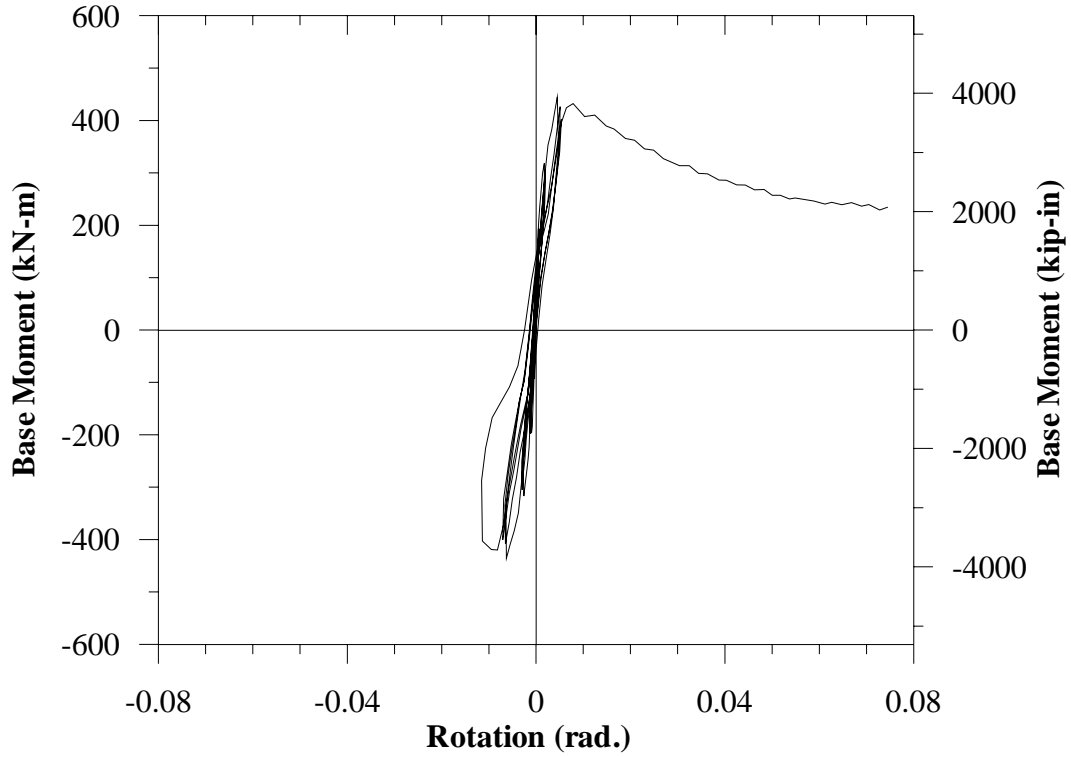


Figure 3.54 - S20HIN Base Moment – Slip Rotation along Lap-splice Length

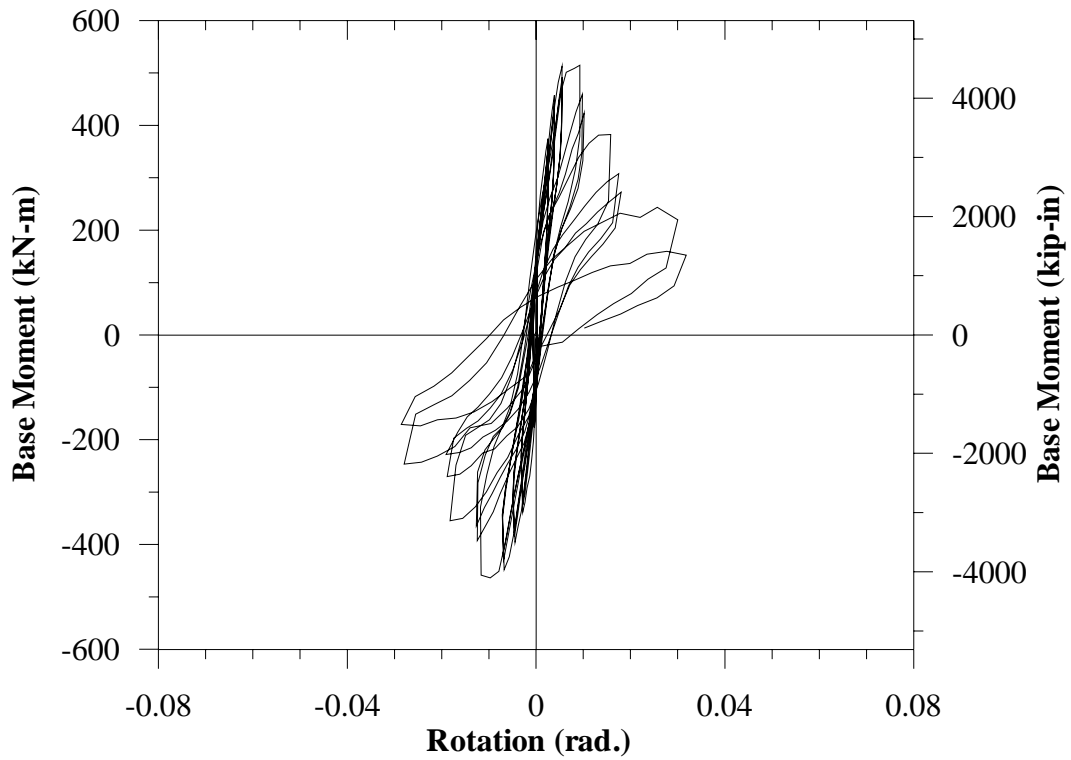


Figure 3.55 – S30XI Base Moment—Slip Rotation along Lap-splice Length

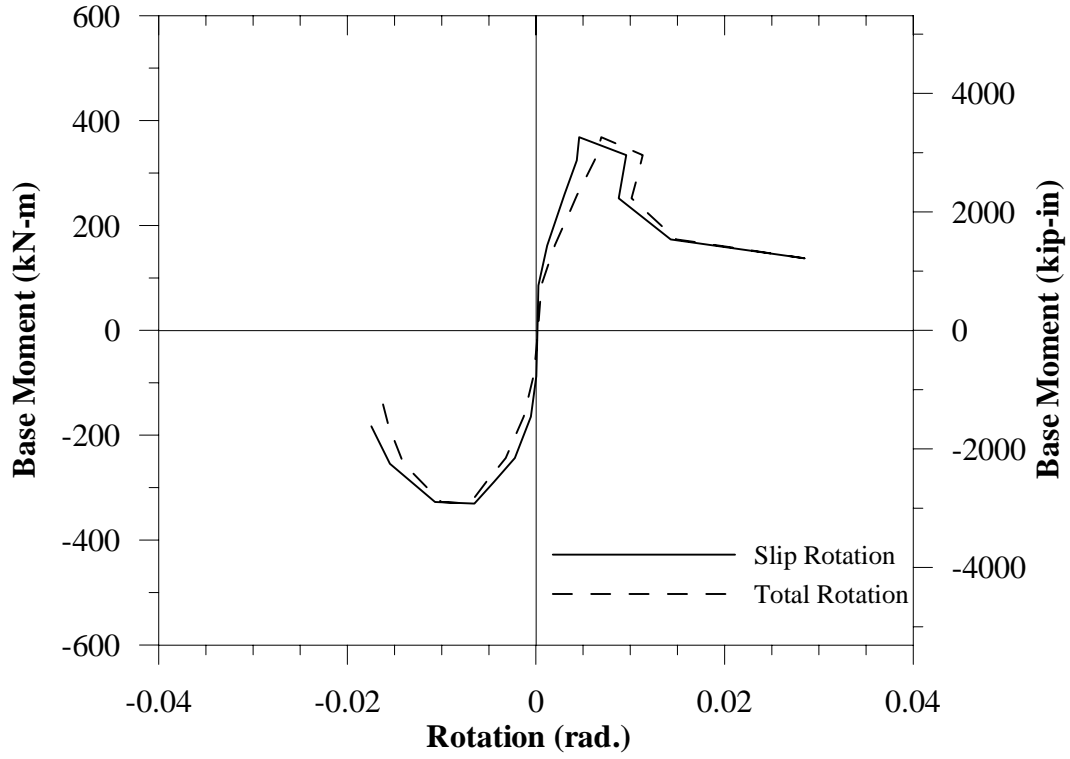


Figure 3.56 – S10MI Moment-Rotation Envelopes

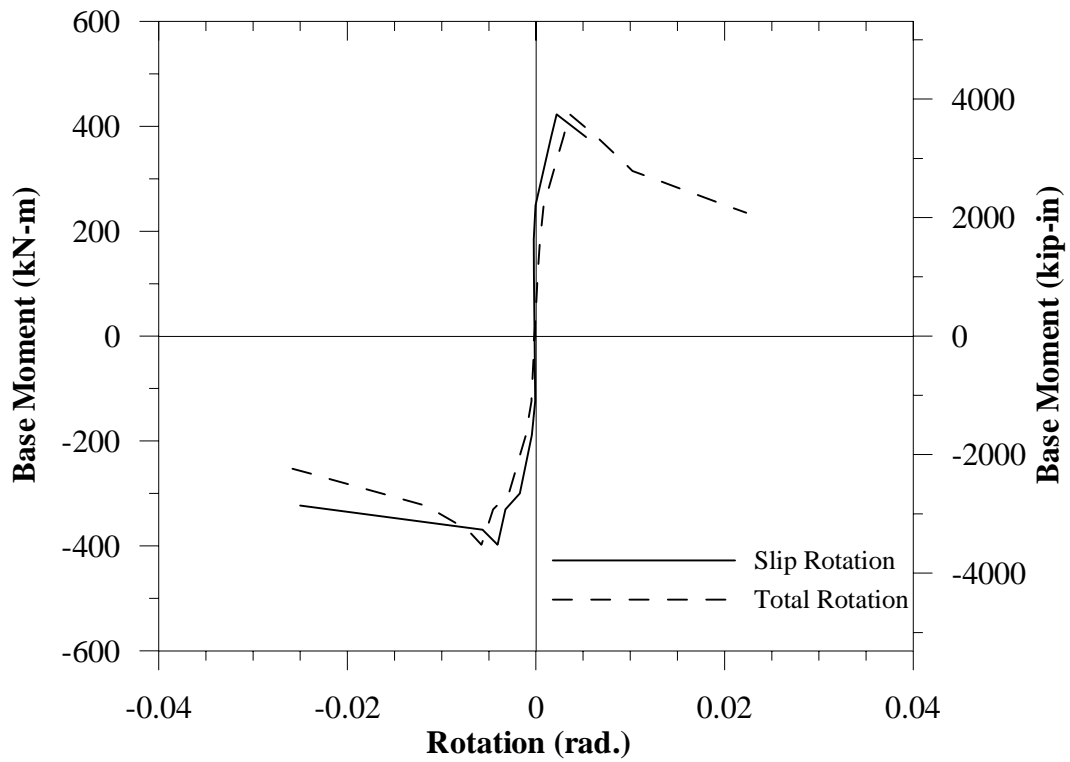


Figure 3.57 – S20MI Moment-Rotation Envelopes

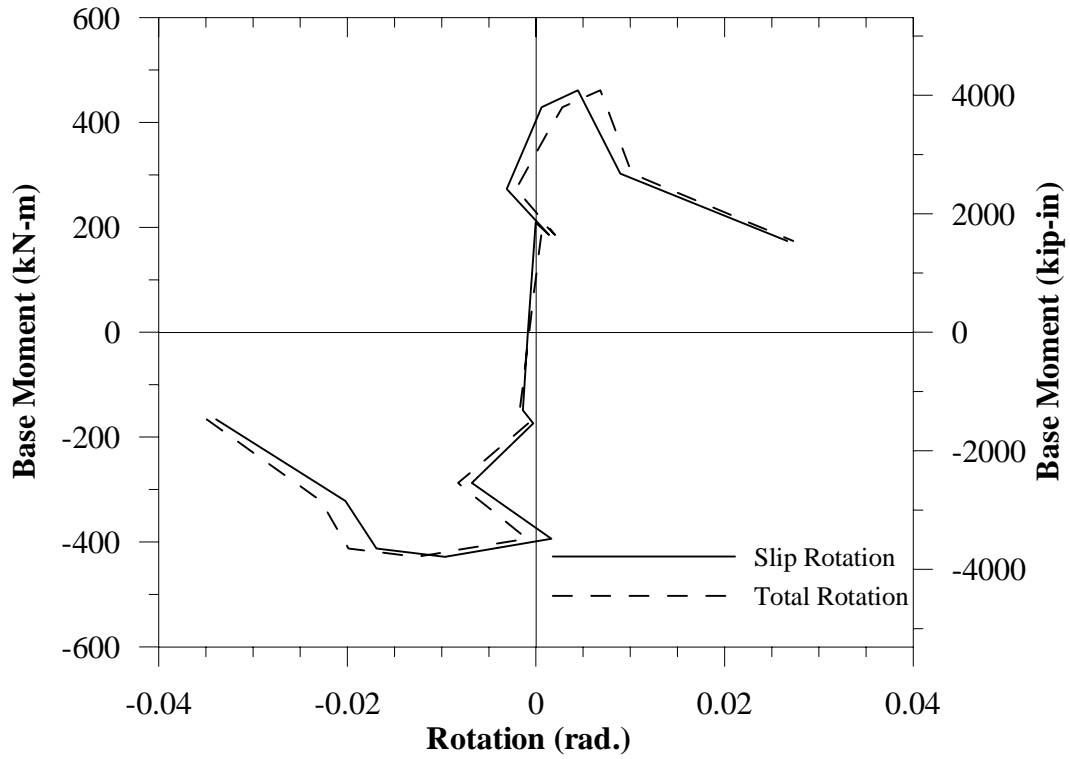


Figure 3.58 – S30MI Moment-Rotation Envelopes

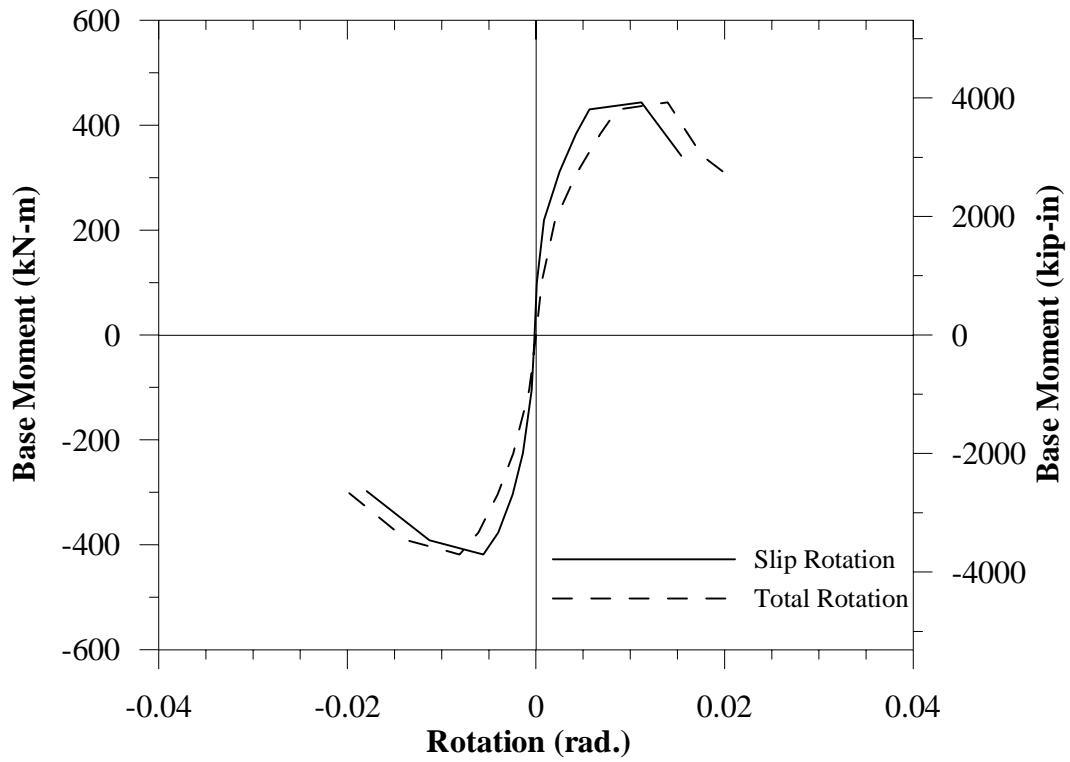


Figure 3.59 – S20HI Moment-Rotation Envelopes

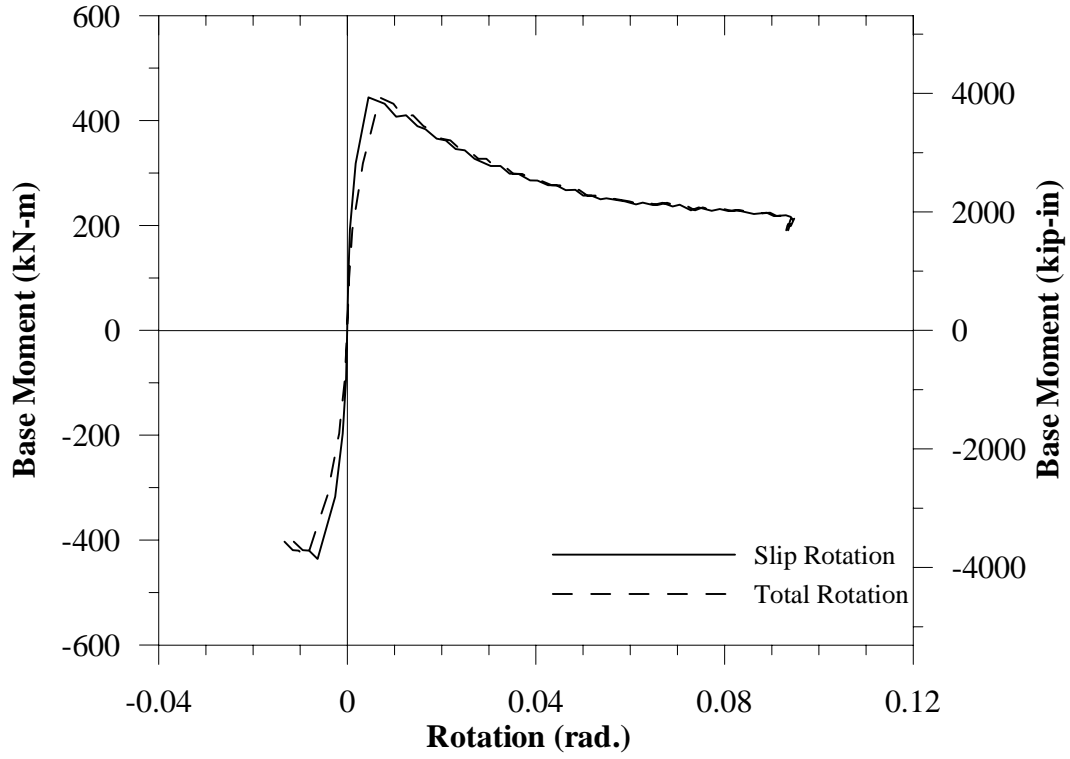


Figure 3.60 – S20HIN Moment-Rotation Envelopes

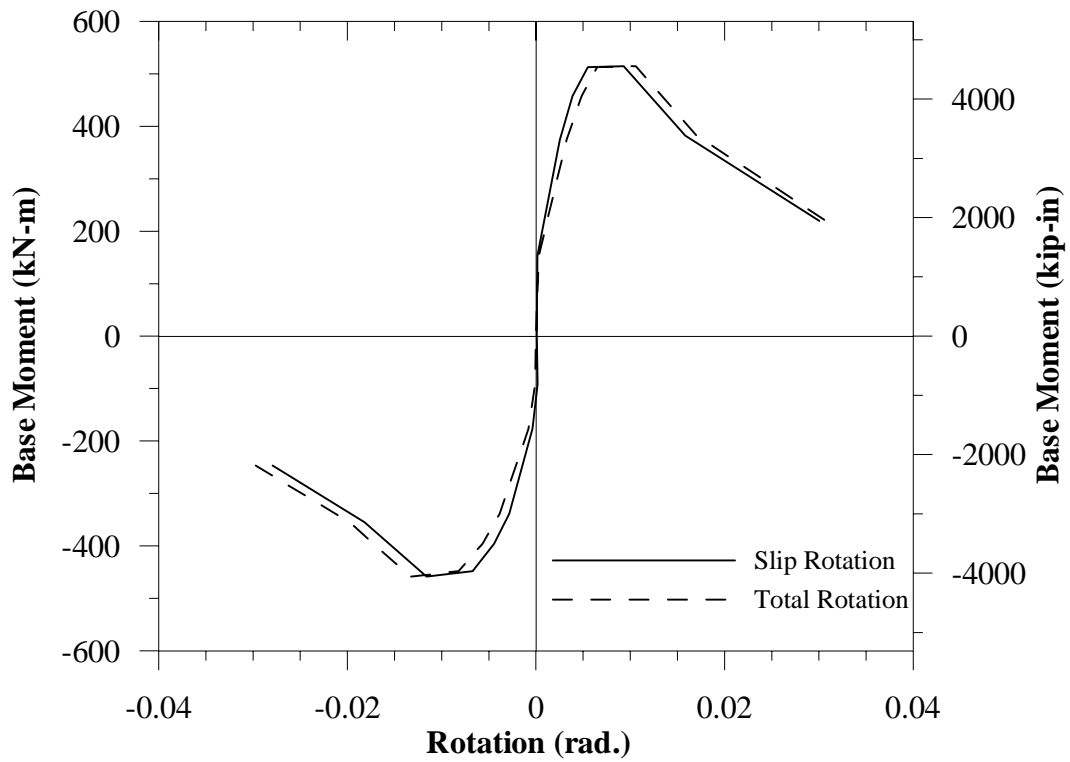


Figure 3.61 – S30XI Moment-Rotation Envelopes

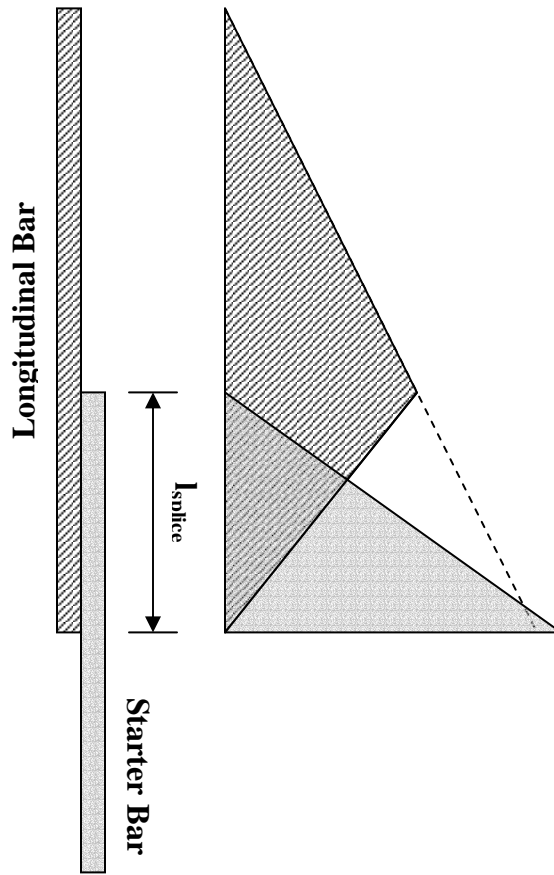


Figure 3.62 - Expected Strain Distribution along Splice Length

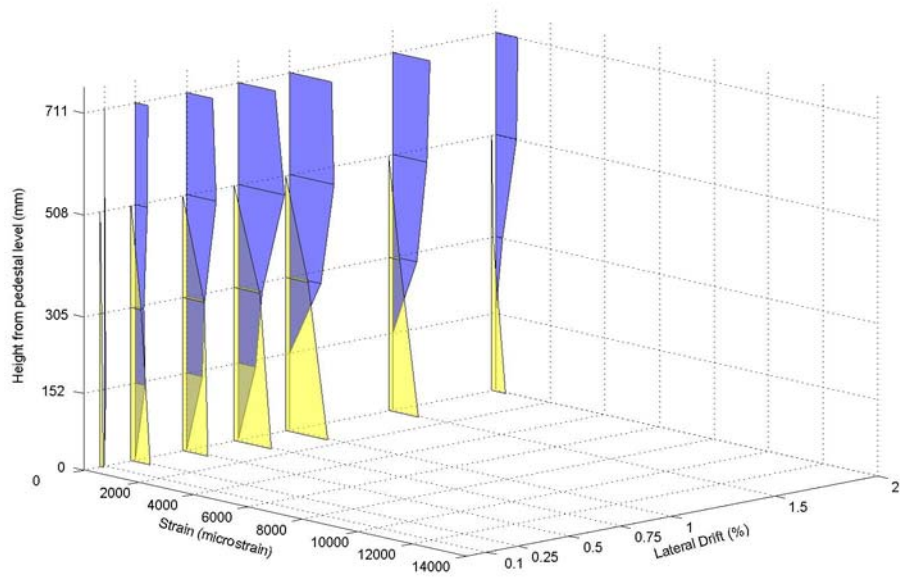


Figure 3.63 – S10MI Strain Distribution along Splice Length—Exterior (NW) Bar

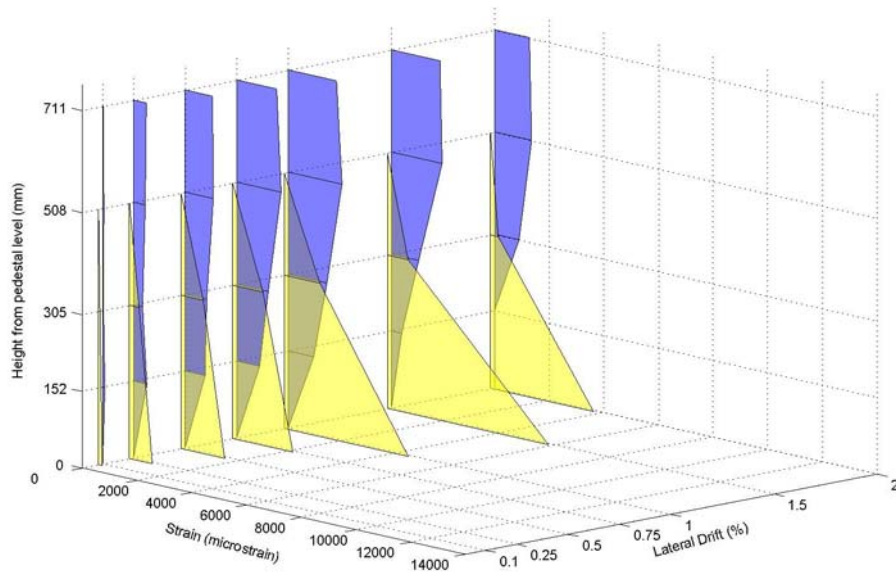


Figure 3.64 – S10MI Strain Distribution along Splice Length—Interior (W) Bar

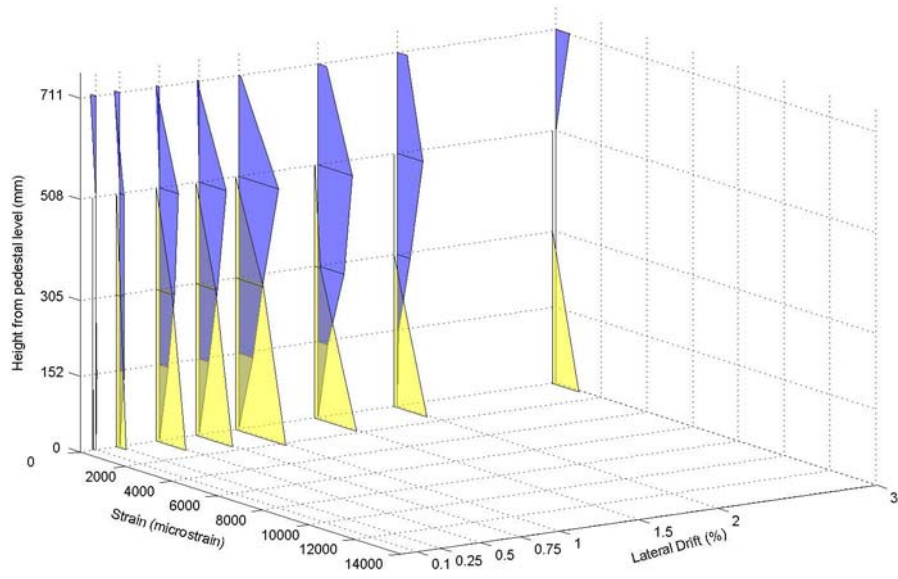


Figure 3.65 – S20MI Strain Distribution along Splice Length—Exterior (NW) Bar

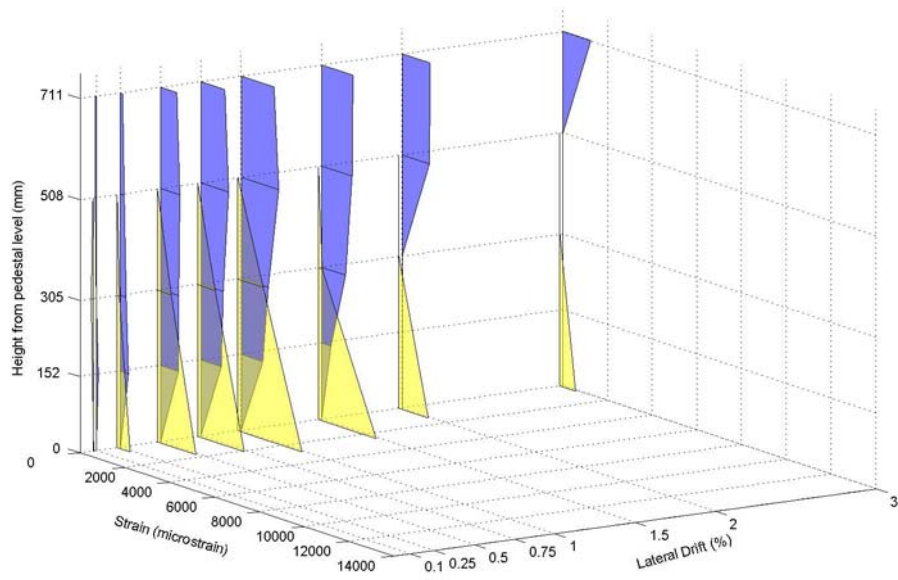


Figure 3.66 – S20MI Strain Distribution along Splice Length—Interior (W) Bar

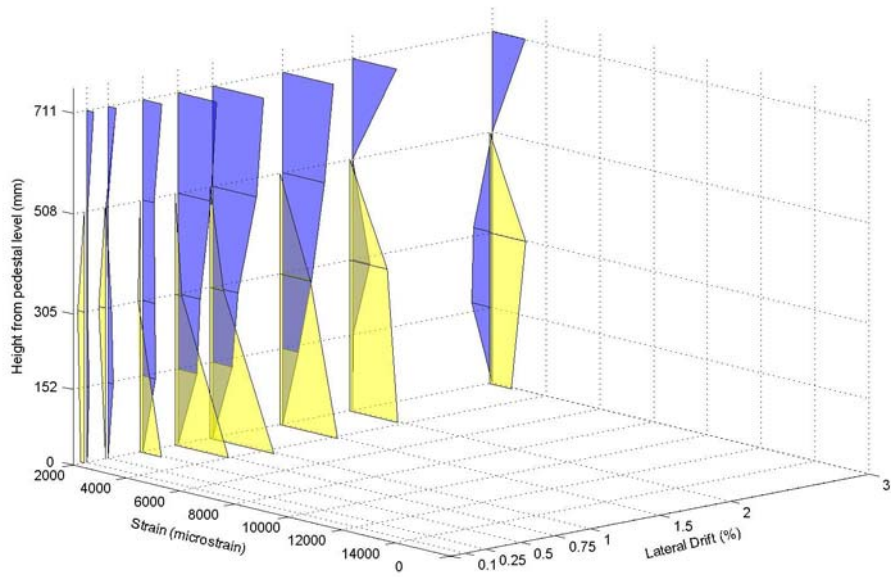


Figure 3.67 – S30MI Strain Distribution along Splice Length—Exterior (NW) Bar

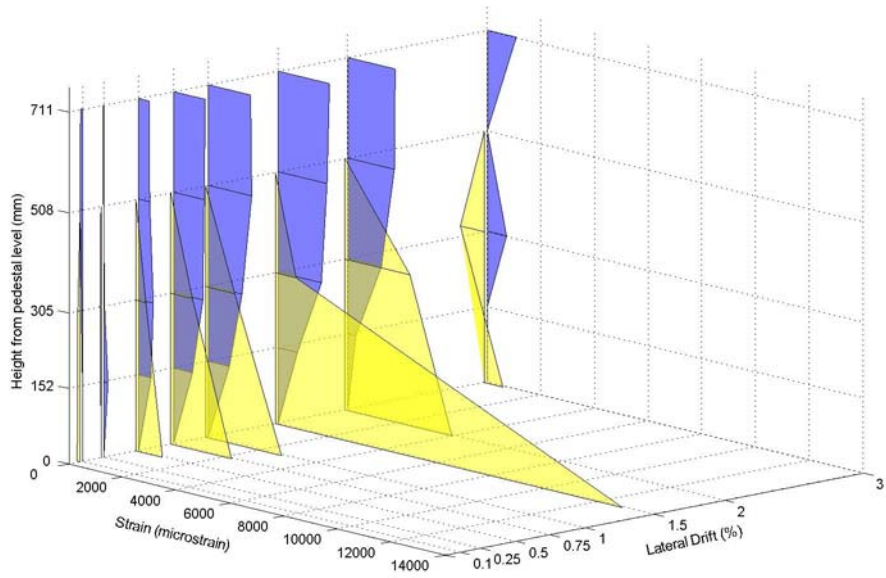


Figure 3.68 – S30MI Strain Distribution along Splice Length—Interior (W) Bar

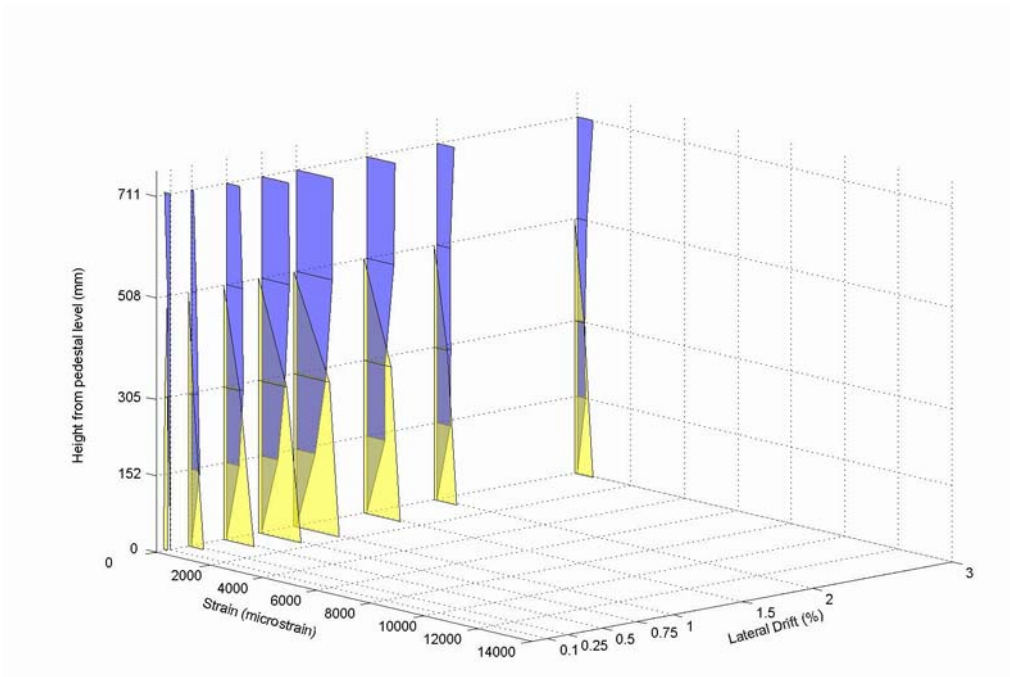


Figure 3.69 – S20HI Strain Bar Distribution along Splice Length—Exterior (NE) Bar

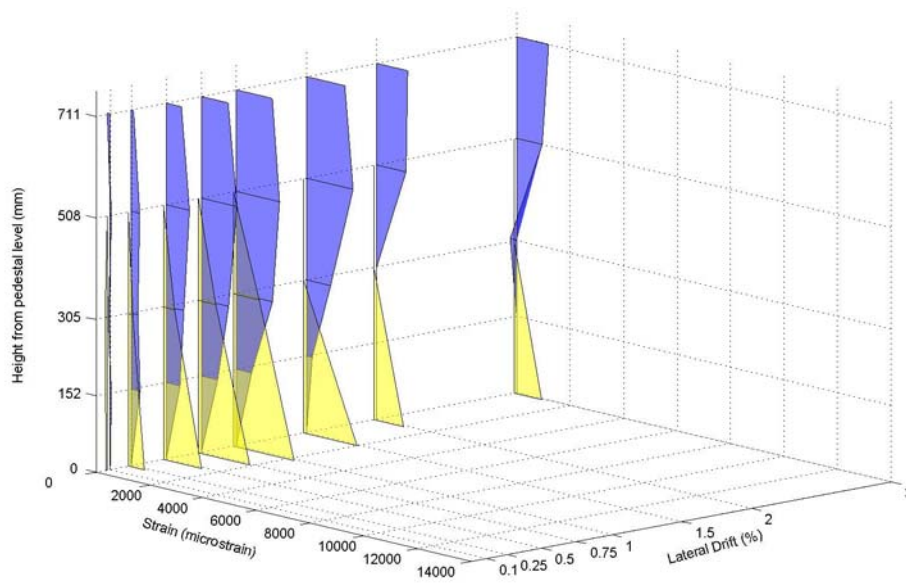


Figure 3.70 – S20HI Strain Distribution along Splice Length—Interior (W) Bar

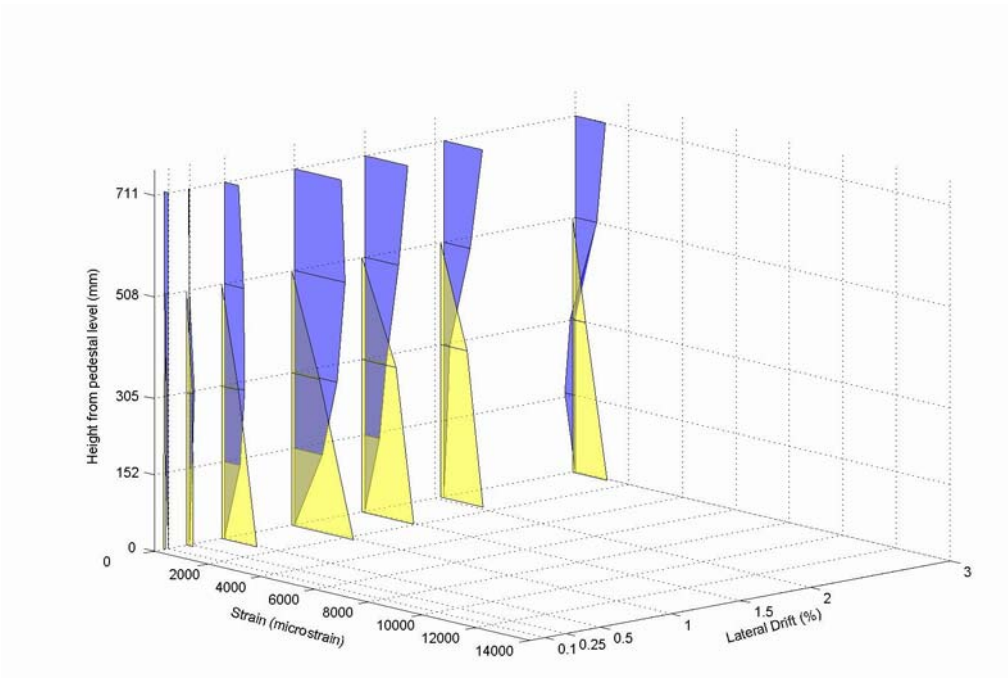


Figure 3.71 – S20HIN Strain Distribution along Splice Length—Exterior (NW) Bar

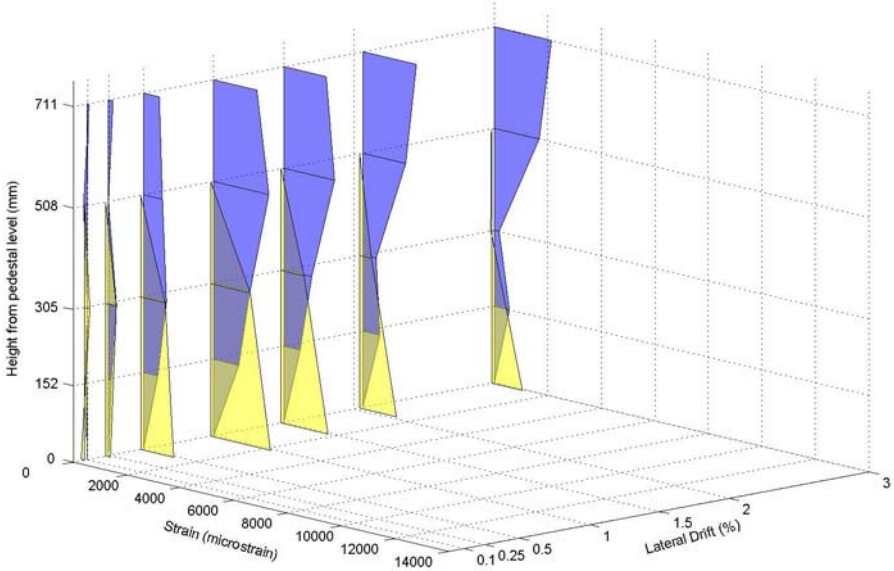


Figure 3.72 – S20HIN Strain Distribution along Splice Length—Interior (W) Bar

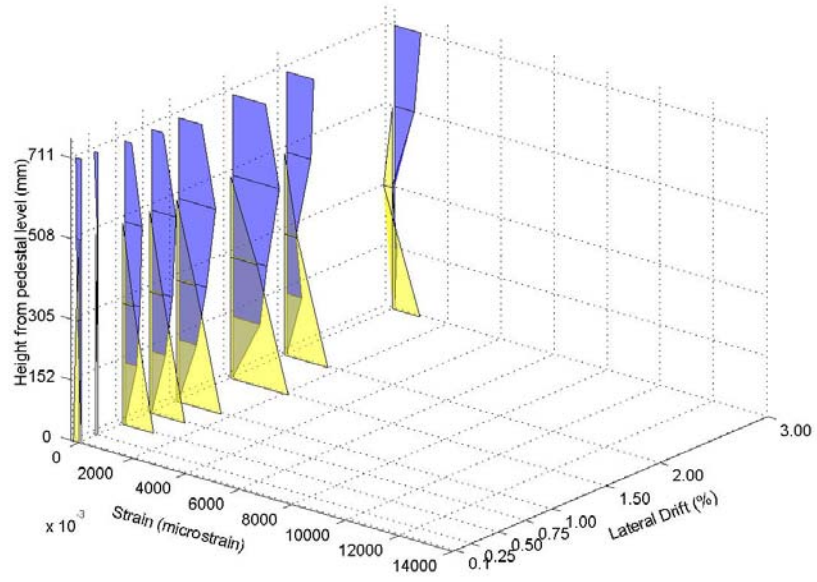


Figure 3.73 – S30XI Strain Distribution along Splice Length—Exterior (NW) Bar

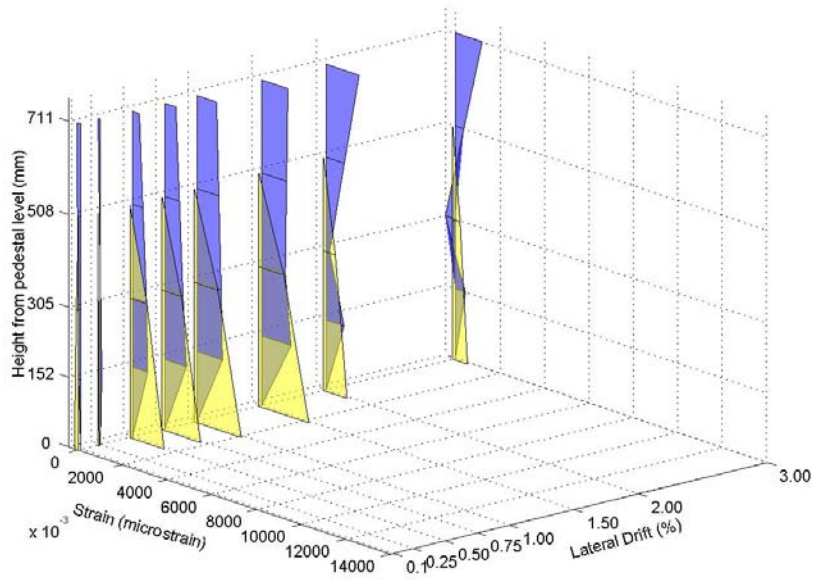


Figure 3.74 – S30XI Strain Distribution along Splice Length—Interior (W) Bar

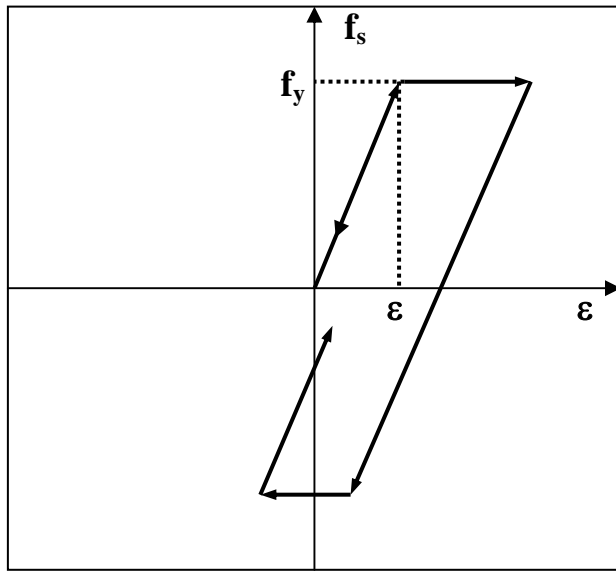


Figure 3.75 – Bilinear Steel Stress-Strain Model

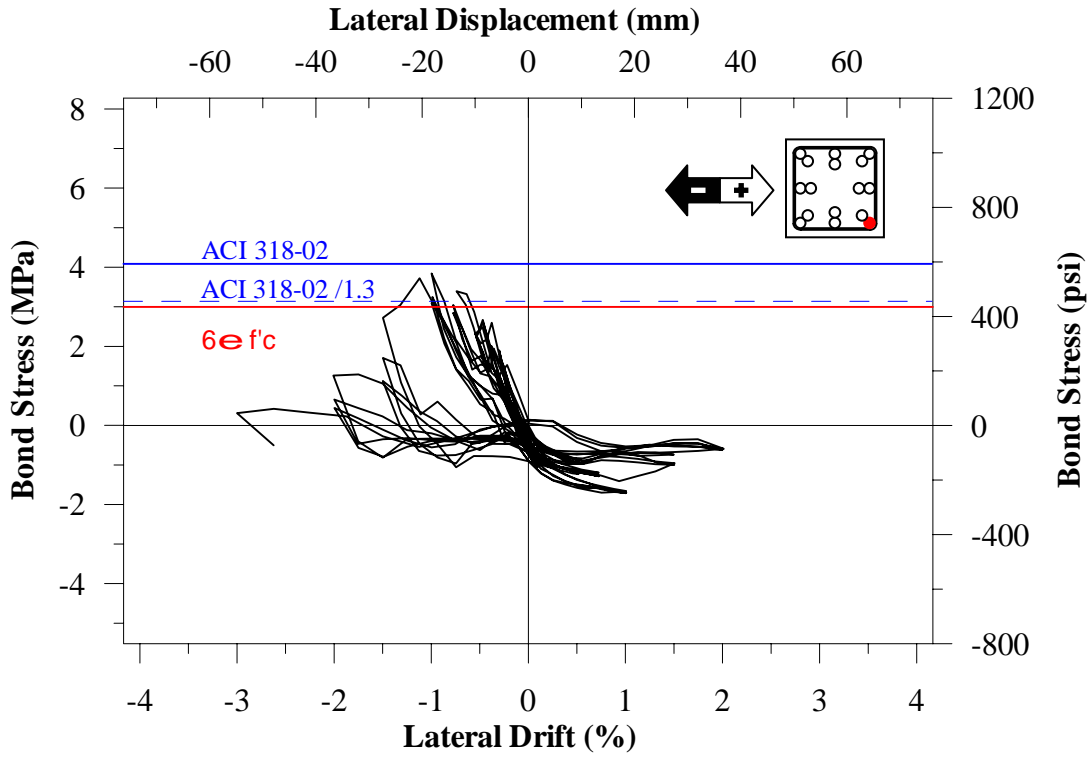


Figure 3.76 - S10MI Bond Stress — Lateral Drift (Bar NW)

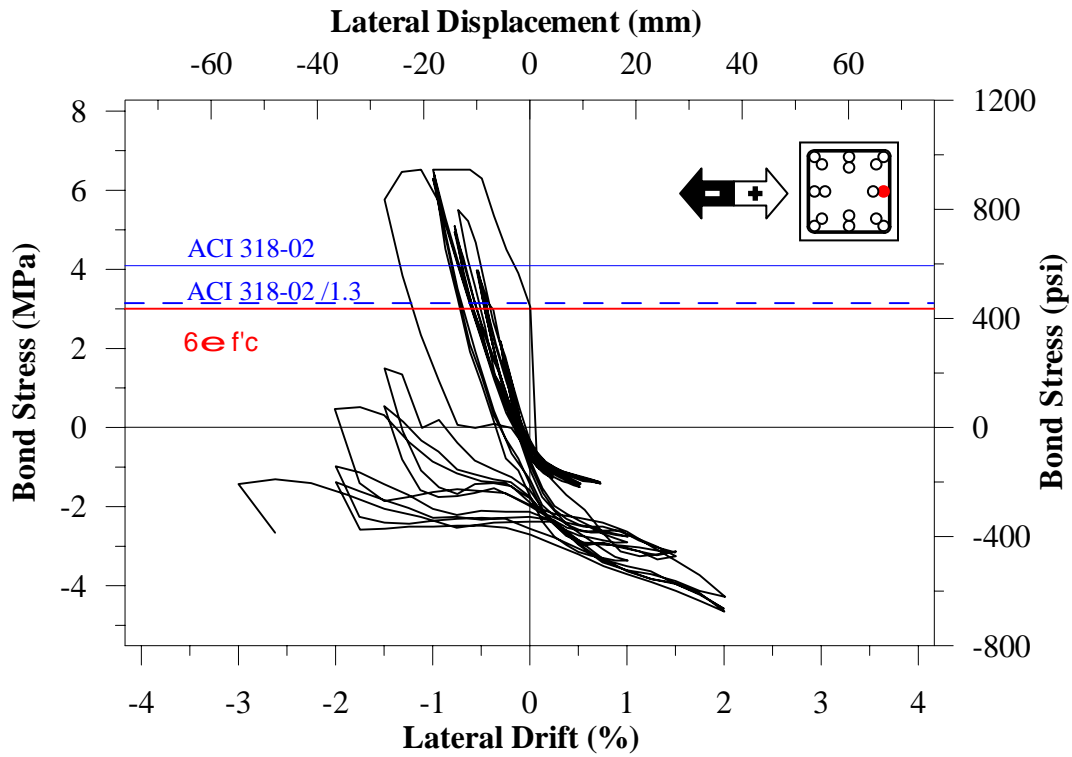


Figure 3.77 - S10MI Bond Stress—Lateral Drift (Bar W)

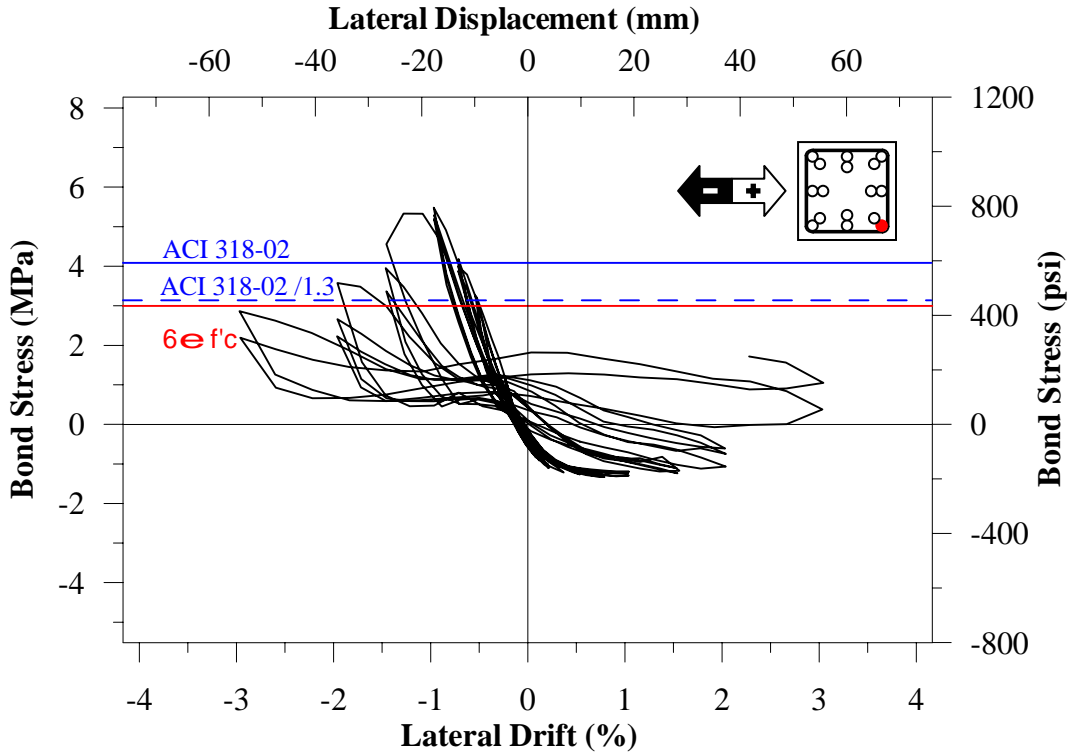


Figure 3.78 - S20MI Bond Stress—Lateral Drift (Bar NW)

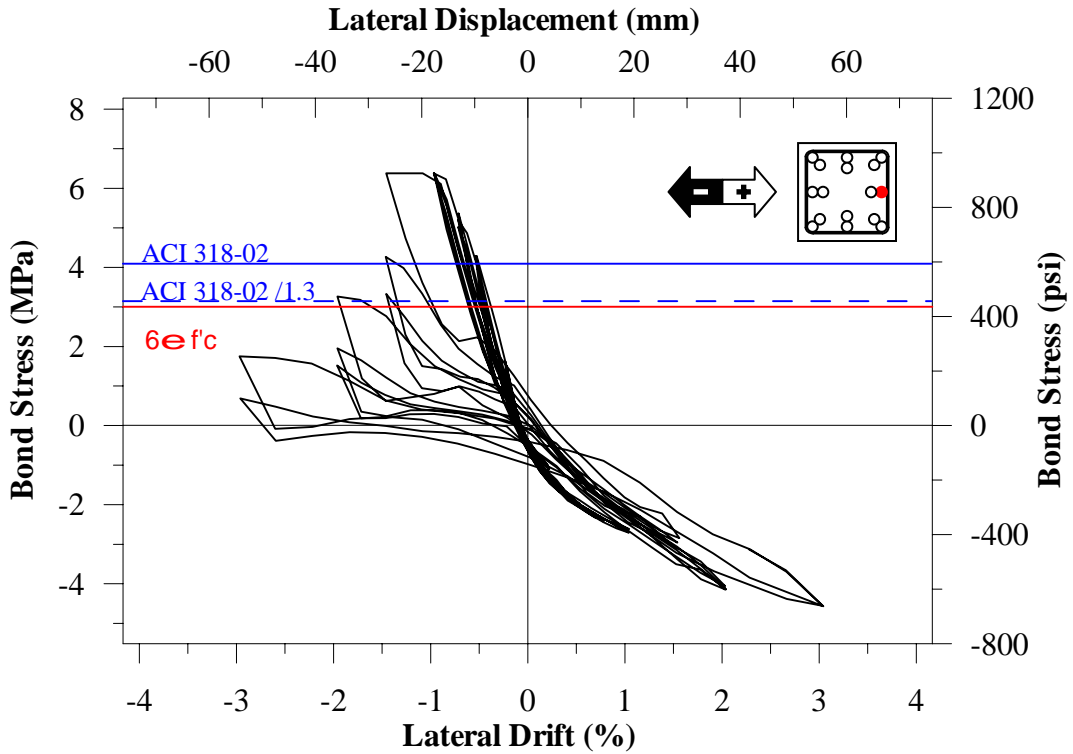


Figure 3.79 - S20MI Bond Stress—Lateral Drift (Bar W)

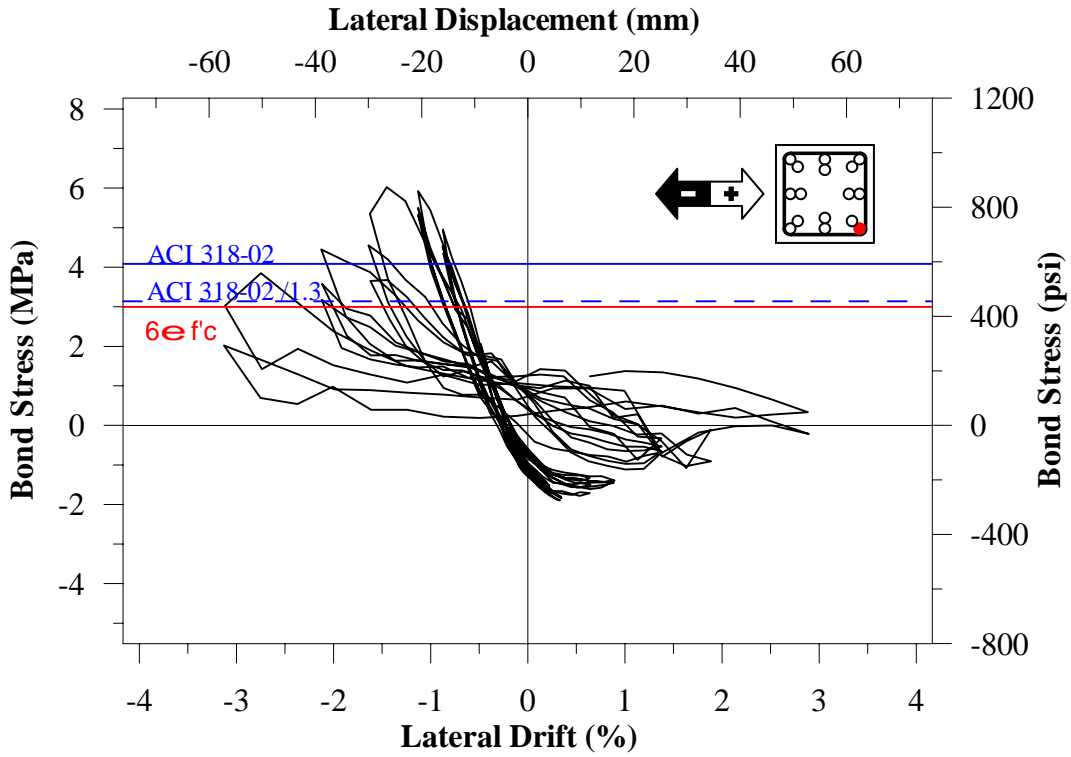


Figure 3.80 - S30MI Bond Stress—Lateral Drift (Bar NW)

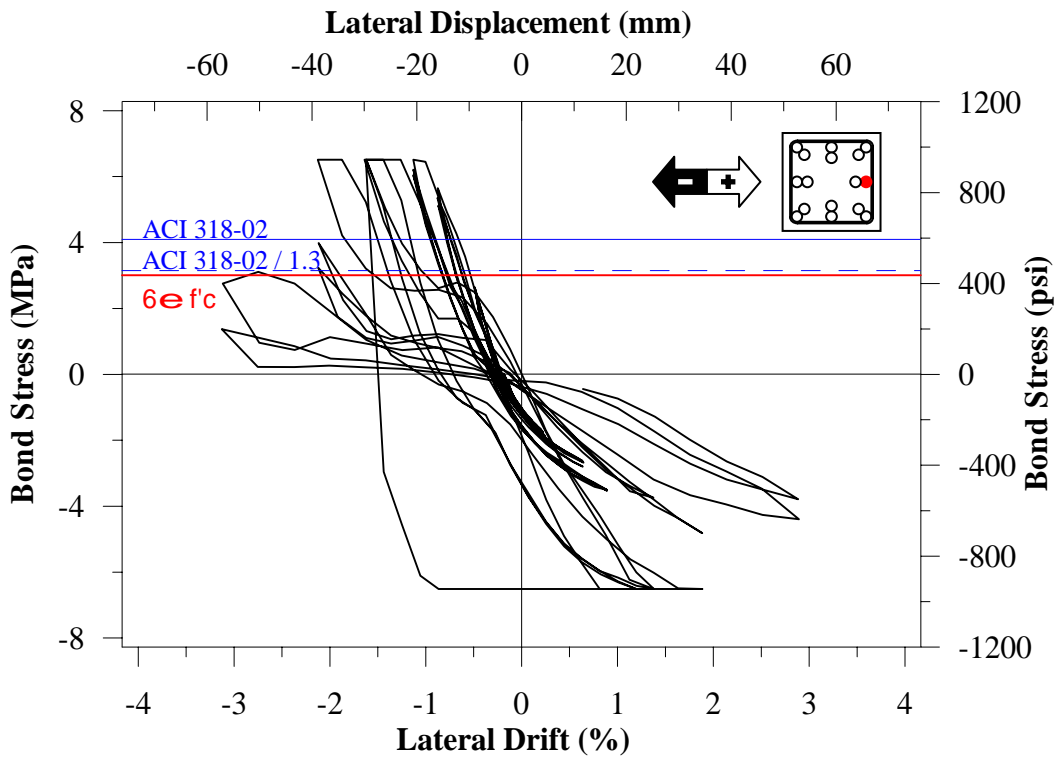


Figure 3.81 - S30MI Bond Stress—Lateral Drift (Bar W)

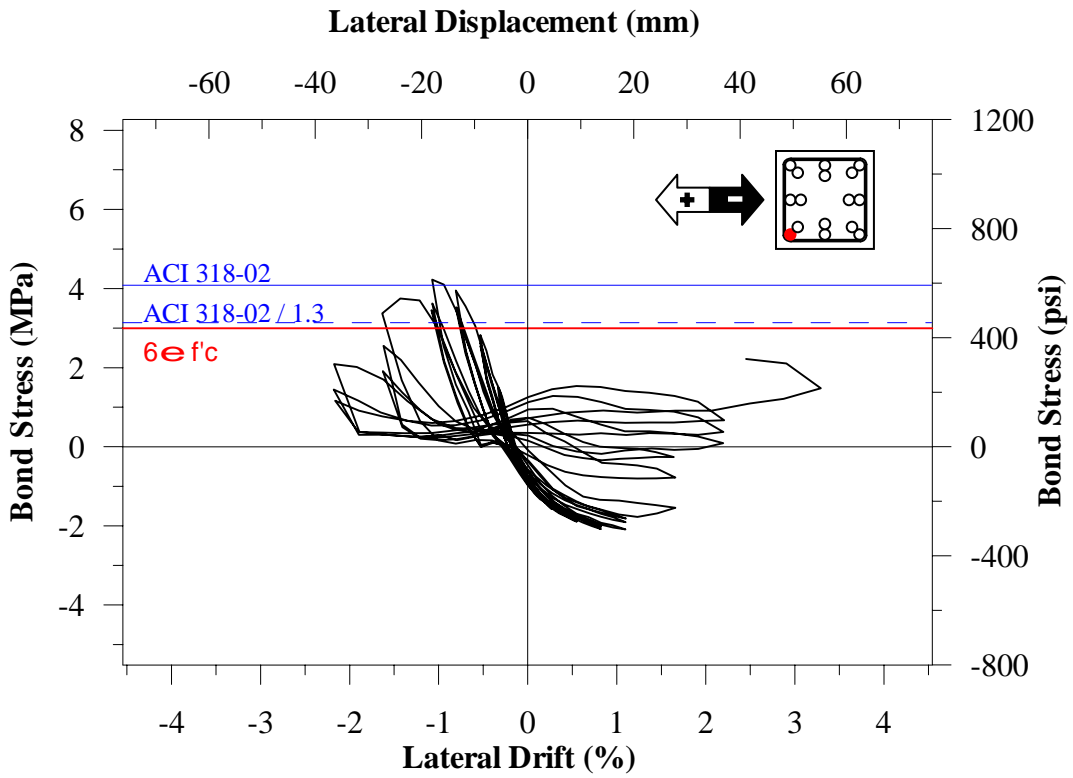


Figure 3.82 - S20HI Bond Stress—Lateral Drift (Bar NE)

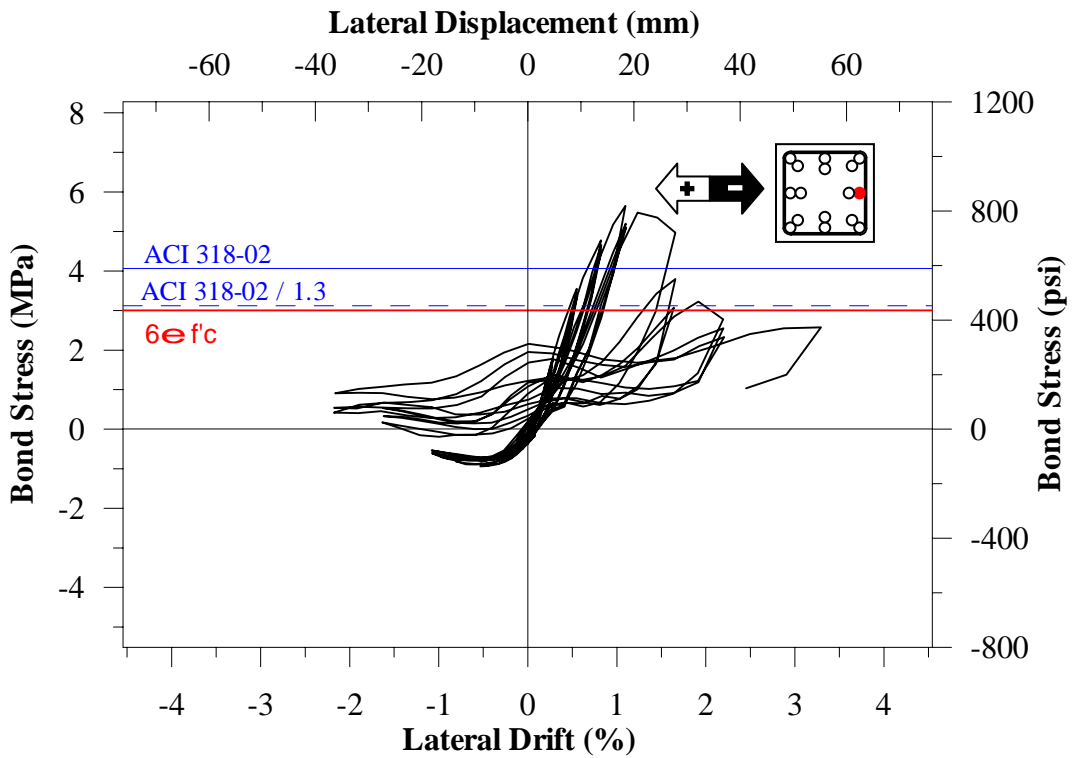


Figure 3.83 - S20HI Bond Stress—Lateral Drift (Bar W)

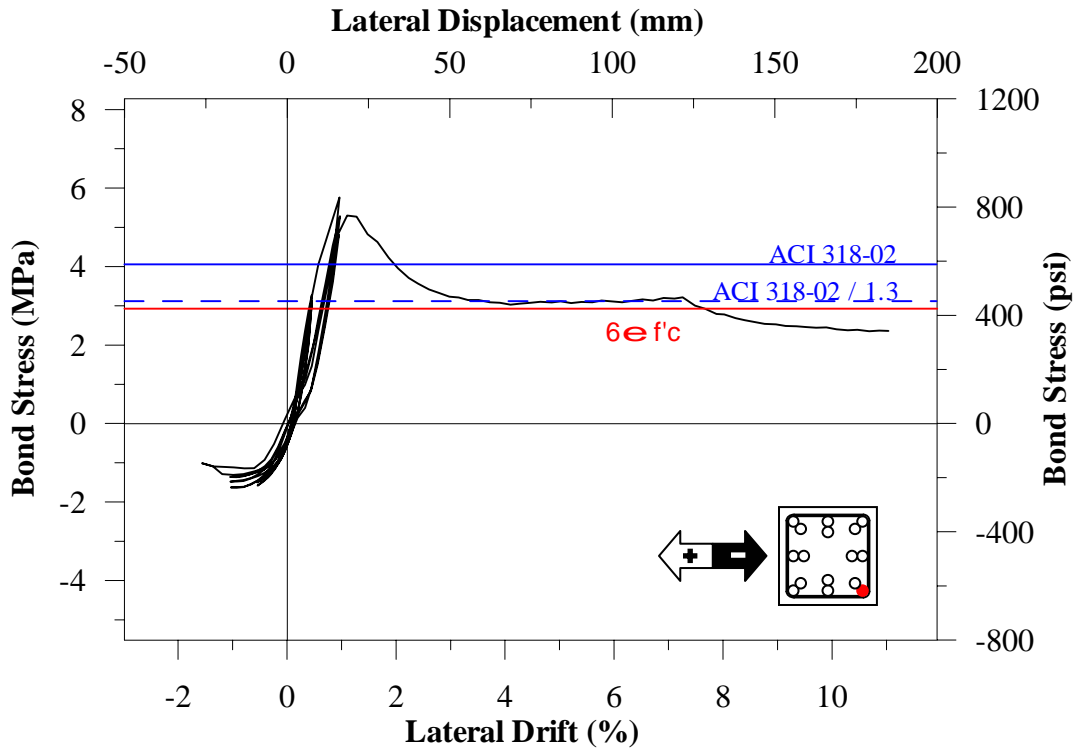


Figure 3.84 - S20HIN Bond Stress – Lateral Drift (Bar NW)

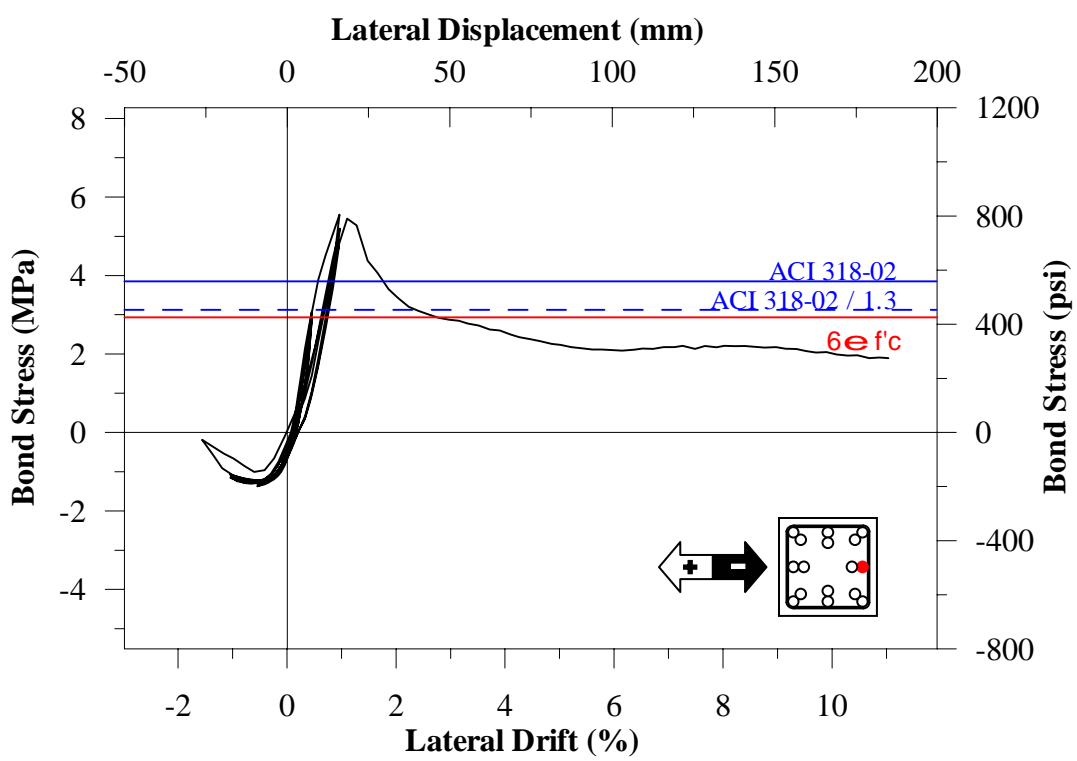


Figure 3.85 - S20HIN Bond Stress—Lateral Drift (Bar W)

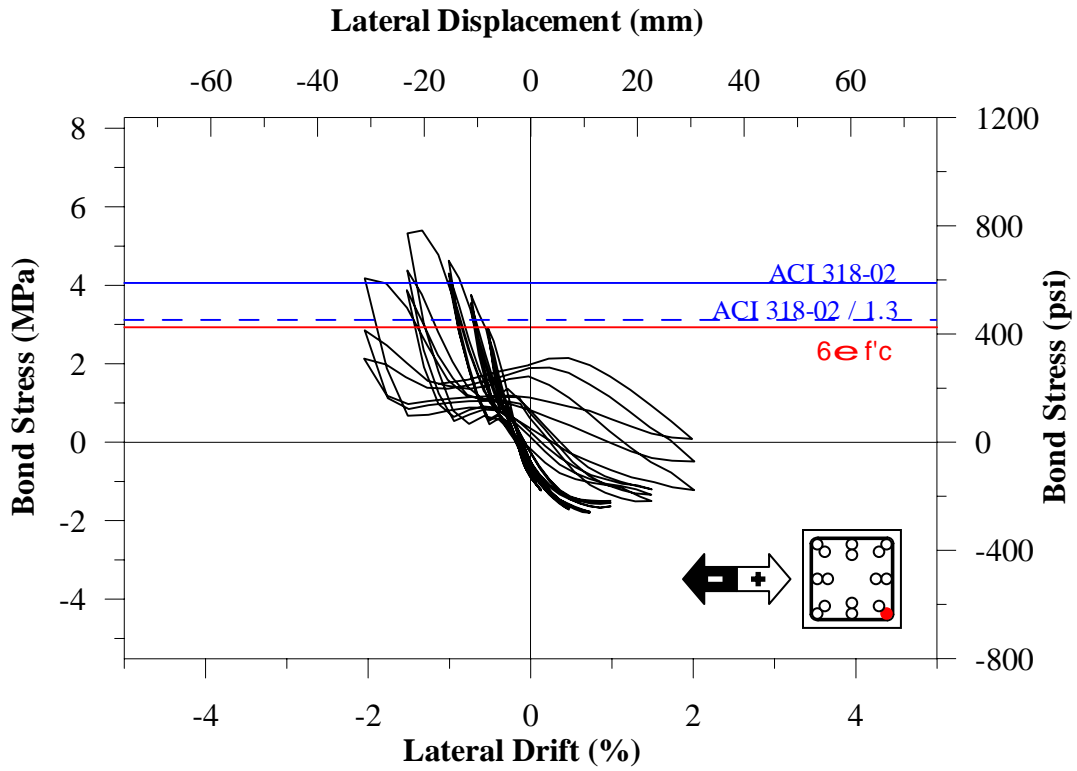


Figure 3.86 – S30XI Bond Stress – Lateral Drift (Bar NW)

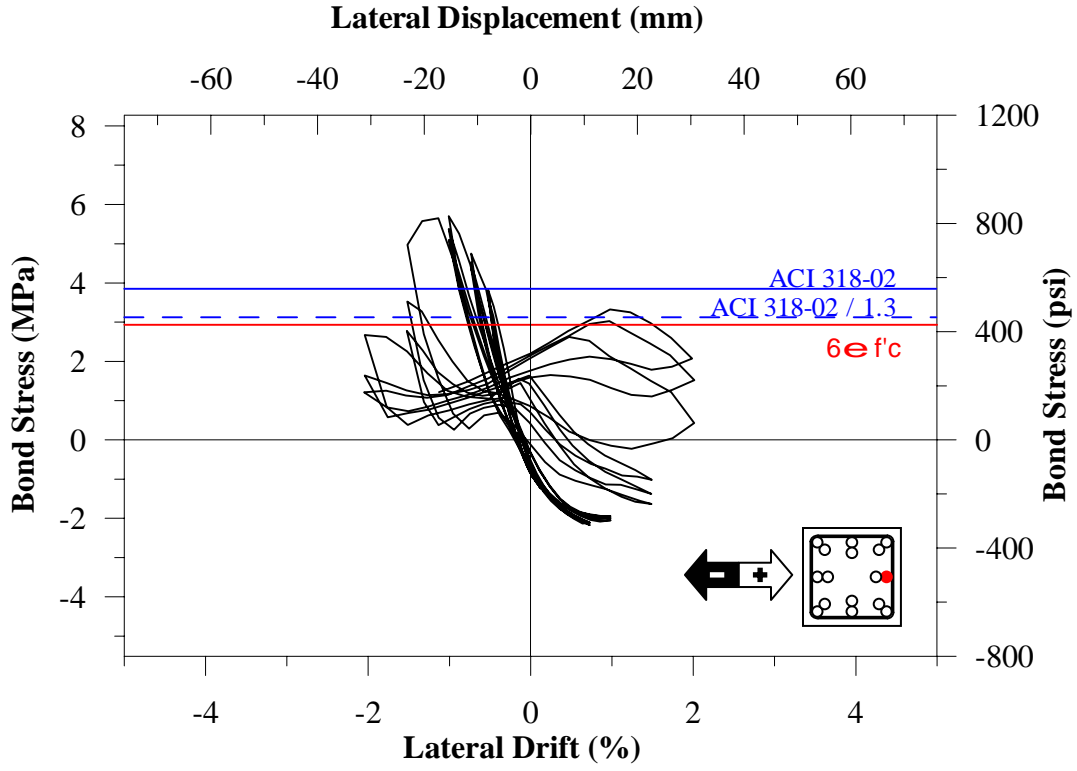


Figure 3.87 – S30XI Bond Stress—Lateral Drift (Bar W)

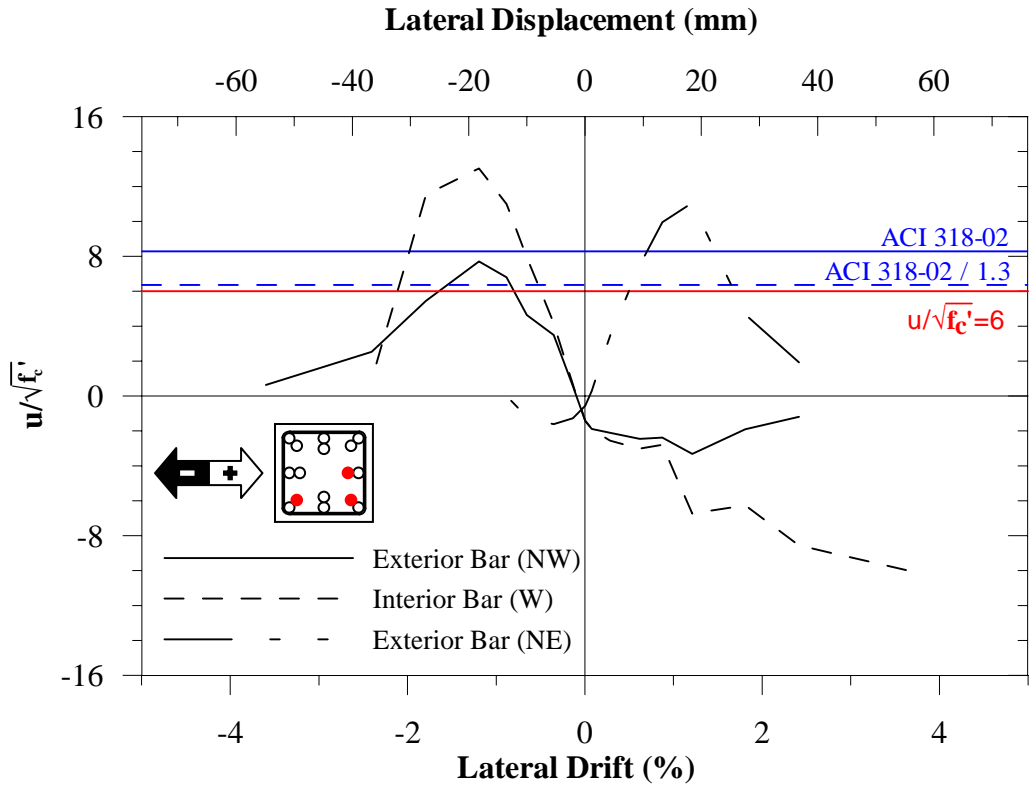


Figure 3.88 – S10MI Normalized Average Bond Stress – Lateral Drift

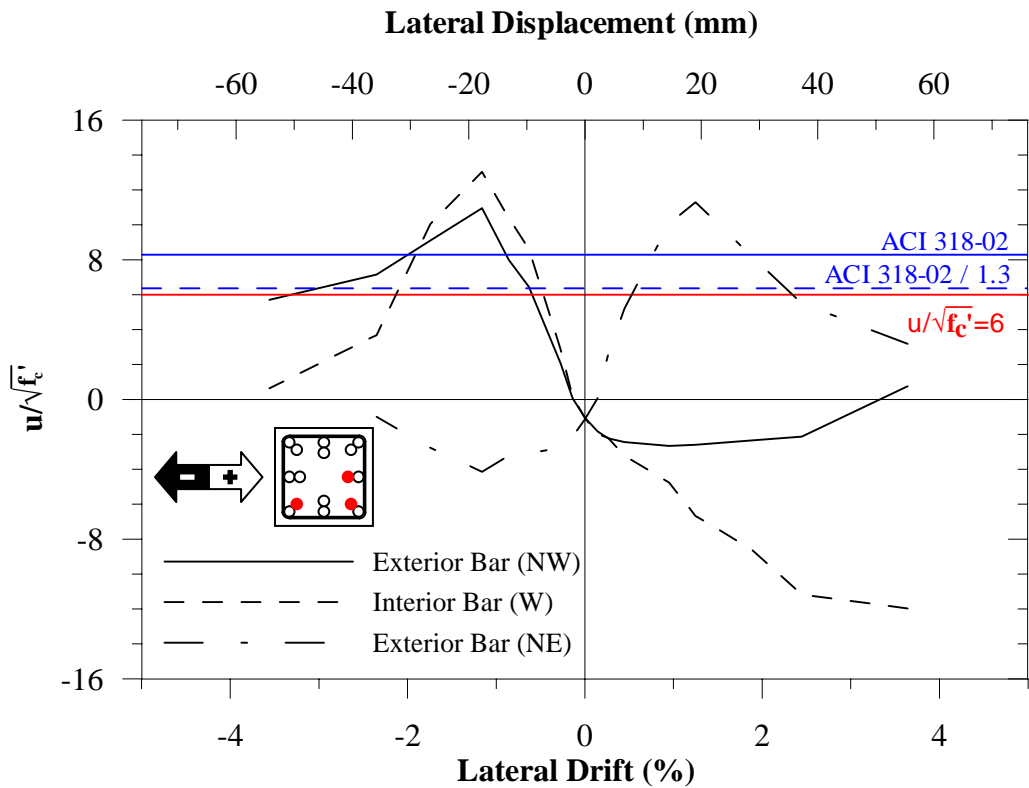


Figure 3.89 – S20MI Normalized Average Bond Stress—Lateral Drift

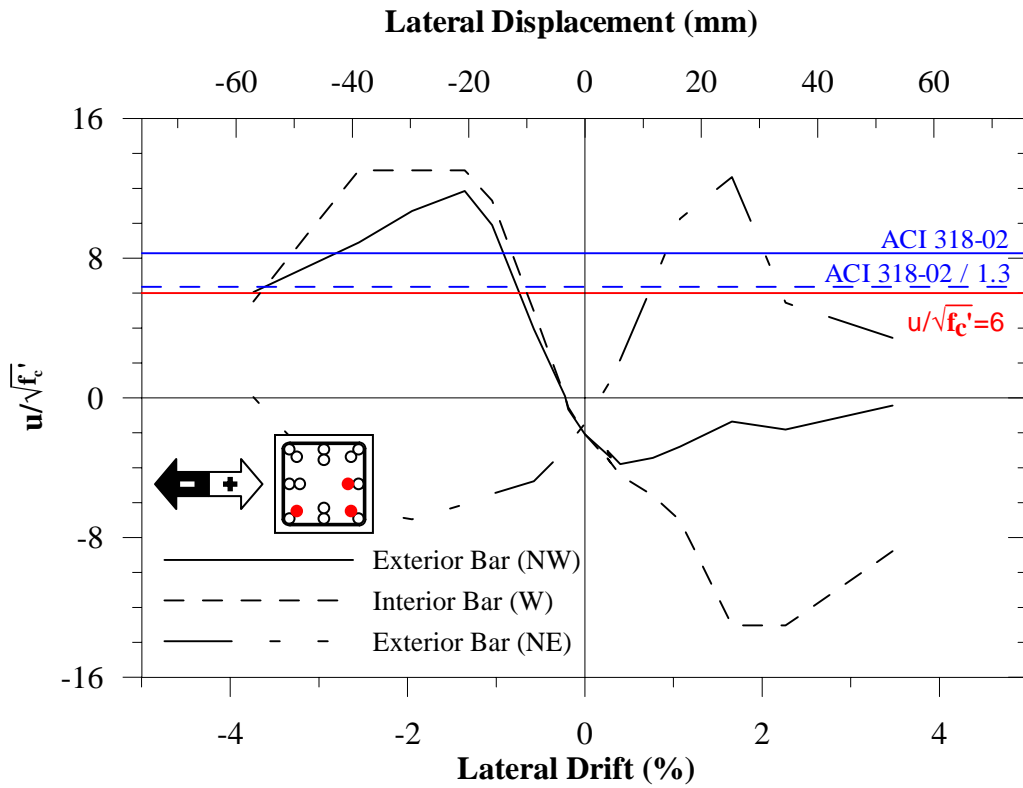


Figure 3.90 – S30MI Normalized Average Bond Stress – Lateral Drift

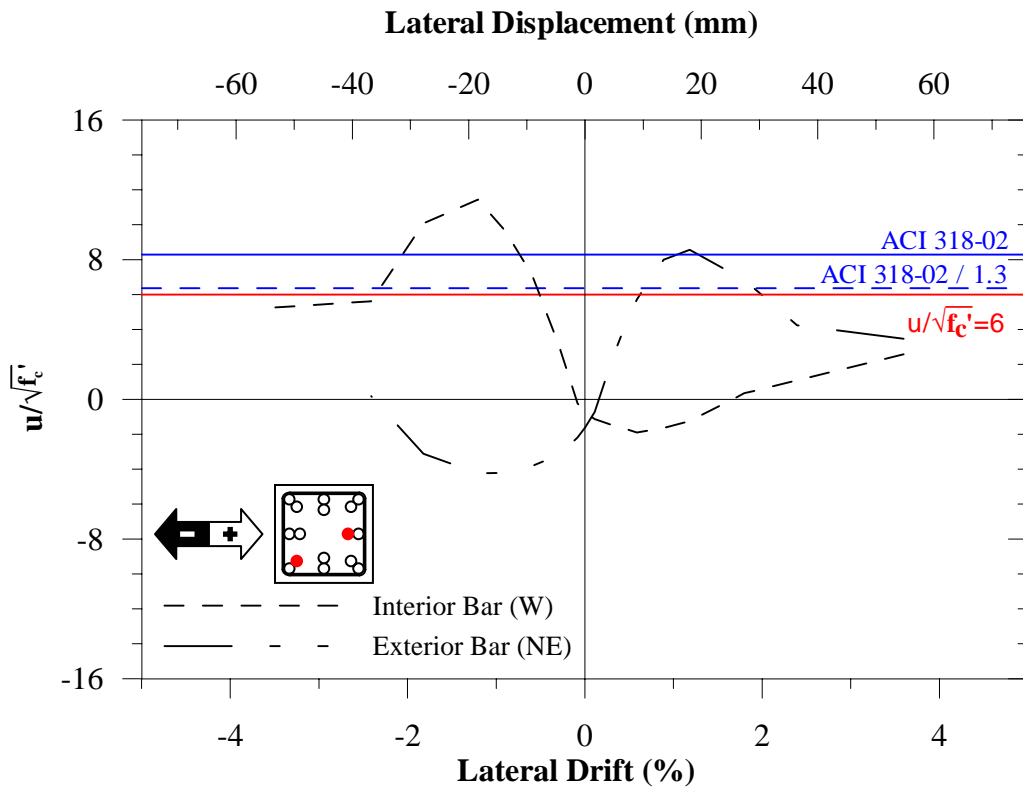


Figure 3.91 – S20HI Normalized Average Bond Stress—Lateral Drift

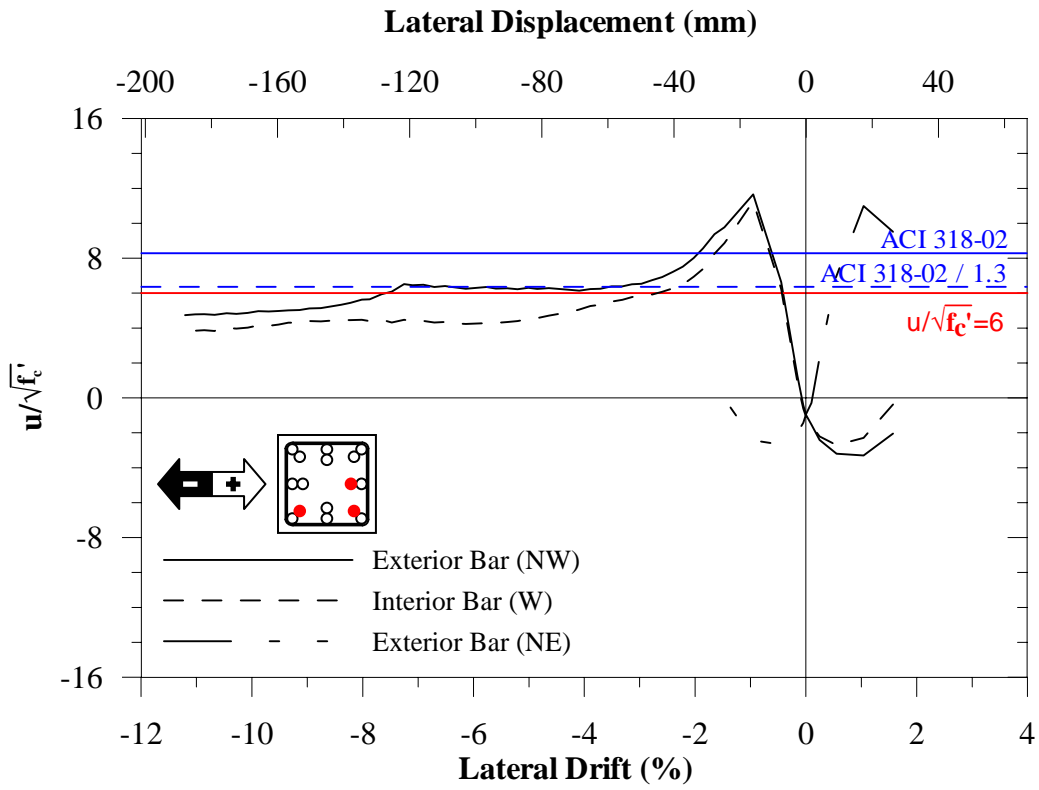


Figure 3.92 – S20HIN Normalized Average Bond Stress – Lateral Drift

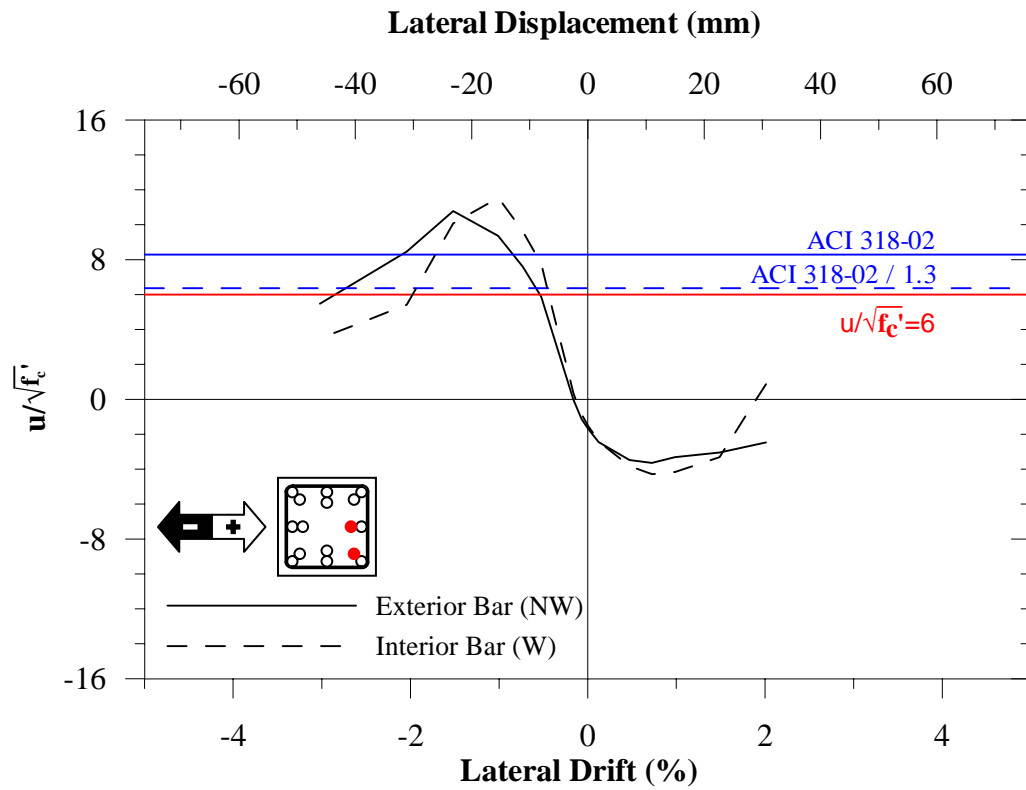


Figure 3.93 – S30XI Normalized Average Bond Stress—Lateral Drift

Table 3.5 Beam Tests Results (Sozen and Moehle (1990))

Experiment	TEST ID	c_{min}/d_b	f_c' (Mpa)	u (Mpa)	$u/\sqrt{f_c'}$
Ferguson et al. (1965)	8F30b	1.50	18.00	3.26	0.77
	8F36c	1.47	18.89	2.91	0.67
	8R18a	1.75	23.92	4.14	0.85
	8R24a	1.67	24.34	4.24	0.86
	8F30a	1.53	20.89	3.02	0.66
	8F36b	1.40	25.99	2.94	0.58
	8F42a	1.56	22.82	2.90	0.61
	8R48a	1.48	20.96	2.61	0.57
	8F36k	1.38	23.86	2.54	0.52
Thompson et al. (1975)	8.15.4	2.00	24.20	6.22	1.26
	8.18.4/3/2.6/6	2.00	32.47	5.54	0.97
	8.18.4/3/2.5/6	2.50	20.13	4.34	0.97
	8.24.4/2/2.6/6	2.00	21.41	3.84	0.83
Heflin (1992)	8-2-6A	2.00	46.16	6.56	0.97
	8-2-6B	2.00	48.95	5.79	0.83
	8-2-4A	2.00	41.37	5.93	0.92
	8-2-4B	2.00	37.92	5.35	0.87
	8-2-3A	1.50	43.44	5.98	0.91
	8-2-3B	1.50	44.68	5.55	0.83
	8-2-2A	1.00	44.92	5.27	0.79
	8-2-2B	1.00	42.78	5.33	0.81
	8-2.5-3A	1.50	39.13	6.09	0.97
	8-2.5-3B	1.50	47.61	6.23	0.90
	8-2-1A	0.50	43.95	4.92	0.74
	8-2-1B	0.50	47.50	4.66	0.68
Mathey (1961)	8-7-1	1.50	27.61	7.05	1.34
	8-14-1	1.50	24.72	4.12	0.83
	8-14-2	1.50	27.96	5.24	0.99
	8-21-1	1.50	29.20	5.08	0.94
	8-21-2	1.50	24.10	4.38	0.89
	8-28-1	1.50	30.92	4.76	0.86
	8-28-2	1.50	25.51	4.43	0.88
	8-34-2	1.50	25.96	4.56	0.89
Jeanty (1988)	B2	1.50	26.82	2.41	0.46
	B4	1.50	29.23	2.68	0.49

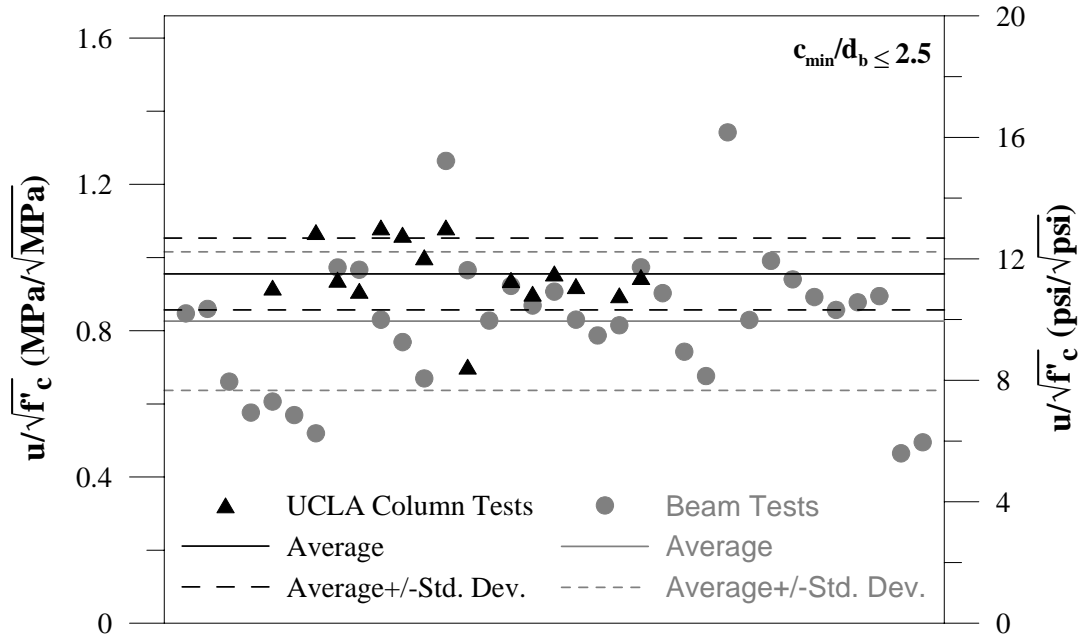


Figure 3.94 – $u/\sqrt{f'_c}$ Comparison of Cyclic Column and Monotonic Beam Tests

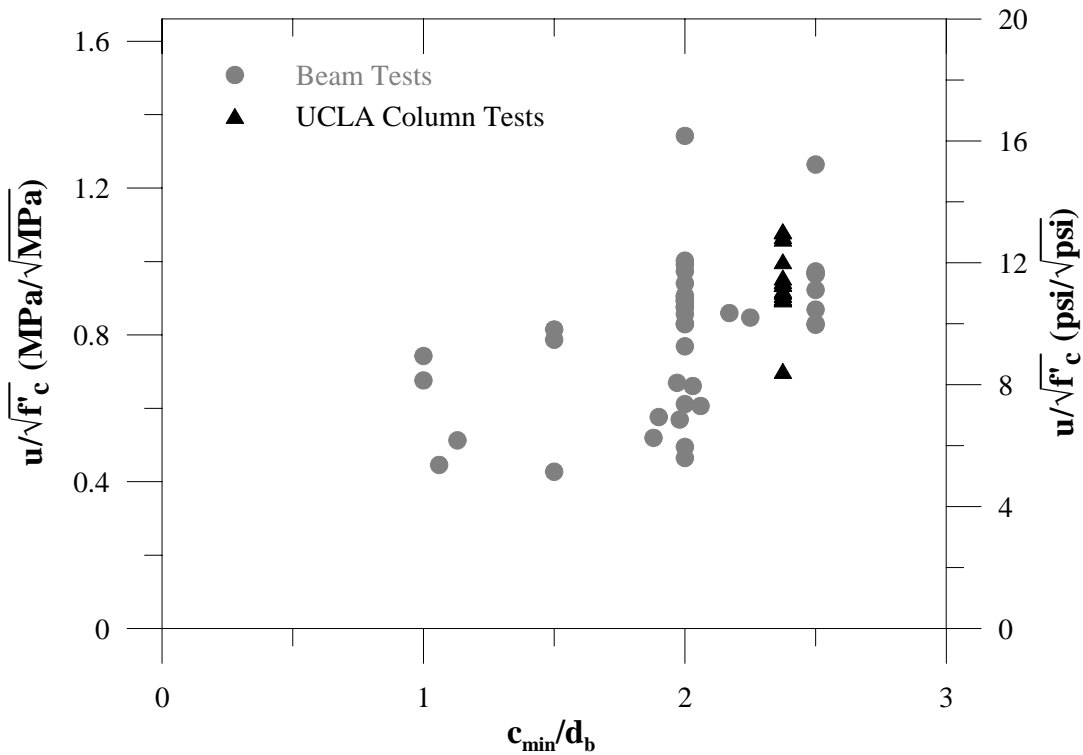


Figure 3.95 – Normalized Bond Stress vs. c_{min}/d_b

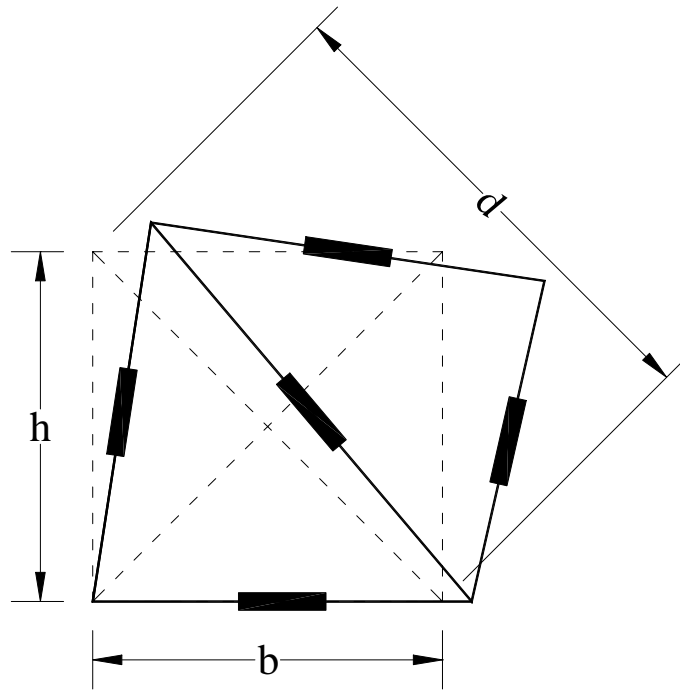


Figure 3.96 – Shear Deformation Measurement (S10MI, S20MI, and S30MI)

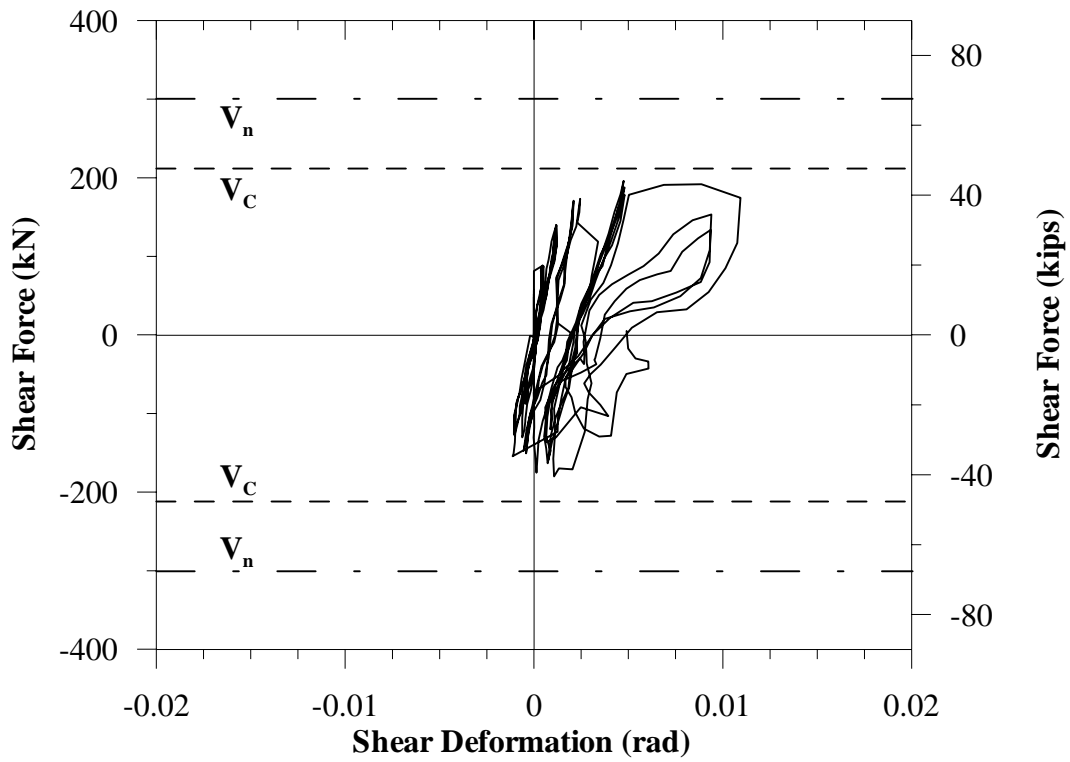


Figure 3.97 – S10MI Shear Deformation along Splice Length ($20d_b$)

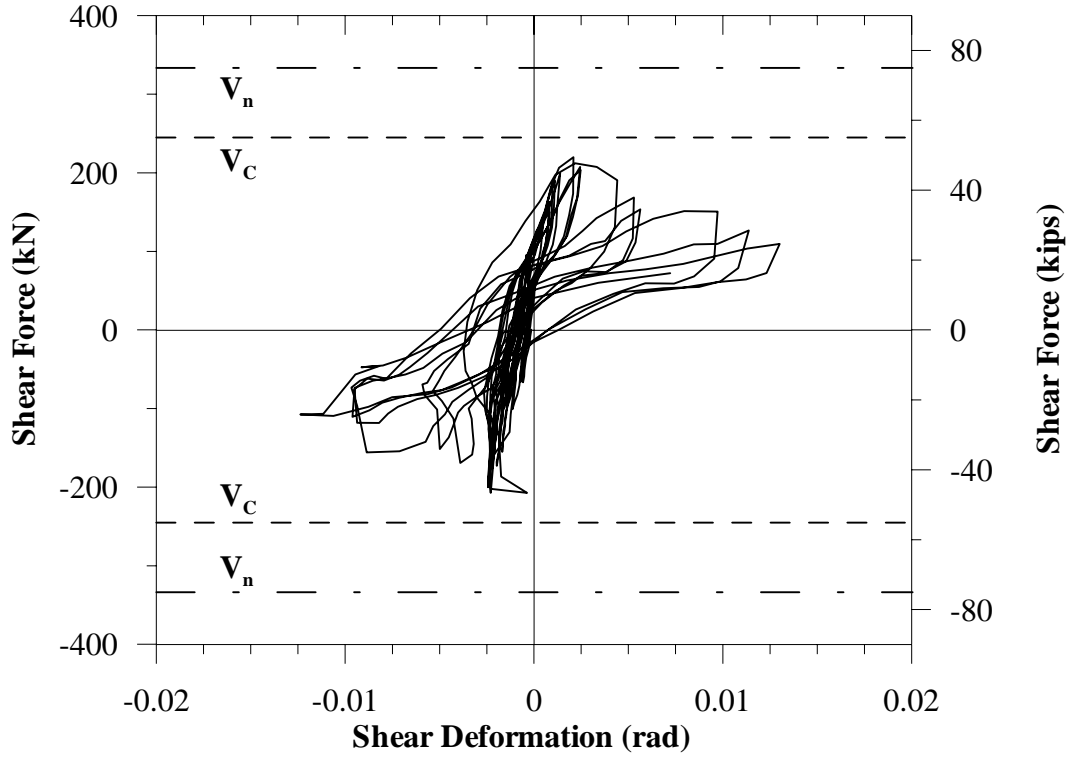


Figure 3.98 – S20MI Shear Deformation along Splice Length (20d_b)

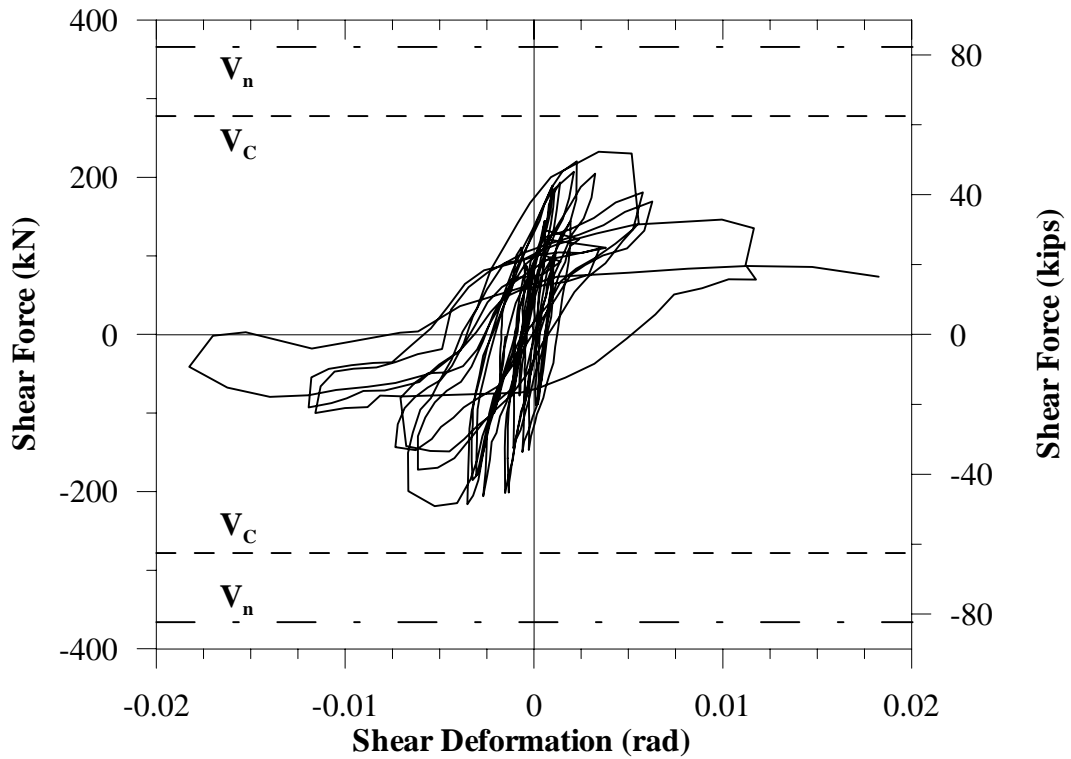
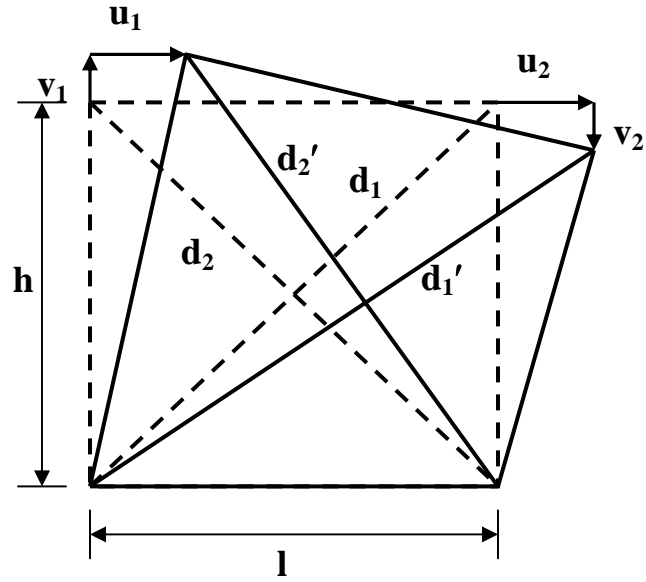


Figure 3.99 – S30MI Shear Deformation along Splice Length (20d_b)



$$d_1' = \sqrt{(h - v_2)^2 + (l + u_2)^2}$$

$$d_2' = \sqrt{(h + v_1)^2 + (l - u_1)^2}$$

$$\gamma_{avg} = \frac{(d_1' - d_1) \cdot d_1 - (d_2' - d_2) \cdot d_2}{2 \cdot h \cdot l}$$

d_1, d_2 = undeformed dimensions of two wire potentiometers

d_1', d_2' = deformed dimensions of two wire potentiometers

h = height of 'X' configuration

l = length of 'X' configuration

Figure 3.100 - Shear Deformation Measurement (S20HI, S20HIN, and S30XI)

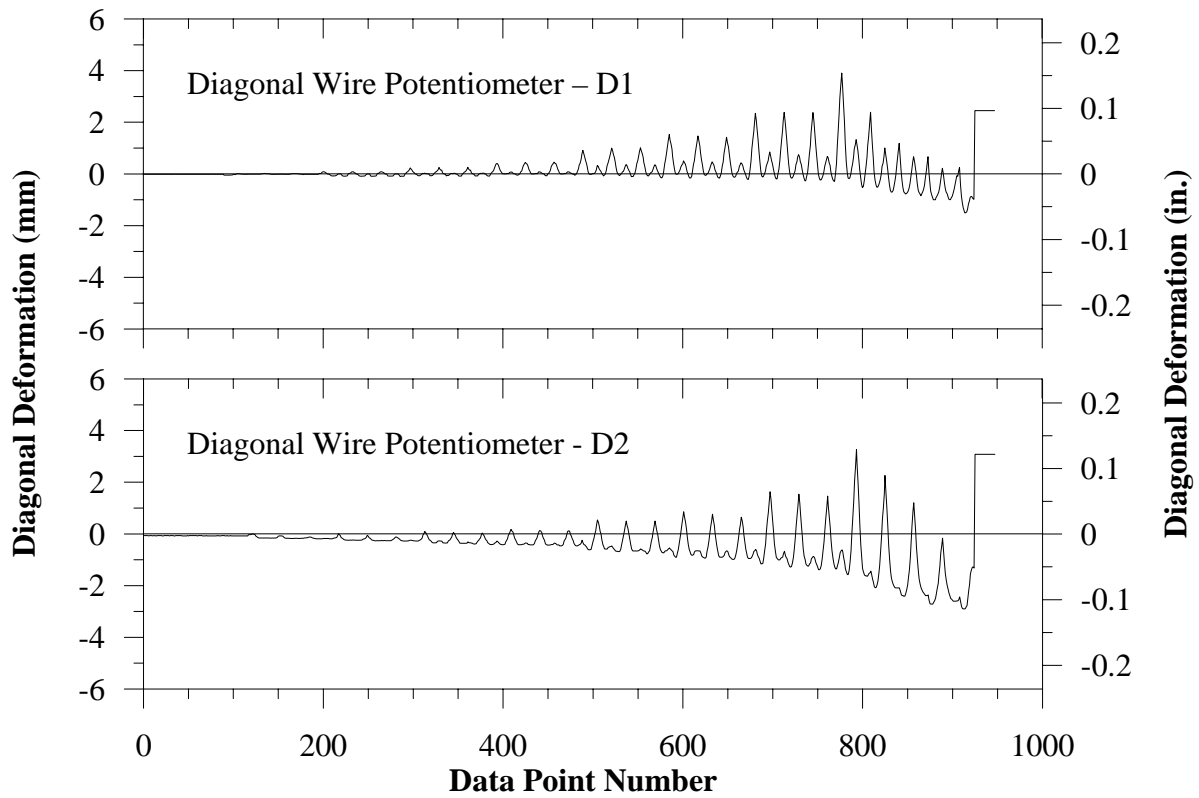
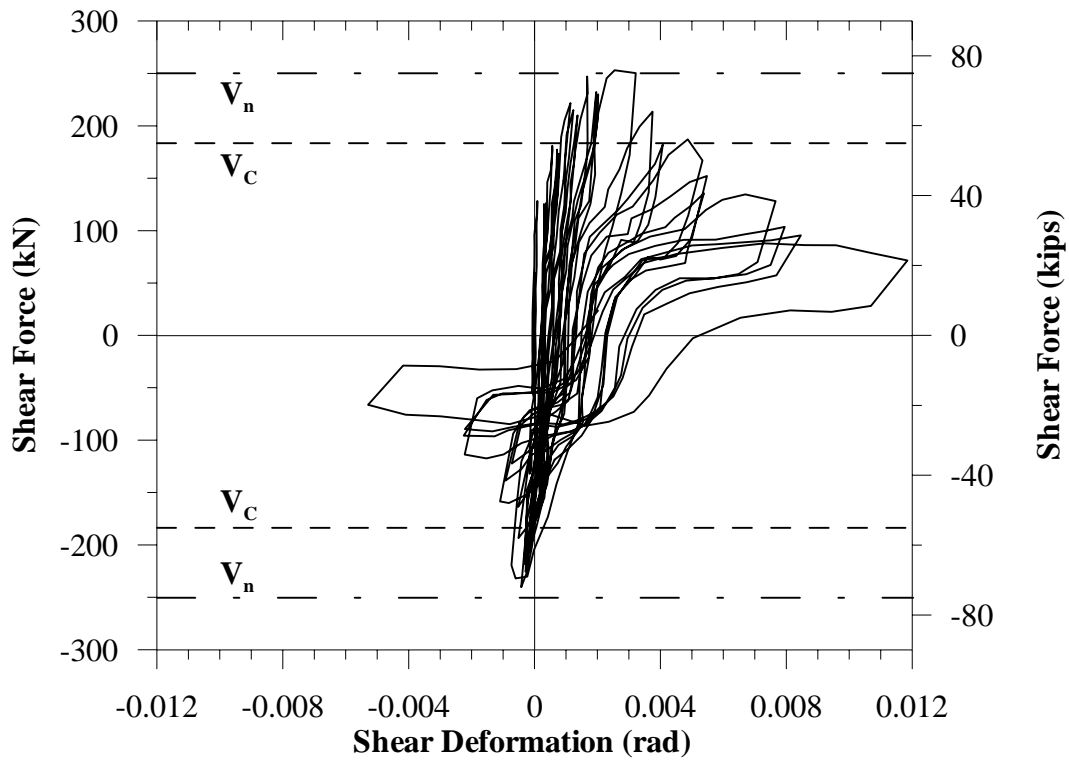


Figure 3.101 - S20HI Shear Deformation along Splice Length ($20d_b$)

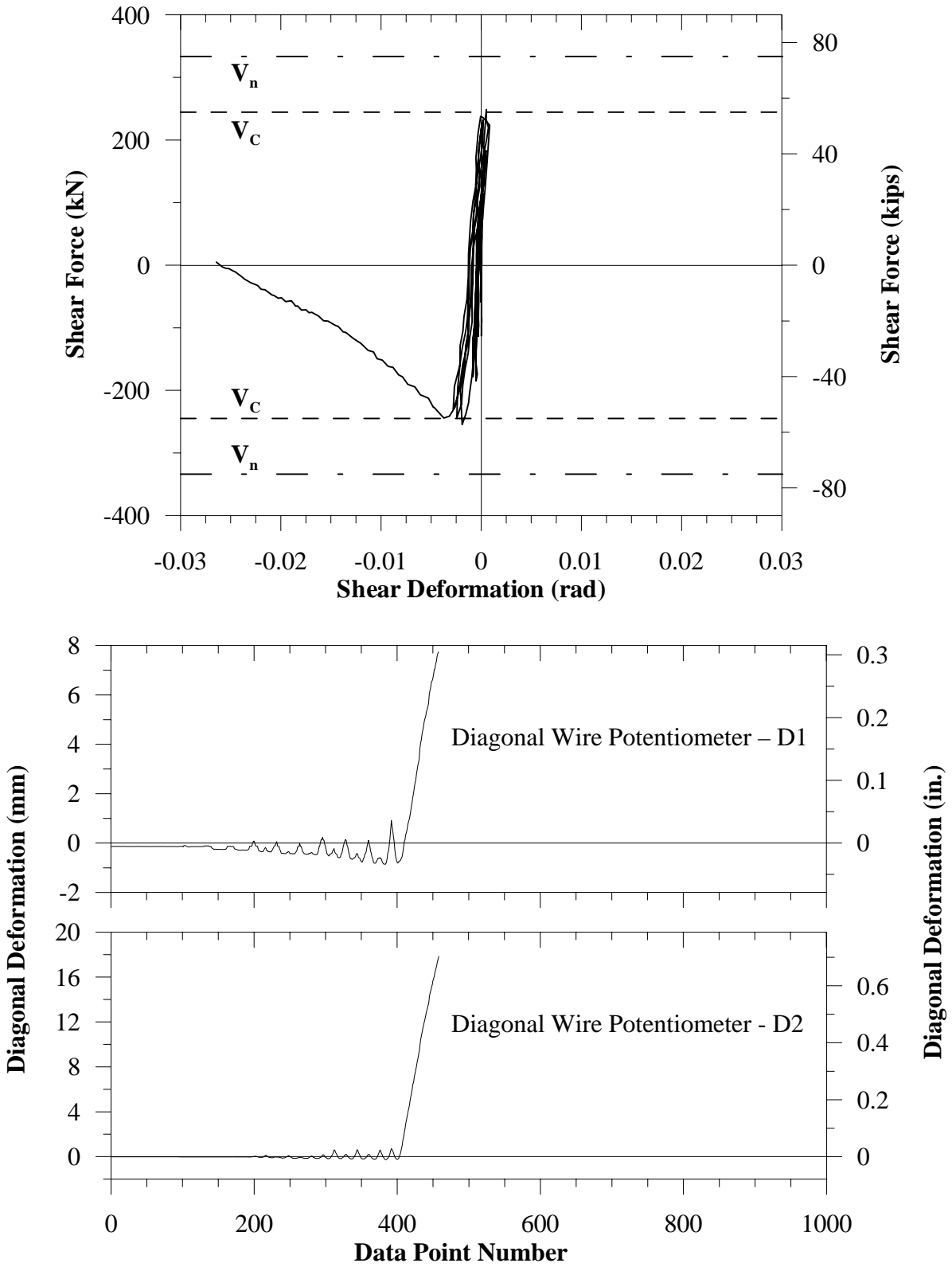


Figure 3.102 - S20HIN Shear Deformation along Splice Length ($20d_b$)

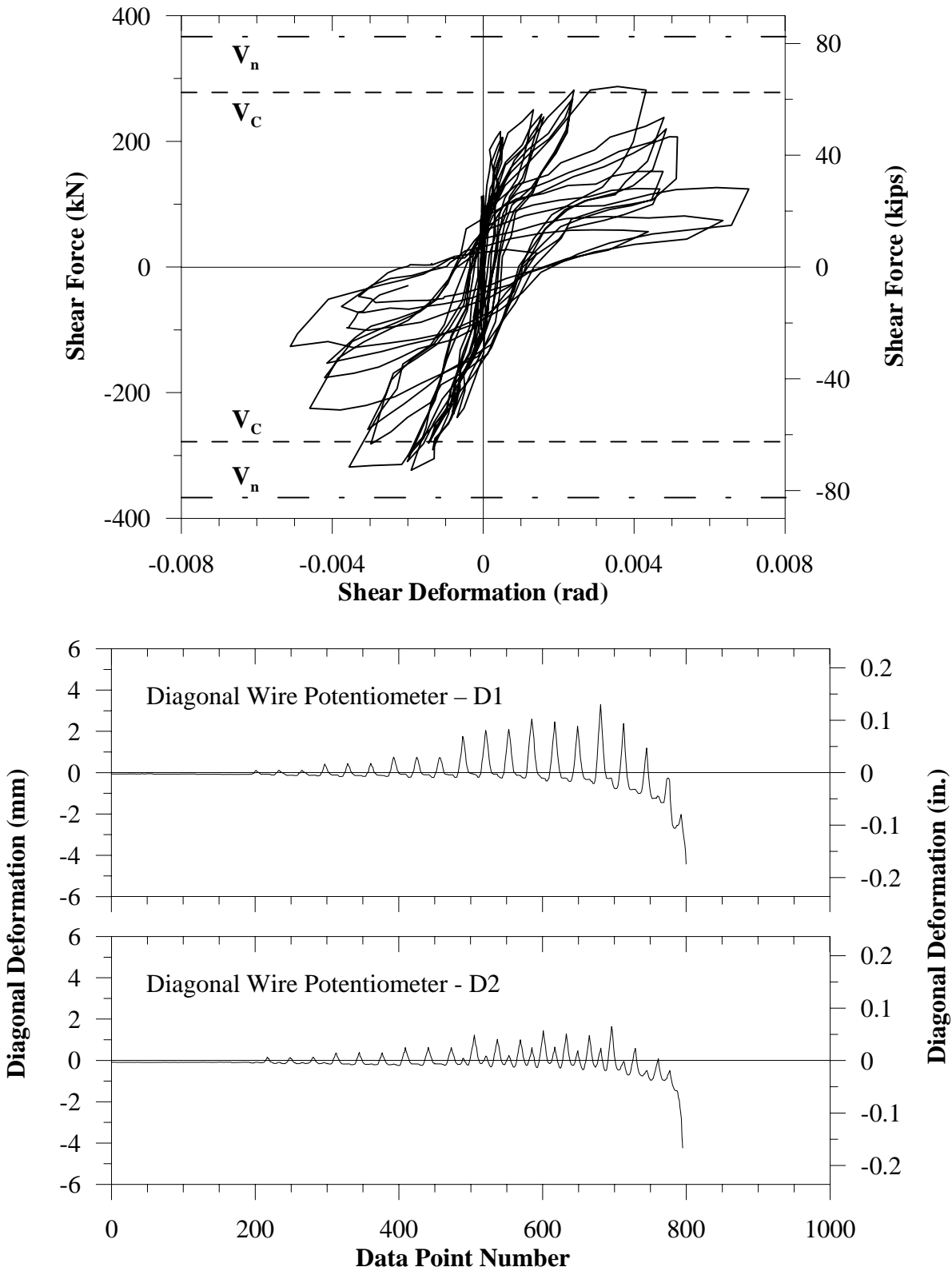
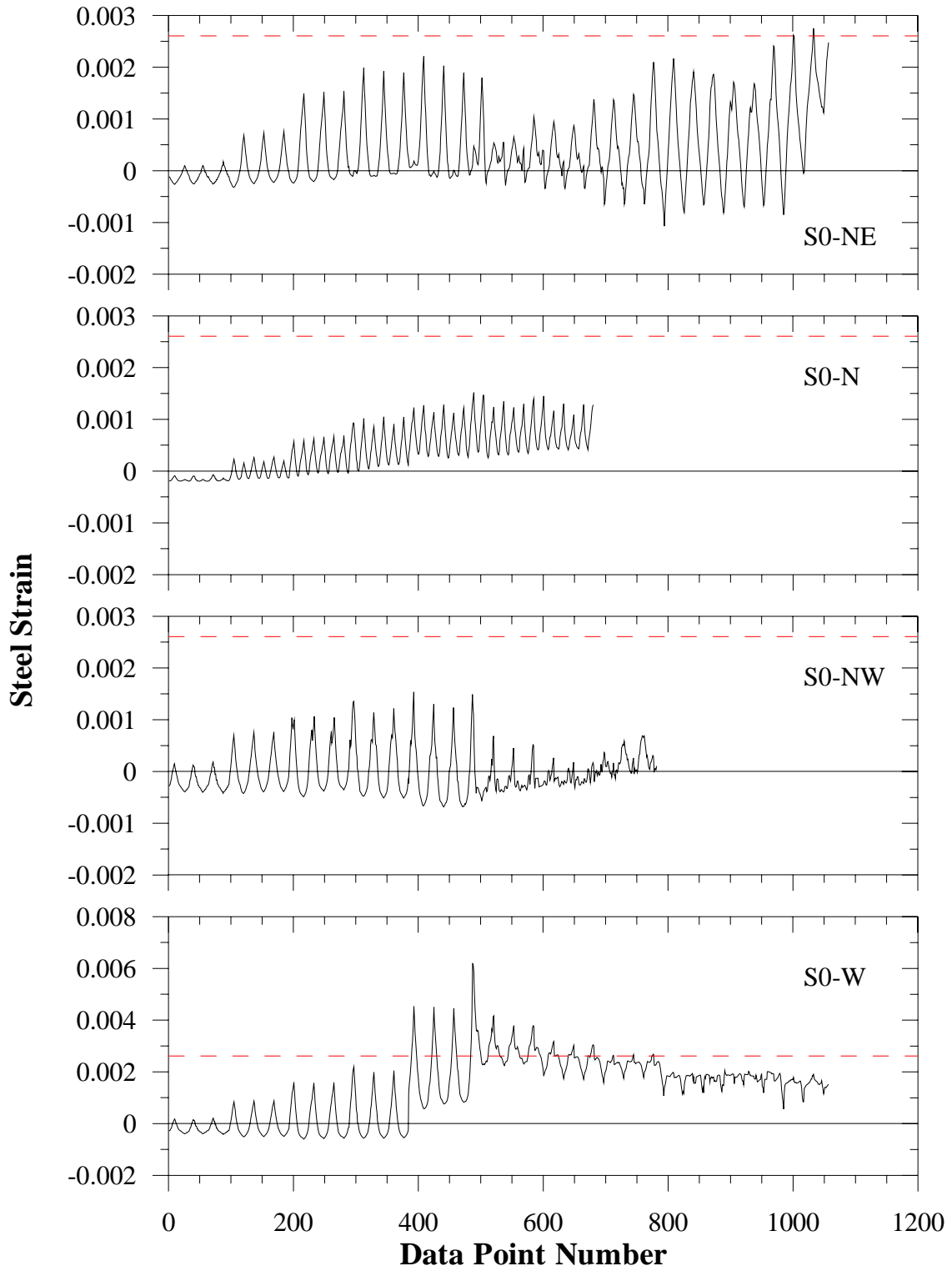
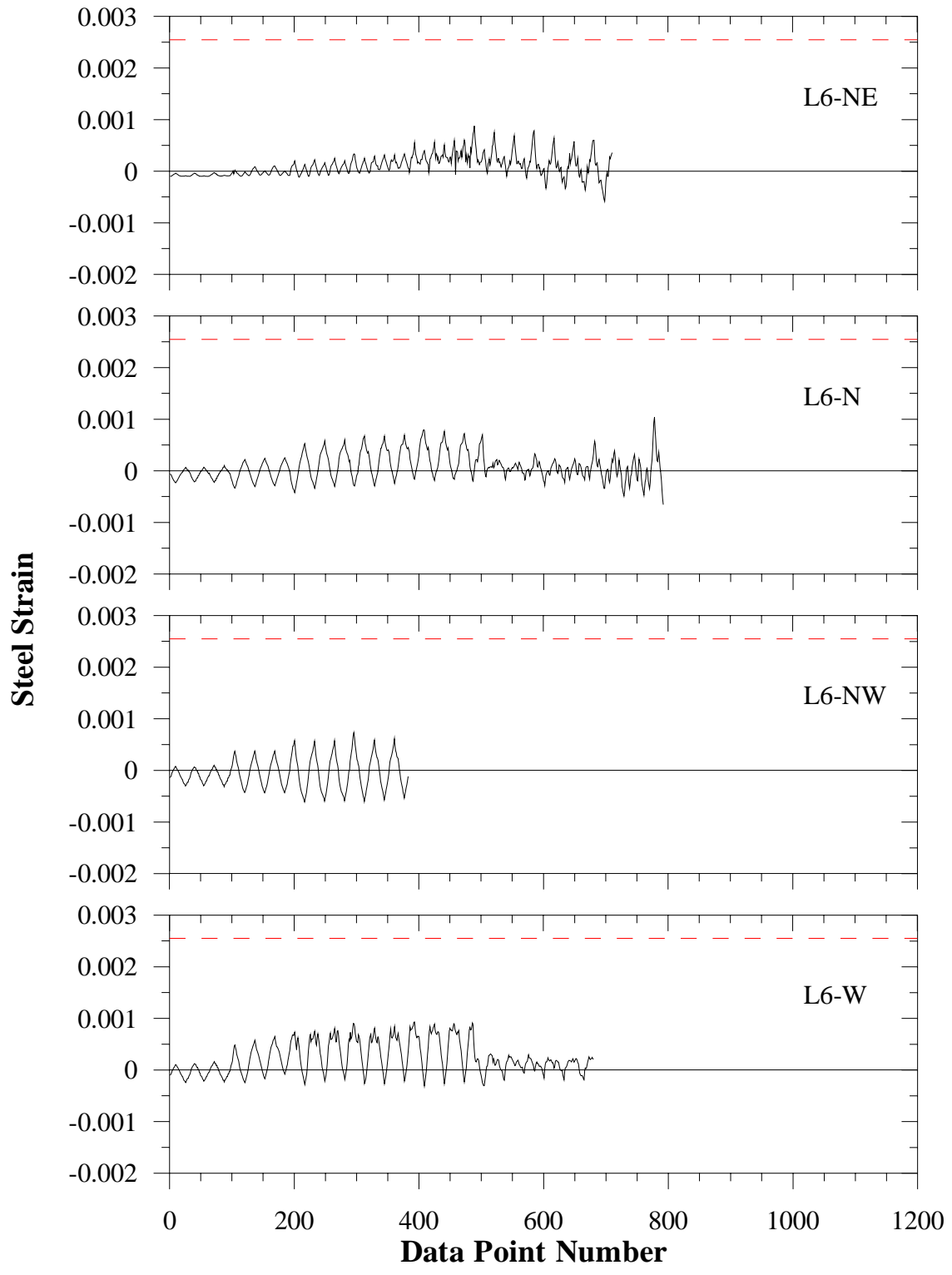


Figure 3.103 - S30XI Shear Deformation along Splice Length ($20d_b$)

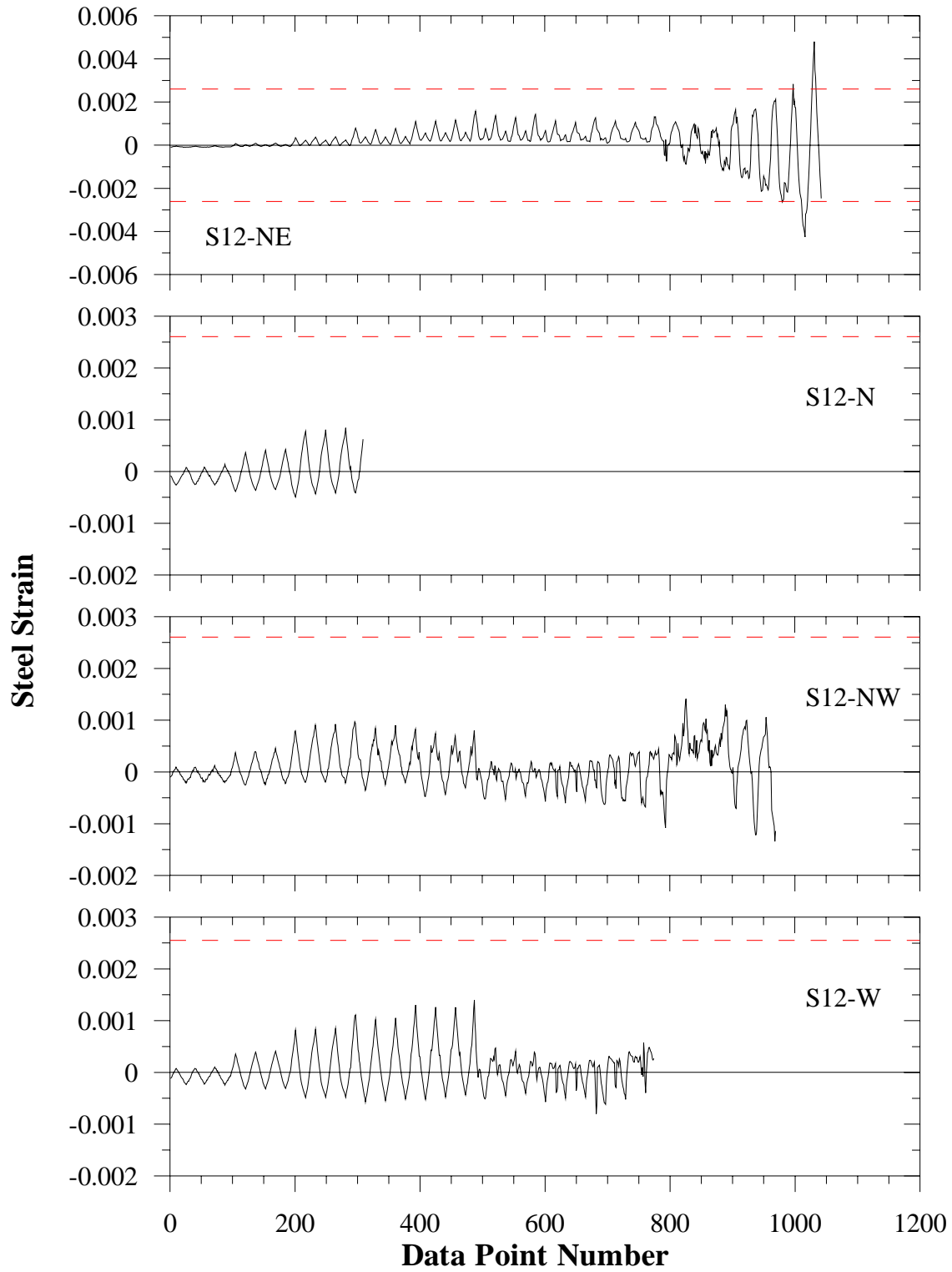
Appendix: Strain Histories



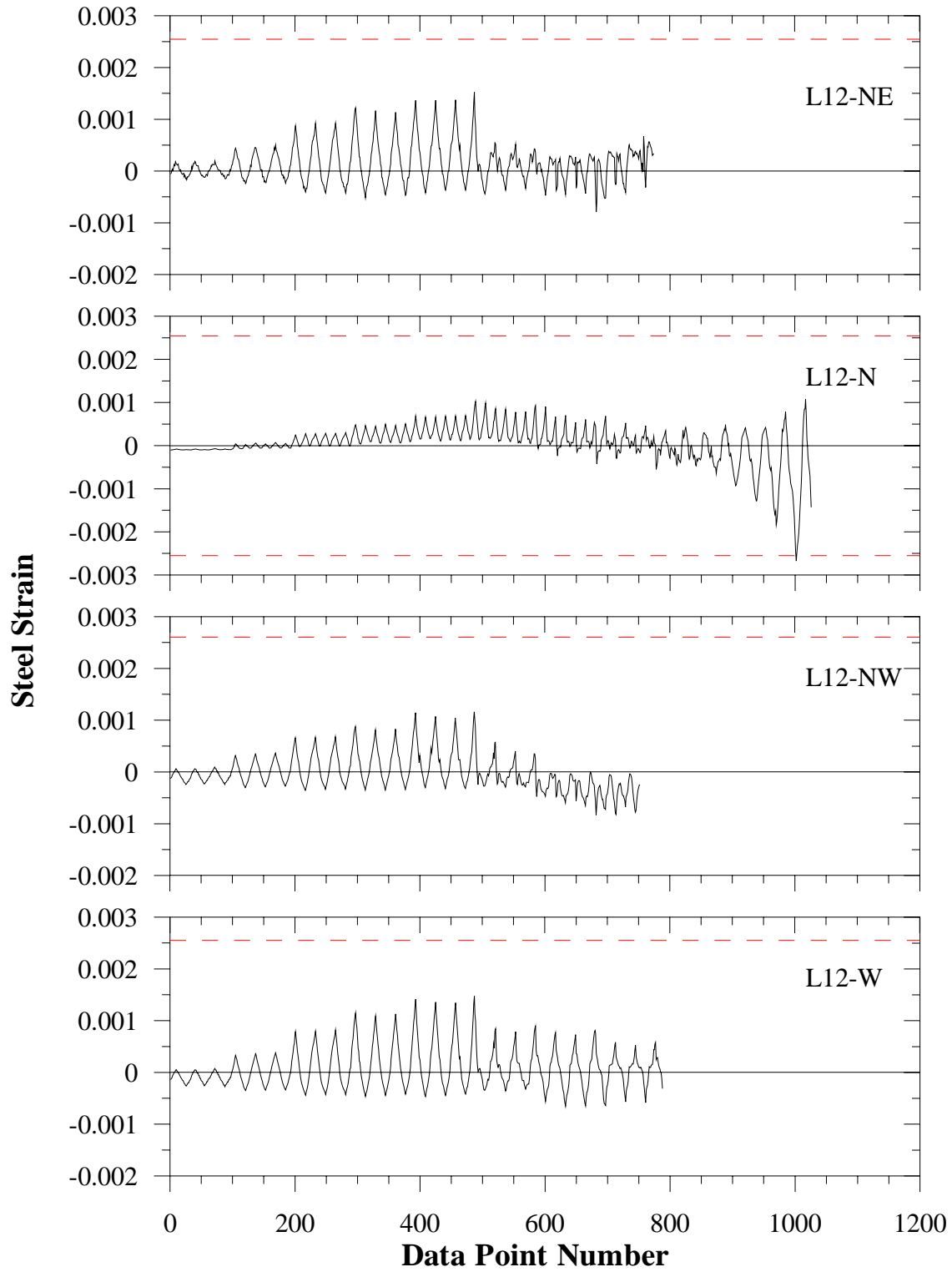
S10MI Longitudinal Steel Strain Histories



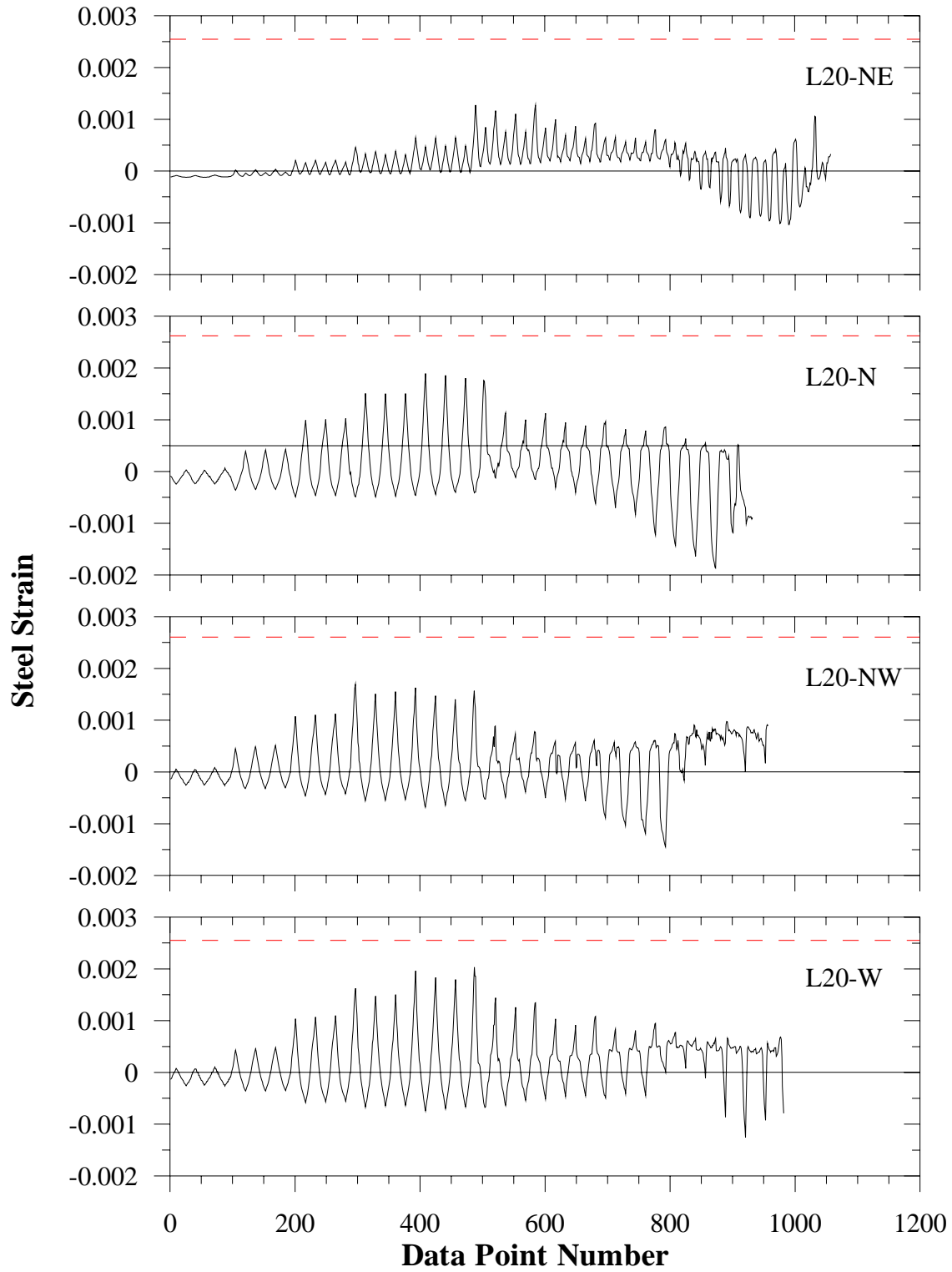
S10MI Longitudinal Steel Strain Histories



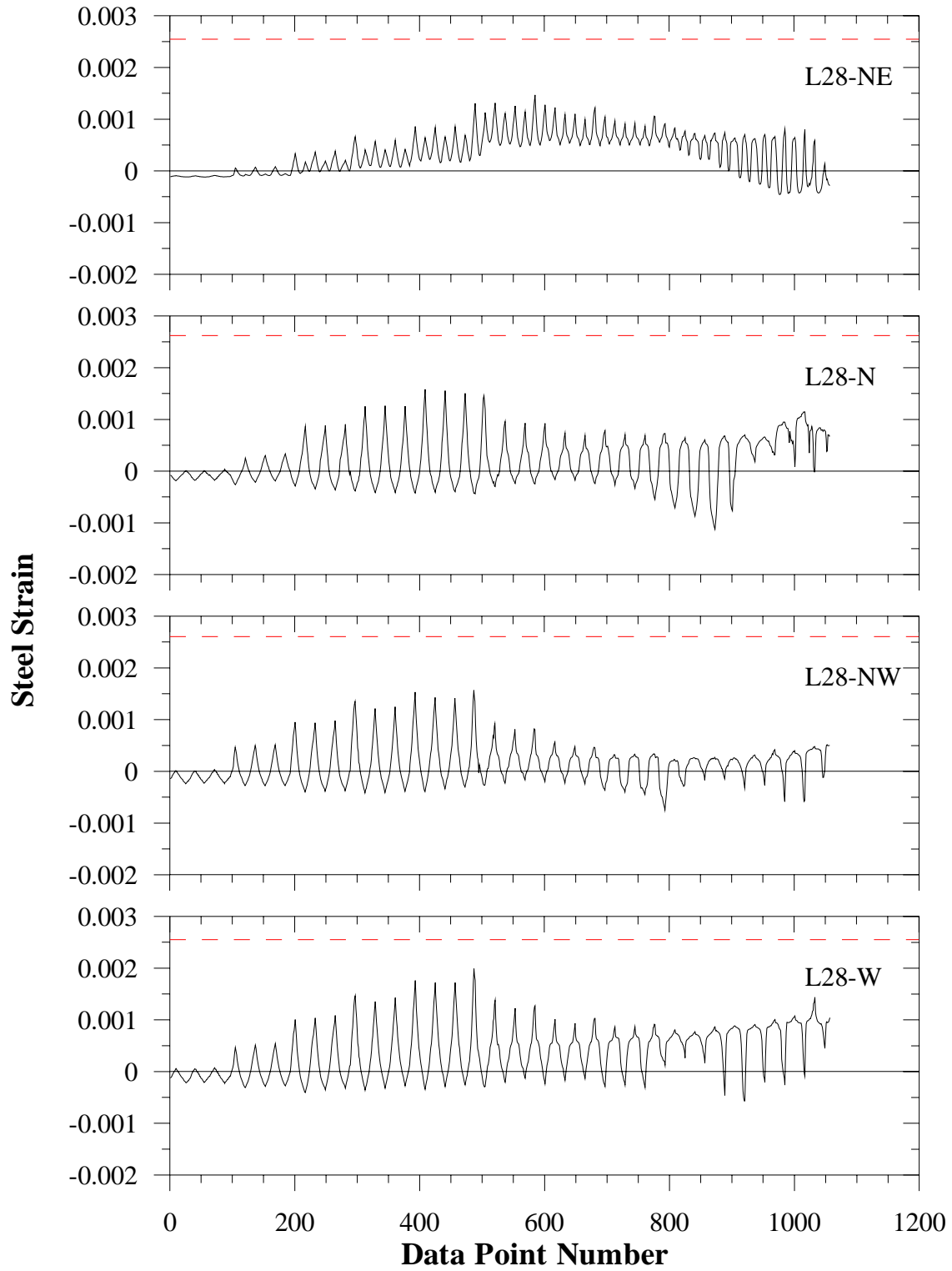
S10MI Longitudinal Steel Strain Histories



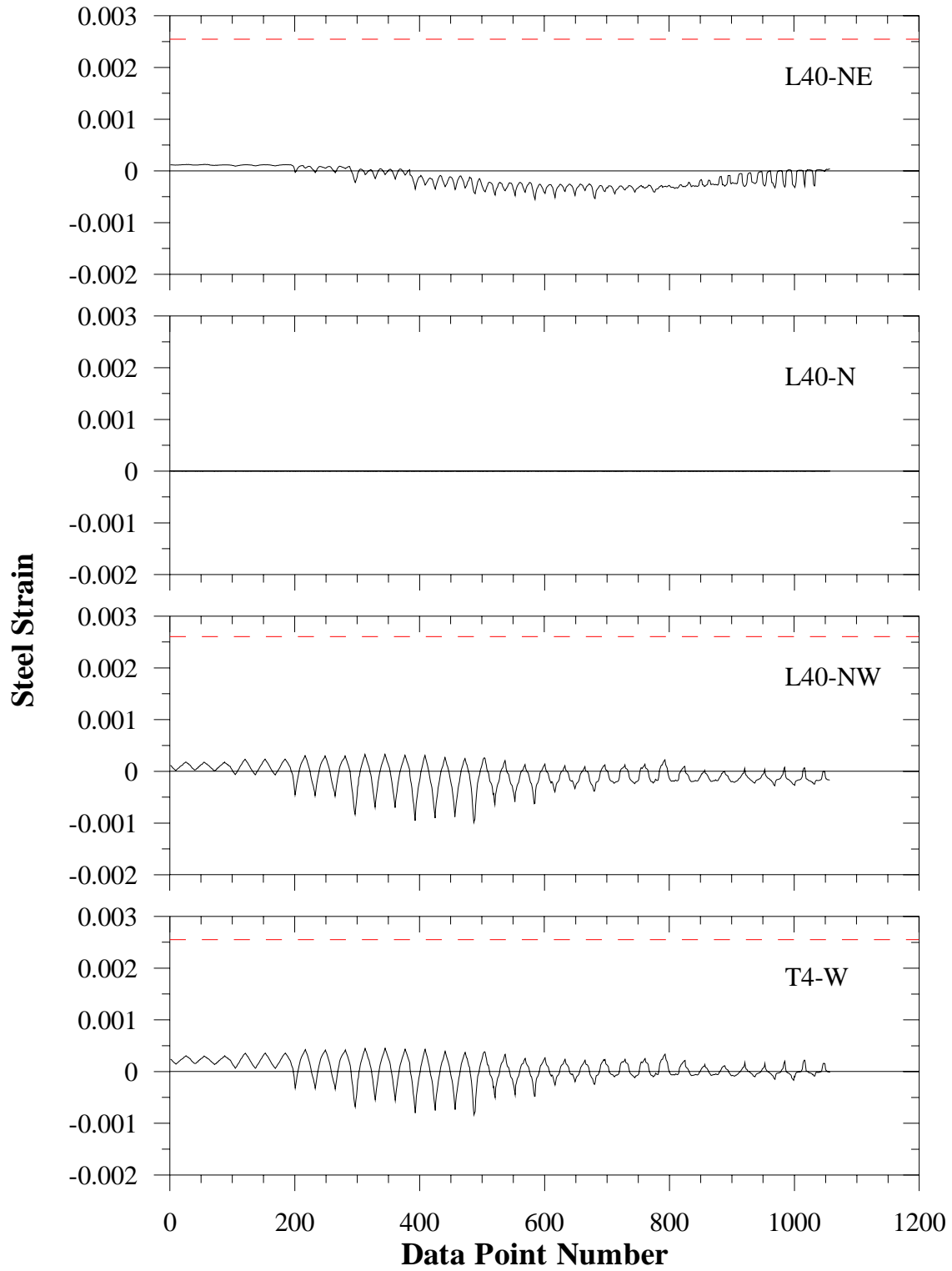
S10MI Longitudinal Steel Strain Histories



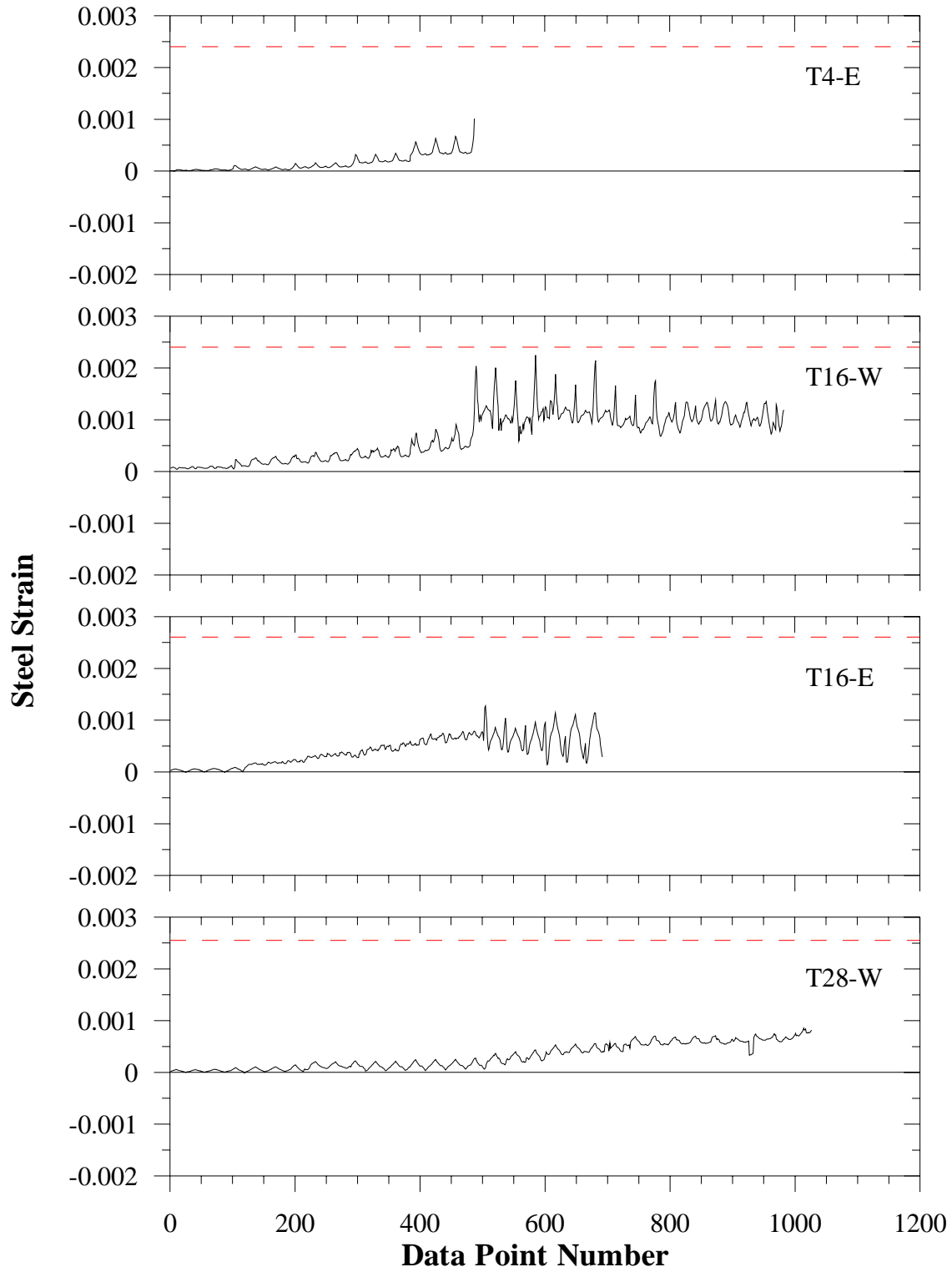
S10MI Longitudinal Steel Strain Histories



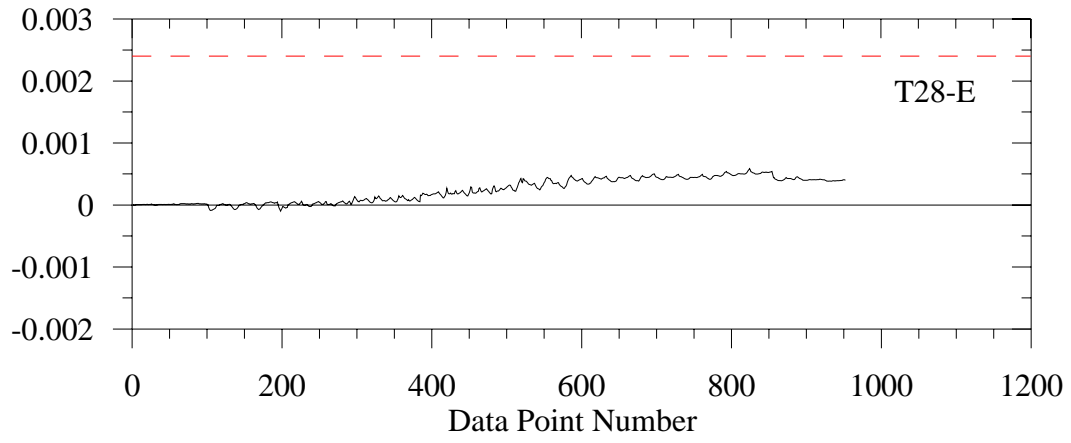
S10MI Longitudinal Steel Strain Histories



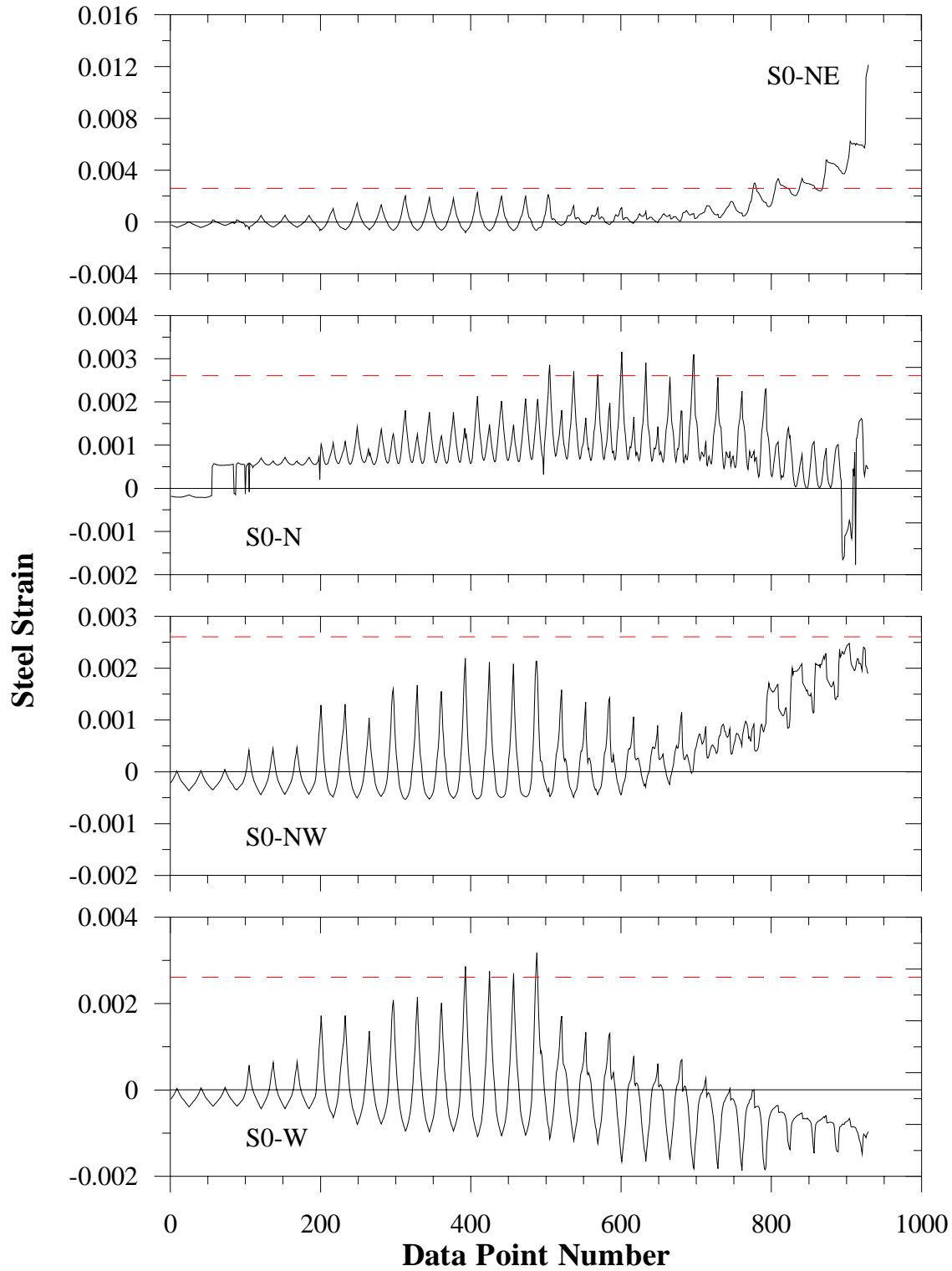
S10MI Longitudinal Steel Strain Histories



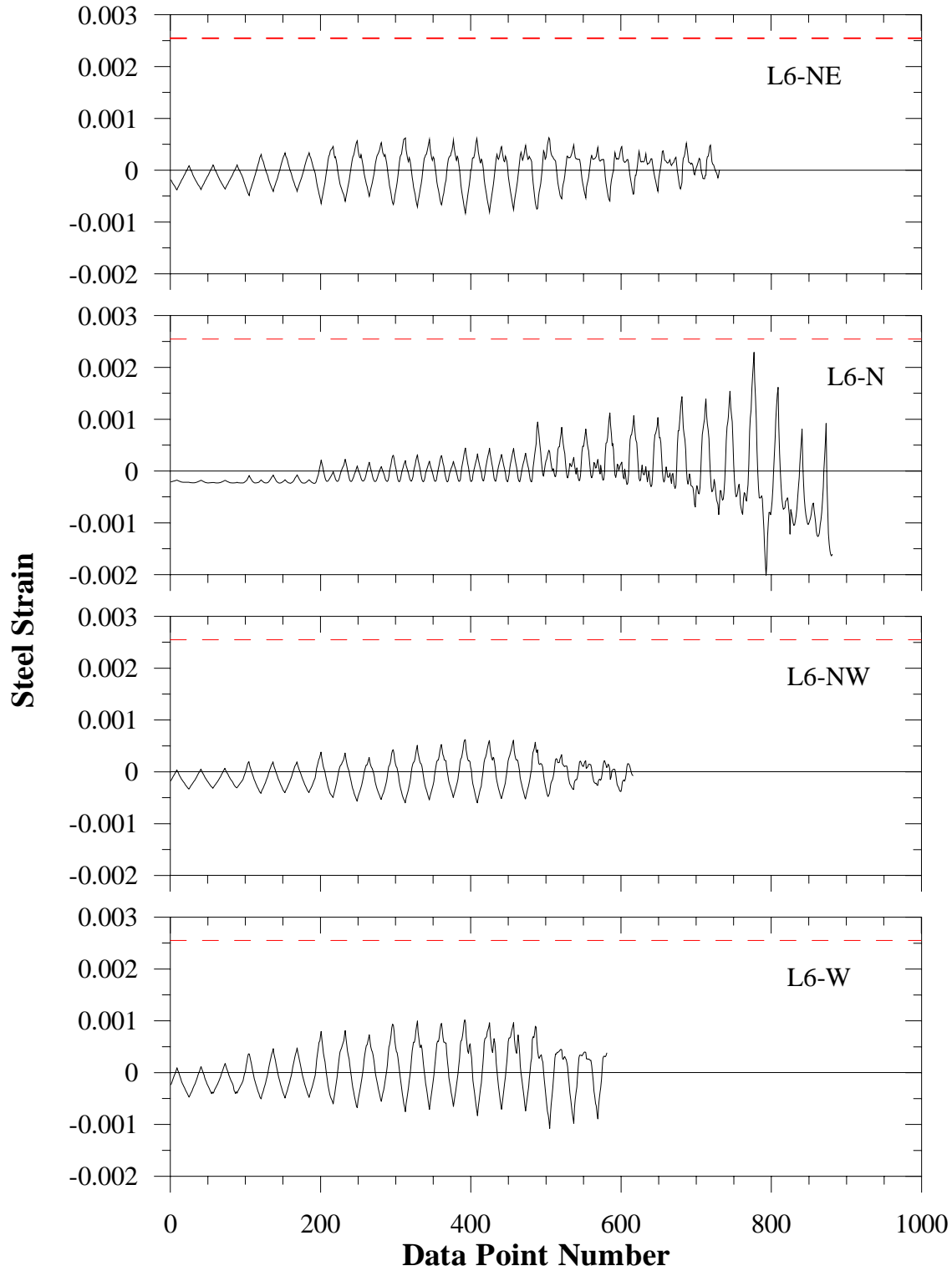
S10MI Longitudinal Steel Strain Histories



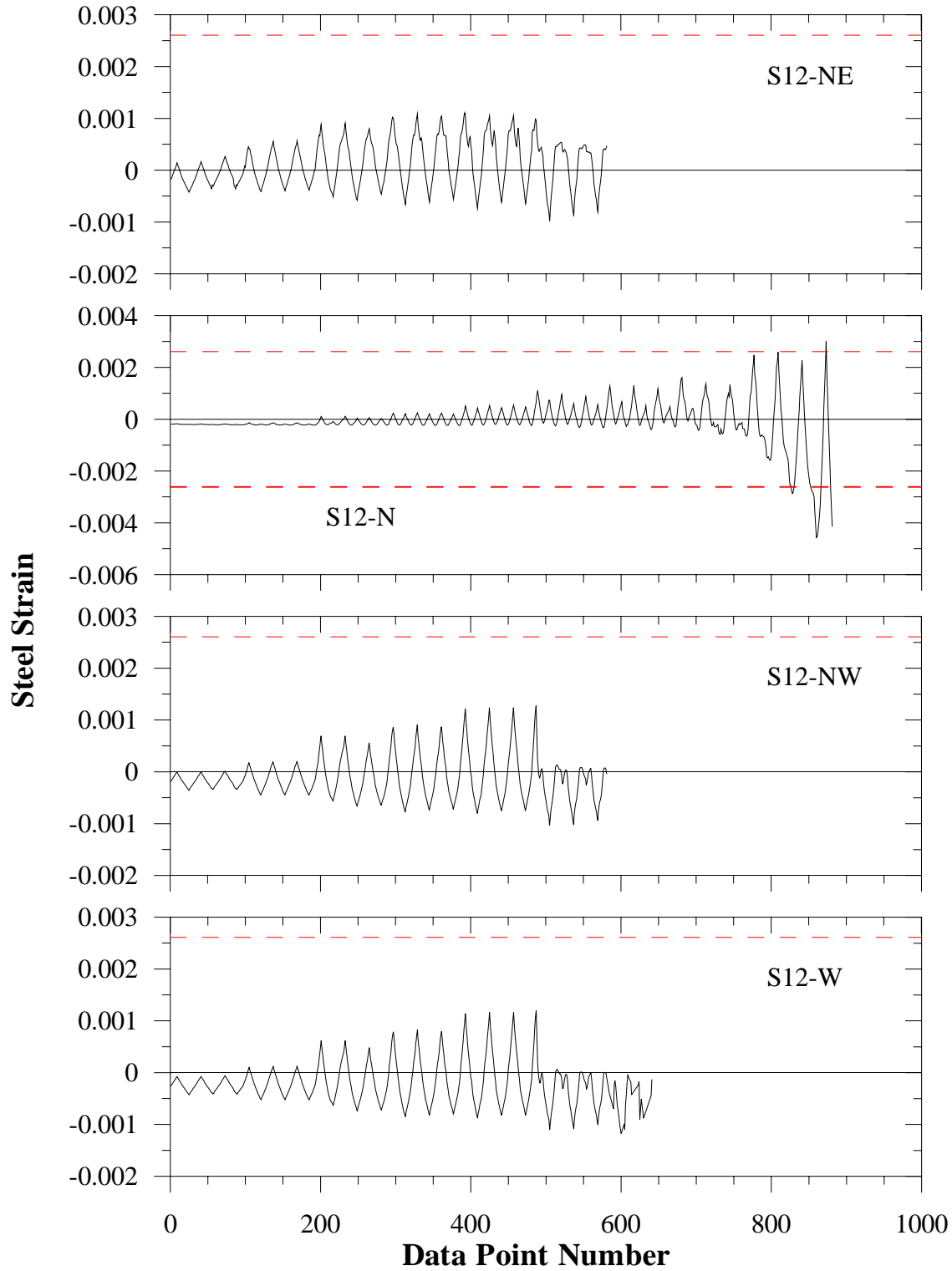
S10MI Longitudinal Steel Strain Histories



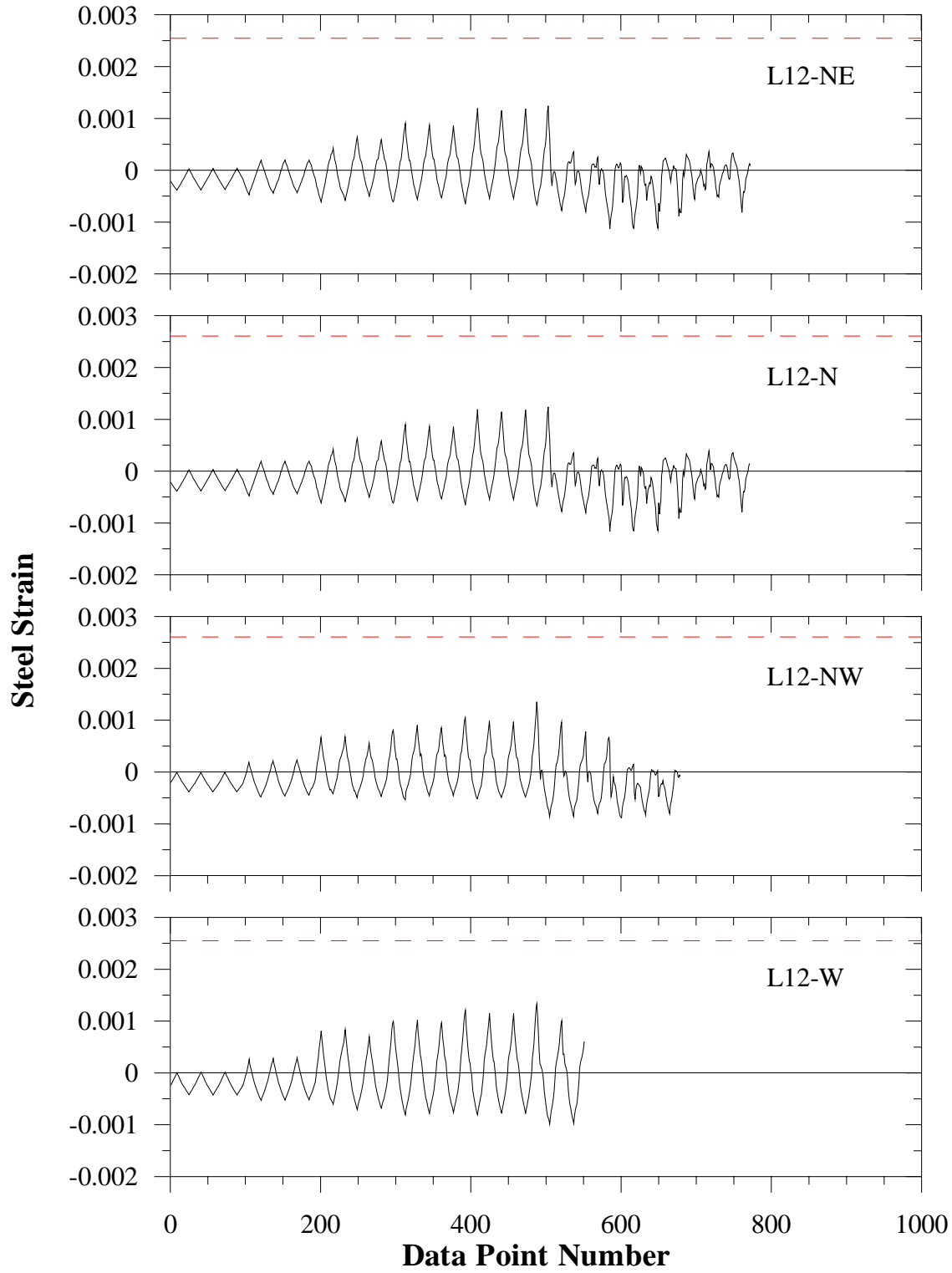
S20MI Longitudinal Steel Strain Histories



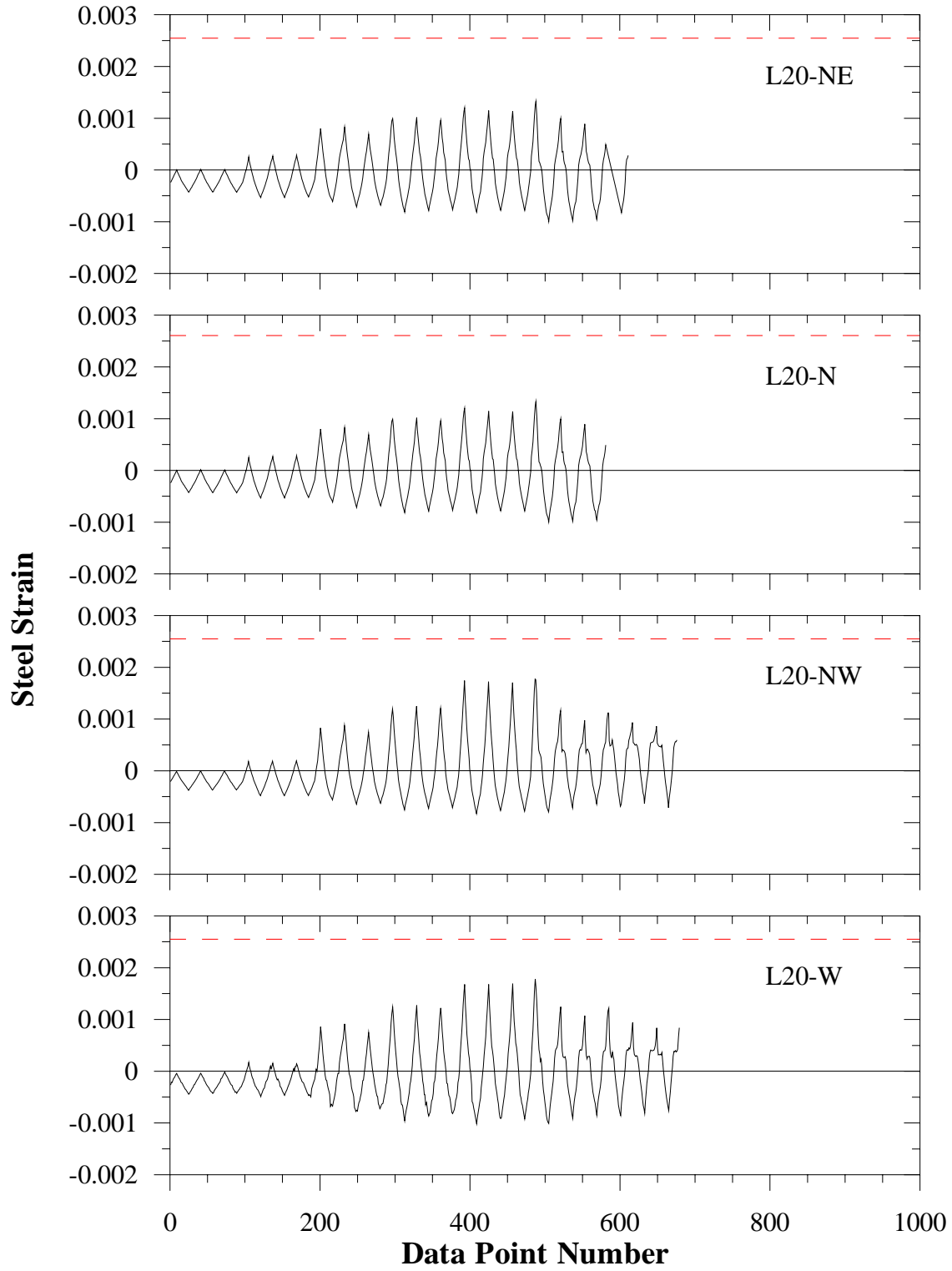
S20MI Longitudinal Steel Strain Histories



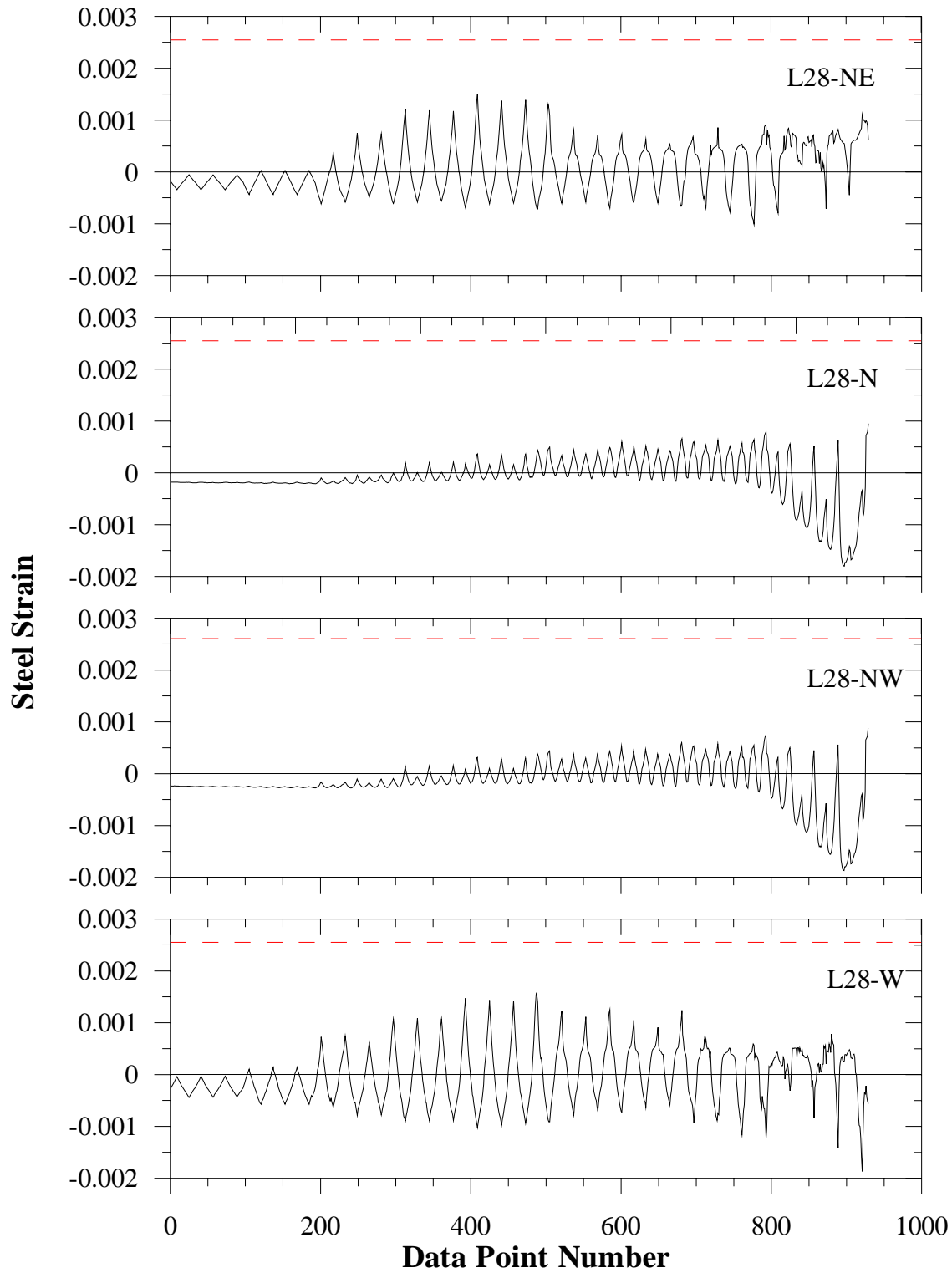
S20MI Longitudinal Steel Strain Histories



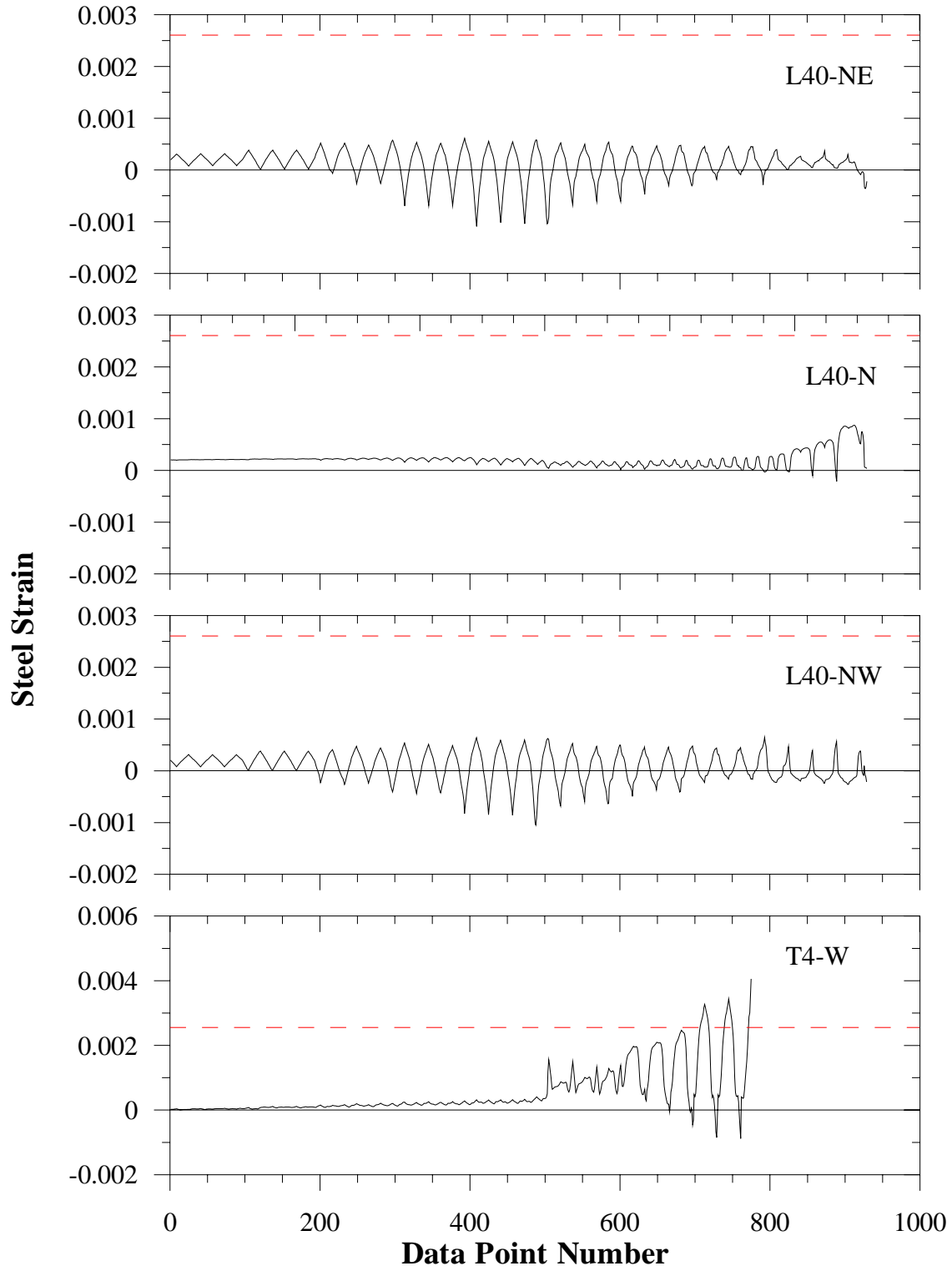
S20MI Longitudinal Steel Strain Histories



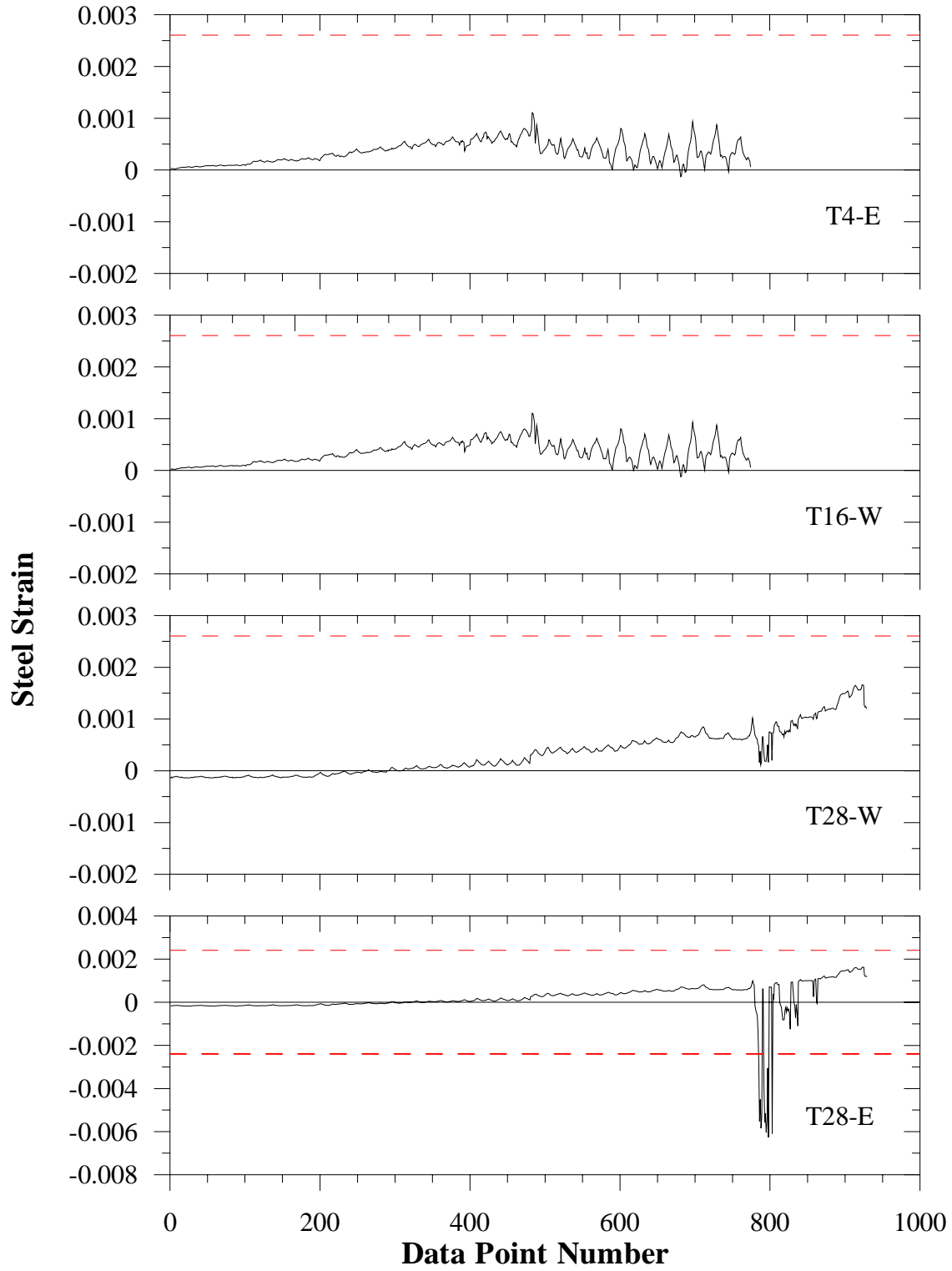
2S20MI Longitudinal Steel Strain Histories



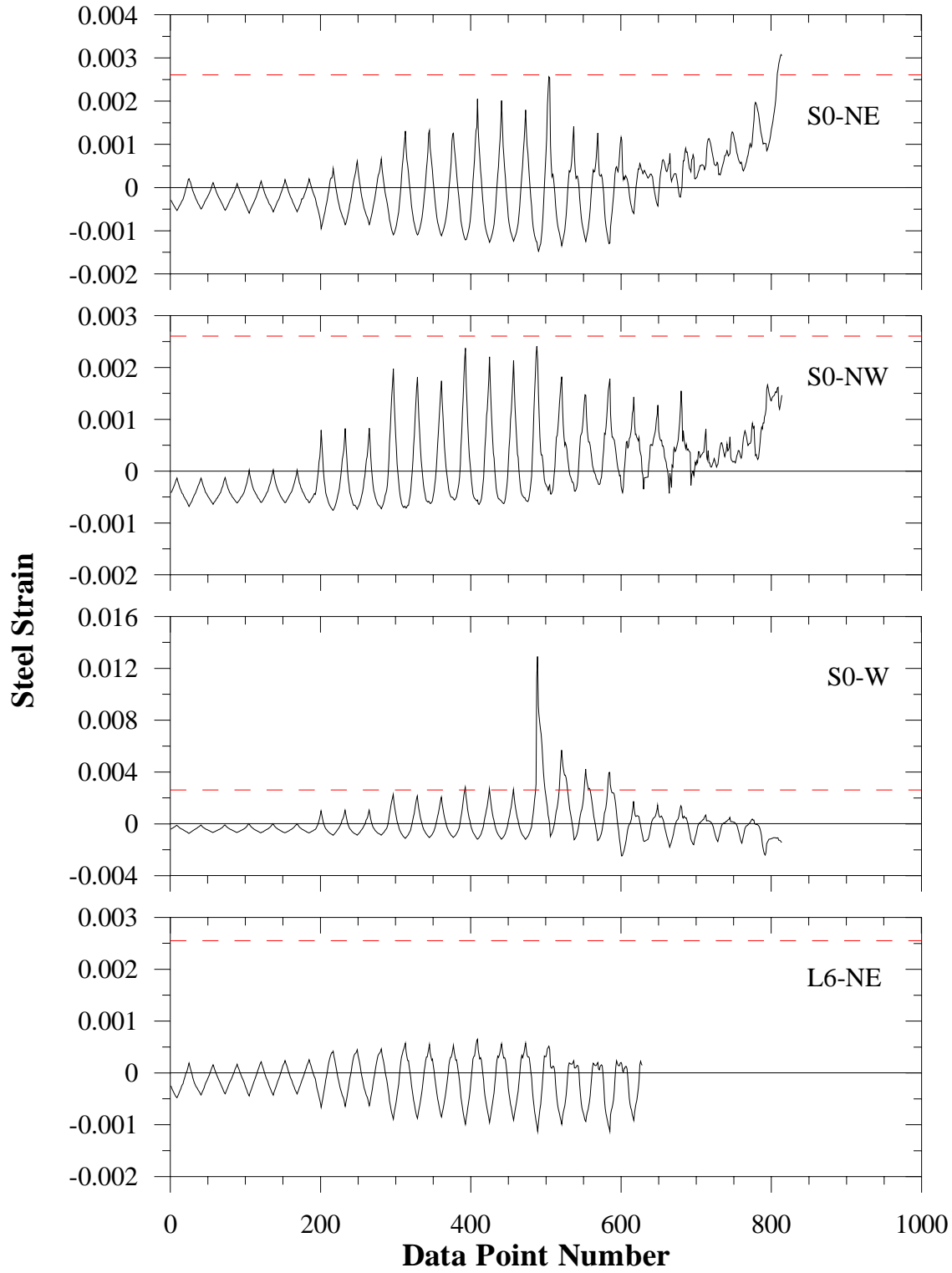
S20MI Longitudinal Steel Strain Histories



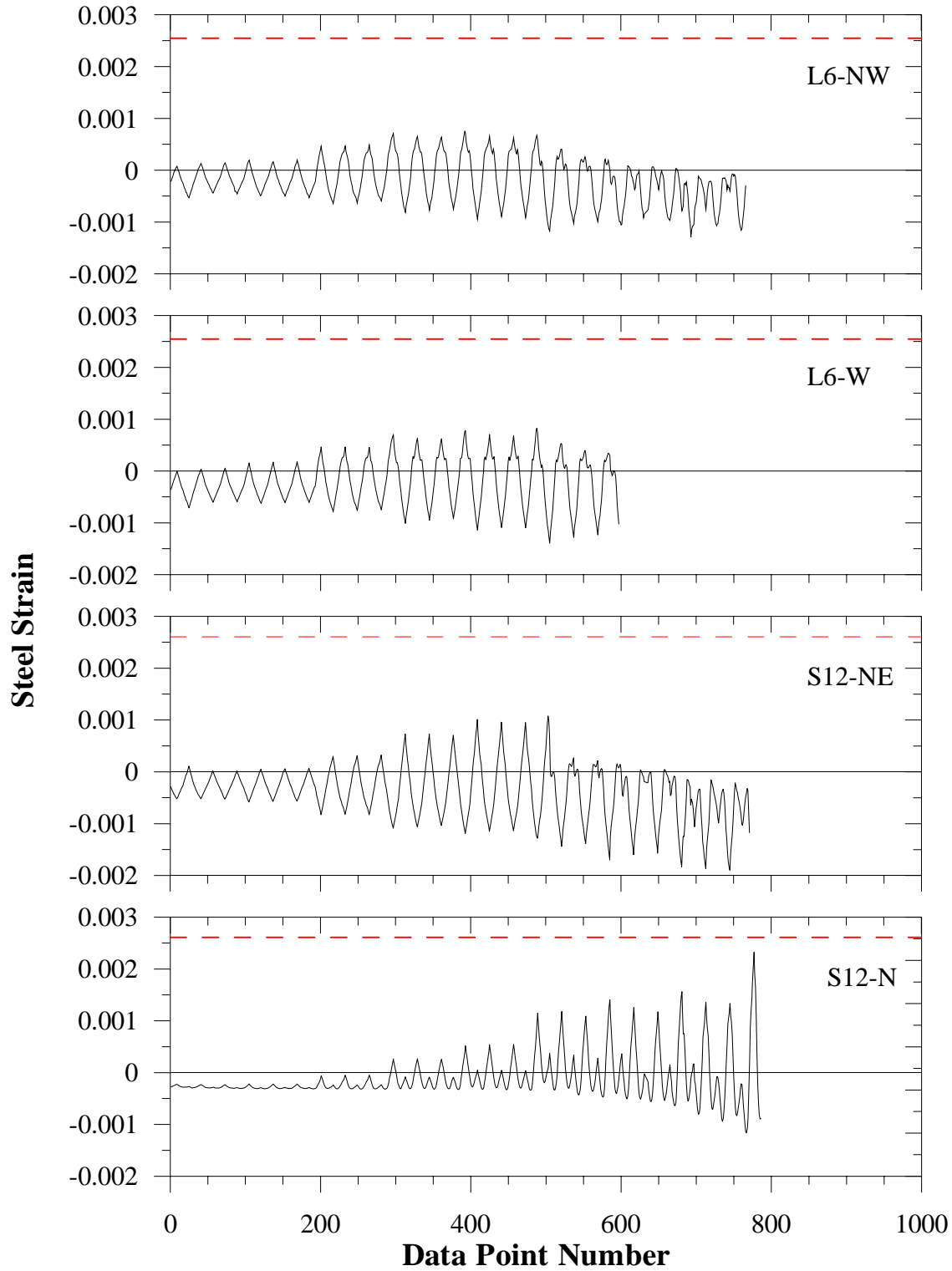
S20MI Longitudinal Steel Strain Histories



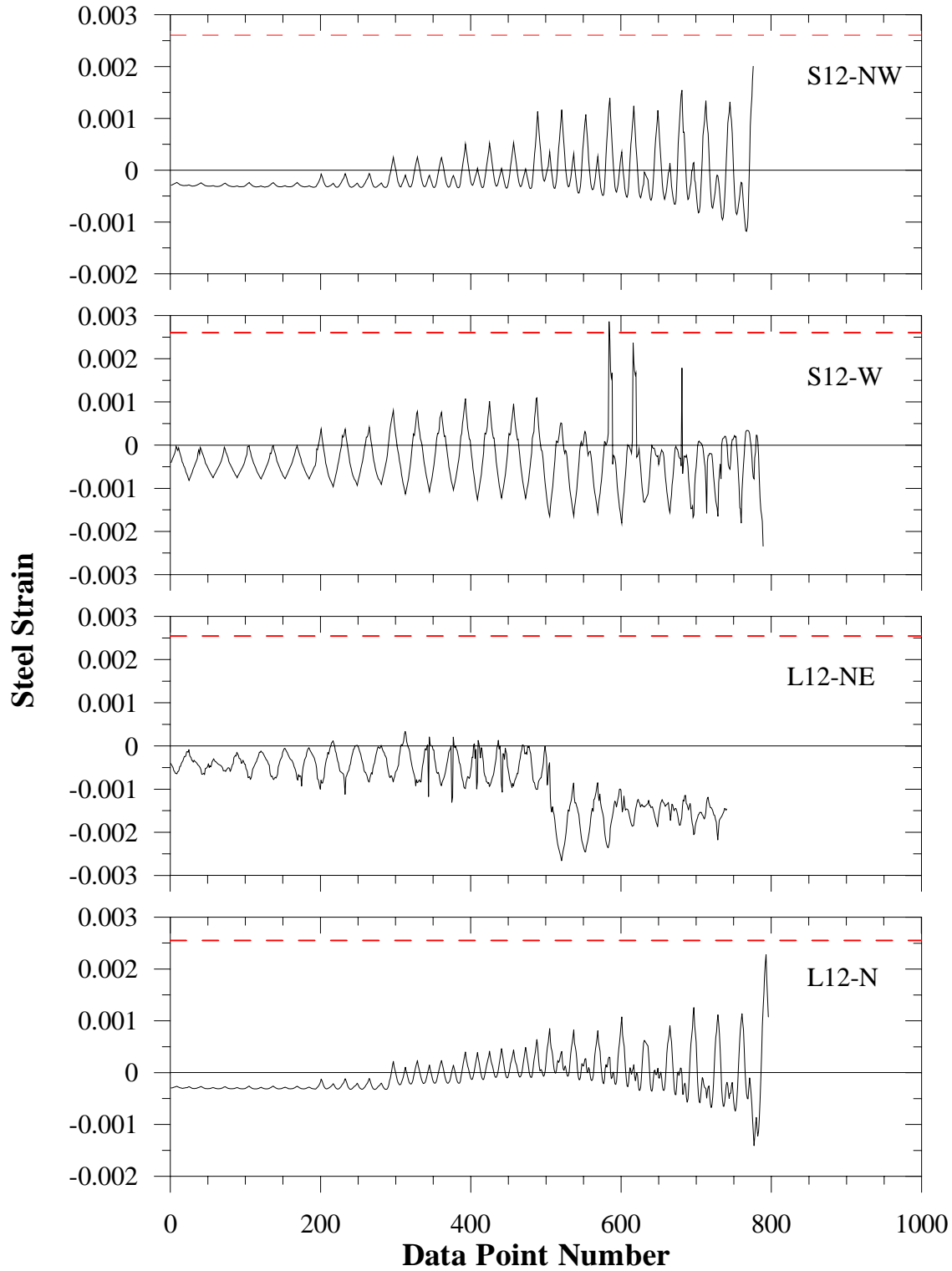
S20MI Longitudinal Steel Strain Histories



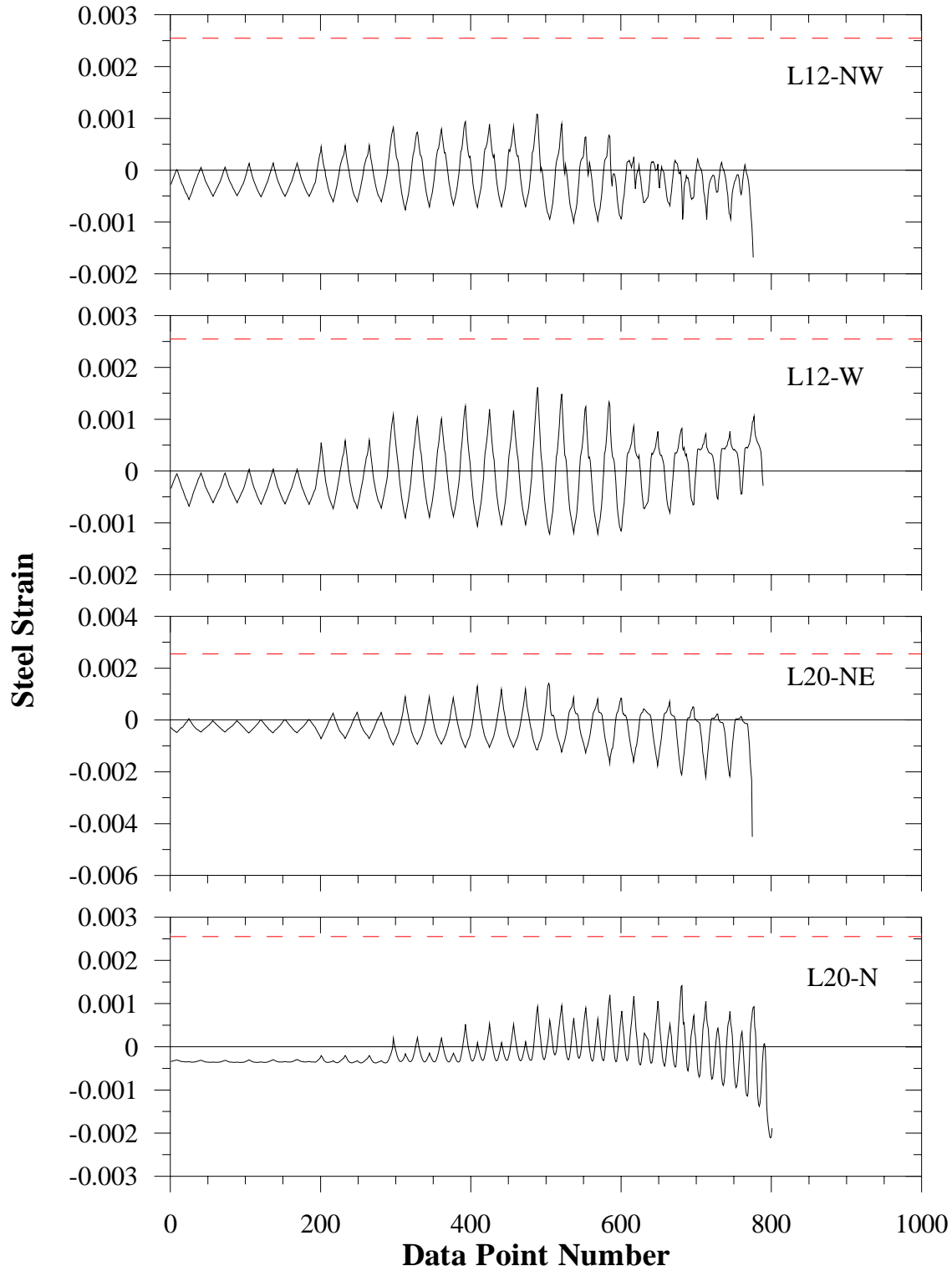
S30MI Longitudinal Steel Strain Histories



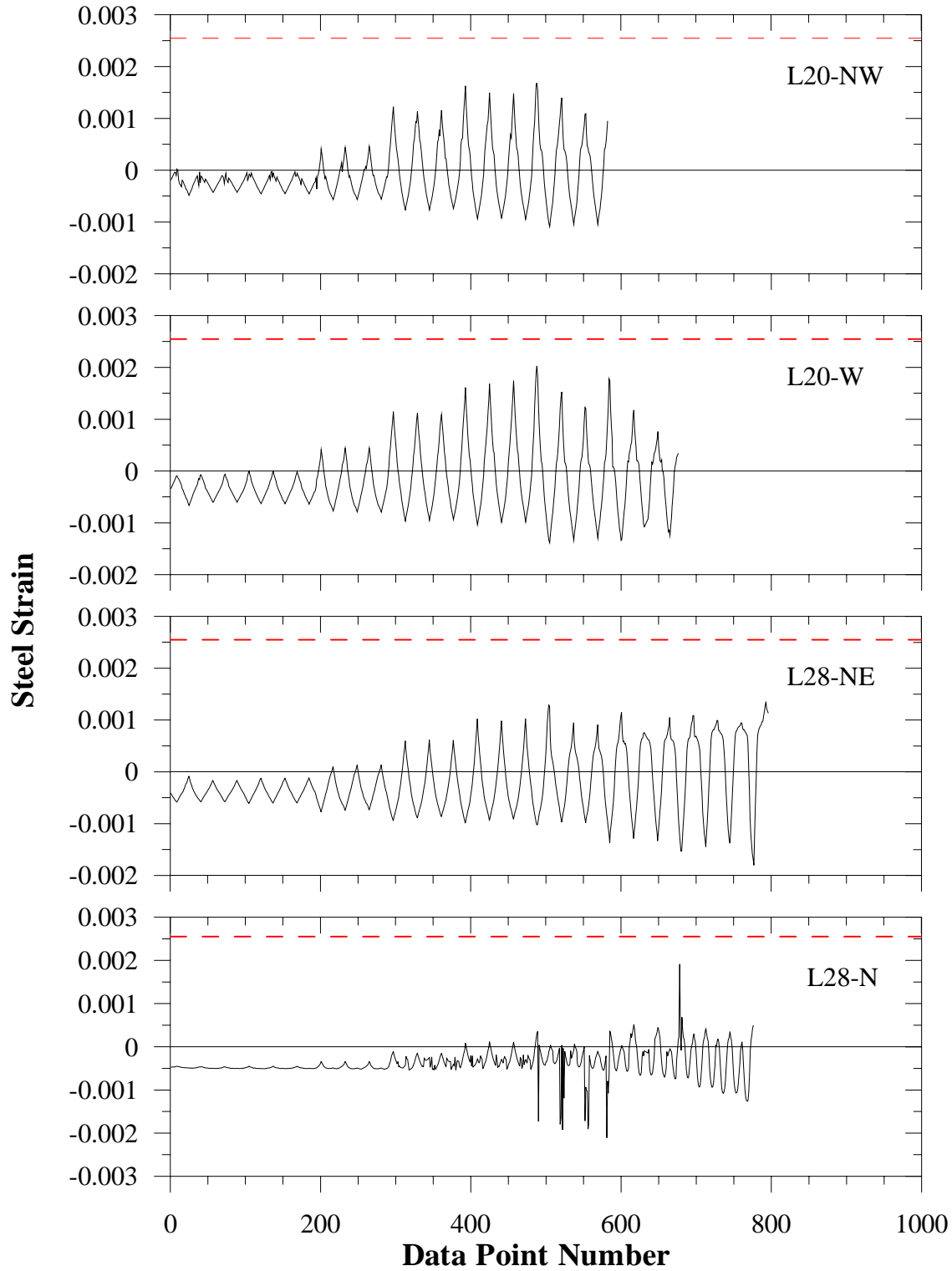
S30MI Longitudinal Steel Strain Histories



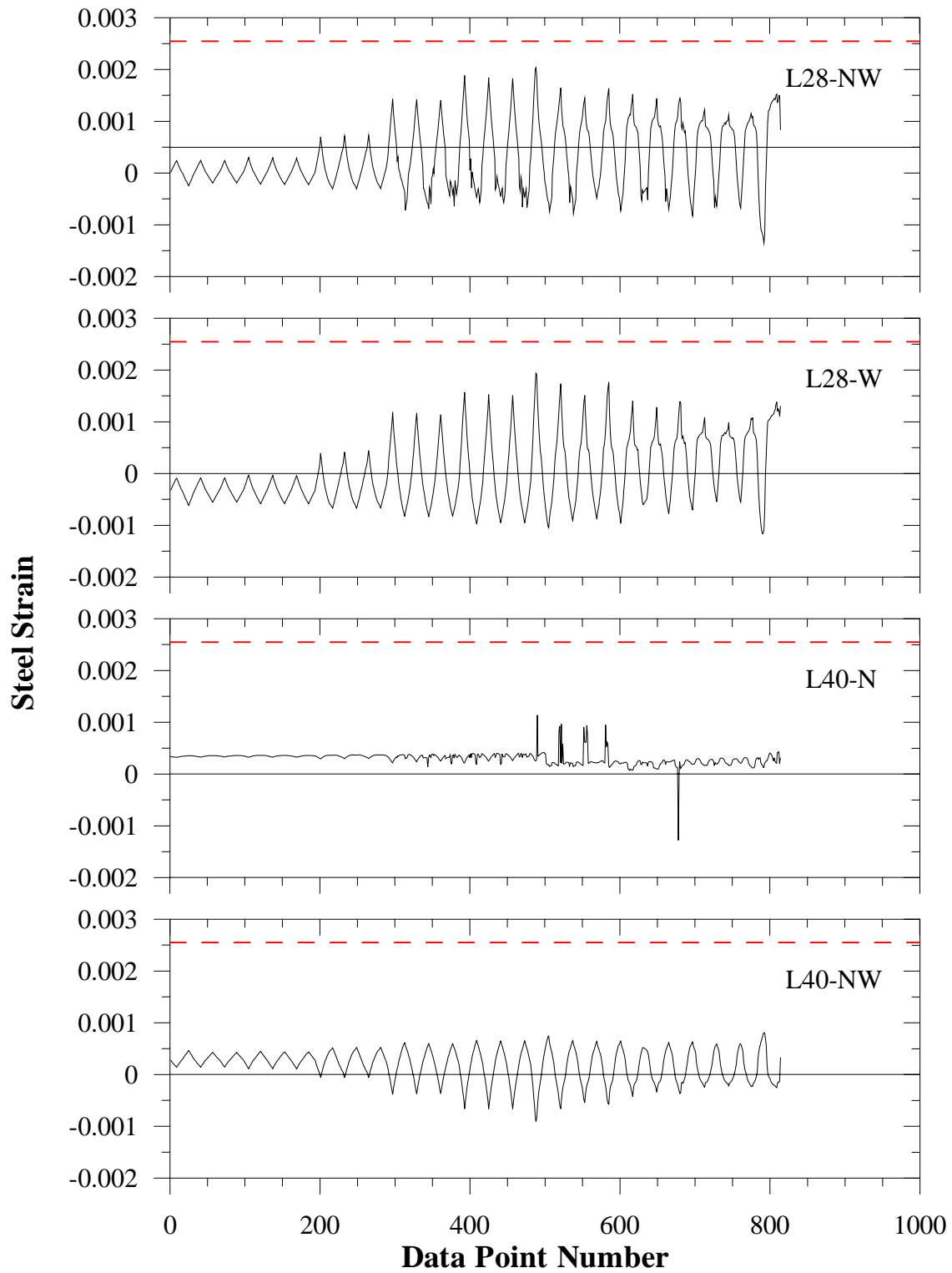
S30MI Longitudinal Steel Strain Histories



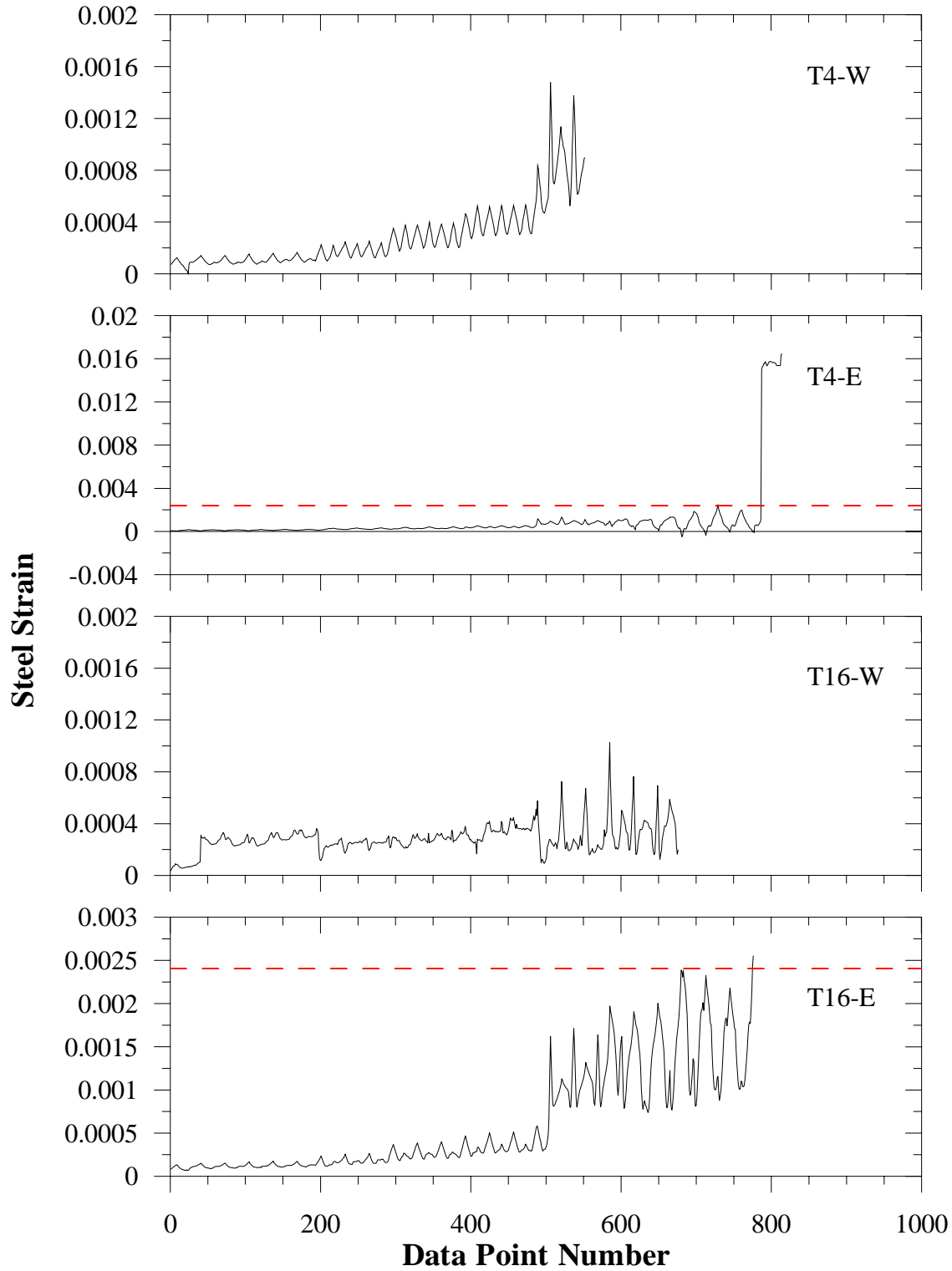
S30MI Longitudinal Steel Strain Histories



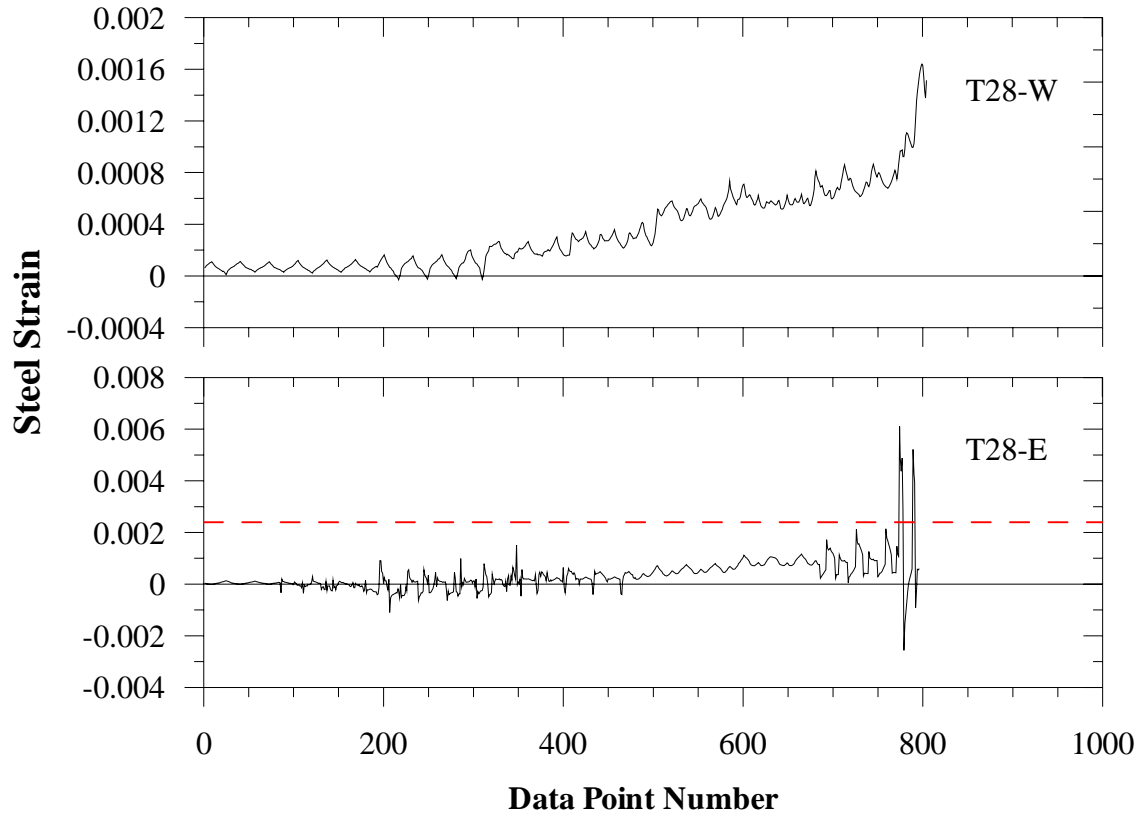
S30MI Longitudinal Steel Strain Histories



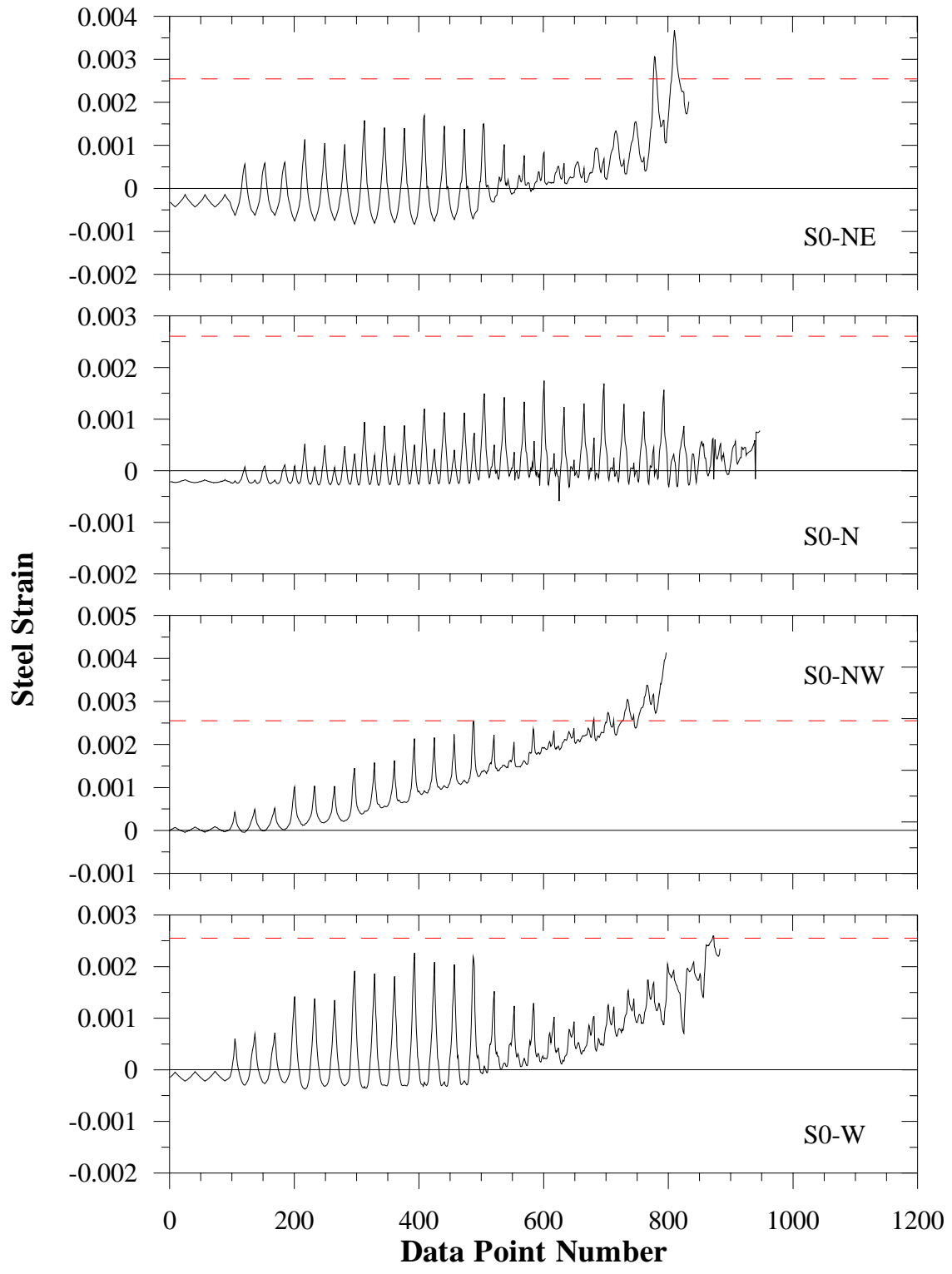
S30MI Longitudinal Steel Strain Histories



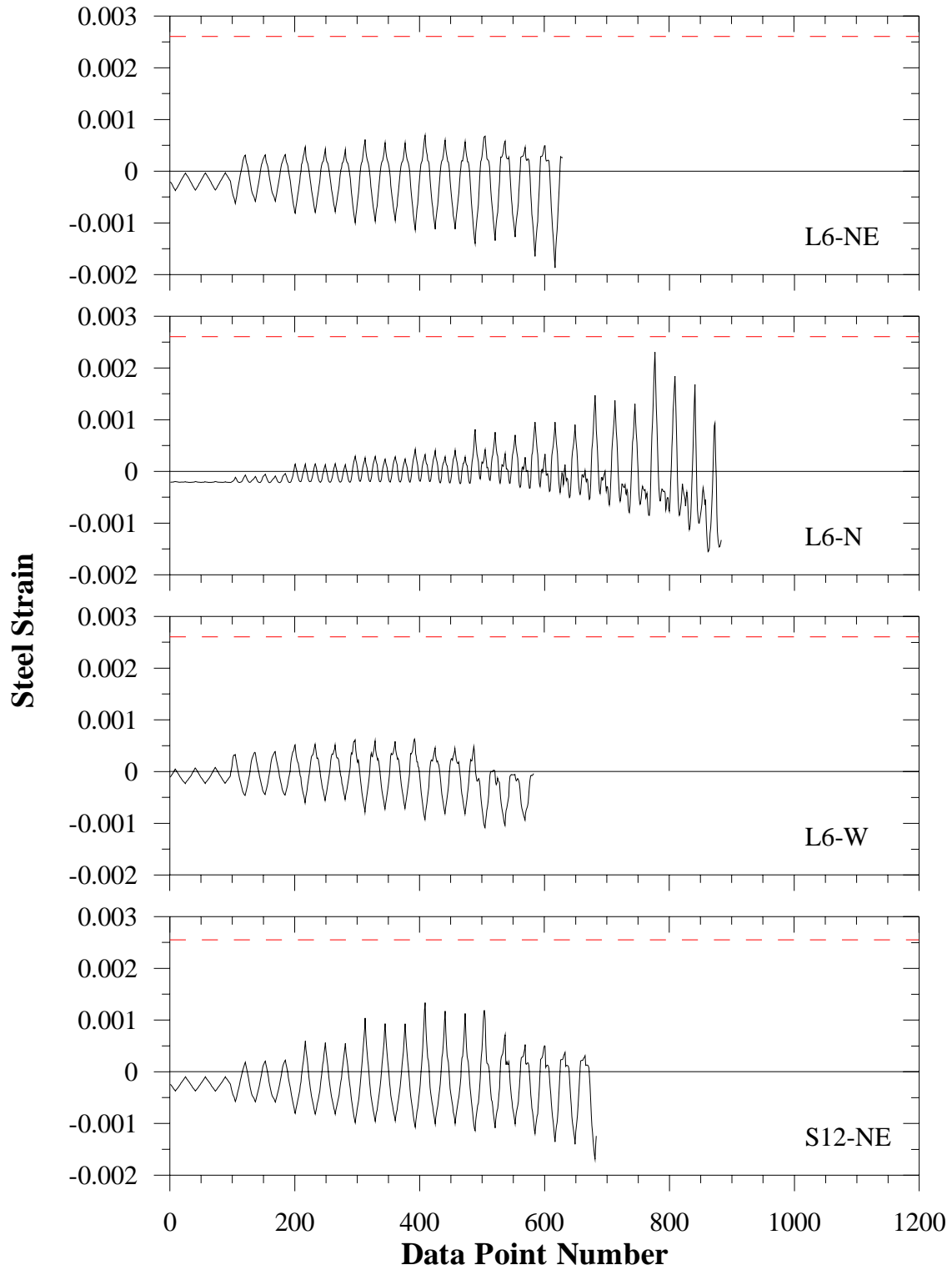
S30MI Longitudinal Steel Strain Histories



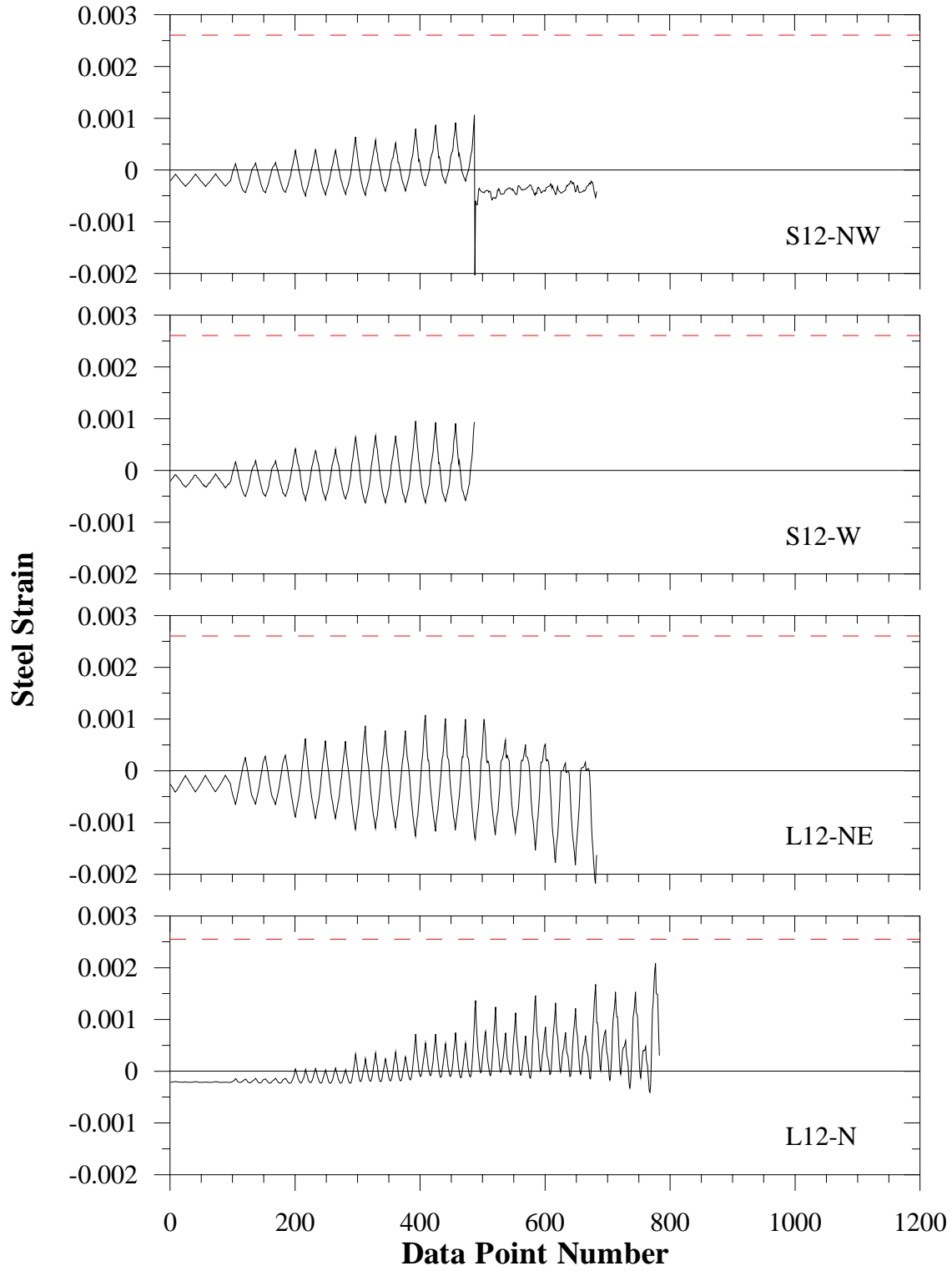
S30MI Longitudinal Steel Strain Histories



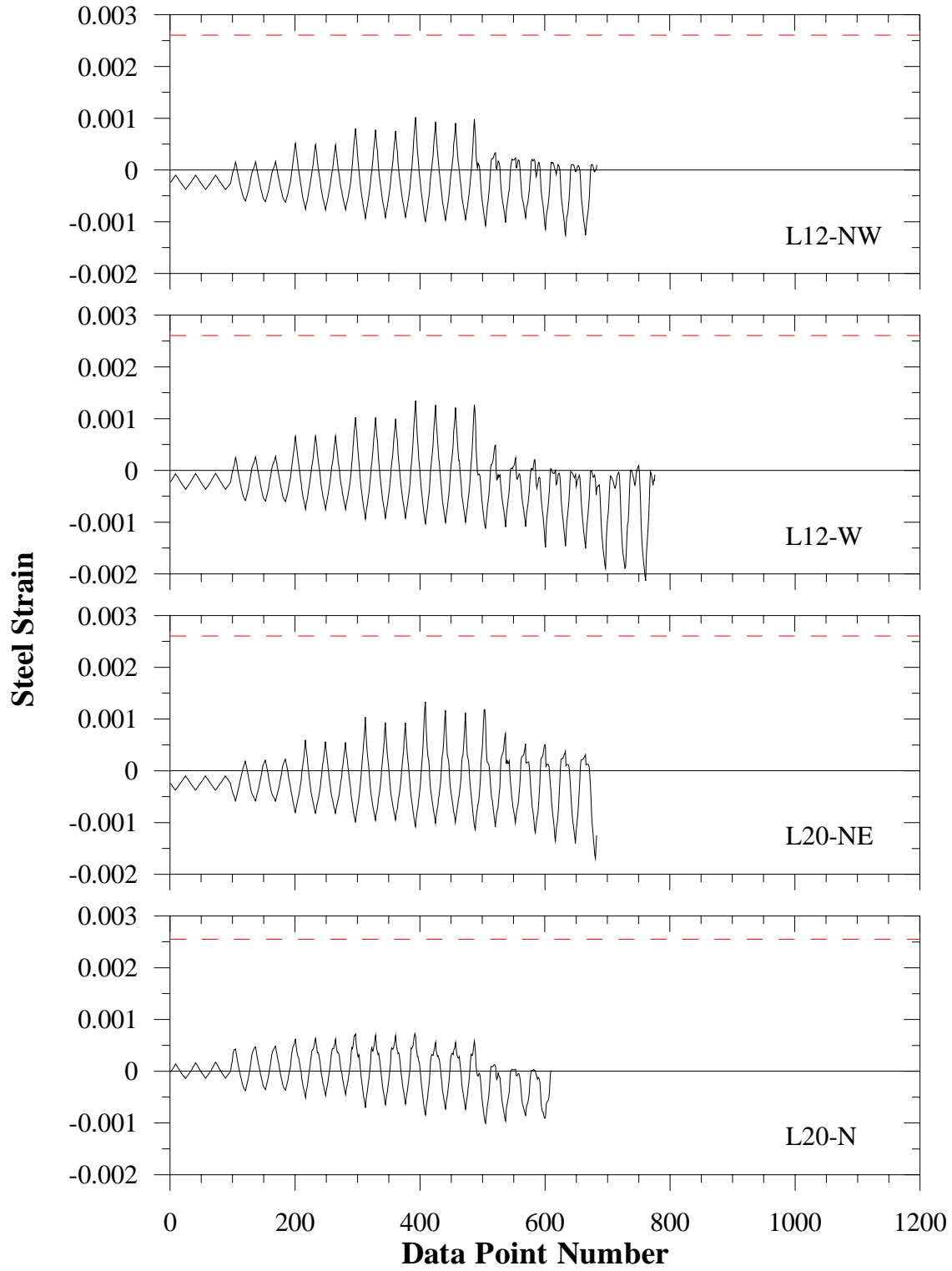
S20HI Longitudinal Steel Strain Histories



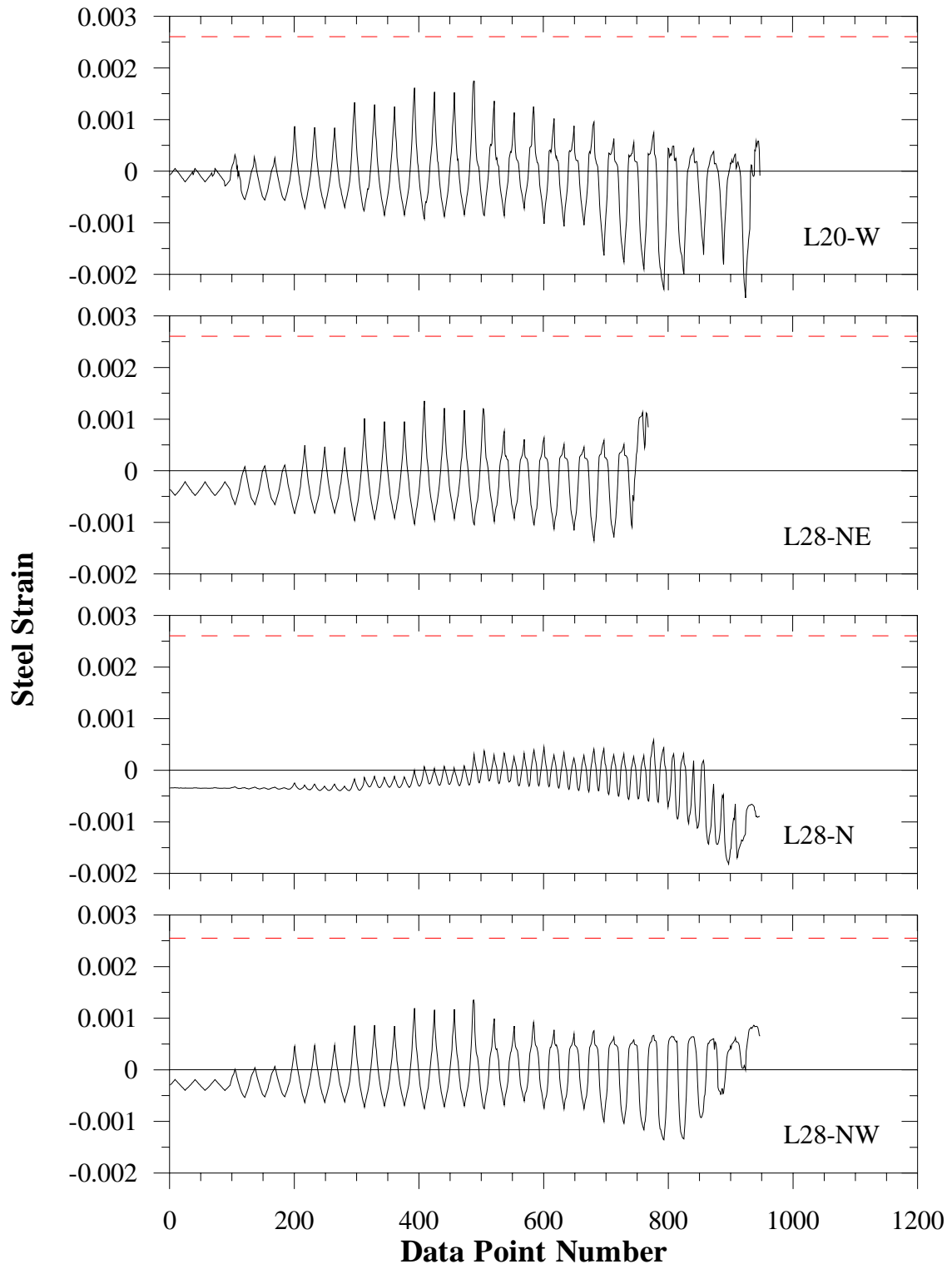
S20HI Longitudinal Steel Strain Histories



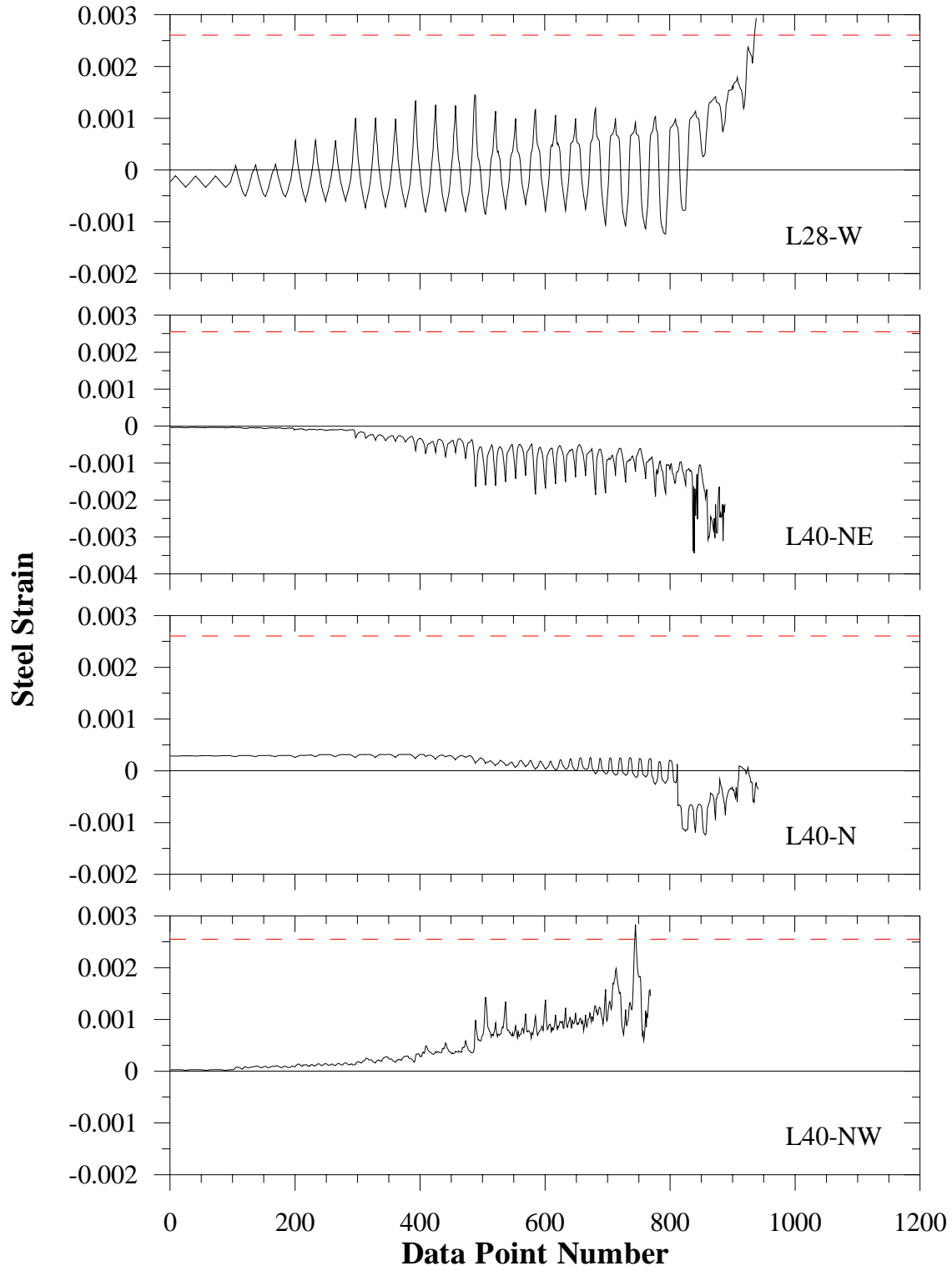
S20HI Longitudinal Steel Strain Histories



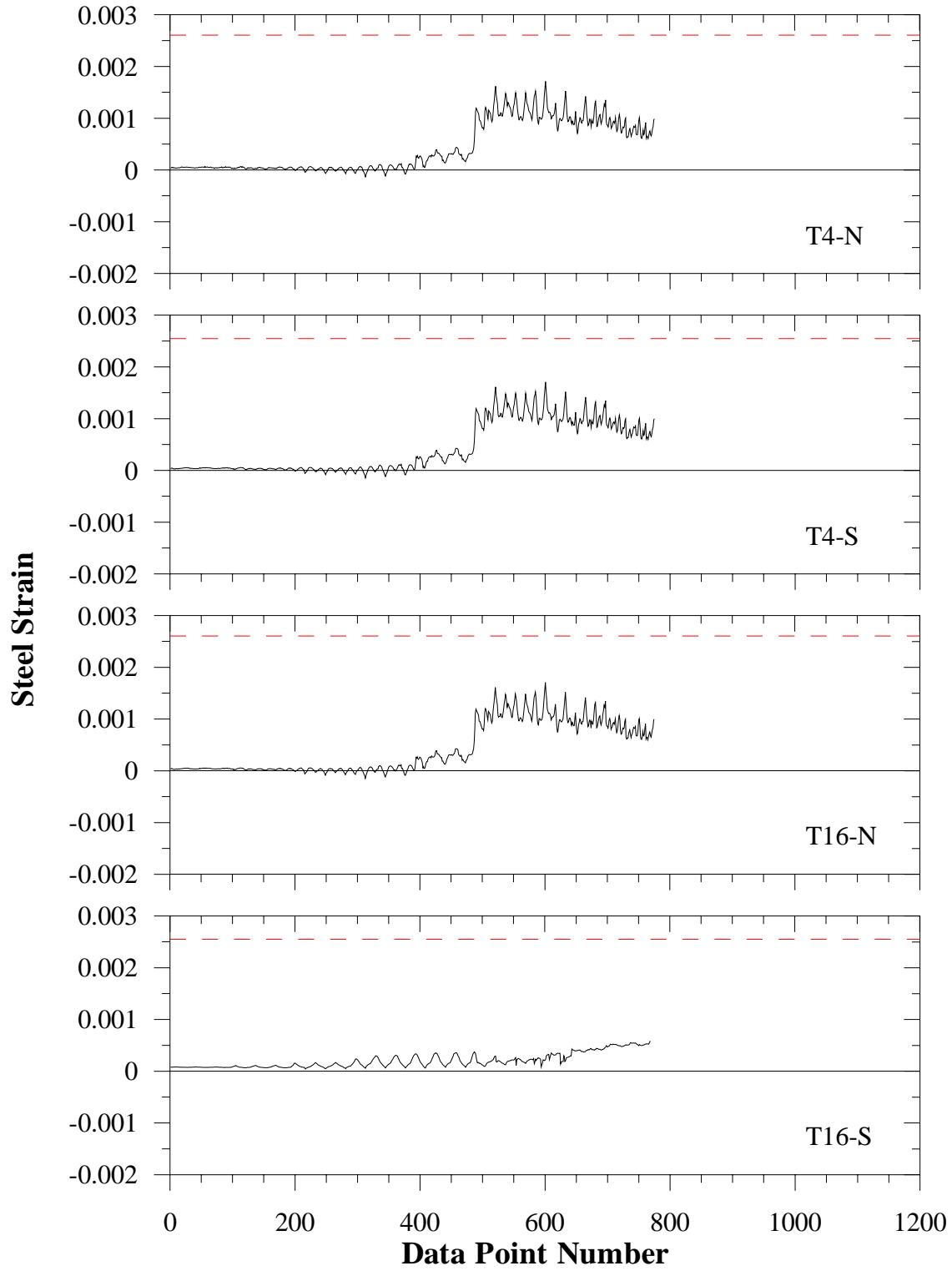
S20HI Longitudinal Steel Strain Histories



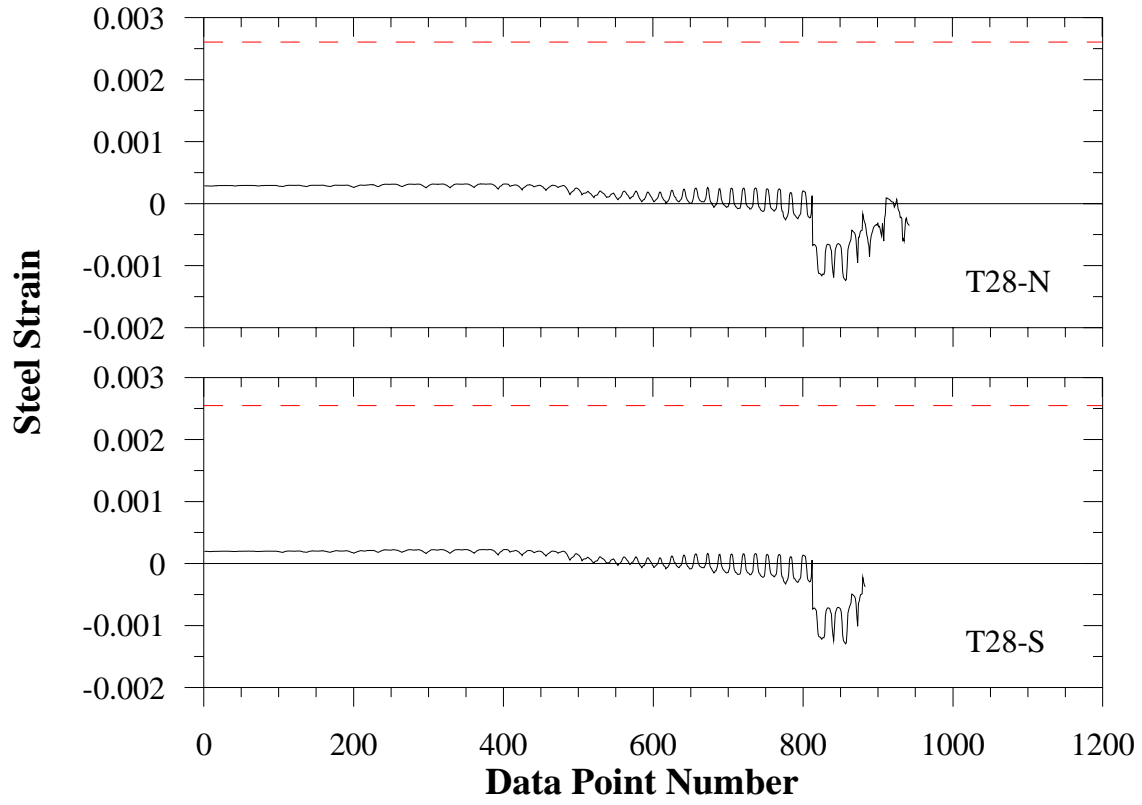
S20HI Longitudinal Steel Strain Histories



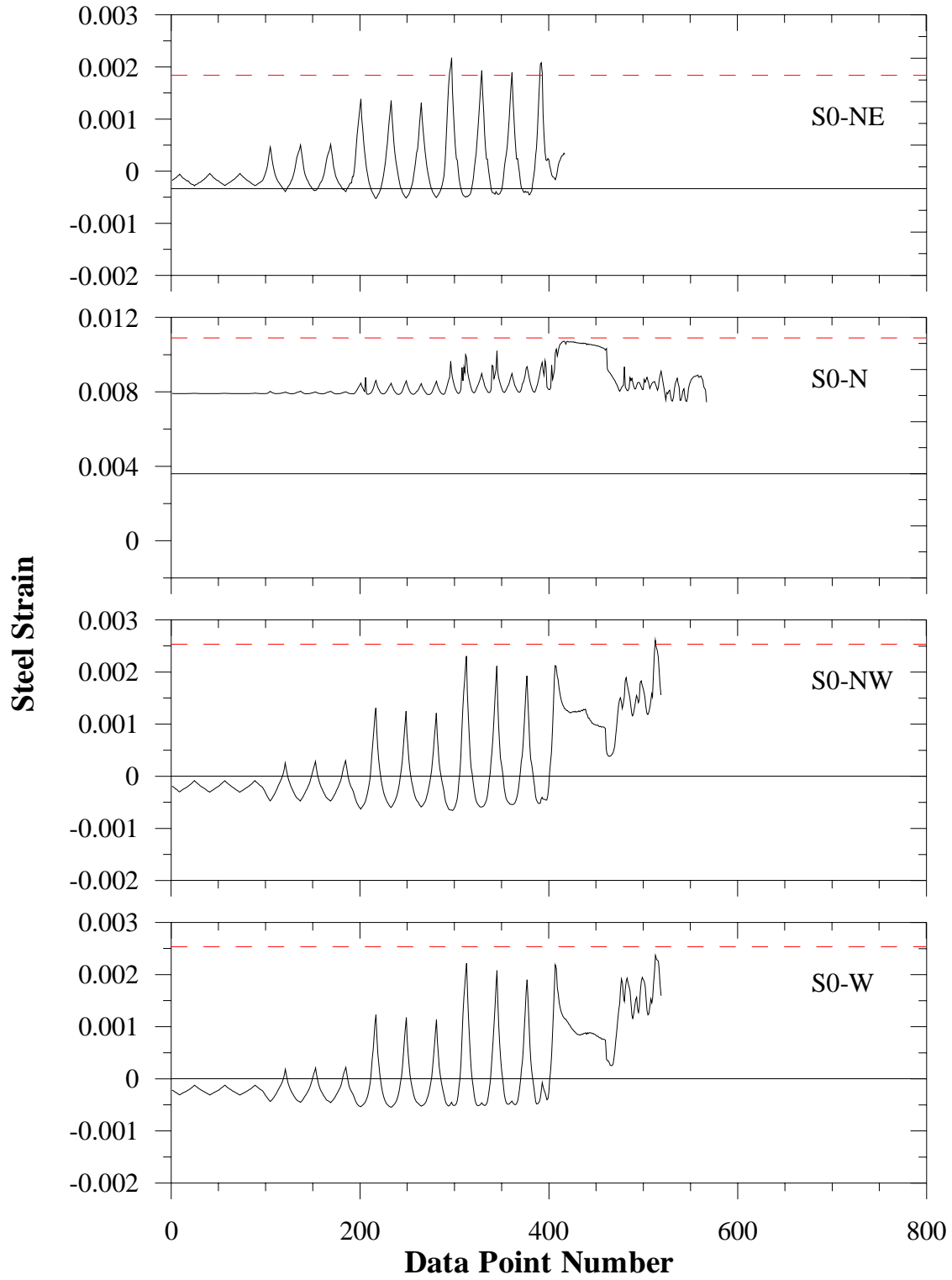
S20HI Longitudinal Steel Strain Histories



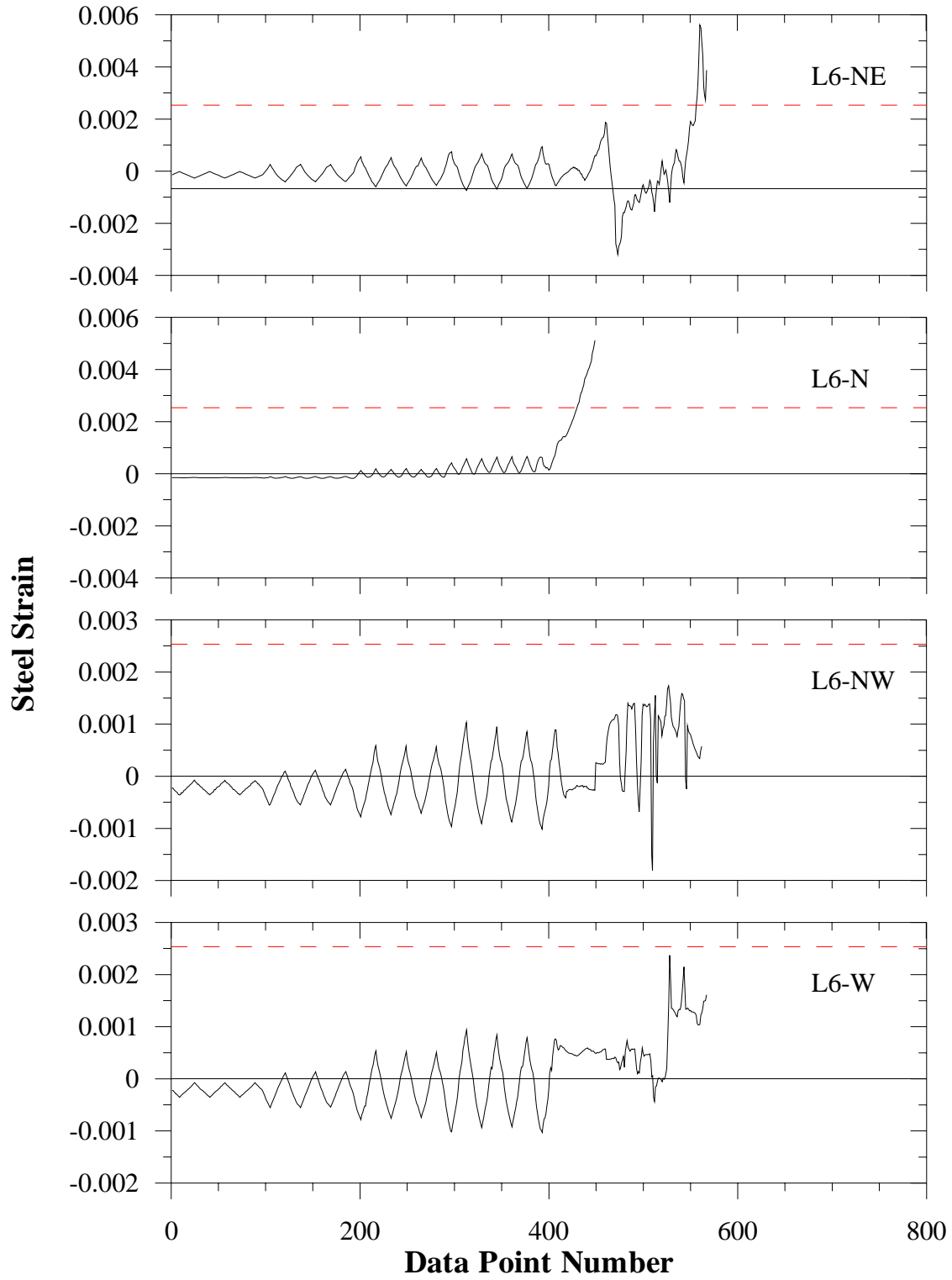
S20HI Longitudinal Steel Strain Histories



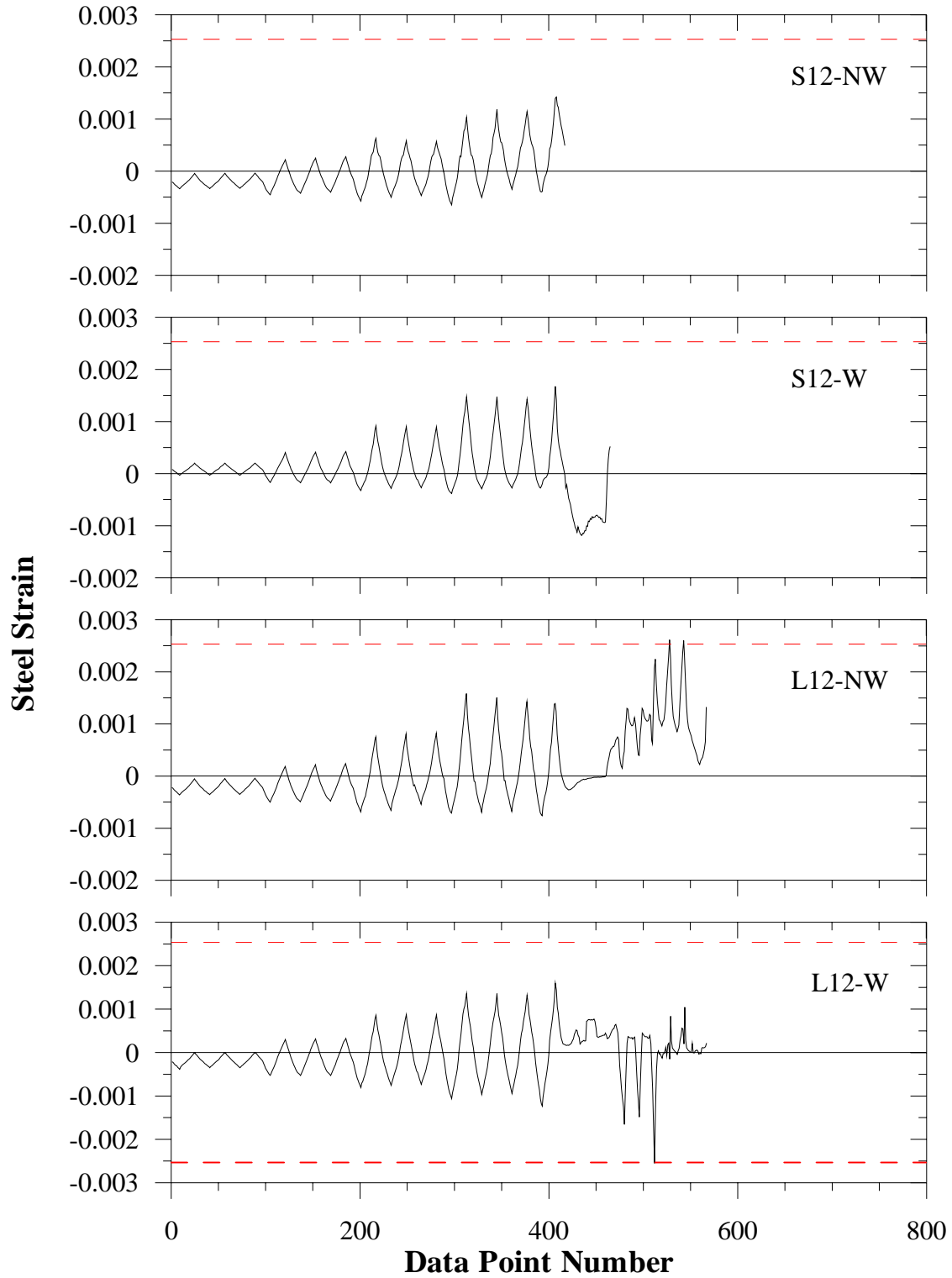
S20HI Longitudinal Steel Strain Histories



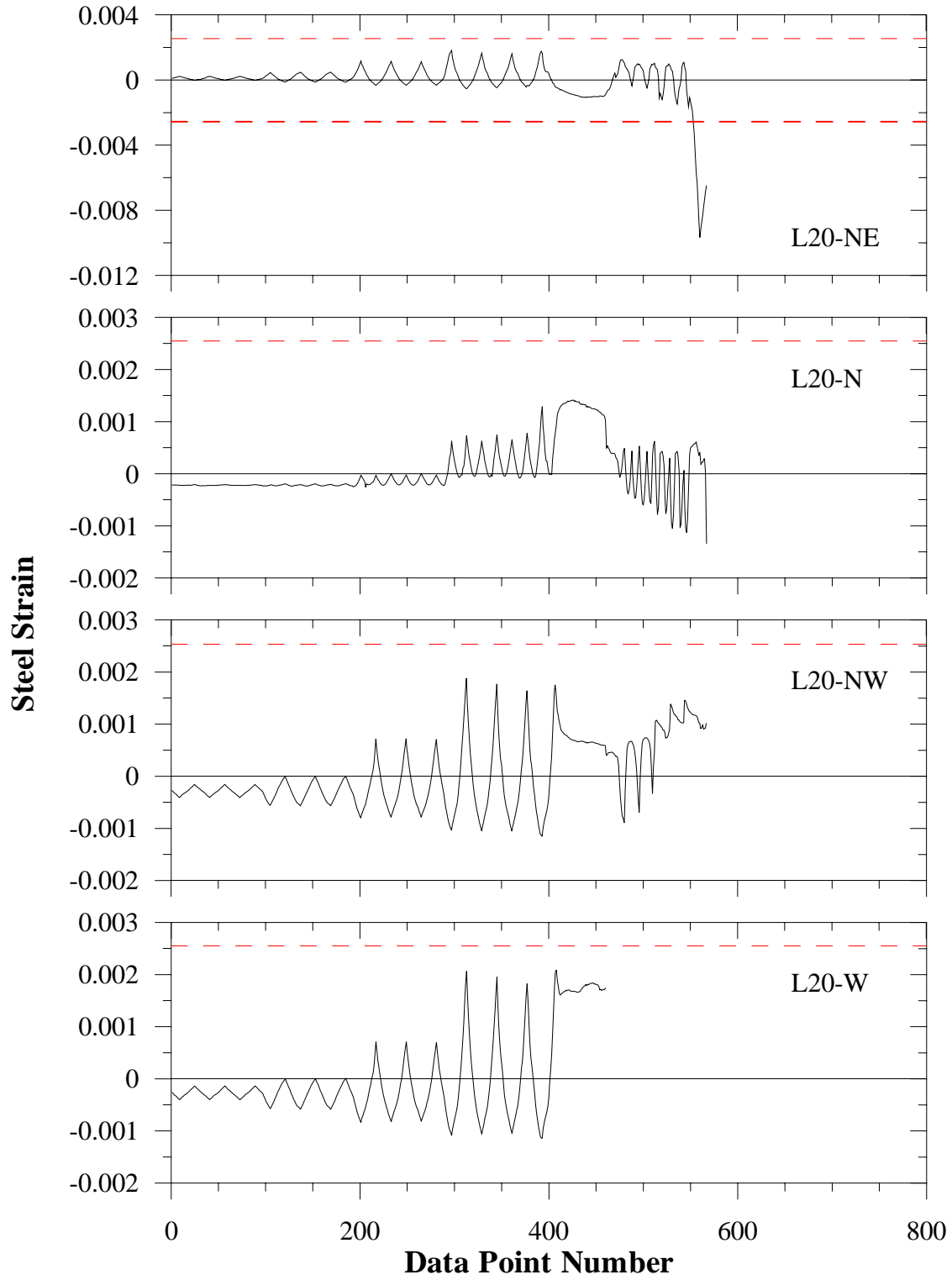
S20HIN Longitudinal Steel Strain Histories



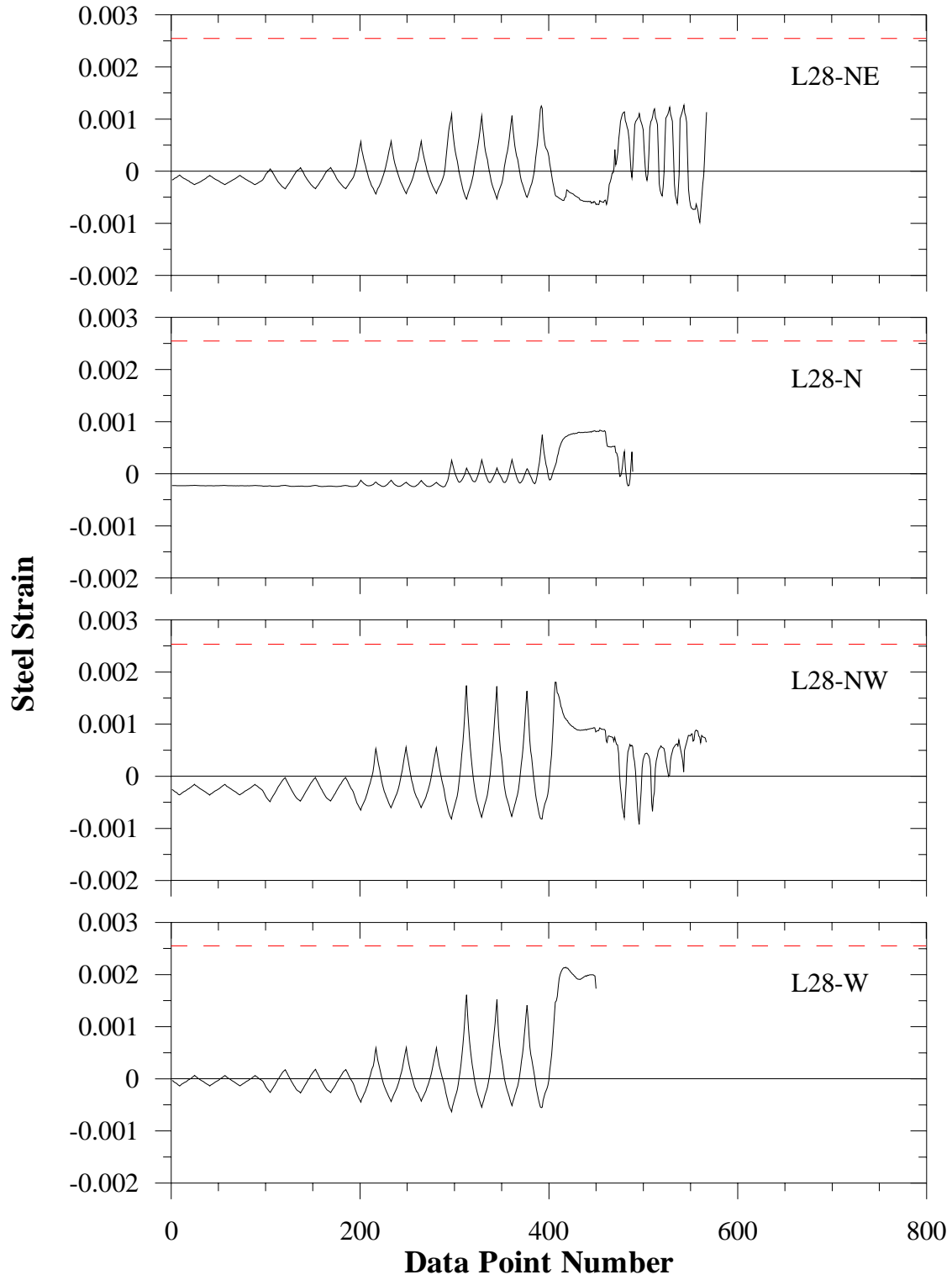
S20HIN Longitudinal Steel Strain Histories



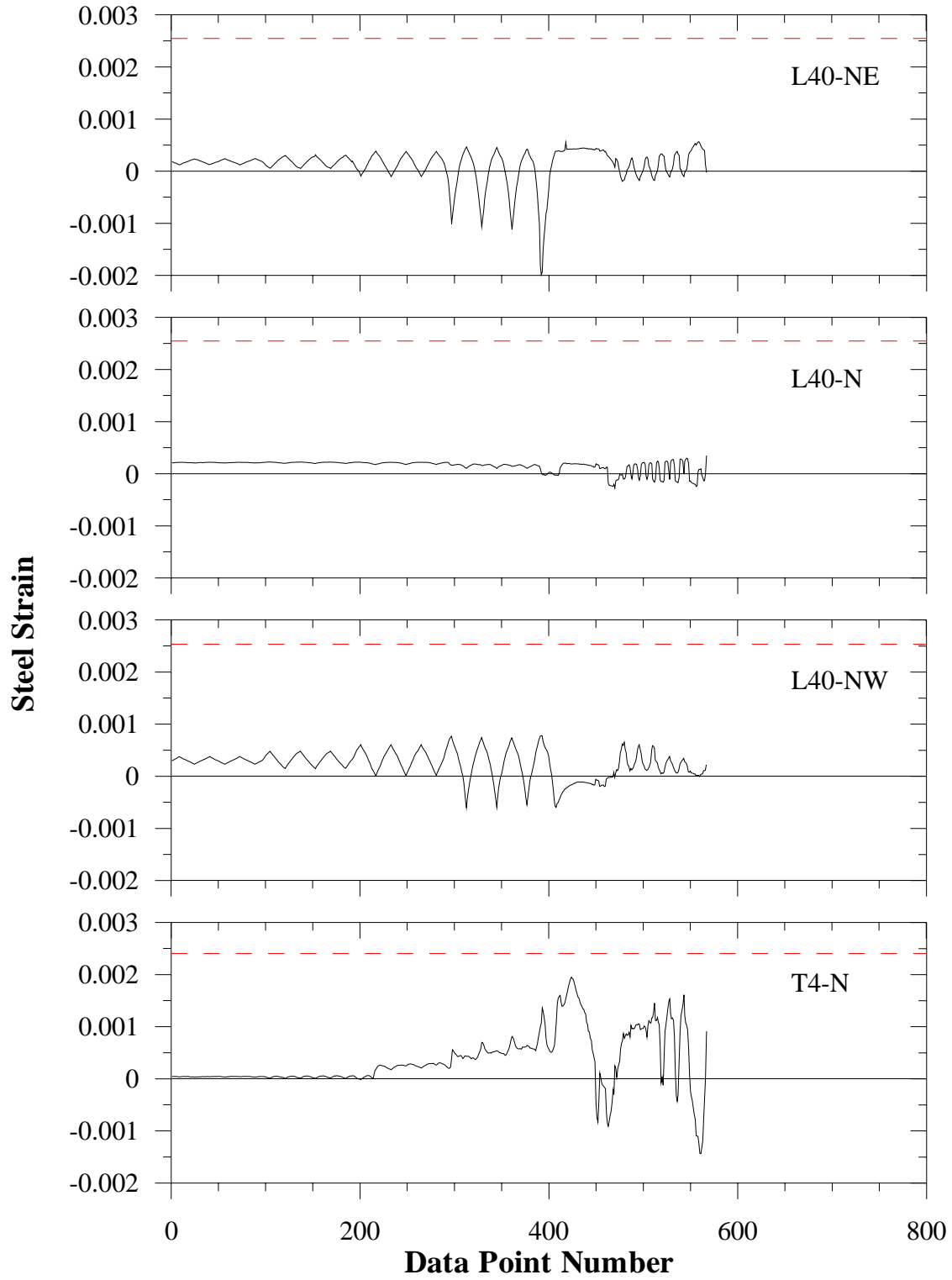
S20HIN Longitudinal Steel Strain Histories



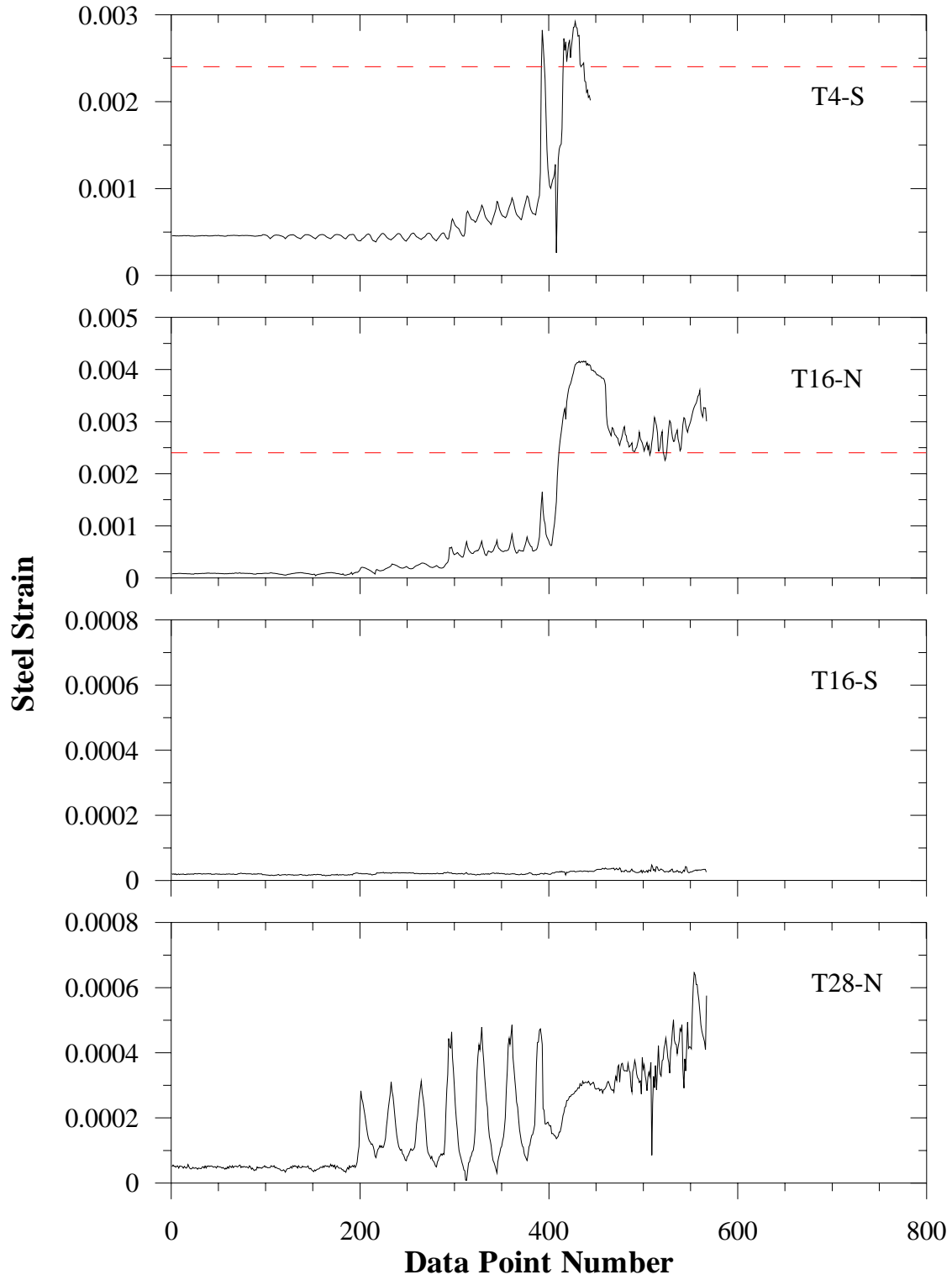
S20HIN Longitudinal Steel Strain Histories



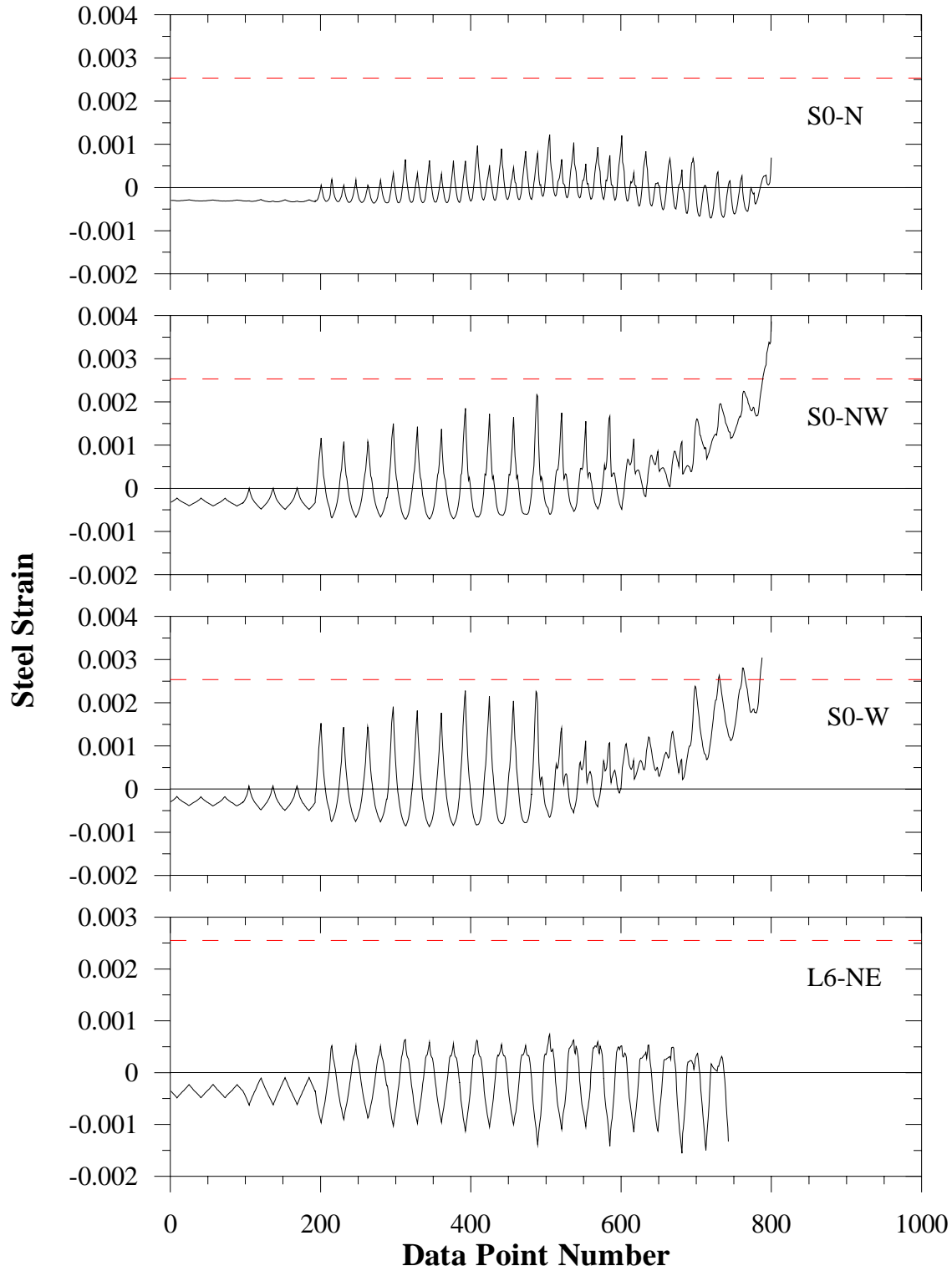
S20HIN Longitudinal Steel Strain Histories



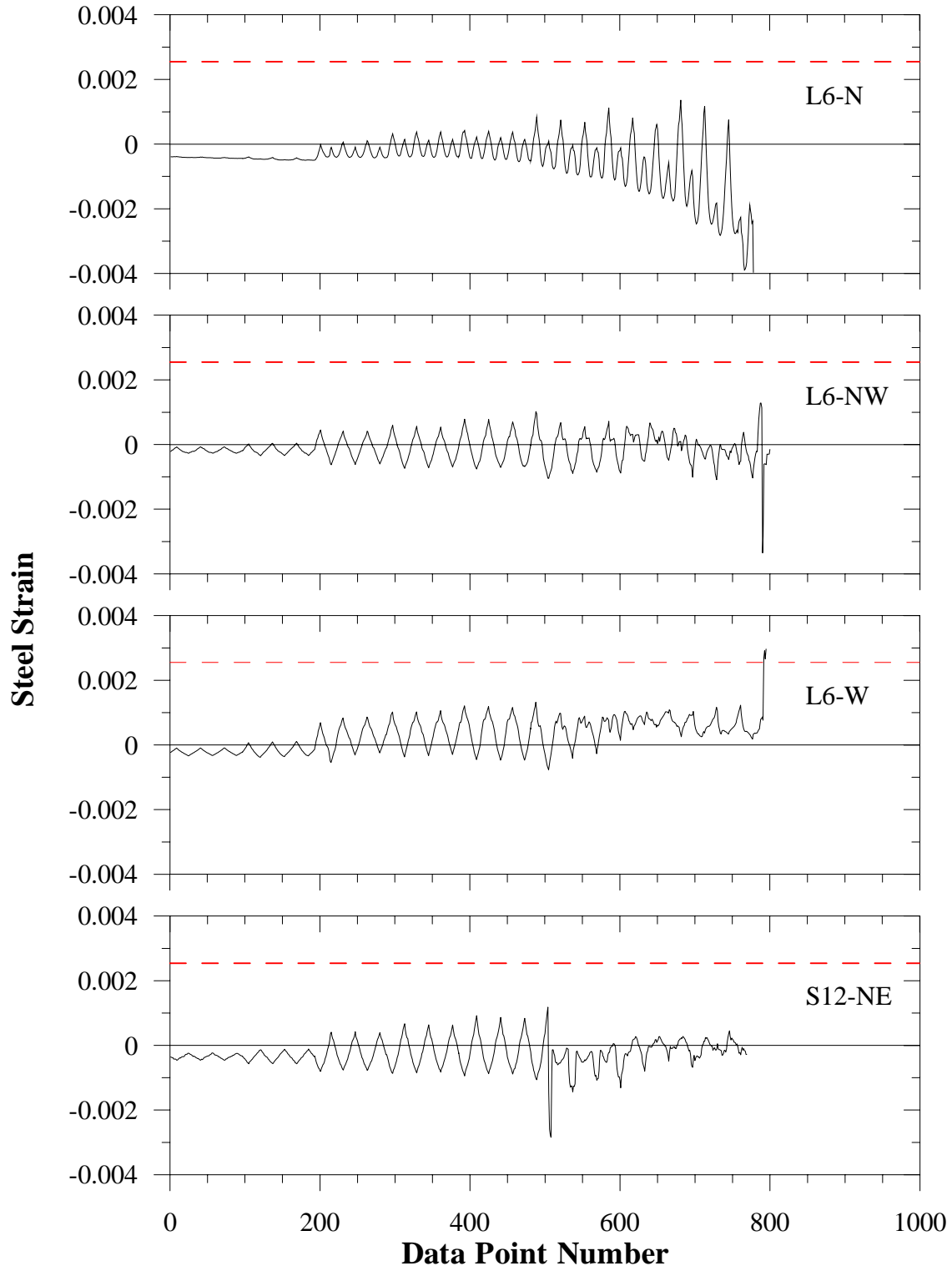
S20HIN Longitudinal Steel Strain Histories



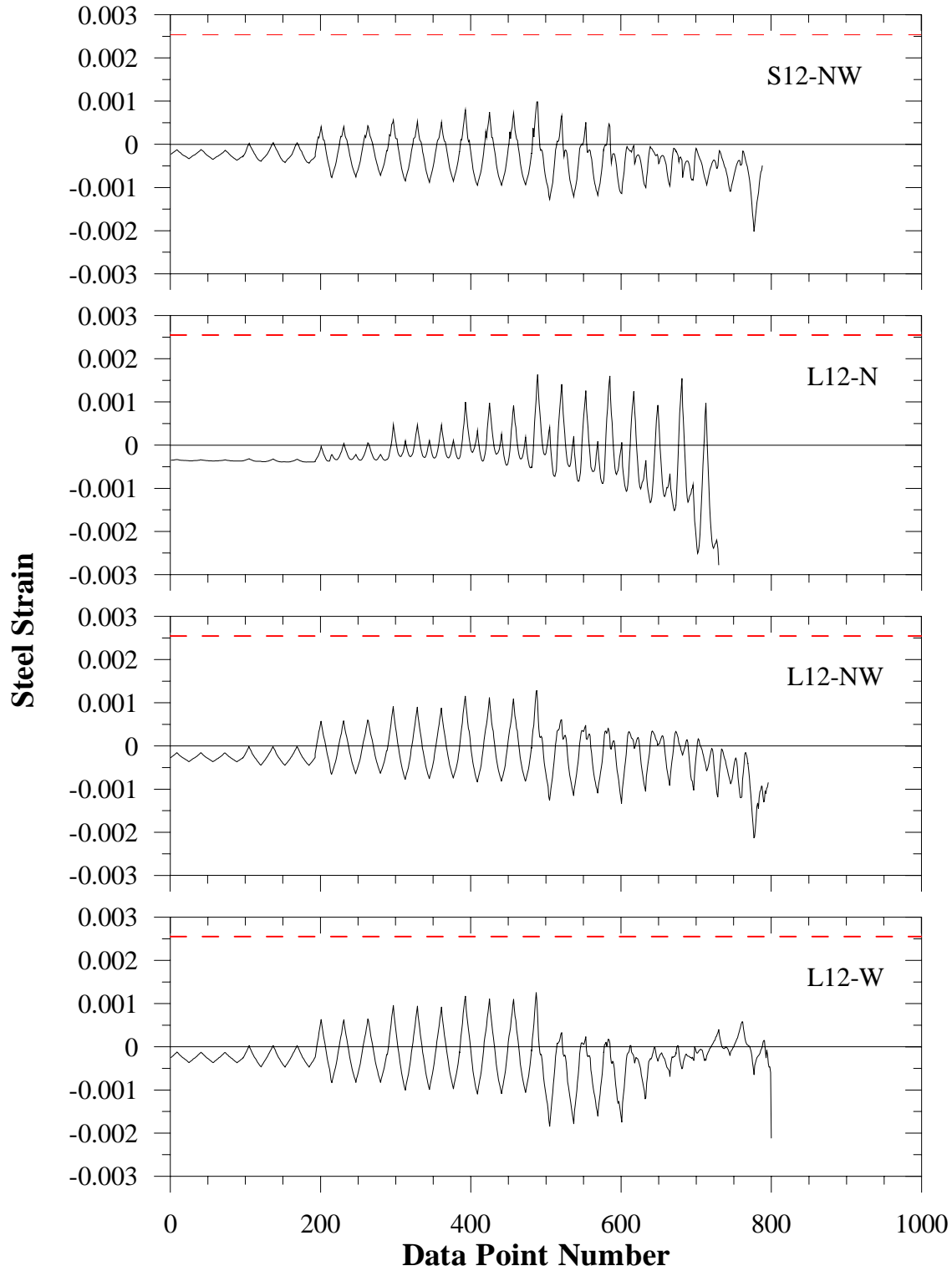
S20HIN Longitudinal Steel Strain Histories



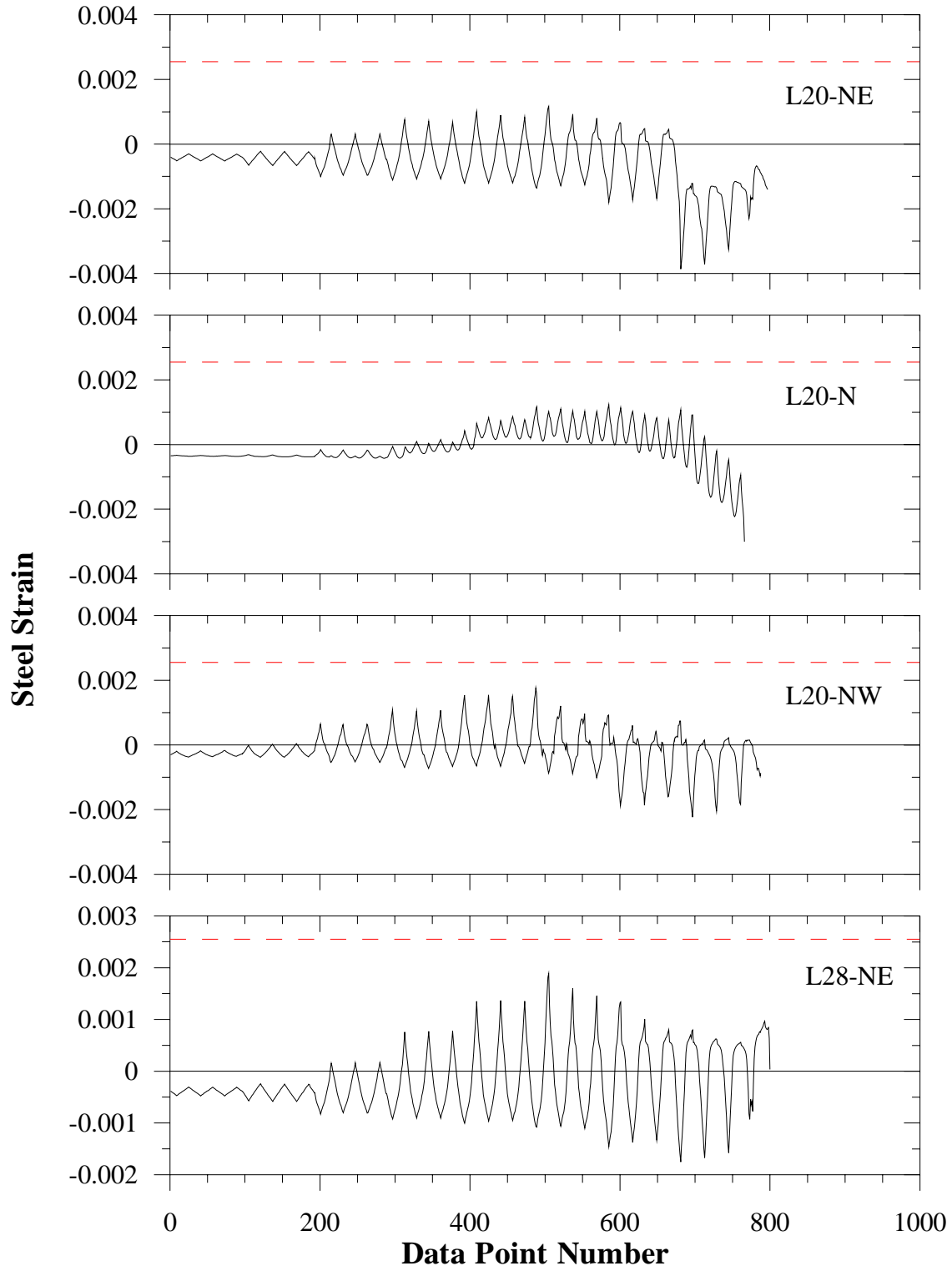
S30XI Longitudinal Steel Strain Histories



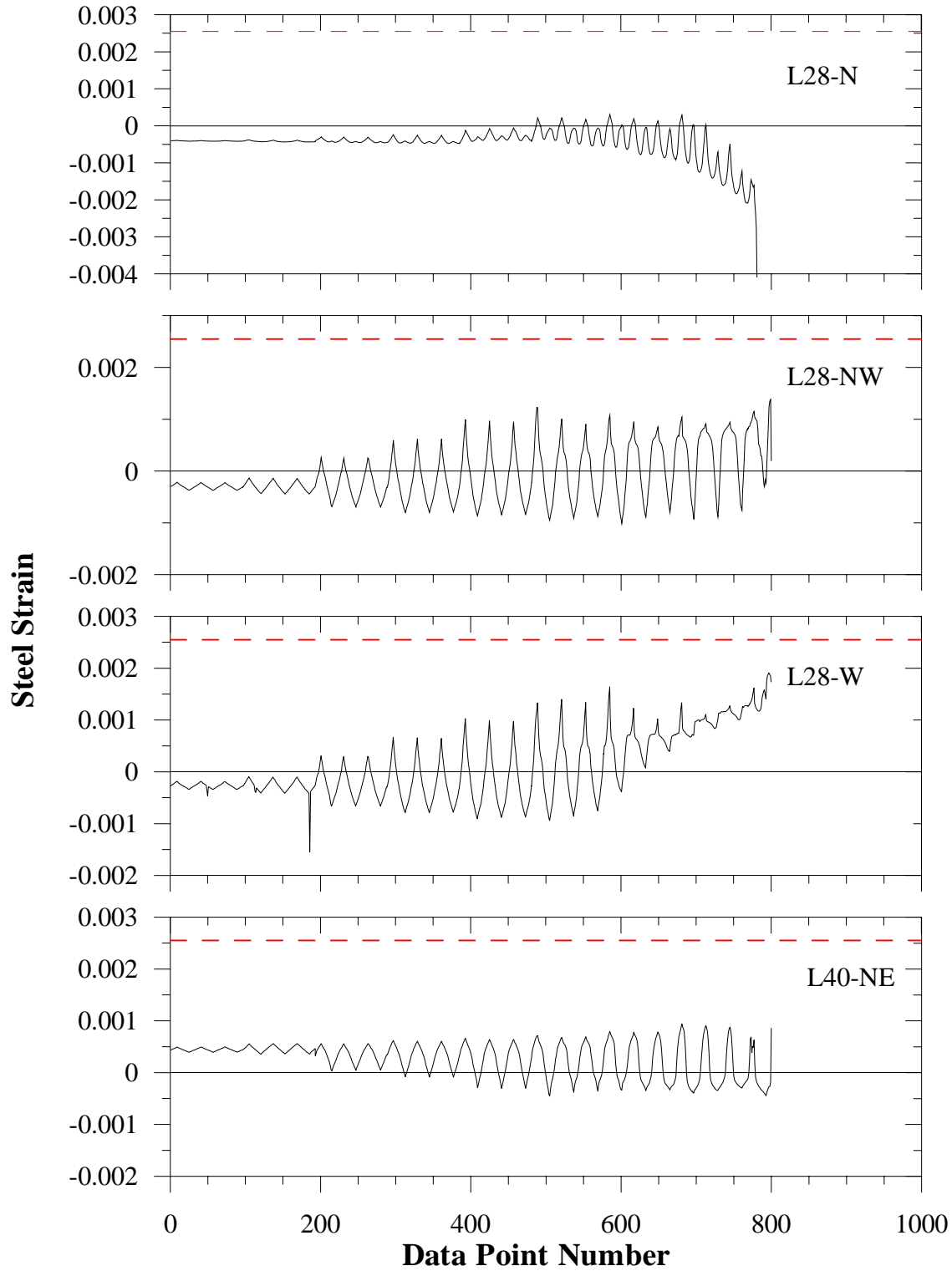
S30XI Longitudinal Steel Strain Histories



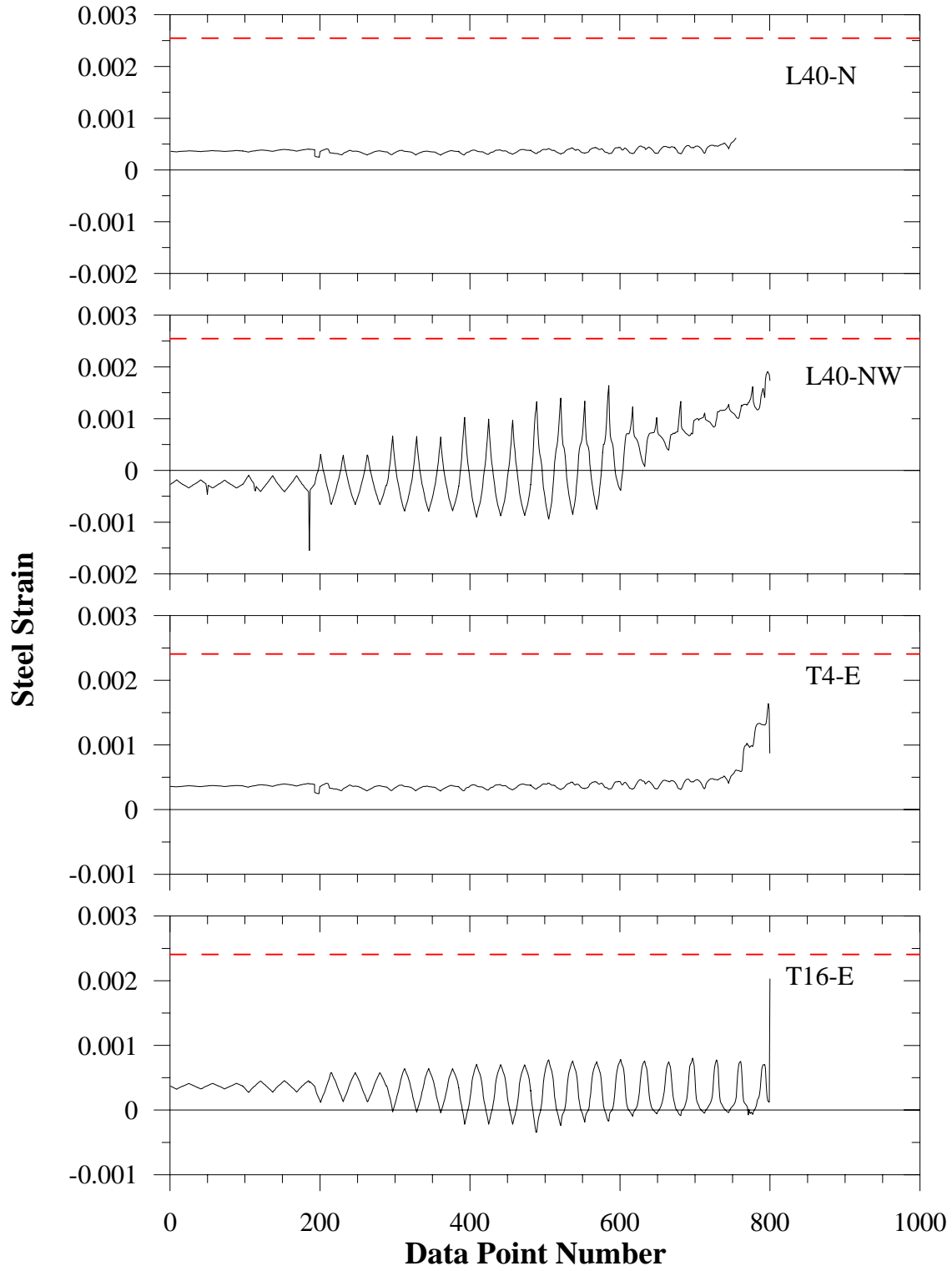
S30XI Longitudinal Steel Strain Histories



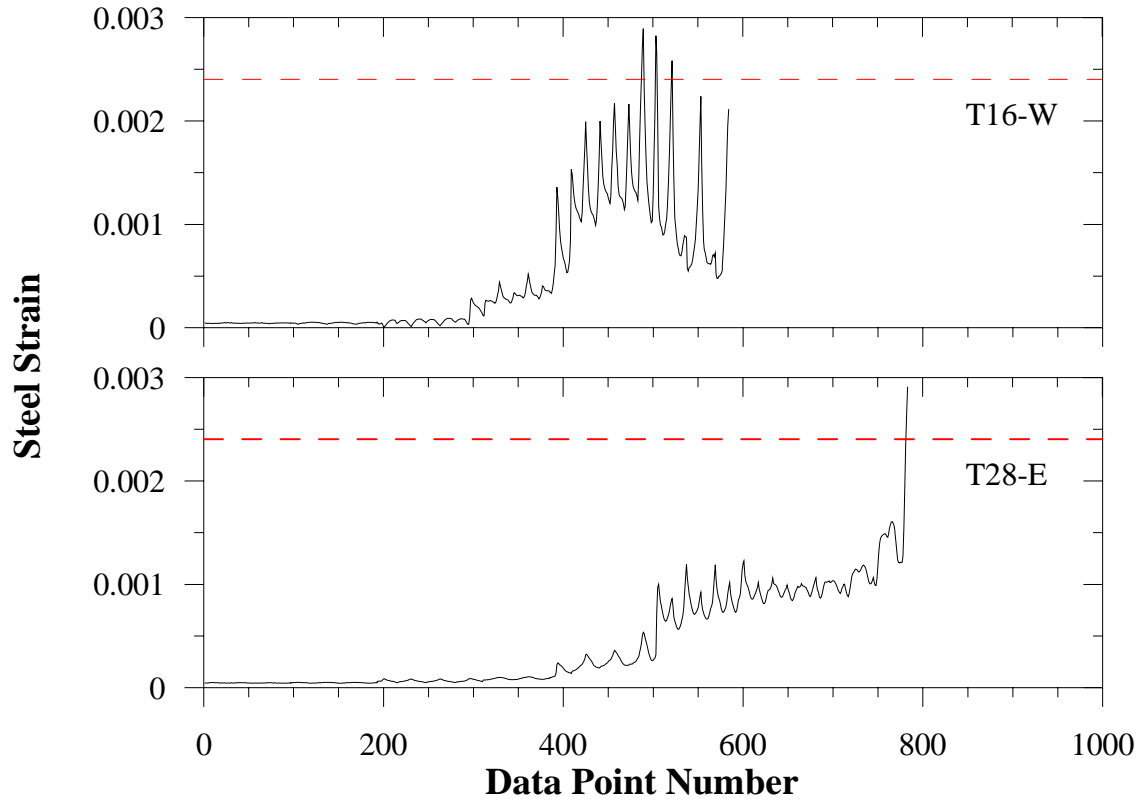
S30XI Longitudinal Steel Strain Histories



S30XI Longitudinal Steel Strain Histories



S30XI Longitudinal Steel Strain Histories



S30XI Longitudinal Steel Strain Histories

PEER REPORTS

PEER reports are available from the National Information Service for Earthquake Engineering (NISEE). To order PEER reports, please contact the Pacific Earthquake Engineering Research Center, 1301 South 46th Street, Richmond, California 94804-4698. Tel.: (510) 231-9468; Fax: (510) 231-9461.

- PEER 2003/06** *Performance of Circular Reinforced Concrete Bridge Columns under Bidirectional Earthquake Loading.* Mahmoud M. Hachem, Stephen A. Mahin, and Jack P. Moehle. February 2003
- PEER 2003/05** *Response Assessment of Nonstructural Building Elements.* Shahram Taghavi and Eduardo Miranda. September 2003.
- PEER 2003/04** *Experimental Assessment of Columns with Short Lap Splices Subjected to Cyclic Loads.* Murat Melek, John W. Wallace, and Joel Conte. April 2003.
- PEER 2003/03** *Probabilistic Response Assessment for Building-Specific Loss Estimation.* Eduardo Miranda and Hesameddin Aslani. September 2003.
- PEER 2003/02** *Software Framework for Collaborative Development of Nonlinear Dynamic Analysis Program.* Jun Peng and Kincho H. Law. September 2003.
- PEER 2002/24** *Performance of Beam to Column Bridge Joints Subjected to a Large Velocity Pulse.* Natalie Gibson, André Filiatrault, and Scott A. Ashford. April 2002.
- PEER 2002/23** *Effects of Large Velocity Pulses on Reinforced Concrete Bridge Columns.* Greg L. Orozco and Scott A. Ashford. April 2002.
- PEER 2002/22** *Characterization of Large Velocity Pulses for Laboratory Testing.* Kenneth E. Cox and Scott A. Ashford. April 2002.
- PEER 2002/21** *Fourth U.S.-Japan Workshop on Performance-Based Earthquake Engineering Methodology for Reinforced Concrete Building Structures.* December 2002.
- PEER 2002/20** *Barriers to Adoption and Implementation of PBEE Innovations.* Peter J. May. August 2002.
- PEER 2002/19** *Economic-Engineered Integrated Models for Earthquakes: Socioeconomic Impacts.* Peter Gordon, James E. Moore II, and Harry W. Richardson. July 2002.
- PEER 2002/18** *Assessment of Reinforced Concrete Building Exterior Joints with Substandard Details.* Chris P. Pantelides, Jon Hansen, Justin Nadauld, and Lawrence D. Reaveley. May 2002.
- PEER 2002/17** *Structural Characterization and Seismic Response Analysis of a Highway Overcrossing Equipped with Elastomeric Bearings and Fluid Dampers: A Case Study.* Nicos Makris and Jian Zhang. November 2002.
- PEER 2002/16** *Estimation of Uncertainty in Geotechnical Properties for Performance-Based Earthquake Engineering.* Allen L. Jones, Steven L. Kramer, and Pedro Arduino. December 2002.

- PEER 2002/15** *Seismic Behavior of Bridge Columns Subjected to Various Loading Patterns.* Asadollah Esmaeily-Gh. and Yan Xiao. December 2002.
- PEER 2002/14** *Inelastic Seismic Response of Extended Pile Shaft Supported Bridge Structures.* T.C. Hutchinson, R.W. Boulanger, Y.H. Chai, and I.M. Idriss. December 2002.
- PEER 2002/13** *Probabilistic Models and Fragility Estimates for Bridge Components and Systems.* Paolo Gardoni, Armen Der Kiureghian, and Khalid M. Mosalam. June 2002.
- PEER 2002/12** *Effects of Fault Dip and Slip Rake on Near-Source Ground Motions: Why Chi-Chi Was a Relatively Mild M7.6 Earthquake.* Brad T. Aagaard, John F. Hall, and Thomas H. Heaton. December 2002.
- PEER 2002/11** *Analytical and Experimental Study of Fiber-Reinforced Strip Isolators.* James M. Kelly and Shakhzod M. Takhirov. September 2002.
- PEER 2002/10** *Centrifuge Modeling of Settlement and Lateral Spreading with Comparisons to Numerical Analyses.* Sivapalan Gajan and Bruce L. Kutter. January 2003.
- PEER 2002/09** *Documentation and Analysis of Field Case Histories of Seismic Compression during the 1994 Northridge, California, Earthquake.* Jonathan P. Stewart, Patrick M. Smith, Daniel H. Whang, and Jonathan D. Bray. October 2002.
- PEER 2002/08** *Component Testing, Stability Analysis and Characterization of Buckling-Restrained Unbonded Braces™.* Cameron Black, Nicos Makris, and Ian Aiken. September 2002.
- PEER 2002/07** *Seismic Performance of Pile-Wharf Connections.* Charles W. Roeder, Robert Graff, Jennifer Soderstrom, and Jun Han Yoo. December 2001.
- PEER 2002/06** *The Use of Benefit-Cost Analysis for Evaluation of Performance-Based Earthquake Engineering Decisions.* Richard O. Zerbe and Anthony Falit-Baiamonte. September 2001.
- PEER 2002/05** *Guidelines, Specifications, and Seismic Performance Characterization of Nonstructural Building Components and Equipment.* André Filiatrault, Constantin Christopoulos, and Christopher Stearns. September 2001.
- PEER 2002/04** *Consortium of Organizations for Strong-Motion Observation Systems and the Pacific Earthquake Engineering Research Center Lifelines Program: Invited Workshop on Archiving and Web Dissemination of Geotechnical Data, 4–5 October 2001.* September 2002.
- PEER 2002/03** *Investigation of Sensitivity of Building Loss Estimates to Major Uncertain Variables for the Van Nuys Testbed.* Keith A. Porter, James L. Beck, and Rustem V. Shaikhutdinov. August 2002.
- PEER 2002/02** *The Third U.S.-Japan Workshop on Performance-Based Earthquake Engineering Methodology for Reinforced Concrete Building Structures.* July 2002.
- PEER 2002/01** *Nonstructural Loss Estimation: The UC Berkeley Case Study.* Mary C. Comerio and John C. Stallmeyer. December 2001.
- PEER 2001/16** *Statistics of SDF-System Estimate of Roof Displacement for Pushover Analysis of Buildings.* Anil K. Chopra, Rakesh K. Goel, and Chatpan Chintanapakdee. December 2001.

- PEER 2001/15** *Damage to Bridges during the 2001 Nisqually Earthquake.* R. Tyler Ranf, Marc O. Eberhard, and Michael P. Berry. November 2001.
- PEER 2001/14** *Rocking Response of Equipment Anchored to a Base Foundation.* Nicos Makris and Cameron J. Black. September 2001.
- PEER 2001/13** *Modeling Soil Liquefaction Hazards for Performance-Based Earthquake Engineering.* Steven L. Kramer and Ahmed-W. Elgamal. February 2001.
- PEER 2001/12** *Development of Geotechnical Capabilities in OpenSees.* Boris Jeremic. September 2001.
- PEER 2001/11** *Analytical and Experimental Study of Fiber-Reinforced Elastomeric Isolators.* James M. Kelly and Shakhzod M. Takhirov. September 2001.
- PEER 2001/10** *Amplification Factors for Spectral Acceleration in Active Regions.* Jonathan P. Stewart, Andrew H. Liu, Yoojoong Choi, and Mehmet B. Baturay. December 2001.
- PEER 2001/09** *Ground Motion Evaluation Procedures for Performance-Based Design.* Jonathan P. Stewart, Shyh-Jeng Chiou, Jonathan D. Bray, Robert W. Graves, Paul G. Somerville, and Norman A. Abrahamson. September 2001.
- PEER 2001/08** *Experimental and Computational Evaluation of Reinforced Concrete Bridge Beam-Column Connections for Seismic Performance.* Clay J. Naito, Jack P. Moehle, and Khalid M. Mosalam. November 2001.
- PEER 2001/07** *The Rocking Spectrum and the Shortcomings of Design Guidelines.* Nicos Makris and Dimitrios Konstantinidis. August 2001.
- PEER 2001/06** *Development of an Electrical Substation Equipment Performance Database for Evaluation of Equipment Fragilities.* Thalia Agnanos. April 1999.
- PEER 2001/05** *Stiffness Analysis of Fiber-Reinforced Elastomeric Isolators.* Hsiang-Chuan Tsai and James M. Kelly. May 2001.
- PEER 2001/04** *Organizational and Societal Considerations for Performance-Based Earthquake Engineering.* Peter J. May. April 2001.
- PEER 2001/03** *A Modal Pushover Analysis Procedure to Estimate Seismic Demands for Buildings: Theory and Preliminary Evaluation.* Anil K. Chopra and Rakesh K. Goel. January 2001.
- PEER 2001/02** *Seismic Response Analysis of Highway Overcrossings Including Soil-Structure Interaction.* Jian Zhang and Nicos Makris. March 2001.
- PEER 2001/01** *Experimental Study of Large Seismic Steel Beam-to-Column Connections.* Egor P. Popov and Shakhzod M. Takhirov. November 2000.
- PEER 2000/10** *The Second U.S.-Japan Workshop on Performance-Based Earthquake Engineering Methodology for Reinforced Concrete Building Structures.* March 2000.
- PEER 2000/09** *Structural Engineering Reconnaissance of the August 17, 1999 Earthquake: Kocaeli (Izmit), Turkey.* Halil Sezen, Kenneth J. Elwood, Andrew S. Whittaker, Khalid Mosalam, John J. Wallace, and John F. Stanton. December 2000.

- PEER 2000/08** *Behavior of Reinforced Concrete Bridge Columns Having Varying Aspect Ratios and Varying Lengths of Confinement.* Anthony J. Calderone, Dawn E. Lehman, and Jack P. Moehle. January 2001.
- PEER 2000/07** *Cover-Plate and Flange-Plate Reinforced Steel Moment-Resisting Connections.* Taejin Kim, Andrew S. Whittaker, Amir S. Gilani, Vitelmo V. Bertero, and Shakhzod M. Takhirov. September 2000.
- PEER 2000/06** *Seismic Evaluation and Analysis of 230-kV Disconnect Switches.* Amir S. J. Gilani, Andrew S. Whittaker, Gregory L. Fenves, Chun-Hao Chen, Henry Ho, and Eric Fujisaki. July 2000.
- PEER 2000/05** *Performance-Based Evaluation of Exterior Reinforced Concrete Building Joints for Seismic Excitation.* Chandra Clyde, Chris P. Pantelides, and Lawrence D. Reaveley. July 2000.
- PEER 2000/04** *An Evaluation of Seismic Energy Demand: An Attenuation Approach.* Chung-Che Chou and Chia-Ming Uang. July 1999.
- PEER 2000/03** *Framing Earthquake Retrofitting Decisions: The Case of Hillside Homes in Los Angeles.* Detlof von Winterfeldt, Nels Roselund, and Alicia Kitsuse. March 2000.
- PEER 2000/02** *U.S.-Japan Workshop on the Effects of Near-Field Earthquake Shaking.* Andrew Whittaker, ed. July 2000.
- PEER 2000/01** *Further Studies on Seismic Interaction in Interconnected Electrical Substation Equipment.* Armen Der Kiureghian, Kee-Jeung Hong, and Jerome L. Sackman. November 1999.
- PEER 1999/14** *Seismic Evaluation and Retrofit of 230-kV Porcelain Transformer Bushings.* Amir S. Gilani, Andrew S. Whittaker, Gregory L. Fenves, and Eric Fujisaki. December 1999.
- PEER 1999/13** *Building Vulnerability Studies: Modeling and Evaluation of Tilt-up and Steel Reinforced Concrete Buildings.* John W. Wallace, Jonathan P. Stewart, and Andrew S. Whittaker, editors. December 1999.
- PEER 1999/12** *Rehabilitation of Nonductile RC Frame Building Using Encasement Plates and Energy-Dissipating Devices.* Mehrdad Sasani, Vitelmo V. Bertero, James C. Anderson. December 1999.
- PEER 1999/11** *Performance Evaluation Database for Concrete Bridge Components and Systems under Simulated Seismic Loads.* Yael D. Hose and Frieder Seible. November 1999.
- PEER 1999/10** *U.S.-Japan Workshop on Performance-Based Earthquake Engineering Methodology for Reinforced Concrete Building Structures.* December 1999.
- PEER 1999/09** *Performance Improvement of Long Period Building Structures Subjected to Severe Pulse-Type Ground Motions.* James C. Anderson, Vitelmo V. Bertero, and Raul Bertero. October 1999.
- PEER 1999/08** *Envelopes for Seismic Response Vectors.* Charles Menun and Armen Der Kiureghian. July 1999.

- PEER 1999/07** *Documentation of Strengths and Weaknesses of Current Computer Analysis Methods for Seismic Performance of Reinforced Concrete Members.* William F. Cofer. November 1999.
- PEER 1999/06** *Rocking Response and Overturning of Anchored Equipment under Seismic Excitations.* Nicos Makris and Jian Zhang. November 1999.
- PEER 1999/05** *Seismic Evaluation of 550 kV Porcelain Transformer Bushings.* Amir S. Gilani, Andrew S. Whittaker, Gregory L. Fenves, and Eric Fujisaki. October 1999.
- PEER 1999/04** *Adoption and Enforcement of Earthquake Risk-Reduction Measures.* Peter J. May, Raymond J. Burby, T. Jens Feeley, and Robert Wood.
- PEER 1999/03** *Task 3 Characterization of Site Response General Site Categories.* Adrian Rodriguez-Marek, Jonathan D. Bray, and Norman Abrahamson. February 1999.
- PEER 1999/02** *Capacity-Demand-Diagram Methods for Estimating Seismic Deformation of Inelastic Structures: SDF Systems.* Anil K. Chopra and Rakesh Goel. April 1999.
- PEER 1999/01** *Interaction in Interconnected Electrical Substation Equipment Subjected to Earthquake Ground Motions.* Armen Der Kiureghian, Jerome L. Sackman, and Kee-Jeung Hong. February 1999.
- PEER 1998/08** *Behavior and Failure Analysis of a Multiple-Frame Highway Bridge in the 1994 Northridge Earthquake.* Gregory L. Fenves and Michael Ellery. December 1998.
- PEER 1998/07** *Empirical Evaluation of Inertial Soil-Structure Interaction Effects.* Jonathan P. Stewart, Raymond B. Seed, and Gregory L. Fenves. November 1998.
- PEER 1998/06** *Effect of Damping Mechanisms on the Response of Seismic Isolated Structures.* Nicos Makris and Shih-Po Chang. November 1998.
- PEER 1998/05** *Rocking Response and Overturning of Equipment under Horizontal Pulse-Type Motions.* Nicos Makris and Yiannis Roussos. October 1998.
- PEER 1998/04** *Pacific Earthquake Engineering Research Invitational Workshop Proceedings, May 14–15, 1998: Defining the Links between Planning, Policy Analysis, Economics and Earthquake Engineering.* Mary Comerio and Peter Gordon. September 1998.
- PEER 1998/03** *Repair/Upgrade Procedures for Welded Beam to Column Connections.* James C. Anderson and Xiaojing Duan. May 1998.
- PEER 1998/02** *Seismic Evaluation of 196 kV Porcelain Transformer Bushings.* Amir S. Gilani, Juan W. Chavez, Gregory L. Fenves, and Andrew S. Whittaker. May 1998.
- PEER 1998/01** *Seismic Performance of Well-Confined Concrete Bridge Columns.* Dawn E. Lehman and Jack P. Moehle. December 2000.